The lunar crust : a study of the lunar crust composition and organisation with spectroscopic data from the Moon Mineralogy Mapper

Mélissa Martinot

N° d'ordre NNT : 2019LYSE1206

THÈSE DE DOCTORAT DE L'UNIVERSITÉ DE LYON
opérée au sein de
l'Université Claude Bernard Lyon 1

École Doctorale N° 52
Physique et Astrophysique de Lyon
Discipline : **Sciences de la Terre et de l'Univers**

Soutenue publiquement le 07 octobre 2019, par :
Mélissa MARTINOT

LA CROÛTE LUNAIRE
Étude de la composition et de l'organisation de la croûte lunaire avec les données spectroscopiques de l'instrument Moon Mineralogy Mapper

---

Devant le jury composé de :

Sautter, Violaine	Directrice de Recherche CNRS, Université Paris 6	Rapporteure
Michaut, Chloé	Professeure, École Normale Supérieure de Lyon	Rapporteure
Donaldson-Hanna, Kerri	Associate Professor, University of Central Florida	Examinatrice
Klima, Rachel	Researcher, Johns Hopkins University	Examinatrice
Allemand, Pascal	Professeur, Université de Lyon (UCBL)	Examinateur
Davies, Gareth	Professor, Vrije Universiteit Amsterdam	Examinateur

Encadrants de thèse :

van Westrenen, Wim	Professor, Vrije Universiteit Amsterdam	Directeur de thèse
Quantin-Nataf, Cathy	Professeure, Université de Lyon (UCBL)	Directrice de thèse
Flahaut, Jessica	Chargée de Recherche, CRPG de Nancy	Co-directrice de thèse
Besse, Sébastien	Science coordinator for ESA's PSA, ESAC	Co-directeur de thèse

VRIJE UNIVERSITEIT

THE LUNAR CRUST

A study of the lunar crust composition and organisation with spectroscopic data from the Moon Mineralogy Mapper

ACADEMISCH PROEFSCHRIFT

ter verkrijging van de graad Doctor of Philosophy aan
de Vrije Universiteit Amsterdam,
op gezag van de rector magnificus
prof.dr. V. Subramaniam,
in het openbaar te verdedigen
ten overstaan van de promotiecommissie
van de Faculteit der Bètawetenschappen
op maandag 7 oktober 2019 om 13.45 uur
in de aula van de universiteit,
De Boelelaan 1105

door

Mélissa Martinot

geboren te Die, Frankrijk

promotoren:	prof.dr. W. van Westrenen prof.dr. C. Quantin-Nataf
copromotoren:	dr. J.D. Flahaut dr. S. Besse

Reading committee:
Prof. Dr. Gareth Davies (chairman)
prof.dr. Pascal Allemand
prof.dr. Violaine Sautter
dr. Kerri Donaldson-Hanna
dr. Rachel Klima
prof.dr. Chloé Michaut

This research was carried out at:

Vrije Universiteit Amsterdam
Faculty of Science
Amsterdam, the Netherlands

University of Lyon
Laboratoire de Géologie de Lyon: Terre, Planètes, Environnement
Lyon, France

THE LUNAR CRUST - A study of the lunar crust composition and organisation with spectroscopic data from the Moon Mineralogy Mapper

Authored by Mélissa Martinot

Credits for the front cover picture: Mélissa Martinot
Credits for the back cover picture: Clément Brustel

Contents

Acknowledgements

This section will not be very long, because I prefer to express my thanks in person rather than write them (it would be too long to list all persons involved in this experience being a success anyway!).

I would like to thank my supervisors and co-supervisors, who guided me through the PhD haze with their many good tips and words! I am seeing the light at the end of the tunnel now (finally!), thank you for your patience.

I would like to thank the reading committee and the members of the jury to take the energy and time to read this manuscript and assist to the defence, as well as their patience for the administrative hiccups during reviewing time.

I would also like to thank my colleagues from everywhere, it was nice to be able to talk to people going through the same haze, or to see that one can survive it!

Finally, I would like to thank my family and friends, who supported me, welcomed me in all kinds of happiness homes. I could find a place to relax and calm down at your places, which helped me tremendously.

Summary

Over the past 50 years, our knowledge of the Moon has grown immensely. Progress in lunar science occurred through several phases. The first phase happened in the 1960s and 70s, during the Apollo and Luna missions, with the study of samples returned from the lunar surface. Petrological characterisation of lunar samples sparked the Lunar Magma Ocean concept, from which ensued the traditional view of the lunar crust and mantle organisation: the crust is plagioclase-rich, and its mafic content increases with increasing depth. The lunar mantle is commonly thought to be olivine-rich, like that of the Earth. The second lunar exploration phase happened in the 1990s, when satellites were launched into lunar orbit, collecting the first global remote sensing datasets. Owing to their wide to global coverage, remote sensing brought new insight into lunar science that is complementary to that provided by lunar samples. During the third, current phase of lunar exploration, new datasets were collected by spacecrafts orbiting the Moon between the 2000s and today. The remote sensing datasets acquired during the second and third phases of lunar exploration progressively complicated the initially simple picture that scientists drew from earlier studies. Indeed, high resolution remote sensing images and radar data led to the identification of volcanic features (domes, irregular mare patches), and the unambiguous discovery of volatiles in permanently shadowed regions and in lunar samples originating at depth in the Moon, demonstrating the Moon's complex geological history.

During this PhD, impact craters were used as natural drill holes through the lunar crust to sample material located underneath the surface. During impact, rocks from depth are emplaced in crater central peaks through elastic rebound, making it possible to investigate the composition of the crust at depth. Spectroscopic data from Chandrayaan-1's Moon Mineralogy Mapper instrument were exploited to gather information on the composition of the crust in those central peaks.

In chapter 1, we present an algorithm for processing Moon Mineralogy Mapper spectroscopic data. The algorithm is tested on the mineralogical diversity Humboldt crater in order to validate it. Multiple pure crystalline plagioclase occurrences were detected in Humboldt crater's central peak, whereas olivine and spinel occurrences possibly linked to a plutonic event were detected in the walls of Humboldt crater.

In chapter 2, we investigate the central peaks and peak rings of 36 craters allegedly sampling material originating between +10 and −20 km around the crust-mantle interface. Our analysis points to the existence of lateral heterogeneities at the crust-mantle interface depth. The vertical transition from crust to mantle material is not sharp, but rather seems gradual. Indeed, although the composition of pyroxene changes with

depth from high-calcium to lower calcium contents, plagioclase was widely detected in craters allegedly sampling mantle material.

Chapter 3 shows that the anorthositic Feldspathic Highlands Terrane (FHT-a) crust does not become drastically more mafic with depth. However, data hint at a pyroxene compositional change with depth in the FHT-a crust, from high calcium to lower calcium contents. Our findings are in agreement with the recently proposed hypothesis that the lunar upper mantle is rich in low calcium pyroxene, rather than olivine.

Chapters 4 and 5 display how the algorithm developed during this thesis can be applied to provide key input for the mineral characterisation of landing sites for future lunar landings.

This work illustrates the use of remote sensing data on crater central peaks in order to constrain the shallow interior of the Moon. Remote sensing data can also be used to help locate which type of samples would need to be returned in the future from the lunar surface, in order to contribute to further elucidating the organisation of the lunar crust and upper mantle.

Samenvatting

In de afgelopen 50 jaar is onze kennis van de maan immens gegroeid. Vooruitgang in de maanwetenschap vond plaats in verschillende fasen. De eerste fase vond plaats in de jaren zestig en zeventig, tijdens de Apollo- en Luna-missies, met de studie van gesteentemonsters teruggebracht van het maanoppervlak. De petrologische karakterisering van maanmonsters leidde tot het "Lunar Magma Ocean" concept, waaruit de traditionele kijk op de organisatie van de maankorst en -mantel voortkwam: een plagioklaas-rijke korst waarvan de mafische inhoud toeneemt met toenemende diepte. De maanmantel wordt algemeen beschouwd als rijk aan olivijn, zoals die van de aarde. De tweede fase van maanverkenning vond plaats in de jaren negentig, toen satellieten in de baan van de maan werden gebracht en de eerste wereldwijde remote sensing-gegevens verzamelden. Door hun brede tot wereldwijde dekking heeft remote sensing nieuw inzicht in de maanwetenschap verschaft die complementair is aan dat van maanmonsters. Tijdens de derde, huidige fase van maanverkenning werden nieuwe gegevenssets verzameld door ruimtevaartuigen die sinds de jaren 2000 tot heden rond de maan draaien. De remote sensing-gegevens die tijdens de tweede en derde fase van de maanverkenning zijn verkregen, hebben het aanvankelijk eenvoudige beeld dat wetenschappers uit eerdere studies hebben getrokken, geleidelijk gecompliceerd. Hoge resolutie remote sensing-beelden en radargegevens hebben inderdaad geleid tot de identificatie van vulkanische kenmerken (koepels, onregelmatige mare vlakten) evenals de eenduidige ontdekking van vluchtige stoffen in permanent beschaduwde gebieden en in diepgevormde maanmonsters, duidend op de complexe geologische geschiedenis van de maan.

Tijdens dit doctoraat zijn inslagkraters gebruikt als natuurlijke boorgaten in de maanbodem om materiaal van onder het oppervlak te bemonsteren. Tijdens inslagen wordt gesteente uit de diepte verplaatst in de centrale pieken van kraters door middel van elastische terugslag, waardoor het mogelijk is om de samenstelling van de korst op diepte te onderzoeken. Spectroscopische gegevens van Chandrayaan-1's "Moon Mineralogy Mapper" instrument zijn gebruikt om informatie te verzamelen over de samenstelling van de korst in deze centrale pieken.

In hoofdstuk 1 presenteren we een algoritme voor de verwerking van spectroscopische gegevens afkomstig van de Moon Mineralogy Mapper. Het algoritme wordt getest op de mineralogische diversiteit van de Humboldt krater, teneinde het te valideren. De meervoudige aanwezigheid van zuiver kristallijn plagioklaas werd gedetecteerd in de centrale piek van de Humboldt krater, terwijl olivijn en spinel, mogelijk verband houdend met een plutonische gebeurtenis, werden gedetecteerd in de wan-

den van de Humboldt krater.

In hoofdstuk 2 onderzoeken we de centrale pieken en piekringen van 36 kraters waarvan wordt beweerd dat ze materiaal bemonsteren afkomstig van +10 tot −20 km rond de korst-mantelgrens. Onze analyse wijst op het bestaan van laterale heterogeniteiten ter diepte van de korst-mantelgrens. De verticale overgang van korst- naar mantelmateriaal is niet abrupt, maar lijkt geleidelijk. Hoewel de samenstelling van pyroxeen verandert met diepte, van hoog naar lager calciumgehalte, werd plagioklaas inderdaad op grote schaal gedetecteerd in kraters waarvan wordt beweerd dat ze mantelmateriaal bemonsteren.

Hoofdstuk 3 toont aan dat de anorthositische "Feldspathic Highlands Terrane (FHT-a)" korst niet drastisch meer mafisch wordt met toenemende diepte. Gegevens wijzen op een verandering in de samenstelling van pyroxeen met diepte in de FHT-a korst, van hoog naar lager calciumgehalte. Onze bevindingen komen overeen met de recent voorgestelde hypothese die stelt dat de bovenste maanmantel rijk is aan pyroxeen met een laag calciumgehalte, in plaats van olivijn.

Hoofdstukken 4 en 5 laten zien hoe het algoritme dat tijdens dit proefschrift is ontwikkeld, kan worden toegepast om belangrijke invoer te leveren voor de mineralogische karakterisering van landingsplaatsen voor toekomstige maanlandingen.

Dit proefschrift illustreert het gebruik van remote sensing-gegevens van kraterpieken om het ondiepe interieur van de maan te onthullen. Remote sensing-gegevens kunnen ook worden gebruikt ten behoeve van het bepalen welk type gesteentemonsters in de toekomst moeten worden teruggebracht vanaf het maanoppervlak, om bij te dragen aan de verdere opheldering van de organisatie van de maankorst en –bovenmantel.

Résumé

Au cours des cinquante dernières années, notre niveau de connaissance sur la Lune a fortement évolué. Les progrès en science lunaire sont survenus selon plusieurs phases. La première phase eut lieu pendant les missions Apollo et Luna dans les années 1960 et 1970, avec l'étude des échantillons de roches lunaires rapportées pendant les missions du même nom. La caractérisation pétrologique des échantillons lunaires a fait naître le concept d'Océan de Magma Lunaire, qui est à l'origine de la vue traditionnelle de la croûte et du manteau lunaires. Ce modèle prédit que la croûte lunaire est riche en plagioclase et que sa composition devient plus mafique en profondeur. Il est communément admis que le manteau lunaire est riche en olivine et qu'il contient du pyroxène, conformément au manteau terrestre. La seconde phase de l'exploration lunaire eut lieu dans les années 1990, lorsque des satellites lancés en orbite lunaire collectèrent les premiers jeux de données globaux de télédétection. En raison de leur couverture spatiale globale, les données de télédétection apportèrent une vision complémentaire à celle conférée par l'étude des échantillons lunaires. Pendant la troisième phase de l'exploration lunaire, qui a commencé dans les années 2000 et a toujours cours aujourd'hui, de nouveaux jeux de données ont été collectés par des satellites en orbite autour de la Lune. Les données de télédétection acquises durant ces deux dernières phases ont permis de prendre connaissance de processus complexes encore inconnus et de nuancer l'image initialement simple que les scientifiques se faisaient de la Lune. En effet, l'étude des jeux de données de haute résolution et des données radar a conduit à l'identification d'édifices volcaniques (dômes ; zones de mare irrégulières, dites irregular mare patches ou IMP), et à la découverte sans équivoque de volatils dans les régions ombragées en permanence. Des volatils ont également été découverts dans des échantillons lunaires issus de l'intérieur de la Lune, démontrant ainsi la complexité de l'histoire géologique de la Lune. Durant cette thèse, des cratères d'impact ont été utilisés comme forages naturels de la croûte lunaire. En effet, lors de l'impact, des roches profondes sont excavées et mises à l'affleurement dans le pic central du cratère par rebond élastique. Il est alors possible d'étudier la composition des roches crustales profondes en examinant le pic central d'un cratère à la surface d'une planète. Ici, le pic central de cratères échantillonnant la croûte lunaire a été étudié avec les données spectroscopiques de l'instrument Moon Mineralogy Mapper (Cartographe de la Minéralogie de la Lune, aussi noté M^3) à bord de la mission Chandrayaan-1.

Dans le premier chapitre, nous présentons un algorithme traitant les données spectroscopiques M^3. L'algorithme est validé en étudiant la diversité minéralogique

du pic central du cratère Humboldt. De multiples détections de plagioclase cristallin pur sont remarquées sur le pic central, alors que de l'olivine et du spinelle potentiellement mis en place suite à un événement plutonique sont détectés dans les murs du cratère Humboldt.

Dans le deuxième chapitre, nous sélectionnons 36 cratères dont le pic central (ou anneau central, dans le cas de plus grands cratères) échantillonne potentiellement du matériel originaire d'une profondeur comprise entre +10 et −20 km autour de l'interface croûte-manteau. Notre analyse montre la présence d'hétérogénéités latérales au niveau de l'interface croûte-manteau. La transition verticale de croûte à manteau n'est pas abrupte, mais semble au contraire graduelle. En effet, du plagioclase est détecté dans le pic central de cratères échantillonnant potentiellement du matériel mantellique. Cependant, la composition du pyroxène change avec la profondeur, depuis des compositions riches en calcium en surface, jusqu'à des compositions pauvres en calcium en profondeur.

Dans le troisième chapitre, nous montrons que la croûte anorthositique des hauts plateaux lunaires feldspathiques ne devient pas drastiquement plus mafique en profondeur. Les résultats suggèrent en revanche que le pyroxène change de composition avec la profondeur dans la croûte, encore une fois depuis des compositions riches en calcium en surface, jusqu'à des compositions pauvres en calcium en profondeur. Nos découvertes sont en accord avec l'hypothèse récemment émise par des confrères qui propose que le manteau lunaire supérieur est riche en pyroxène de composition pauvre en calcium, plutôt qu'en olivine. Les quatrième et cinquième chapitres montrent que l'algorithme développé pendant cette thèse peut être appliqué pour caractériser la minéralogie des sites d'atterrissage des prochaines missions lunaires.

Ce travail illustre l'utilisation de données de télédétection sur le pic central de cratères, dans l'optique de caractériser l'intérieur peu profond de la Lune. Les données de télédétection peuvent également être utilisées pour aider à cibler des régions à la surface de la Lune dont le retour d'échantillons pourrait donner des indices importants sur l'organisation de la croûte et du manteau supérieur lunaires.

0

Introduction

The Moon has been an object of wonder and study for millennia. During the fifth century BCE, the Greek philosopher Anaxagoras — who is thought to have been the first to discover the cause of eclipses — theorized that the Moon is an earthy lump (Curd [2015]). Due to its proximity to the Earth, the Moon was the nearest challenge for planetary exploration. To this day, it is the only other planetary surface upon which humankind has walked.

Short Summary of Lunar Exploration

In a span of 15 years in the 20^{th} century, our knowledge of the Moon increased drastically — from the first observation of its farside, to the collection of samples brought back by the Apollo astronauts and the Luna landers. In 1959, the first picture of the lunar farside was brought back by USSR's Luna 3 satellite. This picture revealed for the first time the stark difference between farside and nearside. Five years later, the first series of high resolution images of the lunar surface were returned by USA's Ranger 7 satellite. These pictures were used in order to study lunar surface properties, and helped to select the landing sites of future manned Apollo missions. Only five years later, the first man set foot on the lunar surface. The lunar farside surface remained untouched until the Chang'E-4 mission, 60 years after the first picture of the lunar farside was captured.

USA's Apollo program focused on manned missions. Apollo missions 11 through 17 brought back an ever increasing mass of samples (with the exception of the Apollo 13 mission), reaching a total of more than 381 kg. On the other hand, USSR's Luna program developed a fully automated sample mission concept, returning a total of 301.1 grams retrieved from the lunar surface.

The era of the Luna and Apollo programs enabled scientists from all countries to study a diversity of rocks brought back from the lunar surface. Most of these rocks are now stored in facilities that aim at preserving the pristine condition of the samples. Preserving material for the future allowed several generations of scientists to use an array of methods in order to study the samples with new techniques.

Emergence of the Lunar Magma Ocean Concept

Petrologic examination of the two rock types brought back from the Apollo 11 mission (basalts and anorthosites, Wood [1970]) sparked the idea that the Moon crystallized from a global Lunar Magma Ocean (LMO). Olivine and pyroxene crystallized first, while plagioclase started to crystallize after approximately half of the magma ocean was already solidified by cooling. Plagioclase was buoyantly separated from the magma, forming an anorthosite crust by flotation (e.g., Smith et al. [1970], Warren [1985], Wood [1970], Fig. 1). The analysis of lunar samples also showed that the Moon is depleted in volatile and siderophile elements with respect to the average composition of the solar system (Taylor and Jakes [1975], Wetherill [1971]). The depletion in volatile elements of the bulk Moon was taken into account in later experimental petrology studies, in order to establish the crystallization sequence of the LMO ("dry" magma ocean in Fig. 2).

The magma ocean concept rapidly spread in the lunar community. However, the depth of the magma ocean, and the thickness and composition of the crust resulting from magma ocean processes were debated.

Upon examination of the topography difference between the maria and the highlands, O'Keefe [1968] postulated that the material constituting the highlands must be lighter than that of the maria. Later on, Wood et al. [1970] proposed that a 25 km thick anorthosite crust floats on a gabbro layer, and acknowledged that a substantial part of the Moon had to be molten in order to allow the formation of a 25 km thick anorthosite layer. Several studies tried to give an estimate of the initial depth of the magma ocean. Assessments span a wide range, from 200 to 400 km (Shirley [1983], Solomon and Chaiken [1976]), to 1000 km (Elkins-Tanton et al. [2011]), to whole-Moon melting (> 1200 km, Steenstra et al. [2016]).

The nearside-farside topography difference is not the only sign of nearside-farside asymmetry. Crustal thickness models and compositional datasets also bear a nearside-farside asymmetry, which hints at a different nearside-farside crystallisation and evolution story. The question of how the nearside-farside asymmetry influences the crust-mantle interface remains open.

Remote Sensing Surveys

In the 1990s, the first orbital gravimetric and geochemical signature of the lunar surface were retrieved from satellites sent to the Moon. More remote sensing missions

were sent to the Moon at the end of the 2000s, acquiring new datasets, among which new gravimetric data, high resolution images, and multispectral and hyperspectral data.

The Clementine and Lunar Prospector missions retrieved the first global gravimetric and geochemical data from the lunar surface, allowing the definition of three major lunar terranes Jolliff et al. [2000]: the Procellarum KREEP Terrane (PKT), the Feldspathic Highlands Terrane (FHT), and the South-Pole Aitken Terrane (SPAT). Data from the Clementine mission were used in order to derive the first crustal thickness maps, ranging from an average of 68 km on the farside, and 60 km on the nearside (Zuber et al. [1994]).

Insight into the surface mineralogy was provided by the Clementine UltraViolet-Visible camera multispectral data. These data allowed Tompkins and Pieters [1999] to study the diversity of the lunar crust laterally and vertically with impact craters, and suggest an evolution of the mineralogical composition with depth.

The Gravity Recovery and Interior Laboratory (GRAIL) mission was sent into lunar orbit in 2011, and acquired new gravimetric data from the Moon. Four crustal thickness models were derived from these data, with a crustal thickness average comprised between 34 and 43 km (Wieczorek et al. [2013]), significantly thinner than the estimates obtained from the Clementine data.

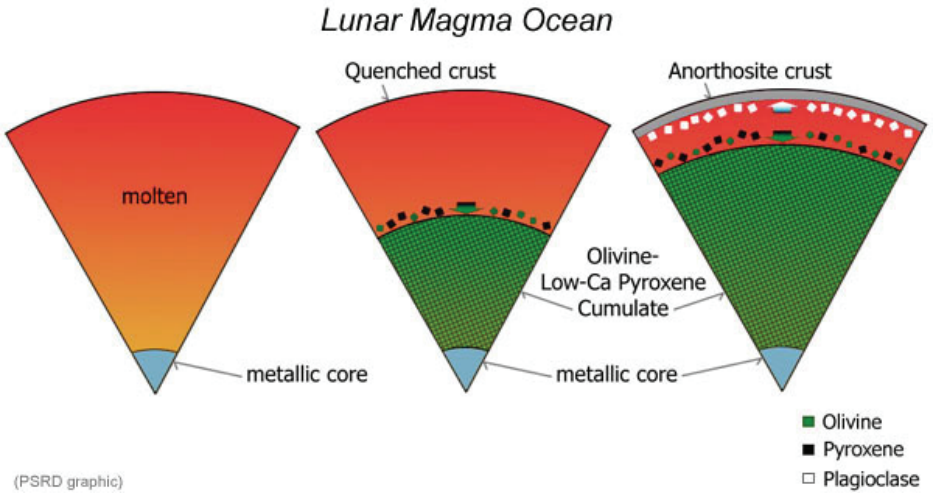

Figure 1: Illustration of the Lunar Magma Ocean concept. At first, the Moon is partially or totally molten. Olivine and pyroxene start to crystallize from the magma ocean. Due to their high density, they sink to the bottom of the magma ocean. The anorthositic crust is formed when plagioclase starts crystallizing from the magma ocean. Lighter, plagioclase floats to the surface of the magma ocean, creating a crust by flotation. Credits: Planetary Science Research Discoveries web page, available at `http://www.psrd.hawaii.edu`.

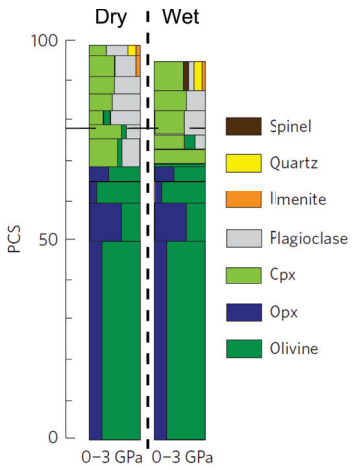

Figure 2: Difference of the crystallisation sequence in a magma ocean 700 km deep: a "dry" magma ocean, and a "wet" magma ocean (containing 3150 ppm water). Modified from Lin et al. [2017]. The vertical axis represents the percentage of solidification by volume.

Visible near-infrared spectroscopy can provide constraints on the chemical make-up of the minerals constituting a planetary surface, and its composition. Indeed, Adams [1975] discussed the uniqueness of rock-forming mineral absorption bands in the visible near-infrared domain (350 nm to 2500 nm), and showed that most of the rock-forming minerals can be distinguished from each other based on their reflectance spectra.

Several visible near-infrared imaging spectrometers were sent to the Moon in the 2000s, with better spatial and/or spectral resolution than earlier mission instruments: Kaguya's Spectral Profiler and Multiband Imager from 2007 to 2009; Chandrayaan-1's Moon Mineralogy Mapper (M^3) from 2008 to 2009. During this PhD project, reflectance data from M^3 were used.

Discovery of Water in the Moon

The view of a volatile-depleted Moon persisted through time and was incorporated in the crystallisation models of LMO ("dry" system in Fig. 2). However, Saal et al. [2008] recently re-analysed the composition and volatile content of pyroclastic glass beads sampled during the Apollo missions. They measured significant amounts of water in these beads, overthrowing the view of a dry Moon. The presence of water on the lunar surface was later confirmed by remote sensing surveys using M^3 data (Klima et al. [2013], Li et al. [2018]). The presence of volatiles in the Moon has to be accounted for in magma ocean crystallisation models, as well as thermal evolution models. Experimental petrology studies have been conducted in order to understand the effect of water on the LMO crystallisation sequence. Lin et al. [2017] showed that the two major differences between a volatile-rich and a volatile-poor magma ocean are the production of a thin crust in the presence of water (40 km with water *versus*

67.5 km without water, see Fig. 2), and the crystallisation of spinel in the later stage of the wet magma ocean solidification. Based on this work, the presence of water in the magma ocean produces a crustal thickness compatible with crustal thickness models from the GRAIL mission data.

Mineralogy of the lunar crust

Owing to their global coverage, remote sensing datasets are complementary to the lunar samples retrieved from nine locations of the lunar nearside, combining the Apollo and Luna missions sampling sites. Spectroscopic datasets can also be used in order to investigate the crustal column, using complex impact craters. Indeed, complex impact craters act as natural drill holes through the lunar crust, bringing material from depth to the surface (Melosh [1996]). This makes impact craters important for studying the lunar crust architecture using remote sensing data, and to test the LMO crystallisation sequence.

Several surveys investigated the global mineralogy of the lunar crust. The results of Tompkins and Pieters [1999] point at a compositionally diverse lunar crust: pure anorthositic, gabbroic, noritic, troctolitic rocks, as well as mixtures of these rocks were detected throughout the lunar crust. Cahill et al. [2009] showed that the mineralogy of the lunar crust varies with crustal thickness: portions of the lunar surface where the crust is thick are generally more plagioclase-rich than portions of the lunar surface where the crust is thin. What is more, the results from Cahill et al. [2009] are consistent with an increase of the proportion of mafic minerals (olivine, pyroxene) with increasing crustal depth. This result was also pointed at by several other surveys (Ryder and Wood [1977], Spudis and Davis [1986], Tompkins and Pieters [1999]), while observations from other studies debate it (Lemelin et al. [2015], Martinot et al. [2018], Song et al. [2013]). A thick, global anorthosite layer buried at depth in the crust was identified with data from three multi-spectral and hyper-spectral instruments (Donaldson Hanna et al. [2014], Hawke et al. [2003], Ohtake et al. [2009], Yamamoto et al. [2012]).

Outline of the thesis

During this PhD project, many of the themes linked to the lunar crust mentioned above were tackled. During the first part of the PhD, an algorithm for removing the continuum on M^3 spectroscopic data was developed and applied to the M^3 mosaic of Humboldt crater in order to verify if the M^3 data processing was valid. The second part of the PhD focused on the investigation of the lateral evolution of the crust-mantle interface, and the characterization of the compositional change at the crust-mantle interface (is the transition from crust to mantle material sharp, gradual?). In the third part of the PhD, I used a similar approach as that used in the second part of the PhD, focusing on the architecture of the crust with craters located in the lunar highlands.

The chapters that follow are a reproduction of the scientific articles published in, or to be submitted to, peer-reviewed journals in the course of this project (chapters 1–3). I also had the opportunity to apply the techniques developed during this thesis to characterize the mineralogy of the landing sites for two Chinese Moon missions, enabling me to contribute directly to today's lunar exploration. Two scientific articles I co-authored (chapters 4 and 5) were published as part of this collaboration.

Bibliography

J. B. Adams. Interpretation of visible and near-infrared diffuse reflectance spectra of pyroxenes and other rock-forming minerals. In *Infrared and Raman Spectroscopy of Lunar and Terrestrial Minerals*, pages 91–116. Academic Press, INC., 1975. doi: 10.1016/B978-0-12-399950-4.50009-4.

J. T. S. Cahill, P. G. Lucey, and M. A. Wieczorek. Compositional variations of the lunar crust: Results from radiative transfer modeling of central peak spectra. *Journal of Geophysical Research E: Planets*, 114(9): 1–17, 2009. ISSN 01480227. doi: 10.1029/2008JE003282.

P. Curd. *Anaxagoras*. The Stanford Encyclopedia of Philosophy, 2015.

K. L. Donaldson Hanna, L. C. Cheek, C. M. Pieters, J. F. Mustard, B. T. Greenhagen, I. R. Thomas, and N. E. Bowles. Global assessment of pure crystalline plagioclase across the Moon and implications for the evolution of the primary crust. *Journal of Geophysical Research: Planets*, 119:1516–1545, 2014. doi: 10.1002/2013JE004476.

L. T. Elkins-Tanton, S. Burgess, and Q. Z. Yin. The lunar magma ocean: Reconciling the solidification process with lunar petrology and geochronology. *Earth and Planetary Science Letters*, 304(3-4):326–336, 2011. ISSN 0012821X. doi: 10.1016/j.epsl.2011.02.004.

B. R. Hawke, C. A. Peterson, D. T. Blewett, D. B. J. Bussey, P. G. Lucey, G. J. Taylor, and P. D. Spudis. Distribution and modes of occurrence of lunar anorthosite. *Journal of Geophysical Research*, 108(E6):1–16, 2003. ISSN 0148-0227. doi: 10.1029/2002JE001890.

B. L. Jolliff, J. J. Gillis, L. A. Haskin, R. L. Korotev, and M. A. Wieczorek. Major lunar crustal terranes: Surface expressions and crust-mantle origins. *Journal of Geophysical Research*, 105(E2):4197, 2000. ISSN 0148-0227. doi: 10.1029/1999JE001103.

R. Klima, J. Cahill, J. Hagerty, and D. Lawrence. Remote detection of magmatic water in Bullialdus Crater on the Moon. *Nature Geoscience*, 6(9):737–741, 2013. ISSN 1752-0894. doi: 10.1038/ngeo1909.

M. Lemelin, P. G. Lucey, E. Song, and G. J. Taylor. Lunar central peak mineralogy and iron content using the Kaguya Multiband Imager: Reassessment of the compositional structure of the lunar crust. *Journal of Geophysical Research: Planets*, 120(5):869–887, 2015. doi: 10.1002/2014JE004778.

S. Li, P. G. Lucey, R. E. Milliken, P. O. Hayne, E. Fisher, J.-P. Williams, D. M. Hurley, and R. C. Elphic. Direct evidence of surface exposed water ice in the lunar polar regions. *Proceedings of the National Academy of Sciences of the USA*, 115(36):8907–8912, 2018. doi: 10.1073/pnas.1802345115.

Y. Lin, E. J. Tronche, E. S. Steenstra, and W. van Westrenen. Evidence for an early wet Moon from experimental crystallization of the lunar magma ocean. *Nature Geoscience*, 1(November):1–6, 2017. ISSN 1752-0894. doi: 10.1038/ngeo2845.

M. Martinot, J. Flahaut, S. Besse, C. Quantin-Nataf, and W. van Westrenen. Compositional variations in the vicinity of the lunar crust-mantle interface from Moon Mineralogy Mapper data. *Journal of Geophysical Research: Planets*, 123, 2018. doi: 10.1029/2018JE005744.

H. J. Melosh. *Impact Cratering A Geologic Process*. Oxford University Press, New York, Oxford, 1996.

M. Ohtake, T. Matsunaga, J. Haruyama, Y. Yokota, T. Morota, C. Honda, Y. Ogawa, M. Torii, H. Miyamoto, T. Arai, N. Hirata, A. Iwasaki, R. Nakamura, T. Hiroi, T. Sugihara, H. Takeda, H. Otake, C. M. Pieters, K. Saiki, K. Kitazato, M. Abe, N. Asada, H. Demura, Y. Yamaguchi, S. Sasaki, S. Kodama, J. Terazono, M. Shirao, A. Yamaji, S. Minami, H. Akiyama, and J.-L. Josset. The global distribution of pure anorthosite on the Moon. *Nature*, 461(7261):236–240, 2009. ISSN 0028-0836. doi: 10.1038/nature08317.

J. A. O'Keefe. Isostasy on the moon. *Science*, 162(3860):1405–1406, 1968. ISSN 00368075. doi: 10.1126/science.162.3860.1405.

G. Ryder and J. A. Wood. Serenitatis and Imbrium impact melts: Implications for large-scale layering in the lunar crust. In *Proc. Lunar Sci. Conf. 8th*, pages 655–668, 1977. ISBN 9780874216561. doi: 10.1007/s13398-014-0173-7.2.

A. E. Saal, E. H. Hauri, M. L. Cascio, J. A. Van Orman, M. C. Rutherford, and R. F. Cooper. Volatile content of lunar volcanic glasses and the presence of water in the Moon's interior. *Nature*, 454(July):192–195, 2008. ISSN 0028-0836. doi: 10.1038/nature07047.

D. N. Shirley. A partially molten magma ocean model. *Journal of Geophysical Research: Solid Earth (1978–2012)*, 88(S02):A519–A527, 1983. ISSN 2156-2202. doi: 10.1029/JB088iS02p0A519.

J. V. Smith, A. T. Anderson, R. C. Newton, E. J. Olsen, P. J. Wyllie, A. V. Crewe, M. S. Isaacson, and D. Johnson. Petrologic history of the moon inferred from petrography, mineralogy, and petrogenesis of Apollo 11 rocks. *Proceedings of the Apollo 11 Lunar Science Conference*, 1:897–925, 1970.

S. C. Solomon and J. Chaiken. Thermal expansion and thermal stress in the Moon and terrestrial planets: Clues to early thermal history. In *Lunar Science Conference 7th*, volume 7th, pages 3229–3243, 1976.

E. Song, J. L. Bandfield, P. G. Lucey, B. T. Greenhagen, and D. A. Paige. Bulk mineralogy of lunar crater central peaks via thermal infrared spectra from the Diviner Lunar Radiometer: A study of the Moon's crustal composition at depth. *Journal of Geophysical Research E: Planets*, 118(4):689–707, 2013. ISSN 01480227. doi: 10.1002/jgre.20065.

P. D. Spudis and P. A. Davis. A chemical and petrological model of the lunar crust and implications for lunar crustal origin. *Journal of Geophysical Research*, 91:E84–E90, 1986. ISSN 0148-0227. doi: 10.1029/JB091iB13p00E84.

E. S. Steenstra, N. Rai, J. S. Knibbe, Y. H. Lin, and W. van Westrenen. New geochemical models of core formation in the Moon from metal – silicate partitioning of 15 siderophile elements. *Earth and Planetary Science Letters*, 441:1–9, 2016. ISSN 0012-821X. doi: 10.1016/j.epsl.2016.02.028.

S. R. Taylor and P. Jakes. The geochemical evolution of the moon. In *Lunar and Planetary Science Conference*, 1975.

S. Tompkins and C. M. Pieters. Mineralogy of the Lunar Crust - Results From Clementine. *Meteoritics & Planetary Science*, 34:25–41, 1999.

P. H. Warren. The magma ocean concept and lunar evolution. *Annual Review of Earth and Planetary Science*, 13:201–40, 1985. ISSN 00846597. doi: 10.1146/annurev.earth.13.1.201.

G. W. Wetherill. Of time and the moon. *Science*, 173(3995):383–392, 1971. ISSN 00368075. doi: 10.1126/science.173.3995.383.

M. A. Wieczorek, G. A. Neumann, F. Nimmo, W. S. Kiefer, G. J. Taylor, H. J. Melosh, R. J. Phillips, S. C. Solomon, J. C. Andrews-Hanna, S. W. Asmar, A. S. Konopliv, F. G. Lemoine, D. E. Smith, M. M. Watkins, J. G. Williams, and M. T. Zuber. The crust of the Moon as seen by GRAIL. *Science (New York, N.Y.)*, 339 (6120):671–5, 2013. ISSN 1095-9203. doi: 10.1126/science.1231530.

J. A. Wood. Petrology of the lunar soil and geophysical implications. *Journal of Geophysical Research*, 75 (32):6497–6513, 1970. ISSN 01480227. doi: 10.1029/JB075i032p06497.

J. A. Wood, J. S. Dickey, U. B. Marvin, and B. N. Powell. Lunar anorthosites. *Science*, 167(3918):602–604, 1970. ISSN 00368075. doi: 10.1126/science.167.3918.602.

S. Yamamoto, R. Nakamura, T. Matsunaga, Y. Ogawa, Y. Ishihara, T. Morota, N. Hirata, M. Ohtake, T. Hiroi, Y. Yokota, and J. Haruyama. Massive layer of pure anorthosite on the Moon. *Geophysical Research Letters*, 39(13):1–6, 2012. ISSN 00948276. doi: 10.1029/2012GL052098.

M. T. Zuber, D. E. Smith, F. G. Lemoine, and G. A. Neumann. The shape and internal structure of the moon from the clementine mission. *Science (New York, N.Y.)*, 266(1974):1839–1843, 1994. ISSN 0036-8075. doi: 10.1126/science.266.5192.1839.

1

Mineralogical diversity and geology of Humboldt crater derived using Moon Mineralogy Mapper data

This chapter is the reproduction of an article published in the Journal of Geophysical Research: Planets.

M. Martinot[1,2], S. Besse[3], J. Flahaut[4], C. Quantin-Nataf[2], L. Lozac'h[2], and W. van Westrenen[1]

[1]Faculty of Science, Vrije Universiteit Amsterdam, De Boelelaan 1085, 1081 HV Amsterdam, The Netherlands
[2]Université Lyon 1, ENS-Lyon, CNRS, UMR 5276 LGL-TPE, F-69622, Villeurbanne, France
[3]European Space Astronomy Centre, P.O. Box 78, 28691 Villanueva de la Canada, Madrid, Spain
[4]Institut de Recherche en Astrophysique et Planétologie, CNRS/UMR 5277, Université Paul Sabatier, 31400 Toulouse, France

Corresponding author: Mélissa Martinot (m.martinot@vu.nl)

Keypoints:

- Multiple pure crystalline plagioclase are detected in the Humboldt crater central uplift, hinting at its crustal origin.

- Olivine, spinel and glass occurrences are detected in the Humboldt crater walls and rim, suggesting a shallow origin of these minerals, potentially linked to a plutonic intrusion.
- Crater counts performed on the Humboldt crater volcanic deposits suggest that volcanic activity in Humboldt crater spanned over a billion years.

Abstract

Moon Mineralogy Mapper (M^3) spectroscopic data and high resolution imagery datasets were used to study the mineralogy and geology of the 207 km diameter Humboldt crater. Analyzes of M^3 data, using an improved method for M^3 spectra continuum removal and spectral parameters calculation, reveal multiple pure crystalline plagioclase detections within the Humboldt crater central uplift, hinting at its crustal origin. However, olivine, spinel and glass are observed in the crater walls and rims, suggesting these minerals derive from shallower levels than the plagioclase of the central uplift. High-Calcium pyroxenes are detected in association with volcanic deposits emplaced on the crater's floor. Geologic mapping was performed, and the age of Humboldt crater's units was estimated from crater counts. Results suggest that volcanic activity within this floor-fractured crater spanned over a billion years. The felsic mineralogy of the central uplift region, which presumably excavated deeper material, and the shallow mafic minerals (olivine and spinel) detected in Humboldt crater walls and rim are not in accordance with the general view of the organization of the lunar crust. Our observations can be explained by the presence of a mafic pluton emplaced in the anorthositic crust prior to the Humboldt-forming impact event. Alternatively, the excavation of Australe basin ejecta could explain the observed mineralogical detections. This highlights the importance of detailed combined mineralogical and geological remote sensing studies to assess the heterogeneity of the lunar crust.

1.1. Introduction

Studies of the organization of the lunar crust are important to constrain the magmatic and thermal evolution of the Moon [e.g., Shearer et al., 2006]. The Lunar Magma Ocean (LMO) concept predicts that the upper part of the lunar crust was formed by floatation of plagioclase on a magma ocean, forming a > 90 % plagioclase-rich, anorthositic upper crust [e.g., Kaula, 1979, Warren, 1985]. Denser minerals formed during the earlier stages of magma ocean crystallization (such as olivine and pyroxene) sank to the bottom the magma ocean, forming the lower crust and mantle [e.g., Lin et al., 2017, Snyder et al., 1992].

A diversity of studies using different remote sensing data have been conducted in order to establish a lunar crustal stratigraphy. Many of these focus on the mineralogical composition of the central uplift of impact craters, where material originating from greater depths is exposed [Cintala & Grieve, 1998]. Scaling laws exist to estimate the depth of origin of central uplift material, which is a function of the crater's diameter [e.g., Cintala & Grieve, 1998, Melosh, 1989]. Tompkins & Pieters [1999] studied the mineralogy of lunar crater's central peaks with Clementine data, and Wieczorek & Zuber [2001] linked the results with Clementine crustal thickness models. The authors observed an increase of the mafic mineral content with depth. More recently, [Song et al., 2013] used Lunar Reconnaissance Orbiter (LRO) Diviner data to calculate the Christiansen Feature (CF) value of lunar crater's central peaks. The CF value is an infrared emission maximum, the position of which is indicative of bulk mineralogy [Logan et al., 1973]. Lemelin et al. [2015] worked with the SElenological and ENgineering Explorer (SELENE) Kaguya Multiband Imager (MI) data, which provides visible near-infrared multispectral images with 5 spectral channels. Both the Song et al. [2013] and Lemelin et al. [2015] studies highlight variations in crustal composition that deviate from the global understanding of the lunar stratigraphy, pointing at the existence of significant heterogeneities within the crust. Head & Wilson [1992] proposed that buoyant diapirs of mantle might have intruded the base of the anorthositic crust during magma ocean crystallization, forming such heterogeneities.

Because the material emplaced in a crater's central uplift originates from deeper than the material observed in the crater's walls, floor and ejecta, detailed mineralogical and geological studies of impact craters can provide constraints on local crustal organization. Here, we assess the mineralogy, geology, and morphology of the Humboldt crater uplift, floor, walls and rim using Moon Mineralogy Mapper (M^3) spectroscopic data, combined with high resolution imagery datasets. We present an improved method to remove the continuum of M^3 spectra and to calculate spectral parameters. Our observations are aimed at shedding new light on the geology, mineralogy, and local crustal organization of the Humboldt area.

1.2. Humboldt Crater

Humboldt crater (27°S, 80.9°W) is a complex crater, 207 km in diameter, located on the eastern limb of the Moon. It was mapped as Upper Imbrian in age by Wilhelms & El-Baz [1977]. It is surrounded by Hecataeus crater (167 km in diameter) to the North, Phillips crater (122 km in diameter) to the West, and Barnard crater (105 km in diameter) to the South-East (Fig. 1.1.a). Four volcanic deposits are emplaced on the Humboldt crater floor, identified as pyroclastic in nature by Gaddis et al. [2003], (arrows in Fig. 1.1.a). The Humboldt crater floor displays numerous radial and concentric fractures [Baldwin, 1968] leading to its classification as a floor-fractured crater, interpreted to be formed by a magmatic intrusion beneath the crater floor [Schultz, 1976]. The observation of vents associated with fractures on the floor of Humboldt

crater by Jozwiak et al. [2016a] supports the presence of a magmatic intrusion beneath the crater floor. The northern part of the crater floor is slightly higher in elevation and more rugged than the southern part [Wilhelms et al., 1987]. A central alignment oriented South-West/North-East and extending from the center of the crater to the rim of the North-East pyroclastic deposit is observed (Fig. 1.1.a and b). The northern part of the central uplift is connected with this peak alignment, which complicates the distinction between central uplift material and peak alignment material. This peak alignment has been described as a *Centralkette* (central chain) by Beer & Madler [1837] and a line of peaks by Wilhelms et al. [1987]. The central uplift of Humboldt crater is made of several elements arranged circularly (Fig. 1.1.a). Based on this observation, Baker et al. [2011] proposed that Humboldt crater is at the transition between a central peak crater and a peak ring basin.

During their global crystalline plagioclase assessment of the lunar crust, Donaldson Hanna et al. [2014] described multiple occurrences of pure crystalline plagioclase (< 1 % olivine and pyroxene in the rock) in the Humboldt crater central uplift. Song et al. [2013] calculated the CF value of the Humboldt crater central uplift and also found that it is consistent with an anorthositic composition. Yamamoto et al. [2010] detected olivine located on the floor of Humboldt crater using Kaguya Spectral Profiler (SP) data. In their study, Gaddis et al. [2003] used Clementine data to analyze the composition of lunar pyroclastic deposits. They plotted Clementine color ratios data at 415/750 nm versus 950/750 nm and found that the Humboldt volcanic deposits plot in the uncontaminated, mature mare soils field from Staid [2000].

1.3. Datasets and Methods

1.3.1. Remote Sensing Data

Moon Mineralogy Mapper

The mineralogy of Humboldt crater was derived from spectroscopic data from the Moon Mineralogy Mapper (M^3) instrument. M^3 is a hyperspectral imager that acquired visible to near-infrared data from the lunar surface between 2008 and 2009, with a spectral range spanning from 430 to 3000 nm over 85 spectral channels [Pieters et al., 2009]. The M^3 data used in this study are the calibrated data archived in the Planetary Data System (PDS, version 1 of Level 2, Besse et al. [2013], Boardman et al. [2011], Clark et al. [2011], Green et al. [2011], Pieters et al. [2009]) from the OP2C1 period of observations, and have a spatial resolution of 280 m/pixel.

High Resolution Images – Lunar Reconnaissance Orbiter and Kaguya Cameras

The geologic context of Humboldt crater and its surroundings was studied with the Lunar Reconnaissance Orbiter Wide Angle Camera (LRO WAC) global map at a resolution of 100 meters per pixel (Robinson et al. [2010], downloaded from the PDS). Kaguya's Terrain Camera (TC) mosaics (with a resolution of 10 meters per pixel) were

used to obtain higher resolution data of the Humboldt crater floor (Haruyama et al. [2008], downloaded from the SELENE data archive: `http://l2db.selene.darts.isas.jaxa.jp/index.html.en`). Crater counts were performed on both TC images and WAC mosaics, and used for age determination with the craterstats tool (Neukum [1983] `http://www.geo.fu-berlin.de/en/geol/fachrichtungen/planet/software/index.html`).

Elevation Data

The Lunar Orbiter Laser Altimeter (LOLA) global Digital Elevation Model (DEM) and LOLA/SELENE TC merged stereo-derived DEMs provide elevation data with 118 and 59 meters per pixel resolution at the equator, respectively [Barker et al., 2016, Smith et al., 2010]. The elevation data was downloaded from the PDS. It enabled us to discriminate the crater central uplift from the crater floor and study the crater topography and geometry.

1.3.2. Extraction of Spectral Parameters

We developed an IDL (Interactive Data Language) algorithm that performs a spectrum analysis on the M^3 reflectance spectra. With the routine, a continuum is automatically removed and band center locations are defined. This approach is similar to the automatic detection of band centers from Horgan et al. [2014]. Horgan et al. [2014] used an upper convex hull to find the spectrum continuum, whereas in this study, linear segments connect the modeled continuum to the original spectrum in points called tie points. The algorithm maximizes the area of lunar mafic minerals and plagioclase absorption bands at 1000 and 2000 nm. The tie points are searched for in fixed intervals (620–1100 nm; 1100–1660 nm) on a spectrum smoothed with a boxcar algorithm with a width of 3 spectral channels in order to limit noise influence on the tie point positions. The highest wavelength tie point position is fixed at 2700 nm. Continuum removal is performed by dividing the initial spectrum by the continuum interpolated spectrum. The two band center locations are extracted from the minimum reflectance of a 4th order polynomial fit around the absolute minimum (400 nm interval) of the original spectrum in the corresponding band. An example of the steps followed in our routine is shown in Fig. 1.2.

The intervals in which a search for the tie points and band centers is performed are optimized for pure mineral occurrences (pyroxenes, olivine, plagioclase and spinel). Spectra displaying complex absorption bands as a result of a mixture between several mineralogical phases might therefore not be processed correctly. Reflectance data at wavelengths lower than 620 nm were not considered because of the low signal-to-noise ratio recovered in this part of the spectrum [Green et al., 2011]. Reflectance data at wavelengths beyond 2700 nm were not considered: the thermal calibration is not optimal in this spectral domain [Clark et al., 2011]. Moreover, Pieters et al. [2009] discovered hydroxyl and water signatures in lunar spectra at these high wavelengths

Table 1.1: List of the Spectral Parameters Calculated by our IDL Routine.
n equals 1 for the 1 μm absorption band, or 2 for the 2 μm absorption band.

Parameter	Notation	Definition
Tie point 1	TP1	Position of the first tie point
Tie point 2	TP2	Position of the second tie point
Band minimum	B_nMIN	Position of the lowest value of the spectrum between 2 tie points
Band center	B_nCEN	Position of the minimum of a fitted 4^{th} degree polynomial, ± 200 nm from the band minimum
Band depth	BD_n	1 − the reflectance value of the band center
Band area	B_nAREA	The sum of the band depth of each spectral channel in the absorption band multiplied by the spectral resolution
Band asymmetry	B_nASYM	Percentage of difference between the area at the left and at the right of the band center, divided by the band area
Interband distance	INTERD	Difference between the position of the band center of the 1000 and the 2000 nm absorption band

that can significantly affect the location of the tie points.

After removing the continuum from the spectra, a number of spectral parameters were derived or calculated for each spectrum (Table 1.1). This spectrum study is repeated on each pixel of the M^3 mosaic, and several data products are extracted: a continuum-removed mosaic is generated, as well as spectral parameter mosaics, where all the spectral parameters calculated are stored as maps.

The parameter maps are then refined using filters to remove noise: all the pixels with a band depth inferior to 2 % are not displayed. Filtered parameter maps are used to make color composites, and stretched using ENVI to highlight pixels displaying spectral characteristics inherent to lunar mineralogy. The spectra corresponding to the displayed pixels are then manually checked and confronted to relevant laboratory spectra (e.g., absorption band center, band asymmetry, shoulders position) in order to confirm or reject a mineralogical detection. The color composites are then imported in a GIS software and compared with other existing datasets. These include the global mosaic of the LRO WAC to visualize the geological context, the LOLA/SELENE TC merged stereo-derived DEM to provide elevation informations, and Kaguya TC mosaics to yield high resolution images.

1.4. Results

1.4.1. Mineralogical Detections

Burns [1970b] showed that minor amounts of FeO (< 1.0 wt%) can be incorporated in lunar calcic plagioclase. Iron-bearing plagioclase is characterized by a diagnostic absorption band centered at 1250 nm [Adams & Goullaud, 1978]. However, as Cheek. et al. [2009] pointed out, olivine and pyroxene absorption bands dominate the near-infrared spectra. In a plagioclase-dominated mixture, as little as 2 vol% of olivine or pyroxene has a strong effect on the bulk spectrum [Cheek & Pieters, 2014], to the extent that plagioclase would not be identifiable in the spectra. Therefore, detecting plagioclase with near-infrared spectra provides a constraint on the plagioclase content of the rock to be superior or equal to 98 % [Donaldson Hanna et al., 2014, Ohtake et al., 2009]. In the selected color composite shown in Fig. 1.3.a and b, plagioclase detections are highlighted in colors from blue to pink, with increasing absorption band strength. Plagioclase is widely detected across the central uplift of Humboldt crater (Fig. 1.3.b), therefore suggesting the presence of nearly pure anorthosites. Fig. 1.3.c gives an example of a typical plagioclase spectrum detected in the central uplift of Humboldt crater. No pure crystalline plagioclase is detected on the linear mountain range.

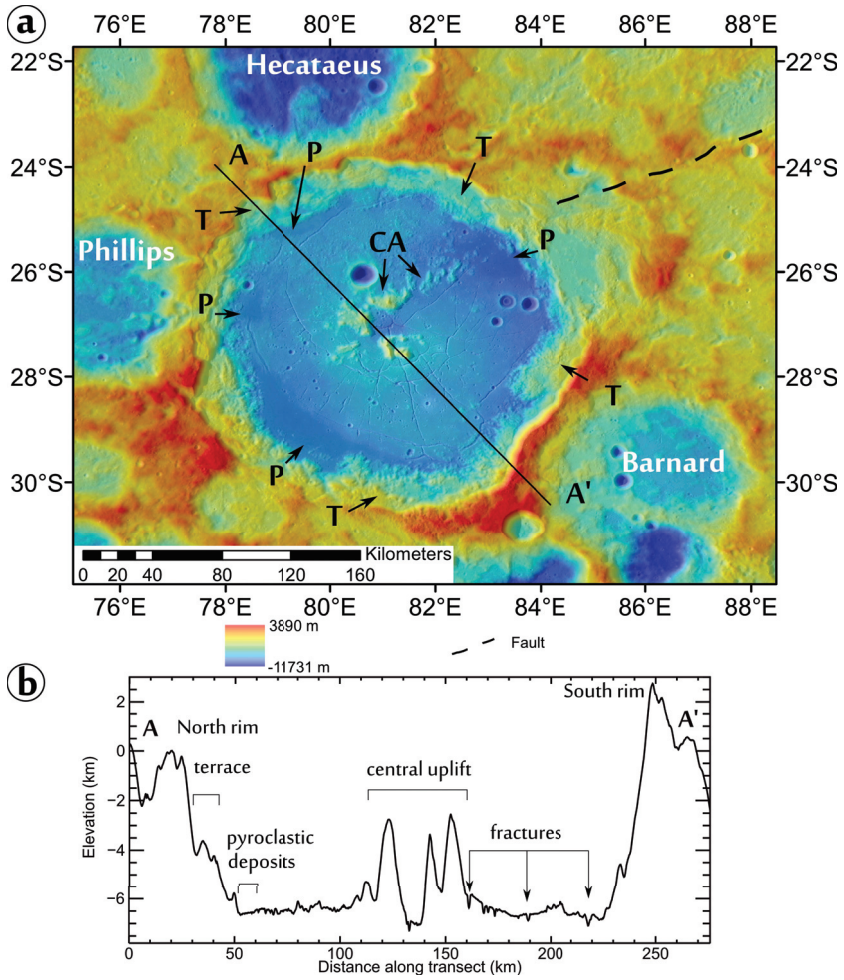

Figure 1.1: Geological context of Humboldt crater. **a**. General view of Humboldt crater and nearby craters with a Lunar Orbiter Laser Altimeter (LOLA) and Kaguya Terrain Camera (TC) merged digital elevation model, overlain in transparency on a LRO WAC mosaic basemap. The Humboldt central uplift region appears in yellow shades at the center of the crater. The linear mountain range extends until the rim of the volcanic deposit located in the North-East portion of the crater. Volcanic deposits are located in lower elevated areas in the periphery of the crater and denoted as **P**. Portions of the terraced walls are marked as **T**. The **AA'** line shows the topographic transect presented in **b**. A fault of same orientation as the linear alignment is observed to the North-West of Humboldt crater. **b**. LOLA/Kaguya merged DEM topographic transect **AA'** of Humboldt crater. The northern rim is slightly lower in elevation than the southern rim. The crater walls are terraced. The volcanic deposits are emplaced in the topographic lows in the periphery of the crater floor.

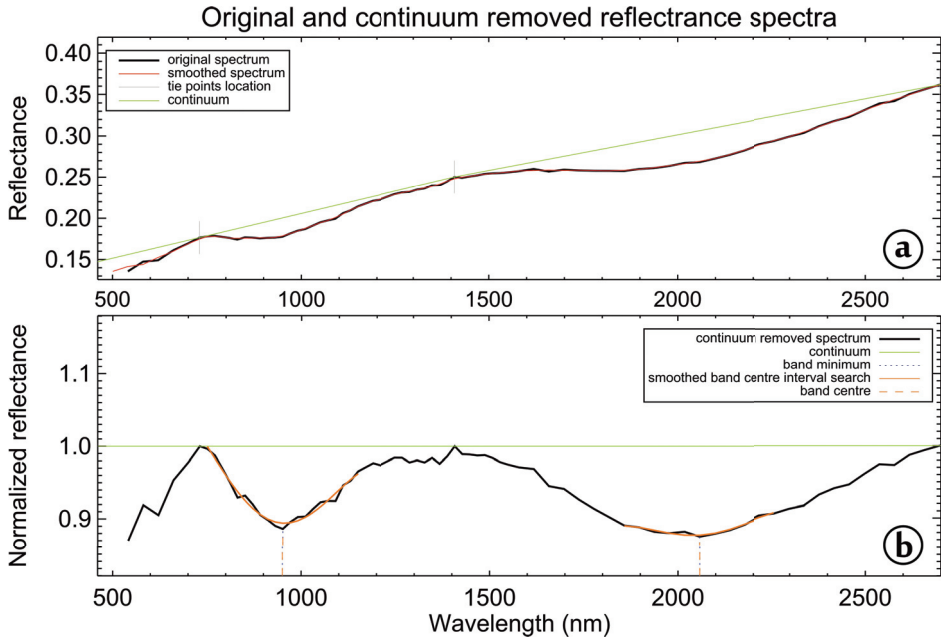

Figure 1.2: M^3 spectrum study with our IDL routine. (**a**) The original spectrum (thick black line) is smoothed (red line) to allow for the tie points search. After the tie points are found (gray vertical segments), the continuum is modeled as linear segments between the tie points (green lines). (**b**) Spectrum after continuum removal (thick black line). After the band minima are found (dotted blue lines), a polynomial fit (orange curve) ± 200 nm around the band minimum is performed. The minimum of this polynomial fit is the band center (dashed orange line).

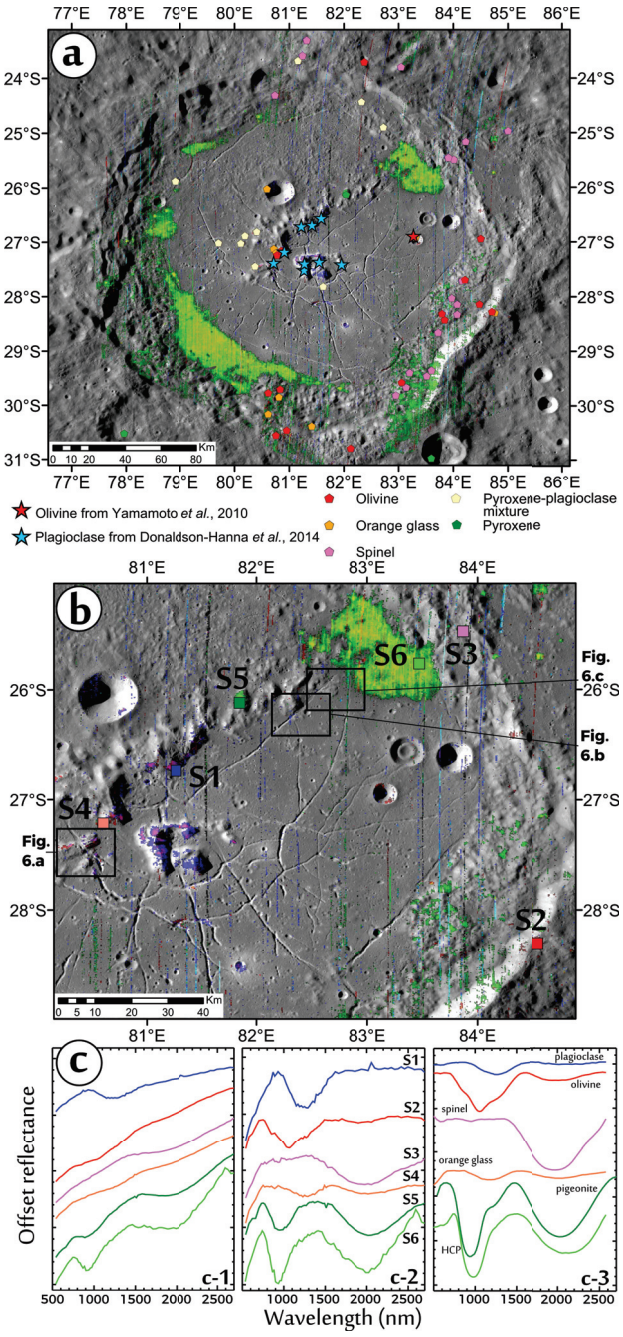

(Caption next page.)

Figure 1.3 *(previous page)*: (Previous page.) Humboldt crater mineralogical diversity. **a**. General view of Humboldt crater with mineralogical detections. The M^3 color composite are overlain on LRO WAC mosaic. R = B1AREA; G = B2AREA; B = B1CEN, see Table 1.1 for parameter details. Plagioclase is highlighted in blue to pink shades, as its absorption band depth increases. Olivine is displayed in red, and pyroxene in bright green. Blue stars denote pure plagioclase detections from Donaldson Hanna et al. [2014]; the red star denotes the olivine detection by [Yamamoto et al., 2010]. The mineralogical detections from this study are reported as pentagons. The spectra associated with the white pentagons are interpreted as pyroxene-plagioclase mixture spectra, as discussed in 1.4.1. **b**. Close-up of the Humboldt crater central uplift and mountain range. The position of the spectra presented in **c** are indicated as colored squares, and the frames are the locations of the areas shown in higher resolution in Fig. 1.6. **c**. Typical M^3 spectra of key mineralogical detections in Humboldt crater as indicated by colored squares in **b**. **c-1**: original M^3 Level 2 spectra; **c-2**: continuum removed spectra, output from the IDL routine; **c-3**: corresponding RELAB database spectra processed by the IDL routine (respective RELAB-ID: LS-CMP-004; LR-CMP-014; PS-TXH-082; LR-CMP-051; DL-CMP-008 and LS-CMP-009 for plagioclase; olivine; spinel; orange glass; pigeonite and High-Calcium Pyroxene).

Olivine spectra are characterized by a single, broad and complex absorption band centered at 1050 nm [Sunshine & Pieters, 1998]. The position of the absorption center shifts towards longer wavelength with increasing iron content [Burns, 1970a], and the absorption band of fayalite is broader and more flat-bottomed than that of forsterite [Sunshine & Pieters, 1998]. Olivine is displayed in red in the color composite shown in Fig. 1.3.a. Olivine is mostly detected in the southern and eastern rims and ejecta of Humboldt crater, and in the walls of a 7 km diameter crater in the East of Humboldt crater's central uplift. One olivine occurrence is observed on the western margin of the central uplift of Humboldt crater, associated with a glass detection. All the olivine spectra observed in Humboldt crater have a narrow absorption band, and the right shoulder of the absorption band is compatible with a forsteritic composition. No major compositional difference is observed between the walls and the central uplift olivine spectra.

Pyroxenes have diagnostic absorption bands located around 1000 and 2000 nm, shifting towards longer wavelength with increasing Iron or Calcium content [Klima et al., 2007]. Low-Calcium Pyroxene (LCP) such as pigeonite or enstatite has an absorption band centered around 900 nm and an absorption band centered around 2000 nm. In contrast, both absorption bands of High-Calcium Pyroxene (HCP) such as augite or diopside are shifted towards longer wavelength. The color composite presented in Fig. 1.3 displays pyroxenes in green to yellow depending on the strength of the absorption bands. The spectra observed in the volcanic deposits and ejecta have spectral characteristics consistent with a HCP composition. The pyroxene detections associated with the walls of Humboldt crater, part of the central peak alignment, and small craters on its South-West and South-East rim, have spectral characteristics consistent with a LCP composition.

Small spinel patches (≤ 1 km in diameter), can be detected in Humboldt crater, mainly concentrated in the eastern part of its walls, rim and ejecta (see Fig. 1.3.a).

Spinel does not display any absorption feature around 1000 nm, but shows a broad absorption band centered at 2000 nm [Cloutis et al., 2004].

Orange glass occurrences are highlighted in red to dark red patches in the color composite (Fig. 1.3.a). Orange glass is defined by broad 1000 nm and 2000 nm absorption features, with centers located near 1150 nm and 1900 nm [Adams et al., 1974] (Fig. 1.3.c). The first detection of lunar glasses from orbit was from Besse et al. [2014]. Several detections of orange glass are observed spatially close to olivine on the rim and ejecta of Humboldt crater, in and near its central uplift, and in the walls of smaller craters on its floor (see Fig. 1.3.c). Horgan et al. [2014] cautioned about the effect of Fe-bearing glass on resulting reflectance spectra when mixed with pyroxene. They showed that when glass is less abundant than 80 wt.% in a glass-pyroxene mixture, the resulting spectrum mimics the spectral characteristics of olivine.

In addition, some spectra with a composite 1000 nm absorption feature were observed on the crater floor and walls (white polygons in Fig. 1.3.a). These spectra have three absorption band centers: one at 970 nm, one at 2020 nm and a third at 1230 nm (red spectrum in Fig. 1.4). Plagioclase-diopside mixture spectra from the RELAB database (`http://www.planetary.brown.edu/relab/`) are shown Fig. 1.4. The plagioclase-diopside mixture spectra containing 7 and 10 % of diospide both have an absorption feature centered at 1250 nm additional to the 1000 and 2000 nm absorption features.
There is a shift in the 1 and 2 μm absorption band centers of the laboratory spectra and the spectra from the M^3 data presented here. This shift can be caused by a composition difference: for instance, HCP have absorption bands shifted towards longer wavelength than LCP Klima et al. [2011]. Fig. 1.4 highlights the composite shape of the absorption band at 1 μm of the mixed laboratory spectra. Taken together, these elements suggest that the locations of spectra denoted by white polygons in Fig. 1.1.a may be characterized by a mixture of plagioclase and pyroxene.

1.4.2. Scatter Plots

The calculation of spectral parameters for each pixel of the M^3 mosaic enables the use of scatter plots, similarly to Horgan et al. [2014]. Fig. 1.5.c presents a scatter plot of the values of the 1 μm band center as a function of the values of the 2 μm band center. The boxes represent fields of band center combinations compatible with the spectral parameters of a mineral. If a spectrum displays a pair of 1 and 2 μm band centers with values consistent with one of the boxes, its pixel is highlighted in Fig. 1.5.a and b. The values bounding the fields are those used by Horgan et al. [2014]. Fig. 1.5.a shows the results of the scatter plot on the map, and Fig. 1.5.b presents a zoomed-in view of the Humboldt crater central uplift. Several vertical bands of pixels are highlighted, which can be explained by the residual noise left after the M^3 radiometric calibration. However, we find some correlations between Fig. 1.5.a and the detections presented in Fig. 1.3.a and b. The pixels highlighted in green in Fig. 1.5.a are the

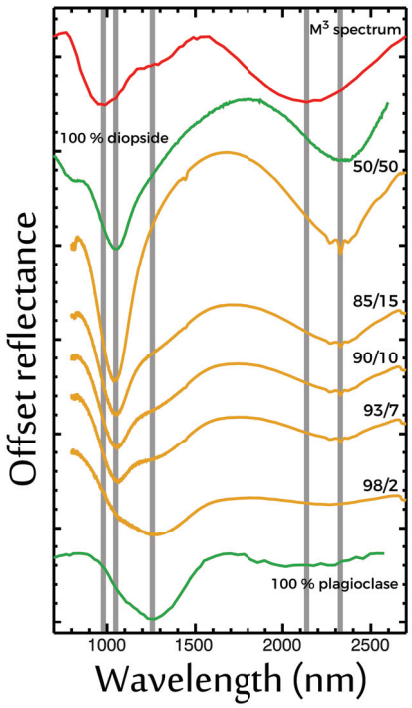

Figure 1.4: RELAB diospide and plagioclase mixture spectra and a M^3 spectrum. From top to bottom: M^3 spectrum collected on Humboldt crater; pure diopside spectrum (PD-CMP-008); laboratory mixture of 50 % plagioclase and 50 % diopside (MX-CMP-104-C); laboratory mixture of 85 % plagioclase and 15 % diopside (MX-CMP-102-C); laboratory mixture of 90 % plagioclase and 10 % diopside (MX-CMP-101-C); laboratory mixture of 93 % plagioclase and 7 % diopside (MX-CMP-100-C); laboratory mixture of 98 % plagioclase and 2 % diopside (MX-CMP-98-C); pure plagioclase spectrum (LS-CMP-004). The spectra RELAB-ID are given in the parentheses. The grey rectangles represent the spectra absorption band centers.

ones with spectra having clinopyroxene-compatible band 1 and 2 μm centers (e.g., pigeonite, augite). This clinopyroxene-compatible signature is in good agreement with the pyroxene signature highlighted in green in the color composite (Fig. 1.3.a and b). Orange pixels represent pixels with spectral band 1 and 2 μm centers compatible with a glass signature. Although the results presented in Fig. 1.5.a and b are noisy, some locations of highlighted pixels are the same as the glass detections indicated as orange polygons in Fig. 1.3. The spectra with band 1 and 2 μm center combinations that are compatible with orthopyroxene (e.g., enstatite) are not correlated to a detection in Fig. 1.3. There was no mineral field for plagioclase in Fig. 1.5.c, but the fact that the central uplift pixels are not highlighted is consistent with their plagioclase signature, shown Fig. 1.3.a and b.

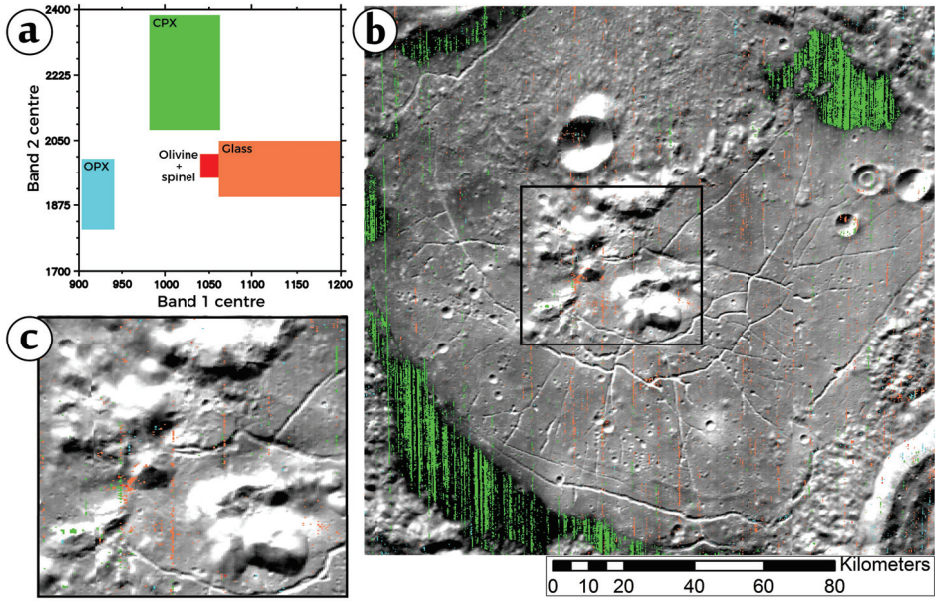

Figure 1.5: **a** Scatter plot presenting the values of the 1 μm band center as a function of the values of the 2 μm band center for the pixels of the M^3 mosaic of Humboldt crater. The drawn boxes represent the field of band centers possibilities for describing a given mineral (green for clinopyroxene, cyan for orthopyroxene, orange for glass and red for olivine with spinel). The pixels falling within the field have spectra exhibiting the combination of band centers and are colored in **c**. The values used for the absorption band centers are those used by Horgan et al. [2014]. **b** Close-up of the Humboldt crater central uplift. **c** M^3 2900 nm band image of the Humboldt crater. The colored pixels are the pixels which 1 μm band center and 2 μm band center values fall in the boxes drawn in **a**.

1.4.3. Crater Morphology

Different geomorphological units can be observed on the Humboldt crater floor, as described in section 1.2. The northern crater rim is lower in elevation than the southern rim. The transect shown in Fig. 1.1.c cuts through one of the volcanic deposits. Several slumps can be observed around the crater, forming wall terraces (marked as T in Fig. 1.1.a). The Humboldt crater's central uplift is made of several blocks organized irregularly around the center of the crater. A linear mountain range (purple in Fig. 1.8.b) is extending from the north-western portion of the central uplift to the rim of the volcanic deposit in the North-East of Humboldt crater.

Floor fractures cut through the least elevated parts of the central uplift (Fig. 1.6.a) and linear mountain range (Fig. 1.6.b), which suggests that these fractures are younger than the central uplift and linear mountain range. In the periphery of the crater, the fractures are covered by volcanic deposits (Fig. 1.6.c), stratiphically constraining the age of the volcanic deposits to be younger than the fractures.

1.4.4. Crater Counts

Absolute ages estimated from crater counts were obtained for various units of Humboldt crater. Crater counts were performed on the northern rugged floor unit, the southern smooth floor unit, all four of the volcanic deposits, as well as a melt pool located on Humboldt proximal ejecta, to the East of the crater (see Fig. 1.7 for locations and age results). The crater counts of volcanic deposits were performed at different spatial resolution, but the crater distributions of the volcanic deposits labeled P2, P3 and P4 are consistent within error with an age of 1 Ga. The crater counts performed on the volcanic deposit labeled P1 yields an older age of 2.5 Ga. The crater counts performed on the melt pool deposited on the rim of Humboldt crater results in an age of 3.5 Ga.

The crater counts performed on the North floor unit and South floor units are more complex. Their respective crater distributions are irregular and exhibit plateaus that indicate resurfacing events. The fitted age of the North unit is probably a resurfacing event dated at 3.2 Ga. The same model age is fitted in the crater distribution of the South unit.

1.5. Discussion

Humboldt Crater's Geological Map

An updated geological map, based on high resolution imagery and our mineralogical detections, is provided in Fig. 1.8.a. For comparison, the initial geological map of the crater by Wilhelms & El-Baz [1977], that combined crater floor, walls and ejecta in one unit, is shown in Fig. 1.8.b. The volcanic deposits were mapped at higher resolution and expanded. The division between crater material and terra material (Floor texture 1 and 2, respectively in the new map) is different as well. In this study, floor tex-

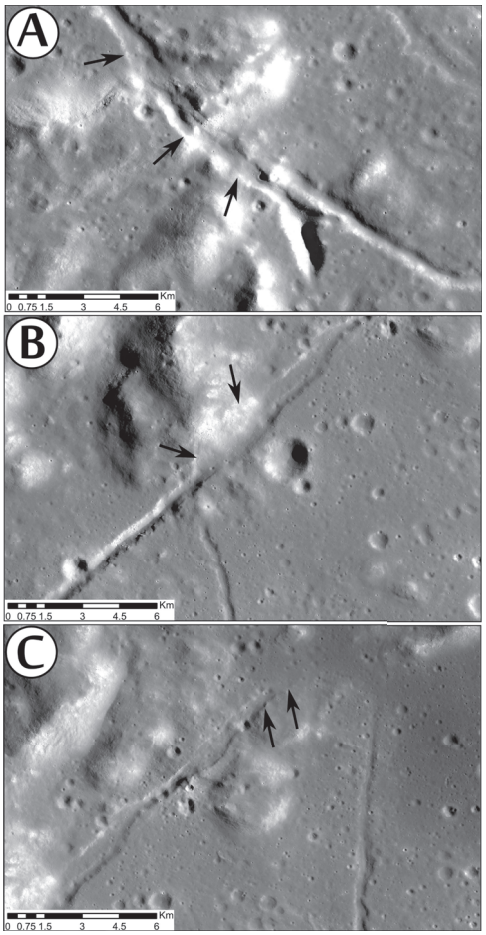

Figure 1.6: Zoomed Kaguya TC views of the Fig. 1.3.b. The fractures are pointed at with arrows. **A** Central uplift cross-cut by a fracture. **B** Linear mountain range cut through by a fracture. **C** Volcanic deposit covering a fracture.

tures and albedo changes were used to distinguish between the two floor units on high resolution imagery, which might explain the differences between the two geological maps.

Central Uplift and Mountain Range

The central uplift and linear mountain range were mapped as distinct units when possible, using a combination of morphological, topographic and mineralogical in-

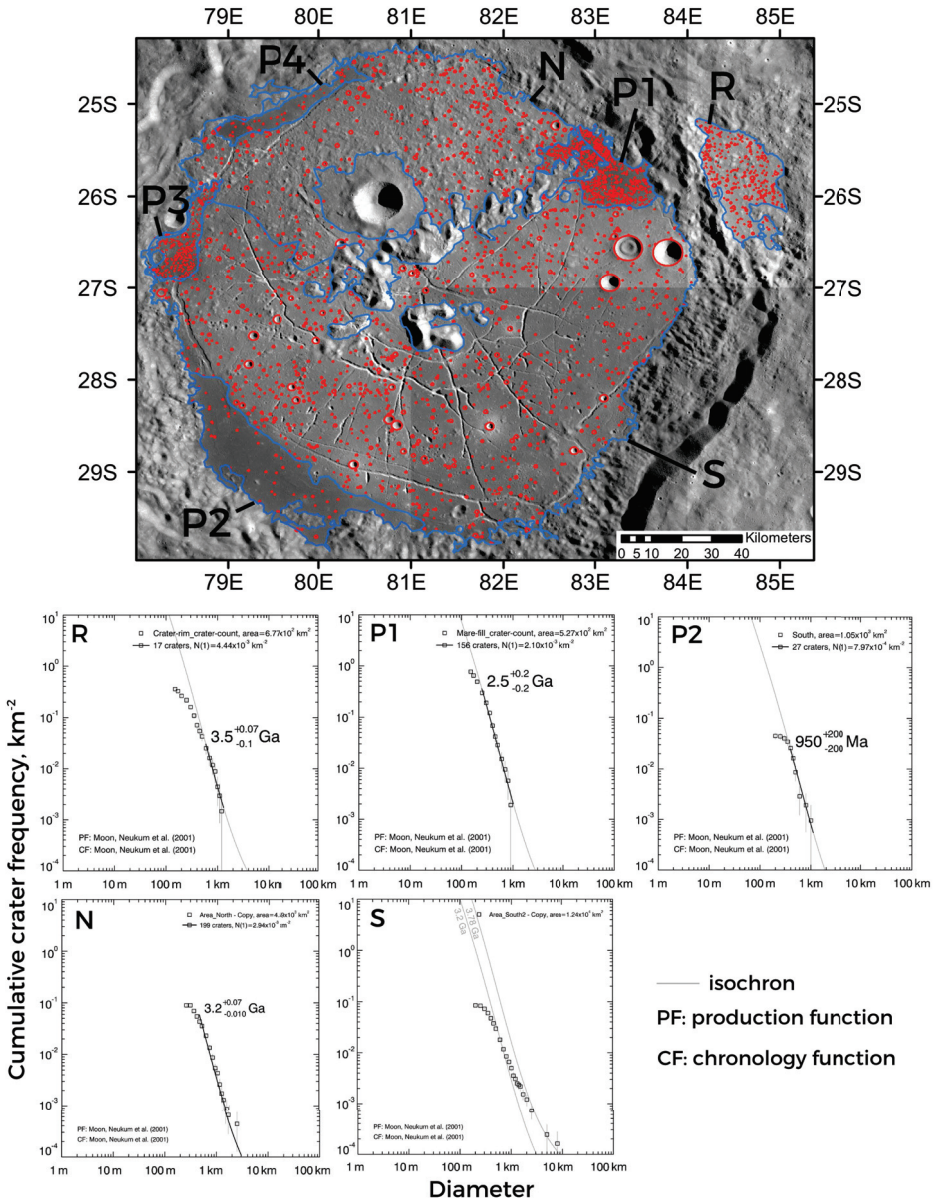

Figure 1.7: Humboldt crater count areas and locations displayed on a Kaguya TC mosaic. The northern part of Humboldt crater is labeled N, its southern part is labeled S, the volcanic deposits are labeled P_n and the melt deposited on the Humboldt crater rim is labeled R. The topography and morphology helped delimiting the crater floor units. The northern crater floor unit exhibits a large crater proportional to the unit surface. The ejecta of this large crater cover the crater floor surface, which biases the age of the surface. In order to prevent this age bias, this large crater and ejectas were excluded from the crater counts. Some age results are presented below, with the production and chronology functions from Neukum et al. [2001]. The melt deposited on the rim of Humboldt crater is consistent with the Humboldt crater age proposed by Wilhelms & El-Baz [1977], while the age obtained on the volcanic deposit labeled P2 is younger than that obtained on the volcanic deposit P1.

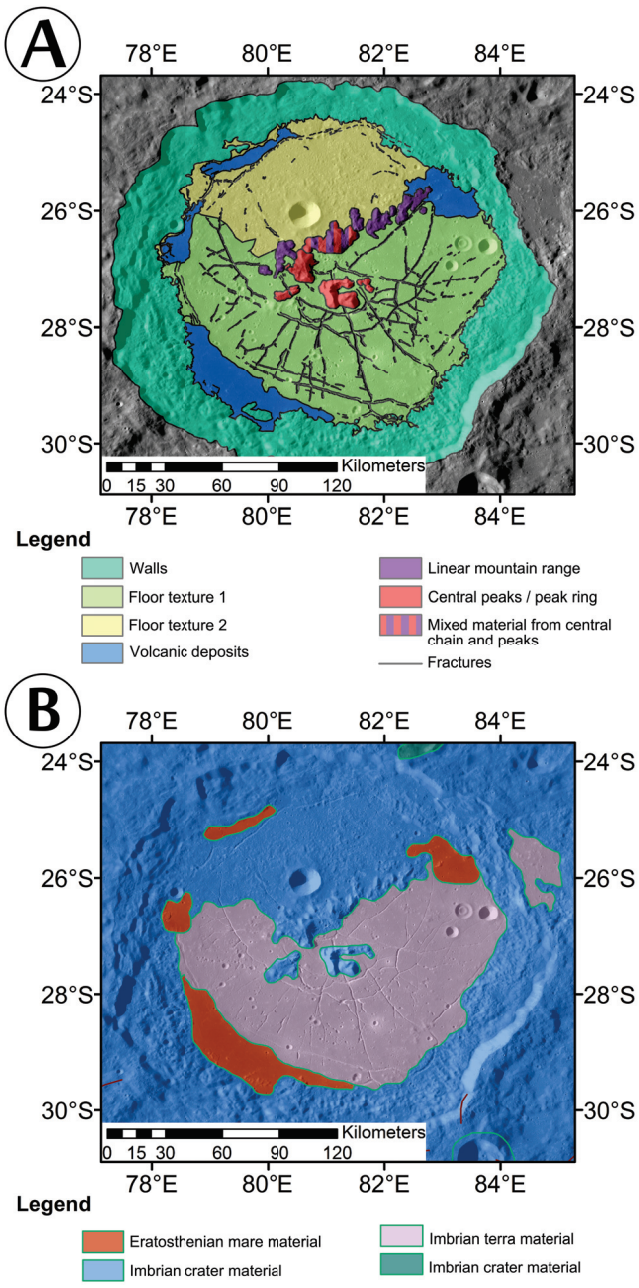

Figure 1.8: (**a**) Humboldt crater geologic map (this study) overlain on the LRO WAC mosaic. The part that is striped pink and purple is material likely pertaining both to the central uplift and the linear mountain range. (**b**) Humboldt crater geologic map from Wilhelms & El-Baz [1977] overlain on the LRO WAC mosaic.

formation. The altitude of the central uplift peaks is greater than the linear mountain range peaks. The linear mountain range exhibits a pyroxene signature, featureless spectra, and spectra displaying absorption features of both pyroxene and plagioclase interpreted as plagioclase-pyroxene mixture spectra. The unit mapped as mixed material (dashed unit in Fig. 1.8.a) is located between the central uplift and the linear mountain range. It is difficult to distinguish it from the central uplift unit or the linear mountain range unit, because it displays plagioclase spectra towards the central uplift on the southern of the unit, and featureless spectra towards the crater floor, on the northern part of the unit.

Donaldson Hanna et al. [2014] described numerous pure crystalline plagioclase occurrences (< 1 % olivine and pyroxene in the rock) on the Humboldt crater central uplift, which is in good agreement with our detections (Fig. 1.3.a). Featureless spectra are also detected on the Humboldt crater central uplift. They exhibit no absorption feature at 1000 and 2000 nm, and have been interpreted to be the signature of shocked plagioclase [Adams et al., 1979], or anorthosite affected by space weathering Lucey [2002]. The multiple detections of pure crystalline plagioclase throughout the Humboldt crater central uplift hint at the crustal origin of the material composing it.

According to their simple uplift model, Song et al. [2013] concluded that the Humboldt crater central uplift material originates from the lower crust, about 2 km above the crust-mantle interface. This result was corroborated by Martinot et al. [2017], who calculated the Humboldt crater proximity value to the crust-mantle interface with the GRAIL crustal thickness models [Wieczorek et al., 2013]. The proximity value to the crust-mantle interface is obtained when subtracting the depth of origin of the material emplaced in the central uplift to the pre-impact crustal thickness [Flahaut et al., 2012]. Martinot et al. [2017] found that the Humboldt crater-forming event likely tapped close to the crust-mantle interface (< 10 km). Song et al. [2013] calculated the CF value of the Humboldt crater central uplift and found it more consistent with an anorthositic composition than a mantle composition. This corroborates the crustal origin of the material composing the Humboldt crater central uplift, and challenges the LMO crystallization view that a more mafic lithology should be encountered closer to the crust-mantle interface [e.g., Lin et al., 2017, Snyder et al., 1992]. Ohtake et al. [2009] defined a purest anorthosite (PAN) rock composed of nearly 100 % anorthosite. They proposed the existence of a PAN-rich global layer in the crust. This PAN-rich layer might be sampled by Humboldt crater central uplift. Alternatively, the crust-mantle interface might be found at greater depth than expected.

Despite its spectral and spatial predominance, plagioclase is not the only mineral detected on the Humboldt crater central uplift. Olivine, glass and plagioclase-pyroxene mixture spectra are marginally observed on one of the mounds of the western part of the central uplift. Lemelin et al. [2015] suggested the presence of heterogeneities in the crust, which is consistent with Pieters et al. [2011] and Jozwiak et al. [2016b] conclusions. The presence of these mafic lithologies could hint at the pres-

ence of a crustal heterogeneity sampled by the Humboldt crater central uplift. Two olivine occurrences and three glass detections are located close to a floor fracture. These minerals may be secondary: they may have crystallized from a volcanic event, or recrystallized from the impact melt. There are signs of volcanism on the Humboldt crater floor (pyroclastic deposits and vents associated to floor fractures, Jozwiak et al. [2016a]). However, no visible sign of a volcanic vent close to the central uplift has been observed, and there is no obvious sign of impact melt on the Humboldt crater central uplift. Alternatively, the glass could have an impact origin. Tompkins & Pieters [2010] indicated that spectrally distinguishing a volcanic glass from an impact glass is difficult. The olivine could be endogenic, being presumably abundant in the lunar mantle and lower crust [e.g., Elardo et al., 2011, Lin et al., 2017, Snyder et al., 1992]. The fact that the olivine and glass occurrences are spatially limited to a small mound peripheral to the central uplift lead us to prefer the hypothesis of a secondary origin for these detections.

Crater Floor and Volcanic Deposits

Four HCP-rich, pyroclastic deposits are emplaced in topographic lows in the periphery of the Humboldt crater floor (Gaddis et al. [2003], Fig. 1.1.a). Jozwiak et al. [2012] showed that floor fractured craters are formed by the intrusion of a magmatic body beneath the crater. Subsequently, Jozwiak et al. [2016b] observed the band-filtered Bouguer solution of Humboldt crater in order to be able to determine density anomalies in the crust. They found that the Humboldt crater volcanic deposits are spatially correlated with positive crustal density anomalies. Thorey et al. [2015] showed that positive signatures in a floor-fractured crater gravity field are consistent with the presence of shallow magmatic intrusions beneath its surface. Such magmatic intrusions could extrude volatile-rich pockets towards the crater floor. The wide age range of the Humboldt crater volcanic deposits could be explained by volatile heterogeneities in the magmatic intrusions, generating different volatile-rich pockets that reach the surface staggered in time.

Crater counts were performed on the volcanic deposits (P1 through 4, locations indicated in Fig. 1.7). The crater distributions on the Humboldt crater volcanic deposits are often irregular, which could lead to an incorrect age. However, the significant age difference between P1 on the one hand, and P2, P3 and P4 on the other hand, leads us to think that Humboldt crater had several episodes of volcanic activity, spanning a period exceeding one billion years. Signs of long lasting volcanic activity (2.7 Ga) were found by Hiesinger [2003] while performing crater counts on mare basalts on the near side. They also found young mare basalts (1.2 Ga old), similar to the model age of the Humboldt crater volcanic deposits P2 through P4. Humboldt crater volcanic deposits have been described as pyroclastic deposits by Gaddis et al. [2003]. Caution needs to be taken when counting craters on pyroclastics, since they can be deposited in very thin layers [Gaddis et al., 2003]. A cratered surface covered by a thin layer of

pyroclastics might retain its topography, challenging crater count dating.

The crater counts performed on the North and the South units have a common model age at 3.2 Ga. In the northern crater floor unit, this model age fits the distribution of the craters between 300 m and 1 km in diameter. In the southern crater floor unit, it fits the distribution of the craters between 300 m and 750 m. The 3.2 Ga isochron does not fit bigger craters, which suggests that the crater floor is older. No isochron fits the South unit distribution of craters between 750 m and 8 km in diameter. This suggests that the unit was regularly resurfaced. This resurfacing process may have decreased in intensity from 3.2 Ga onwards, which might explain the model age observed.

Yamamoto et al. [2010] detected olivine in the walls of a small crater on the Humboldt crater floor using SP data. SP is a continuous line spectrometer with a swath of 500 m, and a spatial resolution of 500 m/pixel [Matsunaga et al., 2008]. Due to the nature of operations and lifetime of the mission and instrument, SP did not cover the whole lunar surface, contrary to M^3. This explains the more numerous olivine occurrences detected here. The olivine occurrence in the walls of the small crater on the Humboldt crater floor is associated with glass. These olivines probably crystallized from the melt generated during the small impact crater-forming event.

Several occurrences of a pyroxene-plagioclase mixture were detected in the South-West of the crater, in association with fresh impact craters. The floor of Humboldt crater does not display a strong spectral signature, except near impact craters, which redistribute underlying, fresher material. This means that the mineralogy beneath the Humboldt crater floor is plagioclase and pyroxene-rich, at least in the South-West of the crater.

Jozwiak et al. [2016b] recently showed that the Humboldt crater floor displays a positive Bouguer anomaly slightly offset from the crater center. The floor fractures observed in Humboldt crater were mapped by Jozwiak et al. [2016a] (Fig. 1.1.a), and differentiated into several categories, two of which are represented in Fig. 1.6. The fractures in Fig. 1.6.a and b were classified as “v" fractures, forming during the uplift of the crater floor associated with the magmatic intrusion emplacement, and resulting in the brittle fracturing of the crater floor Jozwiak et al. [2016a]. The fracture in Fig. 1.6.c was classified as a graben. The fractures are cross-cutting parts of the central uplift (Fig. 1.6.a), as well as the linear mountain range (Fig. 1.6.b). This means that the central uplift and linear mountain range pre-date the fractures. Volcanic deposits are overlying the fractures (Fig. 1.6.c), which constrains the formation of the volcanic deposits to be younger than the fractures. This corroborates the crater counting results. The South-facing sides of the linear mountain range are smooth (Fig. 1.3.B) and similarly oriented, comparable to the morphology of a fault wall. No reference layer was found, making it harder to determine the fault movement. However, the presence of a fault could explain the altitude difference between the northern and southern floor units, accommodating part of the stress caused by the intrusion of a magmatic body

beneath the Humboldt crater floor.
The rugged morphology and altitude of the northern floor unit could be explained by the destabilization of the crater walls leading to the emplacement of debris on the crater floor. This resurfacing event could explain the observed crater distribution of the northern floor unit at 3.2 Ga (Fig. 1.7). The presence of debris on the crater floor could also explain why fewer floor fractures are observed on the northern floor unit than on the southern floor unit. The existence of a discontinuity (e.g., fault) before the formation of Humboldt crater could be reflected in its final morphology, and lead to the formation of the multiple peaks forming the linear mountain range. The linear mountain range could alternatively have been triggered by local or regional stresses after Humboldt crater formation.

Crater Walls and Rim

The rim of Humboldt crater is asymmetric, with the altitude of its northern rim being lower than that of its southern rim (Fig. 1.1.c). A lobe of ejecta from Humboldt crater is deposited on top of the Hecataeus crater floor, to the North of Humboldt crater (Fig. 1.1.a), constraining Humboldt crater to be younger than Hecataeus crater. The formation of Humboldt crater on an irregular pre-impact surface can explain the unevenness of its rim (Fig. 1.1.a). A melt sheet is observed to the North-East of the Humboldt crater rim [Hawke & Head, 1977] (labeled R in Fig. 1.7). Crater counts of this melt sheet constrain the minimum age of the Humboldt crater formation to 3.5 Ga, which is consistent with the upper Imbrian age of the Humboldt crater material proposed by Wilhelms & El-Baz [1977].

Several glass detections are located in the Humboldt crater walls and rims (Fig. 1.3.a). Impact melt distribution has been studied on terrestrial impact craters [Osinski, 2004], showing that impact melt can be deposited on the walls of a crater. This could confirm an impact origin of the glass detections of the walls of Humboldt crater, by recrystallization of the melt produced during the Humboldt crater-forming event. The glass detections observed in the walls and rims of Humboldt crater are associated with small impact craters (< 1 km in diameter). This association of the glass detections with small impact craters corroborates the impact origin of these glass detections. However, it remains unclear which impact crater-forming event these glasses recrystallized from.

Some olivine occurrences are found in the terraced walls and rims of the Humboldt crater (Fig. 1.3.a), and located near fresh impact craters. Small impact crater-forming events rework the target material and lead to the exposure of fresh material. If the olivine occurrences are distributed evenly through the crater's walls and ejecta, then they might originate from the target material (*i.e.*, below the surface). However, if the olivine exposures are only concentrated around the small crater, then they may be secondary. Here, the olivines are located close to the small craters, and not spread out in the small crater ejecta, hinting at a secondary origin. Alternatively, these olivines could be exogenic: olivine is abundant in asteroids, meteorites and chondrules [e.g.,

Brearley & Jones, 1998, Mittlefehldt et al., 1998].

The observation of spinel and olivine in the East walls, and olivine and glass in the South walls of Humboldt crater is interesting because they are observed in the same crater unit. This raises the question of the origin of these minerals, which cannot be accounted for by existing petrogenetic models. The spinel occurrences are typically a few hundred meters across. Spinel detections on the Moon were located within craters and volcanic domes on the nearside [Dhingra et al., 2011] and the farside [Kaur et al., 2013, Pieters et al., 2011]. Pieters et al. [2011] indicated that the detection of spinel constrains the abundance of other mafic minerals (olivine, pyroxene) to less than 5 %, and defined a rock composed of "pink" spinel (owing to the color of Mg-spinels found in lunar samples) and anorthite (PSA).
Several explanations are possible for the spinel detections. It could have an endogenic or an exogenic origin. Pieters et al. [2011] proposed that the origin of olivine and Mg-rich spinel could be linked with plutonic events, resulting in the intrusion of magmatic bodies into the lower crust. The composition of the olivine occurrences (forsteritic), is consistent with a deep origin. Prissel et al. [2014] listed two endogenic petrogenetic models for PSA formations: magma-wallrock interactions in the lunar crust [Gross et al., 2011], and crystallization of a melt mixture between the anorthositic crust and mantle material [Vaughan et al., 2013]. Lin et al. [2017] performed crystallization experiments to simulate lunar magma ocean solidification in water-bearing conditions. The results of their experiments show that spinel is amongst the last minerals to be crystallized during solidification of a water-bearing magma ocean. They calculated that a spinel-bearing layer could be found around 30 km underneath the surface after magma ocean solidification. The walls of Humboldt crater are not likely to cut through 30 km of crust. However, we note that the 880 km pre-Nectarian Australe basin is located 300 km to the South-South-East of Humboldt crater [Wilhelms & El-Baz, 1977]. Australe basin likely ejected deep crustal to mantle material in its ejecta blanket during its formation, which might have been sampled by the Humboldt impact crater-forming event. Most of the spinel detections are concentrated on the South-East walls of Humboldt crater, close to Barnard crater. The south-eastern rims of Humboldt crater are intact, which hints that Humboldt crater was formed after Barnard crater. This could imply that Barnard crater reworked the Australe basin ejecta during its formation, later re-disturbed by the Humboldt crater-forming event, leading to the observed dichotomy in the spinel exposures of the south-eastern walls of Humboldt crater. The spectroscopic study was performed on a mosaic of M^3 data acquired within a single operation period, and over a restricted surface. These combined factors provide a strong constraint on the existence of the observed mineralogical dichotomy.

Implications for the Lunar Crustal Organization

This study showed that understanding the geological setting of a crater is important in order to interpret the crustal organization of its region. The mineralogical

signature of the Humboldt crater central uplift, floor and walls hint that the Humboldt crater-forming event took place in a complex setting. The anorthosite signature of the Humboldt crater central uplift reflects a crustal signature. However, the olivine and spinel detections observed in the Humboldt crater walls suggest the presence of pre-impact heterogeneities in the crust. These heterogeneities could have been generated by the emplacement of a pluton in the crust sampled by the Humboldt crater-forming event. Alternatively, the presence of Australe basin ejecta in the crust before the formation of the Humboldt crater might explain the observed mineralogy.

1.6. Conclusion

An improved continuum removal routine for M^3 data allowed the mineralogical characterization of the Humboldt crater central uplift, floor, linear mountain range, walls and rim. The mineralogy of Humboldt crater reflects its complex geology. The Humboldt crater central uplift is anorthosite-rich — hinting at a crustal origin — whereas multiple mafic minerals (spinel, pyroxene and olivine) and glass occurrences are detected in the walls and rim of the crater.

The Humboldt crater-forming event most likely took place on a disturbed surface, marked by the presence of Hecataeus crater to the North, Phillips crater to the West and Barnard crater to the South-East. The surface was probably covered by the ejecta of Australe basin, reworked by Barnard crater, which can explain the presence of olivine, glass and spinel in the walls of Humboldt crater. Alternatively, the Humboldt crater-forming event might have sampled a mafic pluton in the crust.
The orientation of the linear mountain range observed in Humboldt crater is the same as that of a fault located to the North-East of Humboldt crater. This, and the smooth South-facing slopes of the linear mountain range, hints that it is a tectonic discontinuity that existed before Humboldt crater was formed.
Crater counts were performed on different units of Humboldt crater. The age results are consistent with the observed stratigraphical relationships between the units. The age obtained from the crater counts performed on the crater volcanic deposits span a period of over a billion years, suggesting a long duration of a volcanic activity within the Humboldt crater. This could be explained by the presence of volatile distribution heterogeneities in a magmatic intrusion underneath the crater, extruding volatile-rich pockets staggered in time.

The study of the lunar organization through impact craters is possible, but caution needs to be used in order to identify the origin of the mineralogical detections. The minerals can have a secondary origin: they may have recrystallized from the impact melt, or be part of a former impact structure ejecta. The minerals may otherwise have a primary origin, and reflect the crystallization of the lunar magma ocean. Primary minerals give important insight on the stratification of the crust, and on the presence of crustal heterogeneities.

Acknowledgments

We thank the e-Mars team, Y. Lin, K. Donaldson-Hanna, M. Ohtake, S. Yamamoto, D. Dhingra, B. Horgan, L. Cheek, R. Klima, D. Kring and G. Osinski for kindly sharing their data and for fruitful discussions. This work was supported by a Netherlands Organization for Scientific Research (NWO). Vici grant and a User Support Space Research grant from the Netherlands Space Office (NSO) to WvW. CQN is supported by European Research Council through the FP7/2007-2013/ERC grant agreement 280168. M^3 and LRO data can be accessed in the PDS Geoscience Node, Lunar Orbital Data Explorer (`http://ode.rsl.wustl.edu/`). SELENE data can be accessed on the SELENE data archive (`http://l2db.selene.darts.isas.jaxa.jp/index.html.en`). The LRO LOLA and Kaguya Terrain Camera DEM merge can be accessed on the USGS Astrogeology Science Center (`https://astrogeology.usgs.gov/search/map/Moon/LRO/LOLA/Lunar_LRO_LrocKaguya_DEMmerge_60N60S_512ppd`).

Bibliography

Adams, J., Hörz, F., & Gibbons, R. (1979). Effects of shock-loading on the reflectance spectra of plagioclase, pyroxene, and glass. Paper presented at *Proceedings of the 10th Lunar and Planetary Science Conference* (pp. 5–7).

Adams, J. B., & Goullaud, L. H. (1978). Plagioclase feldspars: visible and near infrared diffuse reflectance spectra as applied to remote sensing. Paper presented at *Proc. Lunar Planet. Sci. Conf.* (pp. 1205–1207). volume 9.

Adams, J. B., Pieters, C., & McCord, T. B. (1974). Orange glass: Evidence for regional deposits of pyroclastic origin on the Moon. Paper presented at *Lunar Science Conference* (pp. 171–186). volume 1.

Baker, D. M. H., Head, J. W., Fassett, C. I., Kadish, S. J., Smith, D. E., Zuber, M. T., & Neumann, G. A. (2011). The transition from complex crater to peak-ring basin on the Moon: New observations from the Lunar Orbiter Laser Altimeter (LOLA) instrument. *Icarus*, *214*, 377–393. doi:10.1016/j.icarus.2011.05.030

Baldwin, R. B. (1968). Rille Pattern in the Lunar Crater Humboldt. *Journal of Geophysical Research*, *73*, 3227–3229.

Barker, M. K., Mazarico, E., Neumann, G. A., Zuber, M. T., Haruyama, J., & Smith, D. E. (2016). A new lunar digital elevation model from the Lunar Orbiter Laser Altimeter and SELENE Terrain Camera. *Icarus*, *273*, 346–355. doi:10.1016/j.icarus.2015.07.039

Beer, W., & Madler, J. H. (1837). *Der Mond nach seinen komischen und individuellen Verhaltnissen oder allgemeine vergleichende Selenographie: mit besondrer Beziehung auf die Verfassern herausgegebene Mapppa Selenographica.* (Schopp ed.). Berlin.

Besse, S., Sunshine, J. M., & Gaddis, L. R. (2014). Volcanic glass signatures in spectroscopic survey of newly proposed lunar pyroclastic deposits. *Journal of Geophysical Research E: Planets*, (pp. 1–21). doi:10.1002/2013JE004518.Received

Besse, S., Sunshine, J. M., Staid, M. I., Boardman, J., Pieters, C., Guasqui, P., Malaret, E., McLaughlin, S., Yokota, Y., & Li, J. Y. (2013). A visible and near-infrared photometric correction for Moon Mineralogy Mapper (M^3). *Icarus*, *222*, 229–242. doi:10.1016/j.icarus.2012.10.036

Boardman, J. W., Pieters, C. M., Green, R. O., Lundeen, S. R., Varanasi, P., Nettles, J., Petro, N. E., Isaacson, P., Besse, S., & Taylor, L. A. (2011). Measuring moonlight: An overview of the spatial properties, lunar coverage, selenolocation, and related Level 1B products of the Moon Mineralogy Mapper. *Journal of Geophysical Research E: Planets*, *116*, 1–15. doi:10.1029/2010JE003730

Brearley, A. J., & Jones, R. H. (1998). No Title. In J. J. Papike, & P. H. Ribbe (Eds.), *Planetary materials* (pp. 1–398). (Mineralogi ed.).

Burns, R. G. (1970a). Crystal field spectra and evidence of cation ordering in olivine minerals. *American Mineralogist*, *55*, 1608.

Burns, R. G. (1970b). *Mineralogical Applications of Crystal Field Theory*. Cambridge University Press. doi:10.1180/minmag.1973.039.301.22

Cheek, L. C., & Pieters, C. M. (2014). Reflectance spectroscopy of plagioclase-dominated mineral mixtures: Implications for characterizing lunar anorthosites remotely. *American Mineralogist*, *99*, 1871–1892. doi:10.2138/am-2014-4785

Cheek., L. C., Pieters, C. M., Dyar, M. D., & Milam, K. A. (2009). Revisiting plagioclase optical properties for lunar exploration. Paper presented at *Lunar and Planetary Institute Science Conference*.

Cintala, M. J., & Grieve, R. A. F. (1998). Scaling impact melting and crater dimensions: Implications for the lunar cratering record. *Meteoritics & Planetary Science*, *33*, 889–912. doi:10.1111/j.1945-5100.1998.tb01695.x

Clark, R. N., Pieters, C. M., Green, R. O., Boardman, J. W., & Petro, N. E. (2011). Thermal removal from near-infrared imaging spectroscopy data of the Moon. doi:10.1029/2010JE003751

Cloutis, E. A., Sunshine, J. M., & Morris, R. V. (2004). Spectral reflectance-compositional properties of spinels and chromites: Implications for planetary remote sensing and geothermometry. *Meteoritics & Planetary Science*, *39*, 545–565. doi:10.1111/j.1945-5100.2004.tb00918.x

Dhingra, D., Pieters, C. M., Boardman, J. W., Head, J. W., Isaacson, P. J., & Taylor, L. a. (2011). Compositional diversity at Theophilus Crater: Understanding the geological context of Mg-spinel bearing central peaks. *Geophysical Research Letters*, *38*, 10–13. doi:10.1029/2011GL047314

Donaldson Hanna, K. L., Cheek, L. C., Pieters, C. M., Mustard, J. F., Greenhagen, B. T., Thomas, I. R., & Bowles, N. E. (2014). Global assessment of pure crystalline plagioclase across the Moon and implications for the evolution of the primary crust. *Journal of Geophysical Research: Planets*, *119*, 1516–1545. doi:10.1002/2013JE004476.Received

Elardo, S. M., Draper, D. S., & Shearer, C. K. (2011). Lunar Magma Ocean crystallization revisited: Bulk composition, early cumulate mineralogy, and the source regions of the highlands Mg-suite. *Geochimica et Cosmochimica Acta*, *75*, 3024–3045. doi:10.1016/j.gca.2011.02.033

Flahaut, J., Blanchette-Guertin, J.-F., Jilly, C., Sharma, P., Souchon, A., Van Westrenen, W., & Kring, D. A. (2012). Identification and characterization of science-rich landing sites for lunar lander missions using integrated remote sensing observations. *Advances in Space Research*, *50*, 1647–1665. doi:10.1016/j.asr.2012.05.020

Gaddis, L. R., Staid, M. I., Tyburczy, J. A., Hawke, B. R., & Petro, N. E. (2003). Compositional analyses of lunar pyroclastic deposits. *Icarus*, *161*, 262–280. doi:10.1016/S0019-1035(02)00036-2

Green, R. O., Pieters, C., Mouroulis, P., Eastwood, M., Boardman, J., Glavich, T., ..., & Wilson, D. (2011). The Moon Mineralogy Mapper (M^3) imaging spectrometer for lunar science: Instrument description, calibration, on-orbit measurements, science data calibration and on-orbit validation. *Journal of Geophysical Research E: Planets*, *116*, 1–31. doi:10.1029/2011JE003797

Gross, J., Treiman, A. H., & Le, L. (2011). Unique spinel-rich lithology in lunar meteorite ALHA81005: origin and possible connection to M^3 observations of the farside highlands. *Lunar and Planetary Science Conference*, *42*, 2–3.

Haruyama, J., Matsunaga, T., Ohtake, M., Morota, T., Honda, C., Yokota, Y., Torii, M., & Ogawa, Y. (2008). Global lunar-surface mapping experiment using the Lunar imager/spectrometer on SELENE. *Earth, Planets and Space*, *60*, 243–255.

Hawke, B. R., & Head, J. W. (1977). Impact melt on lunar crater rims. *Impact and Explosion Cratering*, *1*, 815—-841. doi:10.1017/CBO9781107415324.004 arXiv:arXiv:1011.1669v3.

Head, J. W. I., & Wilson, L. (1992). Lunar mare volcanism - Stratigraphy, eruption conditions, and the evolution of secondary crusts. *Geochim. Cosmochim. Acta*, *56*, 2155–2175. doi:10.1016/0016-7037(92)90183-J

Hiesinger, H. (2003). Ages and stratigraphy of mare basalts in Oceanus Procellarum, Mare Nubium, Mare Cognitum, and Mare Insularum. *Journal of Geophysical Research*, *108*, 5065. URL: http://doi.wiley.com/10.1029/2002JE001985 doi:10.1029/2002JE001985

Horgan, B. H. N., Cloutis, E. A., Mann, P., & Bell, J. F. (2014). Near-infrared spectra of ferrous mineral mixtures and methods for their identification in planetary surface spectra. *Icarus*, *234*, 132–154. doi:10.1016/j.icarus.2014.02.031

Jozwiak, L. M., Head, J. W., & Wilson, L. (2016a). An analysis of eruption styles in lunar floor-fractured craters. Paper presented at *47th Lunar and Planetary Science Conference* 1169. doi:10.1038/ngeo2474.

Jozwiak, L. M., Head, J. W., Zuber, M. T., Smith, D. E., & Neumann, G. A. (2012). Lunar floor-fractured craters: Classification, distribution, origin and implications for magmatism and shallow crustal structure. *Journal of Geophysical Research E: Planets*, *117*, 1–23. doi:10.1029/2012JE004134

Jozwiak, L. M., Head, J. W. I., Neumann, G. A., & Wilson, L. (2016b). Observational constraints on the identification of shallow lunar magmatism: Insights from floor-fractured craters. *Icarus*, *0*, 1–8. doi:10.1016/j.icarus.2016.04.020

Kaula, W. M. (1979). Thermal evolution of Earth and Moon growing by planetesimal impacts. *Journal of Geophysical Research*, *84*, 999–1008. doi:10.1029/JB084iB03p00999

Kaur, P., Chauhan, P., & Ajai, S. A. C. (2013). Exposures of Mg-spinel on an evolved silicic lithology Hansteen Alpha on the Moon. Paper presented at *Lunar and Planetary Institute Science Conference*.

Klima, R. L., Dyar, M. D., & Pieters, C. M. (2011). Near-infrared spectra of clinopyroxenes: Effects of calcium content and crystal structure. *Meteoritics & Planetary Science*, *46*, 379–395. doi:10.1111/j.1945-5100.2010.01158.x

Klima, R. L., Pieters, C. M., & Dyar, M. D. (2007). Spectroscopy of synthetic Mg-Fe pyroxenes I: Spin-allowed and spin-forbidden crystal field bands in the visible and near-infrared. *Meteoritics & Planetary Science*, *42*, 235–253. doi:10.1111/j.1945-5100.2007.tb00230.x

Lemelin, M., Lucey, P. G., Song, E., & Taylor, G. J. (2015). Lunar central peak mineralogy and iron content using the Kaguya Multiband Imager: Reassessment of the compositional structure of the lunar crust. *Journal of Geophysical Research: Planets*, *120*, 869–887. doi:10.1002/2014JE004778

Lin, Y., Tronche, E. J., Steenstra, E. S., & van Westrenen, W. (2017). Evidence for an early wet Moon from experimental crystallization of the lunar magma ocean. *Nature Geoscience*, *1*, 1–6. doi:10.1038/ngeo2845

Logan, L. M., Hunt, G. R., Salisbury, J. W., & Balsamo, S. R. (1973). Compositional implication of Christiansen frequency maximums for infrared remote sensing applications. *Journal of Geophysical Research*, *78*, 430–450. doi:10.1029/JB078i023p04983

Lucey, P. G. (2002). Radiative transfer model constraints on the shock state of remotely sensed lunar anorthosites. *Geophysical Research Letters*, *29*, 1–3. doi:10.1029/2001GL014655

Martinot, M., Flahaut, J., Besse, S., Quantin, C., Van Westrenen, W., Donaldson Hanna, K. L., & Blanchette-Guertin, J.-F. (2017). Lunar crustal composition in the Humboldt crater region. Paper presented at *Lunar and Planetary Science Conference*.

Matsunaga, T., Ohtake, M., Haruyama, J., Ogawa, Y., Nakamura, R., Yokota, Y., ..., & Otake, H. (2008). Discoveries on the lithology of lunar crater central peaks by SELENE spectral profiler. *Geophysical Research Letters*, *35*, 1–5. doi:10.1029/2008GL035868

Melosh, H. J. (1989). *Impact cratering: A geologic process*. Oxford University Press.

Mittlefehldt, D. W., McCoy, T. J., Goodrich, C. A., & Kracher, A. (1998). No Title. In J. J. Papike, & P. H. Ribbe (Eds.), *Planetary Materials* (pp. 1–195). (Mineralogi ed.).

Neukum, G. (1983). *Meteorite Bombardment and Dating of Planetary Surfaces (Meteoritenbombardement und Datierung planetarer Oberflächen)*. Ph.D. thesis University of Munich.

Neukum, G., Ivanov, B. A., & Hartmann, W. K. (2001). Cratering Records in the Inner Solar System in Relation to the Lunar Reference System. *Space Science Reviews*, *96*, 55–86.

Ohtake, M., Matsunaga, T., Haruyama, J., Yokota, Y., Morota, T., Honda, C., ..., & Josset, J.-L. (2009). The global distribution of pure anorthosite on the Moon. *Nature*, *461*, 236–240. doi:10.1038/nature08317

Osinski, G. R. (2004). Impact melt rocks from the Ries structure, Germany: An origin as impact melt flows? *Earth and Planetary Science Letters, 226*, 529–543. doi:10.1016/j.epsl.2004.08.012

Pieters, C. M., Besse, S., Boardman, J., Buratti, B., Cheek, L., Clark, R. N., ..., & Whitten, J. (2011). Mg-spinel lithology: A new rock type on the lunar farside. *Journal of Geophysical Research E: Planets, 116*. doi:10.1029/2010JE003727

Pieters, C. M., Boardman, J., Buratti, B., Chatterjee, A., Clark, R., Glavich, T., ..., & White, M. (2009). The Moon Mineralogy Mapper (M^3) on Chandrayaan-1. *Current Science, 96*, 1–6.

Prissel, T. C., Parman, S. W., Jackson, C. R. M., Rutherford, M. J., Hess, P. C., Head, J. W., Cheek, L., Dhingra, D., & Pieters, C. M. (2014). Pink Moon: The petrogenesis of pink spinel anorthosites and implications concerning Mg-suite magmatism. *Earth and Planetary Science Letters, 403*, 144–156. doi:10.1016/j.epsl.2014.06.027

Robinson, M. S., Brylow, S. M., Tschimmel, M., Humm, D., Lawrence, S. J., Thomas, P. C., ..., & Hiesinger, H. (2010). Lunar reconnaissance orbiter camera (LROC) instrument overview. *Space Science Reviews, 150*, 81–124. doi:10.1007/s11214-010-9634-2

Schultz, P. H. (1976). Floor-fractured lunar craters. *The Moon, 15*, 241–273. doi:10.1007/BF00562240

Shearer, C. K., Hess, P. C., Wieczorek, M. A., Pritchard, M. E., Parmentier, E. M., Borg, L. E., ..., & Wiechert, U. (2006). Thermal and Magmatic Evolution of the Moon. *Reviews in Mineralogy and Geochemistry, 60*, 365–518. doi:10.2138/rmg.2006.60.4

Smith, D. E., Zuber, M. T., Neumann, G. A., Lemoine, F. G., Mazarico, E., Torrence, M. H., ..., & Bartels, A. E. (2010). Initial observations from the Lunar Orbiter Laser Altimeter (LOLA). *Geophysical Research Letters, 37*, 1–6. doi:10.1029/2010GL043751

Snyder, G. A., Taylor, L. A., & Neal, C. R. (1992). A chemical model for generalting the sources of mare basalts: Combined equilibrium and fractional crystallization of th elunar magmasphere. *Geochimica et Cosmochimica Acta, 56*, 3809–3823.

Song, E., Bandfield, J. L., Lucey, P. G., Greenhagen, B. T., & Paige, D. A. (2013). Bulk mineralogy of lunar crater central peaks via thermal infrared spectra from the Diviner Lunar Radiometer: A study of the Moon's crustal composition at depth. *Journal of Geophysical Research E: Planets, 118*, 689–707. doi:10.1002/jgre.20065

Staid, M. I. (2000). *Remote Determination of the Mineralogy and Optical Alteration of Lunar Basalts Using Clementine Multispectral Images: Global Comparisons of Mare Volcanism*. Ph.D. thesis Brown University. URL: https://scholar.google.com/scholar?hl=fr&q=Staid%2C+M.I.%2C+2000.+Remote+determination+&btnG=&lr=.

Sunshine, J. M., & Pieters, C. M. (1998). Determing the composition of olivine from reflectance spectroscopy. *Journal of Geophysical Research, 103*, 675–688.

Thorey, C., Michaut, C., & Wieczorek, M. (2015). Gravitational signatures of lunar floor-fractured craters. *Earth and Planetary Science Letters, 1*, 1–11. doi:10.1016/j.epsl.2015.04.021

Tompkins, S., & Pieters, C. M. (1999). Mineralogy of the Lunar Crust - Results From Clementine. *Meteoritics & Planetary Science, 34*, 25–41.

Tompkins, S., & Pieters, C. M. (2010). Spectral characteristics of lunar impact melts and inferred mineralogy. *Meteoritics and Planetary Science, 45*, 1152–1169. doi:10.1111/j.1945-5100.2010.01074.x

Vaughan, W. M., Head, J. W., Wilson, L., & Hess, P. C. (2013). Geology and petrology of enormous volumes of impact melt on the Moon: A case study of the Orientale basin impact melt sea. *Icarus, 223*, 749–765. doi:10.1016/j.icarus.2013.01.017

Warren, P. H. (1985). The magma ocean concept and lunar evolution. *Annual Review of Earth and Planetary Science, 13*, 201–40. doi:10.1146/annurev.earth.13.1.201

Wieczorek, M. A., Neumann, G. A., Nimmo, F., Kiefer, W. S., Taylor, G. J., Melosh, H. J., ..., & Zuber, M. T. (2013). The crust of the Moon as seen by GRAIL. *Science (New York, N.Y.)*, *339*, 671–5. URL: http://www.ncbi.nlm.nih.gov/pubmed/23223394. doi:10.1126/science.1231530

Wieczorek, M. A., & Zuber, M. T. (2001). The composition and origin of the lunar crust: Constraints from central peaks and crustal thickness modeling. *Geophysical Research Letters*, *28*, 4023–4026. doi:10.1029/2001GL012918

Wilhelms, D. E., & El-Baz, F. (1977). *Geologic map of the east side of the Moon*. Technical Report. URL: http://pubs.er.usgs.gov/publication/i948.

Wilhelms, D. E., McCauley, J. F., & Trask, N. J. (1987). *The geologic history of the Moon*. (United sta ed.).

Yamamoto, S., Nakamura, R., Matsunaga, T., Ogawa, Y., Ishihara, Y., Morota, T., ..., & Haruyama, J. (2010). Possible mantle origin of olivine around lunar impact basins detected by SELENE. *Nature Geoscience*, *3*, 533–536. URL: http://dx.doi.org/10.1038/ngeo897. doi:10.1038/ngeo897

2

Compositional variations in the vicinity of the lunar crust-mantle interface from Moon Mineralogy Mapper data

This chapter is the reproduction of an article published in the Journal of Geophysical Research: Planets.

M. Martinot[1,2], J. Flahaut[3], S. Besse[4], C. Quantin-Nataf[2], and W. van Westrenen[1]

[1]Faculty of Science, Vrije Universiteit Amsterdam, De Boelelaan 1085, 1081 HV Amsterdam, The Netherlands [2]Université de Lyon, UCBL, ENSL, CNRS, LGL-TPE, 69622 Villeurbanne, France [3]Centre de Recherches Pétrographiques et Géochimiques, CNRS/Université de Lorraine, Vandoeuvre-lès-Nancy, France [4]European Space Astronomy Centre, P.O. Box 78, 28691 Villanueva de la Cañada, Madrid, Spain

Corresponding author: Mélissa Martinot (m.martinot@vu.nl)

Keypoints:

- Plagioclase is widely detected in the central peaks of craters allegedly sampling lower crust to mantle material, except in central peaks where low-calcium pyroxene is observed.

- Lateral heterogeneities at the crust-mantle interface are observed, and a pyroxene compositional evolution with depth is observed, from high to low-calcium pyroxene.
- This study's mineralogical observations support the GRAIL crustal thickness model 1 better than the model 3.

Abstract

Moon Mineralogy Mapper (M^3) spectroscopic data were used to investigate the mineralogy of a selection of impact craters' central peaks or peak rings, in order to characterize the lunar crust-mantle interface, and assess its lateral and vertical heterogeneity. The depth of origin of the craters' central peaks or peak rings was calculated using empirical equations, and compared to Gravity Recovery and Interior Laboratory (GRAIL) crustal thickness models to select craters tapping within +10/−20 km of the crust-mantle interface. Our results show that plagioclase is widely detected, including in craters allegedly sampling lower crustal to mantle material, except in central peaks where Low-Calcium Pyroxene (LCP) was detected. Olivine detections are scarce, and identified in material assumed to be derived from both above and below the crust-mantle interface. Mineralogical detections in central peaks show that there is an evolution of the pyroxene composition with depth, that may correspond to the transition from the crust to the mantle. The correlation between High-Calcium Pyroxene (HCP) and some pyroxene-dominated mixture spectra with the location of maria and cryptomaria hints at the existence of lateral heterogeneities as deep as the crust-mantle interface.

2.1. Introduction

Lunar crust composition and stratigraphy provide important constraints on our understanding of its origin and evolution [e.g., *Jaumann et al.*, 2012]. The Lunar Magma Ocean (LMO) hypothesis predicts that minerals crystallized in the order of olivine, LCP, then HCP, and sank to the bottom of the magma ocean, forming the mantle and lower crust [e.g., *Charlier et al.*, 2018, *Elardo et al.*, 2011, *Elkins-Tanton et al.*, 2011, *Lin et al.*, 2017a,b, *Rapp and Draper*, 2018, *Snyder et al.*, 1992]. During later stages of the magma ocean crystallization, lighter minerals like plagioclase formed an anorthositic (> 90 % anorthite-rich plagioclase) upper crust by floatation [e.g., *Kaula*, 1979, *Warren*, 1985]. The last stage of the LMO predicts the crystallization of a deep crustal layer, widespread and uniformly distributed, enriched in incompatible elements, and called urKREEP (Potassium, Rare Earth Elements, Phosphorus) layer [*Shearer et al.*, 2006].

A number of remote sensing studies have informed our knowledge of the lunar crust composition and stratigraphy [e.g., *Donaldson Hanna et al.*, 2014, *Lemelin et al.*, 2015, *Ohtake et al.*, 2009, *Song et al.*, 2013, *Tompkins and Pieters*, 1999], pointing at both vertical and lateral heterogeneities. Because they excavate material from depth, impact craters are a key to probing the composition of the deeper layers of the lunar crust, and its vertical stratification. Several remote sensing studies have been carried out in order to characterize the lunar crust-mantle interface and possible occurrence of mantle material. *Tompkins and Pieters* [1999] used Clementine ultraviolet-visible camera multispectral data. Their results point at a compositionally diverse crust, with a very anorthositic upper crust, and an increase of mafic content with depth. They also found evidence for the presence of mafic plutons in the crust. On the contrary, *Lemelin et al.* [2015] used Kaguya Multiband Imager data, and found no clear evidence of increasing mafic content with depth within the crust. *Pieters et al.* [2011] used spectroscopic data from M^3 instrument to study the Moscoviense impact basin and described so-called OOS rock types, defined by high abundances of Orthopyroxene, Olivine and Mg-rich Spinel. They proposed several origins for the OOS lithologies: they might represent components of the deep crust or even the crust-mantle interface, or alternatively have an exogenic origin. The lack of mafic material observed in the 900 km Orientale basin peak rings led *Head et al.* [1993] and *Pieters et al.* [1993] to propose that the material composing the peak rings originates from the crust. This hypothesis was confirmed by a high spatial resolution spectroscopic study of Orientale basin revealing the overwhelming presence of pure anorthosite (> 90 vol% plagioclase) in Orientale basin peak rings [*Cheek et al.*, 2013].

Melosh et al. [2017] 3D modeled the largest lunar impact basin (SPA, with a diameter exceeding 2200 km [*Howard et al.*, 1974, *Spudis et al.*, 1994]), and showed that the SPA impact event sampled the upper mantle. *Melosh et al.* [2017] combined the results of the simulation with spectroscopic observations of the SPA ejecta blanket, and concluded that the lunar upper mantle has a large Low-Calcium Pyroxene (LCP) component. An alternative hypothesis is that the melt sheet produced by the SPA-forming event differentiated [e.g., *Hurwitz and Kring*, 2014, *Morrison*, 1998, *Nakamura et al.*, 2009], masking any potential mantle signature.

Remote sensing studies have also identified lateral heterogeneities in the lunar crust. *Jolliff et al.* [2000] used global geochemical data derived from Clementine multispectral data and Lunar Prospector gamma-ray data, and showed that there are at least three terranes: the Procellarum KREEP Terrane (PKT), the Feldspathic Highlands Terrane (FHT), and the South-Pole Aitken Terrane (SPAT). *Ohtake et al.* [2009] used spectroscopic data from the Kaguya Multiband Imager and identified a plagioclase-rich layer between 3 and 30 km deep in the lunar crust. *Donaldson Hanna et al.* [2014] used M^3 spectroscopic data and confirmed the wide detection of rocks of high plagioclase abundance where the crust is between 30 and 63 km thick.

Modeling work was performed by *Head and Wilson* [1992b] in order to evaluate

the proportion of magmatic intrusions in the lunar crust. They estimated that a maximum of 37 to 50 % of the lower crust volume is intruded by plutons. The potential presence of magmatic intrusions in the crust should be taken into account when investigating the presence of lateral heterogeneities in the lunar crust through impact craters, because of the discontinuous sampling they provide.

Vertical and lateral variations of the lunar crust-mantle interface have been observed in previous studies, but it is still unclear if the crust-mantle transition is sharp or gradual, or if it occurs at the same depth locally, regionally, or globally. Four crustal thickness models were derived from the recent GRAIL mission's data, assuming different crustal porosities, and adding a seismically determined constraint on the crustal thickness at the Apollo 12 and 14 landing sites [*Wieczorek et al.*, 2013]. The GRAIL crustal thickness models provide different absolute crustal values in each point, and predict an average crust thickness between 34 and 43 km [*Wieczorek et al.*, 2013]. The mineralogical results provided in the present survey could help to determine which GRAIL model estimates best the crustal thickness at the local, regional or global scales. This study aims at further characterizing the vertical and lateral variations of the lunar crust-mantle interface, using the recent GRAIL crustal thickness models to select craters sampling that depth, and the M^3 spectroscopic data to assess the mineralogy of selected impact craters' central peaks or peak rings. This study focuses on a selection of craters tapping the crust-mantle interface, which is deeper than previously investigated [e.g., *Lemelin et al.*, 2015, *Tompkins and Pieters*, 1999]. The potential compositional changes of the crust-mantle interface are surveyed, with a selection of craters sampling material between +10 and −20 km around this interface according to the GRAIL crustal thickness models, and spread over a wide range of latitude and longitude.

2.2. Material and Methods

2.2.1. Datasets

Spectroscopic data from the M^3 instrument were used to derive the mineralogy of selected craters' central peaks or peak rings. M^3 is a hyperspectral imager that acquired visible to near-infrared data of the lunar surface between 2008 and 2009, with 85 spectral channels spanning from 430 to 3000 nm [*Pieters et al.*, 2009]. The M^3 data used here are the calibrated data archived in the Planetary Data System (PDS, version 1 of Level 2), radiometrically corrected [*Green et al.*, 2011], geometrically corrected [*Boardman et al.*, 2011], thermally corrected [*Clark et al.*, 2011], and photometrically corrected [*Besse et al.*, 2013]. Data from the optical period covering the maximal portion of each central peak were used, hence the wide variety of optical periods used (OP1B, OP2A, OP2C1, OP2C2, OP2C3, with a spatial resolution of 140 m/pixel for OP1B and OP2A; and 280 m/pixel for OP2C1, OP2C2, and OP2C3). This study is not comparing absolute reflectance of the surface from one crater to the other, so using data from

several optical periods is not problematic.

Reflectance data at wavelengths lower than 620 nm were not considered because of the low signal-to-noise ratio recovered in this part of the spectrum [*Green et al.*, 2011]. Thermal effects start to appear at wavelengths beyond 2700 nm, due to the contribution of the lunar surface [*Clark et al.*, 2011]. That is why reflectance data at wavelengths beyond 2700 nm were not considered in this analysis. The continuum-removal algorithm developed by *Martinot et al.* [2018] was used. Their approach is similar to that of *Horgan et al.* [2014]. The algorithm maximizes the area of lunar mafic minerals and plagioclase absorption bands at 1000 and 2000 nm. The continuum tie points are searched for in fixed intervals (620–1100 nm; 1100–1660 nm) on a spectrum previously smoothed in order to limit noise influence on the tie point positions. A third tie point is fixed at 2700 nm. Because of the presence of noise in the M^3 data, only band depths superior to 3% were considered in this study. Pixels with absorption band depths lower than 3 % were masked out of the parameter maps. A complete list of output parameter maps is provided in *Martinot et al.* [2018]. The predominantly used color composite for the mineralogical investigation was the one generated by *Martinot et al.* [2018] (R = area of the 1000 nm absorption band; G = area of the 2000 nm absorption band; B = position of the center of the 1000 nm absorption band). Fig. 2.1 shown a color composite of Petavius crater, classified as a floor fractured crater by *Jozwiak et al.* [2012]. The color composite displays plagioclase in blue shades going towards pink, as its absorption band increases; olivine is highlighted in red; and pyroxene in bright green. The color composite was stretched using ENVI. The highlighted pixels were then manually checked and compared to reference spectra from the Reflectance Experiment LABoratory (RELAB) database in order to confirm any mineralogical detection. The color composites were then imported in a GIS software and compared with other existing data sets, specifically: the global mosaic of the Lunar Reconnaissance Orbiter Wide Angle Camera (LRO WAC) at 100 m/pixel, to visualize the geological context, and the Lunar Orbiter Laser Altimeter/SELENE Terrain Camera (LOLA/SELENE TC) merged stereo-derived digital elevation model with a horizontal resolution of about 60 m/pixel, and a vertical accuracy of 4 m, providing information about the topography and elevation. Visible imagery was used to assess the central peak or peak ring morphology in order to confirm that the mineral detections occurred in uplifted material, and not in subsequently emplaced material such as later impact melts.

The GRAIL mission acquired gravimetric data from the Moon between 2011 and 2012. Four crustal thickness models were derived from the mission's data, with different assumptions on the crustal porosity and a constraint on the crustal thickness from the Apollo 12 and 14 landing sites' seismically determined crustal thickness [*Wieczorek et al.*, 2013]. GRAIL crustal thickness models 1 through 4 are reproduced in Fig. 2.2a–d. In this study, we will show the results of the models 1 and 3, which consider a crustal porosity of 12 %, and respectively 29.9 km and 38.1 km as crustal thickness constraint

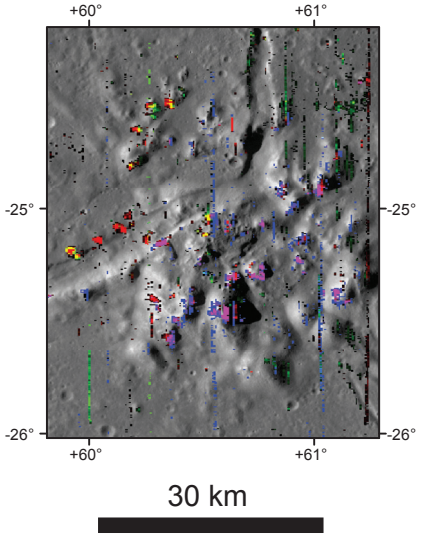

Figure 2.1: Color composite of M^3 spectral parameters covering Petavius crater central peak, overlain on the LRO WAC mosaic. The floor fractures described by *Jozwiak et al.* [2012] are merging in the central peak. R = area of the 1000 nm absorption band; G = area of the 2000 nm absorption band; B = position of the center of the 1000 nm absorption band. The color composite was stretched in order to highlight the mineralogical diversity (R = 10.4–26.4; G = 30–52; B = 1230–1270 nm). The background image is the LRO WAC mosaic. Olivine is displayed in red, pyroxene in green and plagioclase in blue to pink shades, as its absorption band increases. Several vertical stripes of pixels are highlighted, which can be explained by the residual noise left after the M^3 radiometric calibration.

from the Apollo 12 and 14 landing sites. Absolute crustal thickness values from the models 1 and 2, and from the models 3 and 4 are close together (a few kilometers difference), which is why only models 1 and 3 were considered. The choice to compare mineralogical detections to models 1 and 3 over 2 and 4 is arbitrary.

A selection of complex craters and impact basins listed in the Lunar Impact Crater Database (LICD, *Losiak et al.* [2009], revised by Ohman at LPI) were examined in this study.

2.2.2. Lunar Minerals in the Crater Selection

The number of absorption bands and their position in spectroscopic data allow the identification of several minerals on the Moon. Plagioclase, olivine, pyroxene and spinel were detected in the investigated craters.

Minor amounts of FeO (< 1.0 wt %) can be incorporated into lunar calcic plagioclase [*Burns*, 1993], making it detectable with visible near-infrared spectroscopy. Iron-bearing plagioclase spectra are characterized by a single absorption band centered around 1250 nm [*Adams and Goullaud*, 1978]. However, in a mixture with mafic minerals such as olivine of pyroxene, plagioclase is easily masked: *Cheek and Pieters* [2014] showed that as little as 2 vol. % of olivine or pyroxene completely masks the plagioclase signal. Therefore, the detection of plagioclase in near-infrared spectra provides a constraint on the plagioclase content of the rock to be at least 85 % [e.g., *Cheek et al.*, 2013, *Crown and Pieters*, 1987].

Olivine spectra display a single, broad and asymmetric absorption band centered at 1050 nm [*Sunshine and Pieters*, 1998], shifting towards longer wavelength with increasing iron content [*Burns*, 1970]. [*Sunshine and Pieters*, 1998] showed that the absorption band of fayalite is broader and more flat-bottomed than that of forsterite, and that this flattening of the absorption band can also be observed for large (< 60 μm) forsterite grains. It is worth noting that some lunar olivine spectra can have an additional shallow absorption band near 2000 nm caused by the presence of chromite [*Isaacson et al.*, 2011].

Pyroxene spectra have two diagnostic absorption bands located around 1000 and 2000 nm (referred to as band 1 and band 2), shifting towards longer wavelengths with increasing iron or calcium content [*Klima et al.*, 2007]. LCP such as pigeonite or enstatite have an absorption band 1 centered at 900 nm and an absorption band 2 centered at 2000 nm. HCP such as augite or diopside has absorption bands shifted towards longer wavelengths: its absorption band 1 is centered at 1000 nm, and its absorption band 2 is centered at 2200 or 2300 nm [*Adams*, 1974].

Spinel spectra are characterized by a single broad absorption band, centered at 2000 nm [*Cloutis et al.*, 2004]. Mg-spinel has a band 2 centered around 2000 nm, and a third absorption band centered around 3000 nm [*Pieters et al.*, 2014].

2.2.3. Calculation of the Proximity Value to the Crust-Mantle Interface

GRAIL models were used together with LOLA topography to calculate the proximity value to the mantle of all the complex craters listed in the LICD. The proximity to the crust-mantle interface (or material now exposed in a crater's central peak) was defined by *Cahill et al.* [2009] as the difference between the crustal thickness and the peak material depth of origin. In this study, it is referred to as the proximity value to the crust-mantle interface, or P_{cmi} value. The maximum depth of melting (D_m) was used to determine the minimum depth of origin of central peak material [*Cintala and Grieve*, 1998]. The pre-impact crustal thickness was calculated following the method in *Flahaut et al.* [2012], averaging the crustal thickness around the considered impact crater (from the *Wieczorek et al.* [2013] crustal thickness models) at a distance of one crater diameter, ± 10 % of the crater diameter.

If the P_{cmi} value is positive, only the crust should be chemically represented in the crater's central peak. If the P_{cmi} value is negative, material from below the crust-mantle interface was potentially sampled by the impact-forming event and emplaced in the resulting crater's central peak. Therefore, the P_{cmi} values symbolize the distance between the putative crust-mantle interface and the depth of origin of a crater's central peak material (see the Fig. 1 from *Flahaut et al.* [2012]).

2.2.4. Craters Selection

A subset of craters that presumably tap close to the crust-mantle interface was selected from the LICD, based on the following criteria: (1) the presence of an obvious central uplift structure (central peak or peak ring); (2) full or partial coverage of the central uplift structure by M^3 data; (3) a P_{cmi} value calculated with GRAIL crustal thickness models 1 or 3 between +10 km and −20 km. A preliminary study showed that the mineralogical transition from crust to mantle does not seem sharp. Moreover, the complexity of the lunar surface may result in uncertainties in the precision of the craterisation equations, hence the wide P_{cmi} values interval investigated. Tracking the depth of origin of a central peak emplaced on a pre-existing impact crater is not easily feasible. As a result, craters having their central peak located on the rim of a pre-existing crater, and craters located in the SPA basin were discarded from the selection. Based on these criteria, the mineralogy of 27 crater central peaks and 9 crater peak rings was studied. It is difficult to widen the pool of selected craters, because a large number of craters tapping the crust-mantle interface were eroded or subsequently filled by volcanic deposits. All the candidates that sample the crust-mantle interface, with M^3 coverage, were included in the present study. The selection of craters is listed in Table 2.1, together with the crater diameters; the crustal thickness of GRAIL models 1 through 4; the P_{cmi} values calculated from each GRAIL model; the melting depth (or central peak depth of origin, according to *Cintala and Grieve* [1998]); the excavation depth (or ejecta depth of origin, according to *Cintala and Grieve* [1998]); the M^3

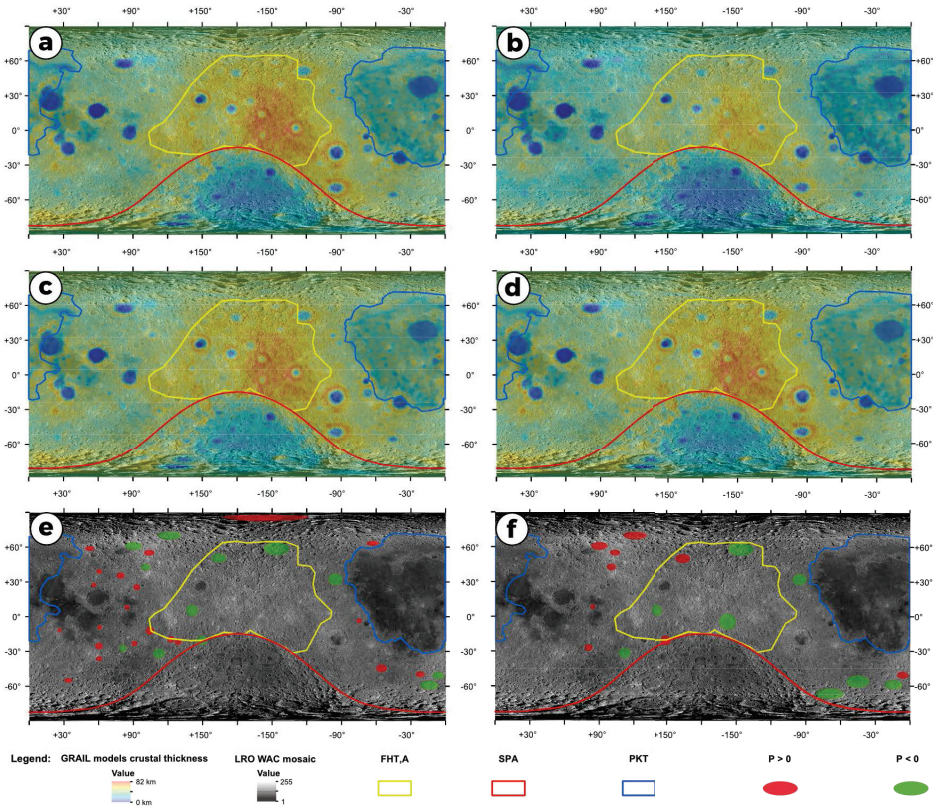

Figure 2.2: Global lunar crustal thickness maps from the GRAIL models 1 through 4, in panels **a** to **d** [*Wieczorek et al.*, 2013]. All crustal thickness maps are stretched between 0 and 82 km. The outlines of three major lunar terranes defined by *Jolliff et al.* [2000] are shown: the PKT in blue, the SPA basin in red, and the anorthositic FHT (FHT-a) in yellow. The outer FHT (FHT-o) was defined as the remainder of the lunar surface that is not part of the FHT-a, PKT, SPAT, or basin-filling mare [*Jolliff et al.*, 2000]. **e**. Craters selected on the basis of the P_{cmi} value calculated with GRAIL crustal thickness model 1 and overlaid on the LRO WAC mosaic. Craters with a P_{cmi} value > 0 are symbolized as red circles, whereas craters with a P_{cmi} value < 0 are symbolized as green circles. **f**. Craters selected on the basis of the P_{cmi} value calculated with GRAIL crustal thickness model 3 (see section 2.2.4) and overlaid on the LRO WAC mosaic. Craters with a P_{cmi} value > 0 are symbolized as red circles, whereas craters with a P_{cmi} value < 0 are symbolized as green circles.

optical period considered; and the crater age. The location of the selected craters are indicated in Fig. 2.2e–f.

Table 2.1: Craters selected for this survey, ranked according to P_{cmi} values calculated with the GRAIL crustal thickness model 1, M1, from greatest to smallest value; GRAIL models 1 through 4 crustal thickness; P_{cmi} value calculated with each GRAIL crustal thickness model; peak depth of origin; ejecta depth of origin; and age of the craters studied during this survey.

Name	LON	LAT	Diam.	GRAIL crust. thick. (km)				P_{cmi} value (km)				Melting depth	Excavation depth	OP	Age
			(km)	M1	M2	M3	M4	M1	M2	M3	M4	(km)	(km)		
Fermi	122.6	−19.3	183	40.2	41.7	49.9	50.4	9.9	11.5	19.6	20.1	30.3	12.5	OP2C2	Pre-Nectarian
Riccioli	−74.6	−3.3	139	32.1	33.1	40.4	40.4	9.6	10.6	17.9	18.0	22.5	9.9	OP1B	Pre-Nectarian
Tsiolkovskiy	128.9	−21.2	185	39.9	41.3	49.5	49.8	9.3	10.7	18.9	19.2	30.6	12.6	OP2C1	Upper Imbrian
Messala	60.5	39.2	125	29.1	29.9	37.8	37.6	9.1	9.8	17.8	17.5	20.1	9.0	OP2C3	Pre-Nectarian
Pythagoras	−63.0	63.5	142	31.9	32.7	41.2	41.0	8.9	9.7	18.2	18.0	23.0	10.1	OP2A	Eratosthenian
Hommel	33.8	−54.7	126	29.0	29.7	37.1	36.8	8.8	9.5	16.9	16.6	20.2	9.1	OP2C1	Pre-Nectarian
Langrenus	61.1	−8.9	127	28.9	29.5	37.8	37.4	8.5	9.2	17.4	17.0	20.4	9.2	OP2C3	Eratosthenian
Furnerius	60.6	−36.0	135	30.0	30.8	38.4	38.2	8.2	9.0	16.6	16.4	21.8	9.7	OP2C3	Pre-Nectarian
de la Rue	52.3	59.1	134	29.8	30.5	38.6	38.3	8.2	8.8	17.0	16.6	21.6	9.6	OP1B	Pre-Nectarian
Theophilus	26.4	−11.4	110	23.8	24.5	31.4	31.2	6.3	7.0	13.9	13.7	17.5	8.1	OP1B	Eratosthenian
Longomontanus	−21.8	−49.6	157	31.9	32.7	40.4	40.2	6.2	7.0	14.7	14.6	25.6	11.0	OP1B	Nectarian
Cleomedes	56.0	27.7	125	25.9	26.5	34.1	33.7	5.9	6.5	14.0	13.7	20.1	9.0	OP1B	Nectarian
Curie	91.0	−22.9	151	30.1	30.8	38.6	38.4	5.5	6.3	14.0	13.8	24.6	10.6	OP2C1	Pre-Nectarian
Joliot	93.1	25.8	164	32.2	33.0	41.6	41.4	5.3	6.2	14.7	14.6	26.9	11.4	OP2C1	Pre-Nectarian
Rozhdestvenskiy	−155.4	85.2	177	33.4	34.2	42.2	42.0	4.2	5.0	13.0	12.8	29.2	12.1	OP2A	Pre-Nectarian
Neper	84.6	8.5	137	24.2	24.6	32.2	31.7	2.0	2.5	10.0	9.6	22.1	9.8	OP2C1	Nectarian
Schickard	−55.3	−44.3	206	36.2	37.3	45.9	45.9	1.8	2.9	11.5	11.5	34.4	13.8	OP2A	Pre-Nectarian
Pasteur	104.6	−11.9	224	39.4	40.9	49.6	49.9	1.8	3.2	11.9	12.3	37.6	14.8	OP2C1	Pre-Nectarian
Gauss	79.0	35.7	177	30.8	31.7	39.6	39.5	1.6	2.5	10.4	10.3	29.2	12.1	OP2C1	Nectarian
Petavius	60.4	−25.1	188	32.8	33.7	42.1	42.0	1.6	2.6	11.0	10.9	31.2	12.8	OP2C3	Lower Imbrian
Compton*	103.8	55.3	162	26.9	27.4	34.6	34.2	0.4	0.8	8.1	7.6	26.5	11.3	OP2C1	Lower Imbrian
Fabry	100.7	42.9	184	30.43	31.3	38.8	38.8	0.0	0.9	8.3	8.3	30.4	12.6	OP2C1	Pre-Nectarian
Humboldt*	80.9	−27.0	189	30.1	30.9	38.8	38.7	−1.2	−0.4	7.5	7.3	31.3	12.8	OP2C1	Upper Imbrian
Maginus	−6.3	−50.5	194	30.2	30.9	38.6	38.2	−2.0	−1.4	6.4	6.0	32.2	13.1	OP1B	Pre-Nectarian
Bel'kovich	90.2	61.1	214	30.7	31.3	39.5	39.0	−5.1	−4.6	3.7	3.2	35.8	14.3	OP2C1	Nectarian
Gagarin	149.2	−20.2	265	36.9	38.2	45.8	46.1	−8.2	−7.0	0.7	1.0	45.1	17.1	OP2C1	Pre-Nectarian
Clavius	−14.1	−58.8	245	32.3	33.1	40.8	40.7	−9.2	−8.4	−0.6	−0.8	41.5	16.0	OP1B	Nectarian
d'Alembert	163.9	50.8	248	40.5	41.8	49.9	50.0	−1.5	−0.3	7.8	8.0	42.0	16.2	OP2C1	Nectarian
Schwarzschild	121.2	70.1	212	30.2	30.8	38.3	38.0	−5.3	−4.6	2.8	2.5	35.5	14.2	OP2C1	Nectarian
Milne	112.2	−31.4	272	34.3	35.2	43.4	43.2	−12.2	−11.2	−3.1	−3.2	46.4	17.5	OP2C2	Pre-Nectarian
Mendeleev	140.9	5.7	313	41.8	43.3	51.4	51.9	−12.3	−10.8	−2.6	−2.2	54.0	19.7	OP2C1	Nectarian
Bailly	−69.1	−66.5	287	35.0	35.9	44.0	43.9	−14.2	−13.3	−5.2	−5.3	49.20	18.3	OP2C1	Nectarian
Lorentz	−95.3	32.6	312	34.5	35.5	43.3	43.3	−19.4	−18.4	−10.6	−10.5	53.8	19.6	OP1B	Pre-Nectarian
Birkhoff	−146.1	58.7	345	39.6	40.7	48.8	48.8	−20.4	−19.3	−11.2	−11.2	60.0	21.4	OP2C2	Pre-Nectarian
Schiller-Zucchius	−45.0	−56.0	335	35.8	36.8	45.0	45.0	−22.3	−21.4	−13.2	−13.2	58.1	20.9	OP1B	Pre-Nectarian
Korolev	−157.4	−4.0	437	48.7	50.5	59.1	59.8	−28.8	−27.0	−18.4	−17.7	77.5	26.1	OP2C1	Nectarian

Craters with * were listed by *Baker et al.* [2011] as transition crater (Compton crater) and crater with ring-like central peak (Humboldt crater).
Crater locations, diameter, melting depth, excavation depth and age are from the Lunar Impact Crater Database; GRAIL crustal thickness models from *Wieczorek et al.* [2013].
Note that the table separates the central peak craters, at the top of the table, from the peak ring craters, at the bottom of the table.

2.3. Results

2.3.1. Mineralogical Detections

The mineralogical diversity of the 36 surveyed craters is summarized in Fig. 2.4. Phases detected include plagioclase, olivine, High-Calcium Pyroxene (HCP), Low-Calcium Pyroxene (LCP), spinel, pyroxene-dominated mixture spectra, and featureless spectra.

Plagioclase was detected in 17 out of 36 craters (Fig. 2.3a–b), and selected plagioclase spectra are shown in Fig. 2.4a. Olivine was detected in 3 out of 36 craters (Fig. 2.3c–d). The narrow absorption band and its right shoulder on the spectra in Fig. 2.4b are compatible with a forsteritic composition. The asymmetry and ratio between the band 1 depth and the band 2 depth of Humboldt and Petavius spectra is compatible with olivine. The shallow absorption band observed near 2000 nm may be caused by the presence of chromite [*Isaacson et al.*, 2011], or small amounts of pyroxene [*Mustard and Pieters*, 1987].

LCP was detected in 3 out of 36 craters (2.3e–f), and the spectra are displayed in Fig. 2.3c. HCP was observed in 4 out of 36 craters (Fig. 2.3e–f), and the spectra are shown in Fig. 2.4d. Spectra displaying two absorption bands which band 1 and 2 centers are close to but different from the LCP or HCP spectra field of values from [*Horgan et al.*, 2014] and [*Martinot et al.*, 2018] were labeled as pyroxene-dominated mixture spectra. Pyroxene-dominated mixture spectra were observed in 20 out of 36 craters (Fig. 2.3g–h). A selection of spectra is shown in Fig. 2.4e, with the LCP and HCP fields represented in light gray and dark gray, respectively. A continuum removal error could cause a displacement of the band centers, but in the case of the pyroxene-dominated mixture spectra, the bands are broad and strong, which strongly suggests a pyroxene-dominated mixture composition.

Spinel spectra were observed in 3 out of 36 craters (Fig. 2.3c). Spectra are shown in Fig. 2.4f. Spinel was not found in the central peaks of the craters selected with the GRAIL crustal thickness model 3.

Spectra with no diagnostic 1000 and 2000 nm absorption bands were reported in previous studies as featureless spectra [e.g., *Hawke et al.*, 2003, *Spudis et al.*, 1984, *Yamamoto et al.*, 2015]. The study of reflectance spectra from shocked plagioclase showed that the weakening and disappearance of plagioclase absorption band can be caused by shock pressures [*Adams et al.*, 1979, *Bruckenthal and Pieters*, 1984], or space weathering of plagioclase [*Lucey*, 2002]. Locations of featureless spectra detections, observed in 14 out of 36 craters, are shown in Fig. 2.3a–b. Featureless spectra, which could correspond to shocked or weathered plagioclase, are presented in Fig. 2.4g.

Spectra observed in Curie and Gagarin craters have shallow absorption features that do not correspond to any typical lunar mineral (plagioclase, HCP, LCP, olivine or spinel), and are different from featureless spectra. Such spectra were labeled as spectra with no particular signature. Examples of spectra detected in Curie and Gagarin are shown in Fig. 2.4h.

2.3.2. Lateral Distribution

The locations of all mineralogical occurrences are summarized in Fig. 2.3. Multiple mineralogical detections are observed in the central peak or peak ring of several craters. Plagioclase, featureless spectra, and pyroxene-dominated mixture spectra occurrences are widely detected in the selected craters. A few plagioclase and featureless spectra are located near the edge of the PKT (in Pythagoras, Lorentz, Riccioli and Theophilus craters), but most detections are located in the FHT-o. Olivine, spinel and HCP detections are concentrated in a relatively restricted latitude and longitude range: 30° N, 35° S; 20° W, 100° E, located in the FHT-o. LCP was scarcely detected in the selected craters. Two detections are located in Clavius and Maginus craters, near the edge of the SPAT, and one occurrence is found in d'Alembert crater, in the FHT-a.

2.3.3. Vertical Distribution

Table 2.2 shows the mineralogical detections of the selection of impact craters sorted by decreasing P_{cmi} value obtained with the GRAIL crustal thickness model 1 (*i.e.*, decreasing distance to the crust-mantle interface). Featureless spectra are detected at all studied P_{cmi} values. Plagioclase is widely detected, even in impact craters supposedly sampling mantle material, except in crater central peaks where LCP is observed. The plagioclase detection associated to the lowest P_{cmi} value in a central peak crater is located in Humboldt crater. The three olivine occurrences are concentrated in a P_{cmi} value interval ranging from +6.3 km to −1.2 km, as calculated with GRAIL crustal thickness model 1, and +13.9 km and +7.5 km as calculated with GRAIL crustal thickness model 3. The three spinel detections are clustered in a narrower P_{cmi} value range, ranking from +6.3 km to +2.0 km with GRAIL crustal thickness model 1, and +13.9 km and +10.0 km with GRAIL crustal thickness model 3. The HCP detections occur between +8.5 km and 0.0 km with GRAIL crustal thickness model 1, and +17.4 km and +8.3 km with GRAIL crustal thickness model 3. The LCP detections range from −1.5 km and −9.2 km with GRAIL crustal thickness model 1, and +7.8 km and −0.6 km with GRAIL crustal thickness model 3. Pyroxene-dominated mixture detections occur at all investigated P_{cmi} values, except where LCP is detected.

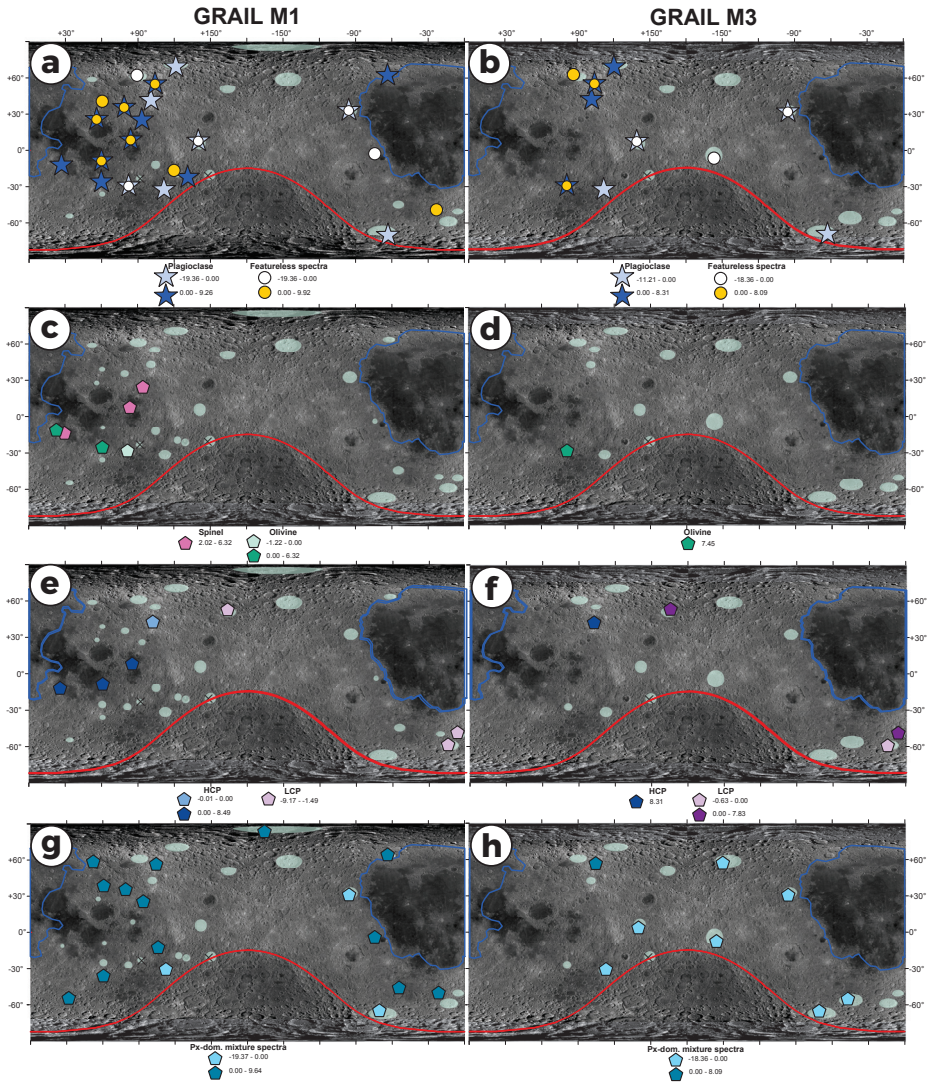

Figure 2.3: Mineralogical detections on the selected craters' central peak or peak ring, overlaid on LRO WAC global mosaic. The red line materializes the border of the SPAT defined by *Jolliff et al.* [2000]. Detections in craters having P_{cmi} values < 0 are represented with light colored symbols, whereas detections in craters having P_{cmi} values > 0 are represented with dark colored symbols. The circles represent the craters selected with the GRAIL crustal thickness model 1 and 3, overlaid on the LRO WAC global mosaic. The black crosses symbolize the craters where no clear mineralogical detection was observed. **a**. Plagioclase and/or featureless spectra occurrences in the craters selected with GRAIL model 1. **b**. Plagioclase and/or featureless spectra occurrences in the craters selected with GRAIL model 3. **c**. Olivine and spinel occurrences in the craters selected with GRAIL model 1. **d**. Olivine occurrences in the craters selected with GRAIL model 3. **e**. HCP and LCP occurrences in the craters selected with GRAIL model 1. **f**. HCP and LCP occurrences in the craters selected with GRAIL model 3. **g**. Pyroxene-dominated mixture detections in the craters selected with GRAIL model 1. **h**. Pyroxene-dominated mixture detections in the craters selected with GRAIL model 3.

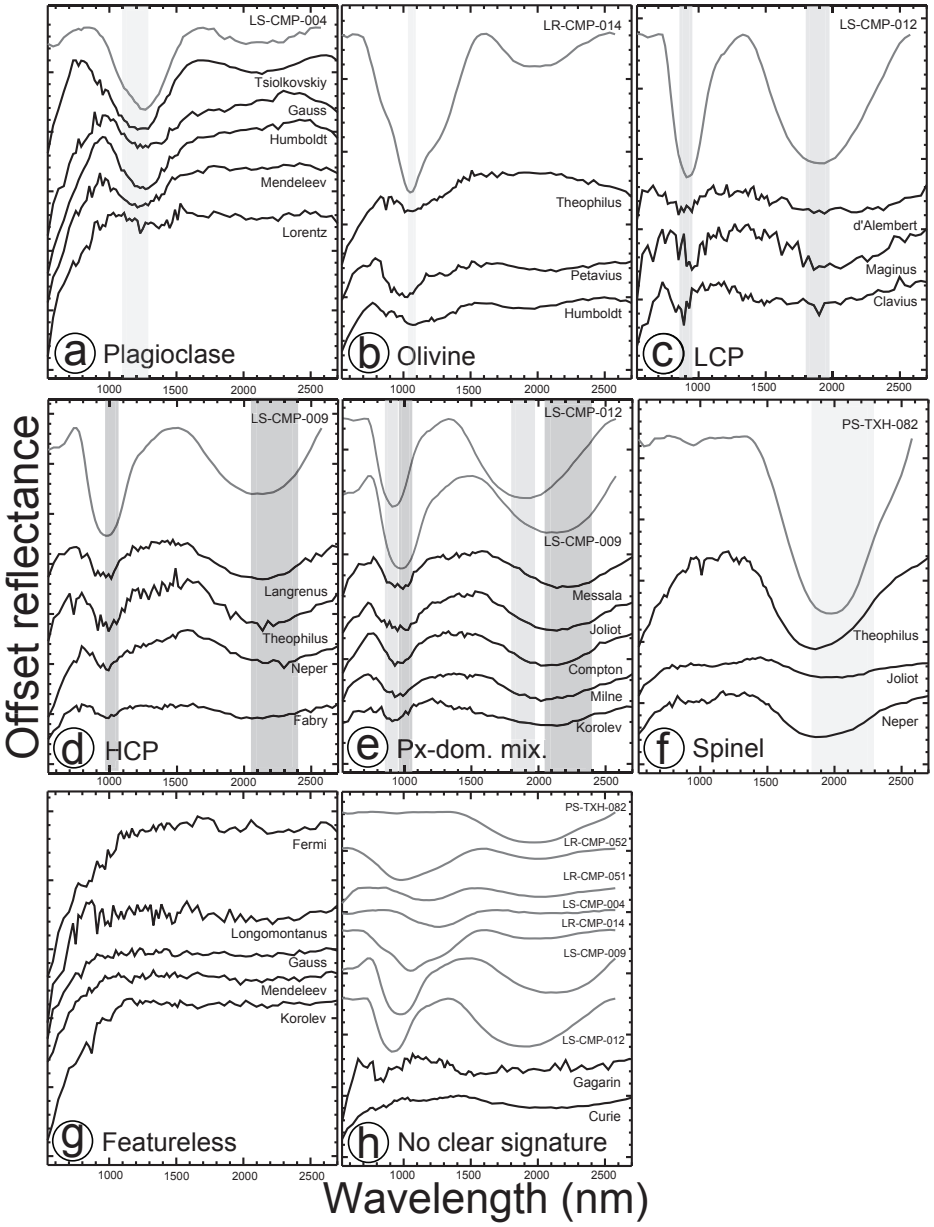

Figure 2.4: Representative continuum removed spectra showing the mineralogical diversity encountered in the selected craters. Black spectra are from the M^3 observations; gray spectra are the corresponding RELAB database spectra. The gray areas materialize the diagnostic absorption regions for each mineral. **a**. Plagioclase spectra. **b**. Olivine spectra. **c**. LCP spectra. **d**. HCP spectra. **e**. Pyroxene-dominated mixture spectra. **f**. Spinel spectra. **g**. Featureless spectra. **h**. Spectra with no particular mineralogical signature (observed in Curie and Gagarin craters). Laboratory spectra from the RELAB database were added in order to show that the observed spectra do not correspond to known lunar mineralogical detections (spectra, from top to bottom: spinel, green glass, orange glass, plagioclase, olivine, HCP, LCP).

Table 2.2: P_{cmi} value calculated with each GRAIL crustal thickness model of the craters studied in this survey, sorted against the P_{cmi} value calculated with GRAIL crustal thickness model 1 (from greatest to smallest value). The first part of the table shows craters with central peak, and the second part of the table lists all craters described as peak-ring craters by *Baker et al.* [2011]. The presence of a mineralogical detection on the central peak and/or peak ring (plagioclase, featureless spectra, HCP, pyxoxene-dominated mixture spectra, LCP, olivine or spinel) is symbolized by a cross.

	P_{cmi} value (km)				Mineralogical detections						
Name	M1	M2	M3	M4	Plagioclase	Featureless	Pyroxene-dominated mixture	HCP	LCP	Olivine	Spinel
Fermi	9.9	11.5	19.6	20.1		X					
Riccioli	9.6	10.6	17.9	18.0		X	X				
Tsiolkovskiy	9.3	10.7	18.9	19.2	X						
Messala	9.1	9.8	17.8	17.5		X	X				
Pythagoras	8.9	9.7	18.2	18.0	X		X				
Hommel	8.8	9.5	16.9	16.6			X				
Langrenus	8.5	9.2	17.4	17.0	X	X		X			
Furnerius	8.2	9.0	16.6	16.4			X				
de la Rue	8.2	8.8	17.0	16.6			X				
Theophilus	6.3	7.0	13.9	13.7	X			X		X	X
Longomontanus	6.2	7.0	14.7	14.6		X	X				
Cleomedes	5.9	6.5	14.0	13.7	X	X					
Curie	5.5	6.3	14.0	13.8							
Joliot	5.3	6.2	14.7	14.6	X		X				X
Rozhdestvenskiy	4.2	5.0	13.0	12.8			X				
Neper	2.0	2.5	10.0	9.6	X	X		X			X
Schickard	1.8	2.9	11.5	11.5			X				
Pasteur	1.8	3.2	11.9	12.3			X				
Gauss	1.6	2.5	10.4	10.3	X	X	X				
Petavius	1.6	2.6	11.0	10.9	X					X	
Compton*	0.4	0.8	8.1	7.6	X	X	X				
Fabry	0.0	0.9	8.3	8.3	X			X			
Humboldt*	−1.2	−0.4	7.5	7.3	X	X				X	
Maginus	−2.0	−1.4	6.4	6.0					X		
Bel'kovich	−5.1	−4.6	3.7	3.2		X					
Gagarin	−8.2	−7.0	0.7	1.0							
Clavius	−9.2	−8.4	−0.6	−0.8					X		
d'Alembert	−1.5	−0.3	7.8	8.0					X		
Schwarzschild	−5.3	−4.6	2.8	2.5	X						
Milne	−12.2	−11.2	−3.1	−3.2	X		X				
Mendeleev	−12.3	−10.8	−2.6	−2.2	X	X	X				
Bailly	−14.2	−13.3	−5.2	−5.3	X		X				
Lorentz	−19.4	−18.4	−10.6	−10.5	X	X	X				
Birkhoff	−20.4	−19.3	−11.2	−11.2	X		X				

Continued on next page

Table 2.2 – *Continued from previous page*

	P_{cmi} value (km)				Mineralogical detections					
Name	M1	M2	M3	M4	Plagioclase	Featureless	Pyroxene-dominated mixture	HCP	LCP	Olivine	Spinel
Schiller-Zucchius	−22.3	−21.4	−13.2	−13.2			X				
Korolev	−28.8	−27.0	−18.4	−17.7	x	X	X				

Previous plagioclase occurrences detected by *Donaldson Hanna et al.* [2014], *Yamamoto et al.* [2010] or *Yamamoto et al.* [2012], as well as this study is denoted as X.
Previous plagioclase occurrences detected by *Yamamoto et al.* [2010], but not our study, are denoted as x.
Craters with *were listed by *Baker et al.* [2011] as transition crater (Compton crater) and crater with ring-like central peak (Humboldt crater).
Note that the table separates the central peak craters, at the top of the table, from the peak ring craters, at the bottom of the table.

2.4. Discussion

2.4.1. Methods Limitations

The lunar crust-mantle interface and its lateral and vertical compositional structure are investigated in this study. However, some limits have to be kept in mind when considering the results presented here: (1) while the relative GRAIL crustal thickness variations are robust, there can be a difference of > 10 km in the absolute crustal thickness values from one model to the other; (2) the melting depth and other the craterisation equations were empirically determined, which can introduce a non-negligible error in the calculation of the proximity value to the crust-mantle interface; (3) the central peak likely contains mixed material that originate from shallower depths than the maximum depth of melting. This implies that shallow layers of the crust can be represented in the central peak.

2.4.2. Previous Studies' Craters P_{cmi} Calculation and Comparison to the Present Survey Crater Selection

Previous surveys [*Lemelin et al.*, 2015, *Tompkins and Pieters*, 1999] have examined craters sampling deep crustal to mantle material. Here, we focus on a specific depth range that presumably includes the transition from the lower crust to the mantle and the potential urKREEP layer.

In order to enable comparison with previous works, the P_{cmi} values of the craters surveyed in *Tompkins and Pieters* [1999] and *Lemelin et al.* [2015] were calculated using the method presented here (the maximum depth of melting representing the minimum depth of origin of the central peak material, and the GRAIL models providing the crustal thickness). Table 2.3 presents the P_{cmi} value range considered in their studies and the present survey. *Tompkins and Pieters* [1999] investigated craters presumably tapping crustal material, while *Lemelin et al.* [2015] surveyed craters sampling deeper material. It is worth noting that the crater sampling deepest material in *Lemelin et al.* [2015] selection, von Kármán crater, is located in the SPA basin, where a thick impact melt sheet was formed during the impact event [*Morrison*, 1998]. The next crater in their selection (Petavius crater) has a P_{cmi} value of +1.6 km. The craters surveyed in the present study are therefore supposedly tapping deeper material than the craters investigated in previous studies.

2.4.3. Spinel and Olivine Detections

Table 2.2 and Fig. 2.5 show that spinel and olivine are concentrated in a latitude and longitude range in the FHT-o defined by *Jolliff et al.* [2000], and a P_{cmi} value range between +6.3 km and −1.2 km as calculated with GRAIL crustal thickness model 1, and +13.9 km and +7.5 km as calculated with GRAIL crustal thickness model 3. According to *Pieters et al.* [2011], olivine and spinel could have a lower crustal origin. *Gross et al.* [2011] proposed that spinel could have formed in the lunar crust by magma-wall rock

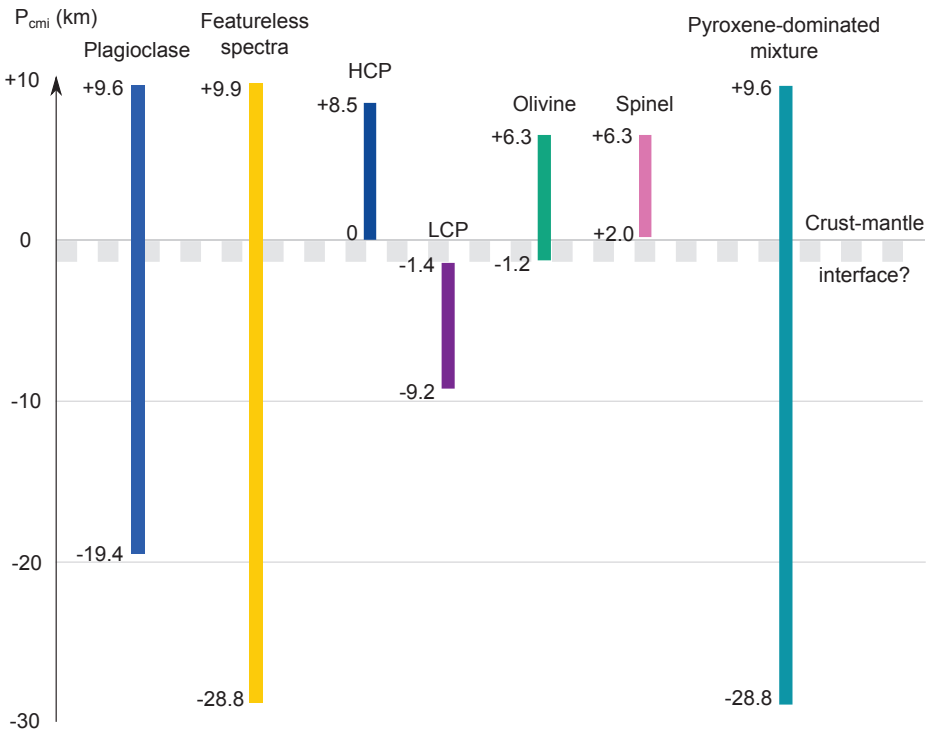

Figure 2.5: Schematic view of the crust-mantle interface presenting the mineralogical detections as a function of the P_{cmi} as calculated with GRAIL crustal thickness model 1. The gray dotted line symbolizes the possible crust-mantle interface.

interactions, and *Vaughan et al.* [2013] suggested that the crystallization of a melt mixture between the anorthositic crust and mantle could form spinel. Spinel could alternatively have formed in the final stages of the LMO solidification: *Lin et al.* [2017b] performed water-bearing LMO crystallization experiments, and showed that spinel is among the last minerals to be crystallized during solidification of a water-bearing magma ocean. According to their calculation, a spinel-bearing layer could be found around 30 km underneath the surface after magma ocean solidification. The urKREEP layer being the last layer to crystallize from LMO solidification [*Shearer et al.*, 2006], it could be stratigraphically linked or mingled with such a spinel-bearing layer. *Warren and Wasson* [1979] estimated that a global urKREEP layer would be thinner than 2 km, whereas *Wieczorek and Phillips* [2000] proposed that it was unevenly distributed, and concentrated under the PKT region instead.

If the surveyed craters where spinel is observed sample depths around 30 km, they may tap this final LMO solidification layer. In the craters where spinel is observed, the minimal depth of origin of the central peak material (maximum depth of melting, *Cintala and Grieve* [1998]) ranges from 17.5 to 26.9 km (Theophilus: 17.5 km; Neper: 22.1 km; Joliot: 26.9 km). However, eleven other craters sampling a depth between 25 and 35 km are included in the study (Compton, Fabry, Fermi, Gauss, Humboldt, Longomontanus, Maginus, Petavius, Rozhdestvenskiy, Schickard, Tsiolkovskiy), and spinel was not detected in any of those, suggesting it might not be a continuous layer. Instead, these central peaks show the presence of plagioclase, pyroxene-dominated mixture spectra or LCP.

Olivine is observed in craters supposedly sampling material from above and below the crust-mantle interface, according to GRAIL crustal thickness model 1. However, olivine detections are scarce in the craters studied here (only 3 craters out of 36), and does not appear to have a major role in the transition from the crust to the mantle. This is consistent with the recent study by *Melosh et al.* [2017], who proposed that the lunar upper mantle has a large LCP component instead of olivine signatures.

Albeit surveying craters supposedly tapping around the crust-mantle interface, where the urKREEP layer would allegedly be observed, we found no evidence of a mineralogically distinct, global urKREEP layer. Our observations rather support the presence of lateral heterogeneity in the crust. Olivine and spinel could have a plutonic origin [*Head and Wilson*, 1992b]. *Pieters et al.* [2014] described the spinel occurrences in Joliot and Theophilus crater as Pink Spinel Anorthosite (PSA, feldspar-dominated rock with Mg-spinel and less than 5 % mafic minerals), and proposed that PSA originates from the lower crust, which is in agreement with the *Lin et al.* [2017b] experiments.

2.4.4. Plagioclase Detections

Fig. 2.5 shows that pure plagioclase occurrences are widely detected, even in craters supposedly tapping lower crustal to mantle material (for example, in Humboldt crater

central peak), except in the central peaks where LCP is observed. This means that plagioclase-rich rocks are present in the lower crust. One could interpret the lack of plagioclase occurrence (crustal material) in the central peaks where LCP is observed as evidence that mantle material is emplaced in the central peaks, and place the crust-mantle interface at P_{cmi} values between those of Humboldt and Maginus craters. However, plagioclase being spectrally nearly transparent, its presence may be masked by LCP. An alternative explanation to the presence of LCP could be that the craters where it is observed are tapping plutons.

In craters where plagioclase was observed, the minimal depth of origin of the central peak material ranges from 17 to 60 km, which is consistent with the existence of a widespread purest anorthositic layer (> 98 vol% plagioclase) that was proposed by *Ohtake et al.* [2009], *Yamamoto et al.* [2012] and *Donaldson Hanna et al.* [2014]. However, HCP, pyroxene-dominated mixture spectra, spinel or olivine were also detected in most of the surveyed central peaks where purest anorthosite was detected in previous studies [*Donaldson Hanna et al.*, 2014, *Yamamoto et al.*, 2010, 2012]. A pure anorthositic layer may exist and be mixed with mafic material originating from other crustal depths in the surveyed central peaks during the impact event. Alternatively, the anorthositic crust may be intruded later by more mafic plutons. *Head and Wilson* [1992b] proposed that as much as 50 % of the lower crust is intruded by plutons; and *Dygert et al.* [2017] proposed that the present-day lunar crust is composed of a relatively impure, old crust, later intruded by pure anorthositic diapirs. Both processes are consistent with the observation of PAN occurrences juxtaposed to mafic detections.

2.4.5. Pyroxene Detections

All pyroxene detections with regards to the crust-mantle interface are shown in Fig. 2.5. Pyroxene-dominated mixture spectra are widely detected in the crust, except in the central peaks or peak rings where HCP or LCP can be identified. The pyroxene-dominated mixture spectra observed in this study have a band 1 center close to the LCP band 1 center values, and a band 2 center that is in the region of the HCP band 2 center. This could result from a mixture of pyroxene and other minerals, resulting in the shift of the absorption band centers beyond the LCP or HCP fields.

The P_{cmi} values associated to this study's HCP and LCP detections show a clear vertical progression: the HCP detections are concentrated in a range of P_{cmi} values that is shallower than that of the LCP detections (+8.5 km to 0 km with GRAIL crustal thickness model 1, and +17.4 km to +8.3 km with GRAIL crustal thickness model 3 for the HCP detections; and −1.5 km to −9.2 km with GRAIL crustal thickness model 1, and +7.4 km and −0.6 km with GRAIL crustal thickness model 3 for the LCP detections).

This supports *Tompkins and Pieters* [1999] observations of an LCP-enrichment with depth. It is worth noting that no other mineral is detected in central peaks where LCP is observed, and the transition from HCP to LCP happens very close to the model crust-mantle interface. This points to the potential existence of a deep LCP-

rich crustal (or upper mantle) layer, consistent with *Melosh et al.* [2017] simulations.

The P_{cmi} values of the first crater where LCP is observed are −2.0 km with GRAIL crustal thickness model 1, and +6.4 km with GRAIL crustal thickness model 3. LCP is observed in the central peaks of two of the central peak craters supposedly tapping the deepest material in the crater selection (Maginus and Clavius craters). Craters with more negative P_{cmi} values were studied, but these craters have peak rings instead of central peaks. According to *Baker and Head* [2015] and *Miljković et al.* [2017], the maximum depth of melting for peak-ring basins can not be taken as a proxy for estimating the depth of origin of the material exposed in the peak rings. Therefore, the P_{cmi} values calculated for the peak-ring craters of this study may not be appropriate reflections of the exhumation process. This is strengthened by the results of a spectroscopic survey of Orientale basin peak rings by *Cheek et al.* [2013], finding that Orientale basin peak rings are composed of pure anorthositic material. *Cheek et al.* [2013] confirmed the hypothesis that the material composing the Orientale basin peak rings originated from the crust [*Head et al.*, 1993, *Pieters et al.*, 1993]. All peak ring craters apart from d'Alembert and Schiller-Zucchius display plagioclase in their peak ring, which confirms their crustal origin. The mafic detections in d'Alembert and Schiller-Zucchius peak rings may be caused by the sampling of plutons at depth.

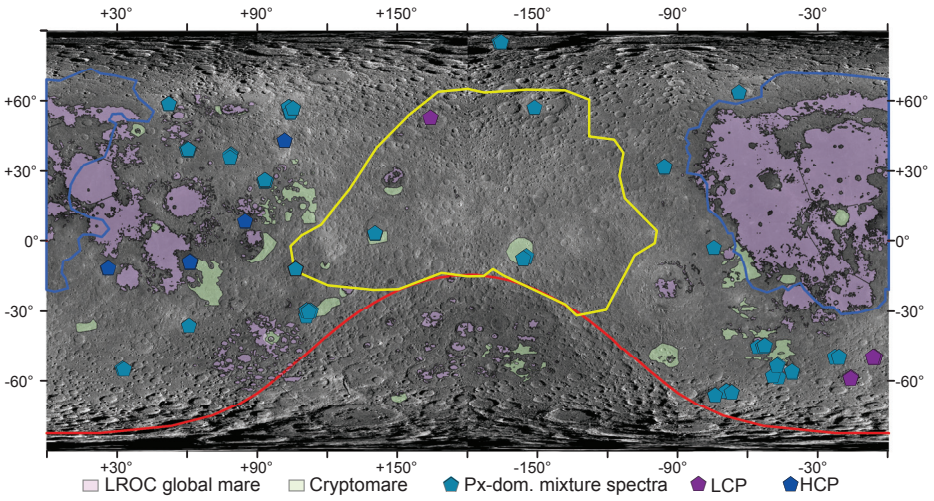

Figure 2.6: Global map with maria and cryptomaria locations (from the LRO archive and *Kring et al.* [2012], *Appendix Table 2.3*, for a summary of cryptomaria locations from the literature) and all pyroxene detections of this study. The background image is the LRO WAC global mosaic. The outlines of three major lunar terranes defined by [*Jolliff et al.*, 2000] are shown: the PKT in blue, the SPA basin in red, and the anorthositic FHT in yellow.

2.4.6. Comparison Between Pyroxene Detections and Mare / Cryptomare Locations

Fig. 2.6 shows the location of maria and cryptomaria on the Moon, with this study's pyroxene detections (shapefiles from *Whitten and Head* [2015]). Cryptomare were defined by *Head and Wilson* [1992a] as mare deposits that were subsequently covered by higher albedo deposits. All pyroxene detections in craters located near maria or cryptomaria have a HCP or pyroxene-dominated mixture spectra signature. In some craters, the HCP or pyroxene-dominated mixture spectra occurrences are located near the bottom of the central peak. The altitude difference between the HCP or pyroxene-dominated mixture spectra detections and the crater floor can be as low as 2 km. In these instances, contamination by surficial volcanic units is possible. The P_{cmi} value range considered in this study highlights the crust-mantle interface. If the central peak and peak rings were not contaminated by surficial volcanic units, the link between maria and cryptomaria locations (which have a pyroxene signature), and HCP and some pyroxene-dominated mixture detections may point at the presence of lateral heterogeneities at the crust-mantle interface.

2.4.7. Summary

The results presented here rely on the accuracy of the GRAIL models crustal thickness estimates, and the craterisation equations. The results tend to show that there is an evolution of the composition of pyroxene with depth (from HCP to LCP), that may correspond to the transition between the crust and the mantle. Olivine and spinel detections are concentrated in a thin interval of the lower crust, however they do not seem to be linked with the emplacement of a specific layer like urKREEP material; but rather seem to have a plutonic origin. Plagioclase is detected widely in the crust, including in craters supposedly sampling lower crust to mantle material. However, other minerals like HCP, spinel, olivine of pyroxene-dominated mixture spectra are also detected in most of the surveyed central peaks where plagioclase is detected. If a global anorthositic layer exists, as suggested by *Ohtake et al.* [2009], *Yamamoto et al.* [2012] and *Donaldson Hanna et al.* [2014], it may be mixed by subsequent impact events. According to impact simulations of *Melosh et al.* [2017], the lower crust to mantle is LCP-rich, also supported by the observations of LCP-enrichment with depth from *Tompkins and Pieters* [1999]. The transition between HCP to LCP in our data occurs close to the model crust-mantle interface, and could correspond to the transition from crust to mantle. Moreover, plagioclase was not detected in craters where LCP occurrences are found. The transition from crust to mantle appears to be gradual, with plagioclase and pyroxene-dominated mixture spectra being observed throughout the investigated crustal and putative mantle column. The mineralogical observations reported in this study fit the GRAIL crustal thickness model 1 better than the model 3, although the small number of observations reported here does not allow strong conclusions to be drawn.

2.5. Conclusions

Spectroscopic data of a selection of 36 craters central peaks and peak rings distributed on the lunar surface, coupled with their P_{cmi} value, show that plagioclase is widely present throughout the crust, except in central peaks where LCP is detected. An evolution of pyroxene composition with depth that may correspond to the transition between the crust and the mantle is observed. According to the mineralogical detections reported here, a crust-mantle interface could be placed at P_{cmi} values between Humboldt and Maginus craters −1.2 km with GRAIL crustal thickness model 1, and +7.5 km with GRAIL crustal thickness model 3 for Humboldt crater; −2.0 km with GRAIL crustal thickness model 1, and +6.4 km with GRAIL crustal thickness model 3 for Maginus crater). Lateral heterogeneities seem to exist at the depth of the crust-mantle interface, as the HCP detections and some pyroxene-dominated mixture spectra are situated close to maria and cryptomaria locations. The GRAIL crustal thickness model 1 fits these mineralogical detections better than model 3. This study illustrates how mineralogical detections in crater central peaks can be used to provide independent constraints on interior models.

Acknowledgments

We appreciated receiving positive and insightful reviews from Vivian Sun and an anonymous reviewer. We also thank the editors for their time. Jean-François Blanchette-Guertin provided useful inputs for the P_{cmi} value calculation. We thank Mark Wieczorek, Kerri Donaldson-Hanna, Makiko Ohtake and Satoru Yamamoto for kindly sharing their data. This work was supported by a Netherlands Organization for Scientific Research (NWO) Vici grant and a User Support Space Research grant from the Netherlands Space Office (NSO) to W.v.W. J.F. is funded by APR-CNES Luna. C.Q.N. is supported by European Research Council through the FP7/2007-2013/ERC grant agreement 280168. M^3 and LRO data can be accessed in the PDS Geoscience Node, Lunar Orbital Data Explorer (`http://ode.rsl.wustl.edu/`). The global mosaic of the LRO WAC is available at `https://astrogeology.usgs.gov/search/map/Moon/LRO/LROC_WAC/Lunar_LRO_LROC-WAC_Mosaic_global_100m_June2013`. LRO LOLA/SELENE Terrain Camera merged stereo-derived digital elevation model can be found at `https://astrogeology.usgs.gov/search/map/Moon/LRO/LOLA/Lunar_LRO_LrocKaguya_DEMmerge_60N60S_512ppd`. The Lunar Impact Crater Database can be found at `https://www.lpi.usra.edu/lunar/surface/Lunar_Impact_Crater_Database_v08Sep2015.xls`. The global maria shapefiles can be found in the LRO archive (`http://lroc.sese.asu.edu/data/LRO-L-LROC-5-RDR-V1.0/LROLRC_2001/EXTRAS/SHAPEFILE/LROC_GLOBAL_MARE/`). The cryptomaria shapefile can be found in the LPI concept 3 archive (`https://www.lpi.usra.edu/exploration/CLSE-landing-site-study/`). Laboratory spectra can be found in the RELAB spectral database archive (`http://www.planetary.brown.edu/relab/`).

Table 2.3: Table comparing the P_{cmi} values range considered in previous studies (that used a different set of craters) and this survey. The P_{cmi} values were calculated using the GRAIL crustal thickness models, and the maximum depth of melting as the minimum depth of origin of the central peak material.

Tompkins and Pieters [1999]	GRAIL M1	GRAIL M3
P_{cmi} max (km)	+46.2	+57.4
P_{cmi} min (km)	+0.4	+8.1
Lemelin et al. [2015]	GRAIL M1	
P_{cmi} max (km)	+41.1	
P_{cmi} min (km)	+1.6 (and von Kármán, in SPA, with $P_{cmi} = -11.4$)	
Our study	GRAIL M1	GRAIL M3
P_{cmi} max (km)	+10.0	+10.0
P_{cmi} min (km)	-20.0	−20.0

Bibliography

Adams, J. B. (1974), Visible and near-infrared diffuse reflectance spectra of pyroxenes as applied to remote sensing of solid objects in the solar system, *Journal of Geophysical Research*, *79*(32), 4829, doi:10.1029/JB079i032p04829.

Adams, J. B., and L. H. Goullaud (1978), Plagioclase feldspars: visible and near infrared diffuse reflectance spectra as applied to remote sensing, in *Proc. Lunar Planet. Sci. Conf.*, vol. 9, pp. 1205–1207.

Adams, J. B., F. Hörz, and R. V. Gibbons (1979), Effects of shock-loading on the reflectance spectra of plagioclase, pyroxene, and glass, in *Proceedings of the 10th Lunar and Planetary Science Conference*, pp. 5–7.

Baker, D. M. H., and J. W. Head (2015), Constraints on the depths of origin of peak rings on the Moon from Moon Mineralogy Mapper data, *Icarus*, *258*, 164–180, doi:10.1016/j.icarus.2015.06.013.

Baker, D. M. H., J. W. Head, C. I. Fassett, S. J. Kadish, D. E. Smith, M. T. Zuber, and G. A. Neumann (2011), The transition from complex crater to peak-ring basin on the Moon: New observations from the Lunar Orbiter Laser Altimeter (LOLA) instrument, *Icarus*, *214*(2), 377–393, doi:10.1016/j.icarus.2011.05.030.

Besse, S., J. M. Sunshine, M. I. Staid, J. Boardman, C. Pieters, P. Guasqui, E. Malaret, S. McLaughlin, Y. Yokota, and J. Y. Li (2013), A visible and near-infrared photometric correction for Moon Mineralogy Mapper (M^3), *Icarus*, *222*, 229–242, doi:10.1016/j.icarus.2012.10.036.

Boardman, J. W., C. M. Pieters, R. O. Green, S. R. Lundeen, P. Varanasi, J. Nettles, N. E. Petro, P. Isaacson, S. Besse, and L. A. Taylor (2011), Measuring moonlight: An overview of the spatial properties, lunar coverage, selenolocation, and related Level 1B products of the Moon Mineralogy Mapper, *Journal of Geophysical Research E: Planets*, *116*(6), 1–15, doi:10.1029/2010JE003730.

Bruckenthal, E. A., and C. M. Pieters (1984), Spectral effects of natural shock on plagioclase felsdpar, *Lunar and Planetary Institute*, pp. 96–97, doi:10.1017/CBO9781107415324.004.

Burns, R. G. (1970), Crystal field spectra and evidence of cation ordering in olivine minerals, *American Mineralogist*, *55*, 1608.

Burns, R. G. (1993), *Mineralogical Applications of Crystal Field Theory*, second edi ed., Cambridge University Press, Cambridge, doi:10.1017/CBO9780511524899.

Cahill, J. T. S., P. G. Lucey, and M. A. Wieczorek (2009), Compositional variations of the lunar crust: Results from radiative transfer modeling of central peak spectra, *Journal of Geophysical Research E: Planets*, *114*(9), 1–17, doi:10.1029/2008JE003282.

Charlier, B., T. L. Grove, O. Namur, and F. Holtz (2018), Crystallization of the lunar magma ocean and the primordial mantle-crust differentiation of the Moon, *Geochimica et Cosmochimica Acta*, *234*, 50–69, doi:10.1016/j.gca.2018.05.006.

Cheek, L. C., and C. M. Pieters (2014), Reflectance spectroscopy of plagioclase-dominated mineral mixtures: Implications for characterizing lunar anorthosites remotely, *American Mineralogist*, *99*(10), 1871–1892, doi:10.2138/am-2014-4785.

Cheek, L. C., K. L. Donaldson Hanna, C. M. Pieters, J. W. Head, and J. L. Whitten (2013), The distribution and purity of anorthosite across the Orientale basin: New perspectives from Moon Mineralogy Mapper data, *Journal of Geophysical Research: Planets*, *118*(9), 1805–1820, doi:10.1002/jgre.20126.

Cintala, M. J., and R. A. F. Grieve (1998), Scaling impact melting and crater dimensions: Implications for the lunar cratering record, *Meteoritics \& Planetary Science*, *33*(4), 889–912, doi:10.1111/j.1945-5100.1998.tb01695.x.

Clark, R. N., C. M. Pieters, R. O. Green, J. W. Boardman, and N. E. Petro (2011), Thermal removal from near-infrared imaging spectroscopy data of the Moon, doi:10.1029/2010JE003751.

Cloutis, E. A., J. M. Sunshine, and R. V. Morris (2004), Spectral reflectance-compositional properties of spinels and chromites: Implications for planetary remote sensing and geothermometry, *Meteoritics \& Planetary Science*, *39*(4), 545–565, doi:10.1111/j.1945-5100.2004.tb00918.x.

Crown, D. A., and C. M. Pieters (1987), Spectral properties of plagioclase and pyroxene mixtures and the interpretation of lunar soil spectra, *Icarus*, *72*(3), 492–506, doi:10.1016/0019-1035(87)90047-9.

Donaldson Hanna, K. L., L. C. Cheek, C. M. Pieters, J. F. Mustard, B. T. Greenhagen, I. R. Thomas, and N. E. Bowles (2014), Global assessment of pure crystalline plagioclase across the Moon and implications for the evolution of the primary crust, *Journal of Geophysical Research: Planets*, *119*, 1516–1545, doi:10.1002/2013JE004476.Received.

Dygert, N., J.-F. Lin, E. W. Marshall, Y. Kono, and J. E. Gardner (2017), A Low Viscosity Lunar Magma Ocean Forms a Stratified Anorthitic Flotation Crust With Mafic Poor and Rich Units, *Geophysical Research Letters*, pp. 1–10, doi:10.1002/2017GL075703.

Elardo, S. M., D. S. Draper, and C. K. Shearer (2011), Lunar Magma Ocean crystallization revisited: Bulk composition, early cumulate mineralogy, and the source regions of the highlands Mg-suite, *Geochimica et Cosmochimica Acta*, *75*(11), 3024–3045, doi:10.1016/j.gca.2011.02.033.

Elkins-Tanton, L. T., S. Burgess, and Q. Z. Yin (2011), The lunar magma ocean: Reconciling the solidification process with lunar petrology and geochronology, *Earth and Planetary Science Letters*, *304*(3-4), 326–336, doi:10.1016/j.epsl.2011.02.004.

Flahaut, J., J.-F. Blanchette-Guertin, C. Jilly, P. Sharma, A. Souchon, W. Van Westrenen, and D. A. Kring (2012), Identification and characterization of science-rich landing sites for lunar lander missions using integrated remote sensing observations, *Advances in Space Research*, *50*(12), 1647–1665, doi:10.1016/j.asr.2012.05.020.

Green, R. O., C. Pieters, P. Mouroulis, M. Eastwood, J. Boardman, T. Glavich, P. Isaacson, M. Annadurai, S. Besse, D. Barr, B. Buratti, D. Cate, A. Chatterjee, R. Clark, L. Cheek, J. Combe, D. Dhingra, V. Essandoh, S. Geier, J. N. Goswami, R. Green, V. Haemmerle, J. Head, L. Hovland, S. Hyman, R. Klima, T. Koch, G. Kramer, A. S. K. Kumar, K. Lee, S. Lundeen, E. Malaret, T. McCord, S. McLaughlin, J. Mustard, J. Nettles, N. E. Petro, K. Plourde, C. Racho, J. Rodriquez, C. Runyon, G. Sellar, C. Smith, H. Sobel, M. I. Staid, J. M. Sunshine, L. Taylor, K. Thaisen, S. Tompkins, H. Tseng, G. Vane, P. Varanasi, M. White, and D. Wilson (2011), The Moon Mineralogy Mapper (M$ˆ3$) imaging spectrometer for lunar science: Instrument description, calibration, on-orbit measurements, science data calibration and on-orbit validation, *Journal of Geophysical Research E: Planets*, *116*(10), 1–31, doi:10.1029/2011JE003797.

Gross, J., A. H. Treiman, and L. Le (2011), Unique spinel-rich lithology in lunar meteorite ALHA81005: origin and possible connection to M$ˆ3$ observations of the farside highlands, *Lunar and Planetary Science Conference*, *42*, 2–3.

Hawke, B. R., C. A. Peterson, D. T. Blewett, D. B. J. Bussey, P. G. Lucey, G. J. Taylor, and P. D. Spudis (2003), Distribution and modes of occurrence of lunar anorthosite, *Journal of Geophysical Research*, *108*(E6), 1–16, doi:10.1029/2002JE001890.

Head, J. W., and L. Wilson (1992a), Lunar mare volcanism: Stratigraphy, eruption conditions, and the evolution of secondary crusts, *Geochimica et Cosmochimica Acta*, *56*(6), 2155–2175, doi:10.1016/0016-7037(92)90183-J.

Head, J. W., S. Murchie, J. F. Mustard, C. M. Pieters, G. Neukum, A. McEwen, R. Greeley, E. Nagel, and M. J. S. Belton (1993), Lunar impact basins: New data for the western limb and far side (Orientale and South Pole-Aitken Basins) from the first Galileo flyby, *Journal of Geophysical Research*, *98*(E9), 17,149–17,182.

Head, J. W. I., and L. Wilson (1992b), Lunar mare volcanism - Stratigraphy, eruption conditions, and the evolution of secondary crusts, *Geochim. Cosmochim. Acta*, *56*, 2155–2175, doi:10.1016/0016-7037(92)90183-J.

Horgan, B. H. N., E. A. Cloutis, P. Mann, and J. F. Bell (2014), Near-infrared spectra of ferrous mineral mixtures and methods for their identification in planetary surface spectra, *Icarus*, *234*, 132–154, doi:10.1016/j.icarus.2014.02.031.

Howard, K. A., D. E. Wilhelms, and D. H. Scott (1974), Lunar basin formation and highland stratigraphy, *Reviews of Geophysics*, *12*(3), 309–327, doi:10.1029/RG012i003p00309.

Hurwitz, D. M., and D. A. Kring (2014), Differentiation of the South Pole–Aitken basin impact melt sheet: Implications for lunar exploration, *Journal of Geophysical Research: Planets*, *119*, 1110–1133, doi:10.1002/2014JE004657.Received.

Isaacson, P. J., C. M. Pieters, S. Besse, R. N. Clark, J. W. Head, R. L. Klima, J. F. Mustard, N. E. Petro, M. I. Staid, J. M. Sunshine, L. A. Taylor, K. G. Thaisen, and S. Tompkins (2011), Remote compositional analysis of lunar olivine-rich lithologies with Moon Mineralogy Mapper (M$ˆ3$) spectra, *Journal of Geophysical Research E: Planets*, *116*(4), 1–17, doi:10.1029/2010JE003731.

Jaumann, R., H. Hiesinger, M. Anand, I. A. Crawford, R. Wagner, F. Sohl, B. L. Jolliff, F. Scholten, M. Knapmeyer, H. Hoffmann, H. Hussmann, M. Grott, S. Hempel, U. Köhler, K. Krohn, N. Schmitz, J. Carpenter, M. A. Wieczorek, T. Spohn, M. S. Robinson, and J. Oberst (2012), Geology, geochemistry, and geophysics of the Moon: Status of current understanding, *Planetary and Space Science*, *74*(1), 15–41, doi:10.1016/j.pss.2012.08.019.

Jolliff, B. L., J. J. Gillis, L. A. Haskin, R. L. Korotev, and M. A. Wieczorek (2000), Major lunar crustal terranes: Surface expressions and crust-mantle origins, *Journal of Geophysical Research*, *105*(E2), 4197, doi:10.1029/1999JE001103.

Jozwiak, L. M., J. W. Head, M. T. Zuber, D. E. Smith, and G. A. Neumann (2012), Lunar floor-fractured craters: Classification, distribution, origin and implications for magmatism and shallow crustal structure, *Journal of Geophysical Research E: Planets*, *117*(11), 1–23, doi:10.1029/2012JE004134.

Kaula, W. M. (1979), Thermal evolution of earth and moon growing by planetesimal impacts, *Journal of Geophysical Research*, *84*(2), 999–1008, doi:10.1029/JB084iB03p00999.

Klima, R. L., C. M. Pieters, and M. D. Dyar (2007), Spectroscopy of synthetic Mg-Fe pyroxenes I: Spin-allowed and spin-forbidden crystal field bands in the visible and near-infrared, *Meteoritics \& Planetary Science*, *42*(2), 235–253, doi:10.1111/j.1945-5100.2007.tb00230.x.

Kring, D. A., D. D. Durda, K. O. Sullivan, J. Barnes, D. M. Blair, K. D. Runyon, K. Singer, P. Donohue, S. Crites, and C. Santiago (2012), A Global Lunar Landing Site Study to Provide the Scientific Context for Exploration of the Moon Edited by, p. 695.

Lemelin, M., P. G. Lucey, E. Song, and G. J. Taylor (2015), Lunar central peak mineralogy and iron content using the Kaguya Multiband Imager: Reassessment of the compositional structure of the lunar crust, *Journal of Geophysical Research: Planets*, *120*(5), 869–887, doi:10.1002/2014JE004778.

Lin, Y., E. J. Tronche, E. S. Steenstra, and W. van Westrenen (2017a), Experimental constraints on the solidification of a nominally dry lunar magma ocean, *Earth and Planetary Science Letters*, *471*, 104–116, doi:10.1016/j.epsl.2017.04.045.

Lin, Y., E. J. Tronche, E. S. Steenstra, and W. van Westrenen (2017b), Evidence for an early wet Moon from experimental crystallization of the lunar magma ocean, *Nature Geoscience*, *1*(November), 1–6, doi:10.1038/ngeo2845.

Losiak, A., D. E. Wilhelms, C. J. Byrne, K. Thaisen, S. Z. Weider, T. Kohout, K. O'Sullivan, and D. A. Kring (2009), A new lunar impact crater database, in *Lunar and Planetary Science Conference*.

Lucey, P. G. (2002), Radiative transfer model constraints on the shock state of remotely sensed lunar anorthosites, *Geophysical Research Letters*, *29*(10), 1–3, doi:10.1029/2001GL014655.

Martinot, M., S. Besse, J. Flahaut, C. Quantin-Nataf, L. Lozac'h, and W. van Westrenen (2018), Mineralogical Diversity and Geology of Humboldt Crater Derived Using Moon Mineralogy Mapper Data, *Journal of Geophysical Research: Planets*, *123*, doi:10.1002/2017JE005435.

Melosh, H. J., J. Kendall, B. Horgan, B. C. Johnson, T. Bowling, P. G. Lucey, and G. J. Taylor (2017), South Pole-Aitken basin ejecta reveal the Moon's upper mantle, *Geology*, *45*(12), 1063–1066, doi:10.1130/G39375.1.

Miljković, K., M. Lemelin, and P. G. Lucey (2017), Depth of Origin of the Peak (Inner) Ring in Lunar Impact Basins, *Geophysical Research Letters*, pp. 1–7, doi:10.1002/2017GL075207.

Morrison, D. A. (1998), Did a thick South Pole-Aitken basin melt sheet differentiate to form cumulates?, *Lunar and Planetary Science Conference*, pp. 2–3.

Mustard, J. F., and C. M. Pieters (1987), Quantitative Abundance Estimates From Bidirectional Reflectance Measurements, *Journal of Geophysical Research*, *92*(B4), E617–E626, doi:10.1029/JB092iB04p0E617.

Nakamura, R., T. Matsunaga, Y. Ogawa, S. Yamamoto, T. Hiroi, K. Saiki, N. Hirata, T. Arai, K. Kitazato, H. Takeda, T. Sugihara, S. Kodama, M. Ohtake, J. Haruyama, and Y. Yokota (2009), Ultramafic impact melt sheet beneath the South Pole-Aitken basin on the Moon, *Geophysical Research Letters*, *36*(22), 7–11, doi:10.1029/2009GL040765.

Ohtake, M., T. Matsunaga, J. Haruyama, Y. Yokota, T. Morota, C. Honda, Y. Ogawa, M. Torii, H. Miyamoto, T. Arai, N. Hirata, A. Iwasaki, R. Nakamura, T. Hiroi, T. Sugihara, H. Takeda, H. Otake, C. M. Pieters, K. Saiki, K. Kitazato, M. Abe, N. Asada, H. Demura, Y. Yamaguchi, S. Sasaki, S. Kodama, J. Terazono, M. Shirao, A. Yamaji, S. Minami, H. Akiyama, and J.-L. Josset (2009), The global distribution of pure anorthosite on the Moon., *Nature*, *461*(7261), 236–240, doi:10.1038/nature08317.

Pieters, C. M., J. W. Head, J. M. Sunshine, E. M. Fischer, S. L. Murchie, M. Belton, A. McEwen, L. Gaddis, R. Greeley, G. Neukum, R. Jaumann, and H. Hoffmann (1993), Crustal Diversity of the Moon: Compositional Analyses of Galileo Solid State Imaging Data, *Journal of Geophysical Research*, *98*.

Pieters, C. M., J. Boardman, B. Buratti, A. Chatterjee, R. Clark, T. Glavich, R. Green, J. W. I. Head, P. Isaacson, E. Malaret, T. Mccord, J. Mustard, N. E. Petro, C. Runyon, M. I. Staid, J. M. Sunshine, L. Taylor, S. Tompkins, P. Varanasi, and M. White (2009), The Moon Mineralogy Mapper (M^3) on Chandrayaan-1, *Current Science*, *96*(4), 1–6.

Pieters, C. M., S. Besse, J. Boardman, B. Buratti, L. Cheek, R. N. Clark, J. P. Combe, D. Dhingra, J. N. Goswami, R. O. Green, J. W. Head, P. Isaacson, R. Klima, G. Kramer, S. Lundeen, E. Malaret, T. McCord, J. Mustard, J. Nettles, N. Petro, C. Runyon, M. Staid, J. Sunshine, L. A. Taylor, K. Thaisen, S. Tompkins, and J. Whitten (2011), Mg-spinel lithology: A new rock type on the lunar farside, *Journal of Geophysical Research E: Planets*, *116*(4), doi:10.1029/2010JE003727.

Pieters, C. M., H. Kerri Donaldson, L. Cheek, D. Dhingra, T. Prissel, C. Jackson, D. Moriarty, S. Parman, and L. A. Taylor (2014), The distribution of Mg-spinel across the Moon and constraints on crustal origin, *American Mineralogist*, *99*(10), 1893–1910, doi:10.2138/am-2014-4776.

Rapp, J. F., and D. S. Draper (2018), Fractional crystallization of the lunar magma ocean : Updating the dominant paradigm, *Meteoritics \& Planetary Science*, *24*, 1–24, doi:10.1111/maps.13086.

Shearer, C. K., P. C. Hess, M. A. Wieczorek, M. E. Pritchard, E. M. Parmentier, L. E. Borg, J. Longhi, L. T. Elkins-Tanton, C. R. Neal, I. Antonenko, R. M. Canup, A. N. Halliday, T. L. Grove, B. H. Hager, D.-C. Lee, and U. Wiechert (2006), Thermal and Magmatic Evolution of the Moon, *Reviews in Mineralogy and Geochemistry*, *60*(1610), 365–518, doi:10.2138/rmg.2006.60.4.

Snyder, G. A., L. A. Taylor, and C. R. Neal (1992), A chemical model for generalting the sources of mare basalts: Combined equilibrium and fractional crystallization of th elunar magmasphere, *Geochimica et Cosmochimica Acta*, *56*, 3809–3823.

Song, E., J. L. Bandfield, P. G. Lucey, B. T. Greenhagen, and D. A. Paige (2013), Bulk mineralogy of lunar crater central peaks via thermal infrared spectra from the Diviner Lunar Radiometer: A study of the Moon's crustal composition at depth, *Journal of Geophysical Research E: Planets*, *118*(4), 689–707, doi:10.1002/jgre.20065.

Spudis, P. D., B. R. Hawke, and P. Lucey (1984), Composition of orientale basin deposits and implications for the lunar basin-forming process, *Journal of Geophysical Research: Solid Earth*, *89*(S01), C197—-C210, doi:10.1029/JB089iS01p0C197.

Spudis, P. D., J. J. Gillis, and R. A. Reisse (1994), Ancient multiring basins on the moon revealed by clementine laser altimetry., *Science (New York, N.Y.)*, *266*(5192), 1848–1851, doi:10.1126/science.266.5192.1848.

Sunshine, J. M., and C. M. Pieters (1998), Determing the composition of olivine from reflectance spectroscopy, *Journal of Geophysical Research*, *103*, 675–688.

Tompkins, S., and C. M. Pieters (1999), Mineralogy of the Lunar Crust - Results From Clementine, *Meteoritics \& Planetary Science*, *34*, 25–41.

Vaughan, W. M., J. W. Head, L. Wilson, and P. C. Hess (2013), Geology and petrology of enormous volumes of impact melt on the Moon: A case study of the Orientale basin impact melt sea, *Icarus*, *223*(2), 749–765, doi:10.1016/j.icarus.2013.01.017.

Warren, P. H. (1985), The magma ocean concept and lunar evolution, *Annual Review of Earth and Planetary Science*, *13*, 201–40, doi:10.1146/annurev.earth.13.1.201.

Warren, P. H., and J. T. Wasson (1979), The origin of KREEP, *Reviews of Geophysics and Space Physics*, *17*(1), doi:10.1029/RG017i001p00073.

Whitten, J. L., and J. W. Head (2015), Lunar cryptomaria: Physical characteristics, distribution, and implications for ancient volcanism, *Icarus*, *247*, 150–171, doi:10.1016/j.icarus.2014.09.031.

Wieczorek, M. A., and R. J. Phillips (2000), The "Procellarum KREEP Terrane": Implications for mare volcanism and lunar evolution, *Journal of Geophysical Research*, *105*(E8), 20,417–20,430.

Wieczorek, M. A., G. A. Neumann, F. Nimmo, W. S. Kiefer, G. J. Taylor, H. J. Melosh, R. J. Phillips, S. C. Solomon, J. C. Andrews-Hanna, S. W. Asmar, A. S. Konopliv, F. G. Lemoine, D. E. Smith, M. M. Watkins, J. G. Williams, and M. T. Zuber (2013), The crust of the Moon as seen by GRAIL., *Science (New York, N.Y.)*, *339*(6120), 671–5, doi:10.1126/science.1231530.

Yamamoto, S., R. Nakamura, T. Matsunaga, Y. Ogawa, Y. Ishihara, T. Morota, N. Hirata, M. Ohtake, T. Hiroi, Y. Yokota, and J. Haruyama (2010), Possible mantle origin of olivine around lunar impact basins detected by SELENE, *Nature Geoscience*, *3*(8), 533–536, doi:10.1038/ngeo897.

Yamamoto, S., R. Nakamura, T. Matsunaga, Y. Ogawa, Y. Ishihara, T. Morota, N. Hirata, M. Ohtake, T. Hiroi, Y. Yokota, and J. Haruyama (2012), Massive layer of pure anorthosite on the Moon, *Geophysical Research Letters*, *39*(13), 1–6, doi:10.1029/2012GL052098.

Yamamoto, S., R. Nakamura, T. Matsunaga, Y. Ogawa, Y. Ishihara, T. Morota, N. Hirata, M. Ohtake, T. Hiroi, Y. Yokota, and J. Haruyama (2015), Featureless spectra on the Moon as evidence of residual lunar primordial crust, *Journal of Geophysical Research E: Planets*, *120*, 2190–2205, doi:10.1002/2015JE004935.

3

Mineralogical survey of the Anorthositic Feldspathic Highlands Terrane crust using Moon Mineralogy Mapper data

This chapter the reproduction of an article draft, soon to be submitted to Icarus.

M. Martinot[1,2], J. Flahaut[3], S. Besse[4], C. Quantin-Nataf[2], and W. van Westrenen[1]

[1]Faculty of Science, Vrije Universiteit Amsterdam, De Boelelaan 1085, 1081 HV Amsterdam, The Netherlands [2]Université de Lyon, UCBL, ENSL, CNRS, LGL-TPE, 69622 Villeurbanne, France [3]Centre de Recherches Pétrographiques et Géochimiques, CNRS/Université de Lorraine F-54500, Vandoeuvre-lès-Nancy, France [4]European Space Astronomy Centre, P.O. Box 78, 28691 Villanueva de la Cañada, Madrid, Spain

Corresponding author: Mélissa Martinot (m.martinot@vu.nl)

Abstract

Spectroscopic data from the Moon Mineralogy Mapper (M^3) instrument are used to study the mineralogy of the central peak or peak ring of 75 craters located in the

lunar anorthositic Feldspathic Highlands Terrane (FHT-a), as defined by Jolliff et al. [2000]. The thickness of South-Pole Aitken (SPA) ejecta at the location of the selected craters is estimated, and crustal thickness models and empirical cratering equations are used to estimate the depth of origin of the material excavated in the studied central peaks, and its distance to the crust-mantle interface. The goal of the survey is to study the composition of the FHT-a crust, and the extent of its potential lateral and vertical heterogeneities. High-Calcium Pyroxene (HCP) and featureless spectra are mostly detected throughout the entire FHT-a, whereas the number of pure plagioclase detections is small. No relationship between the central peak composition and the distance to SPA or the depth within the SPA ejecta is observed. The SPA ejecta material cannot be distinguished from crustal material. We interpret the paucity of plagioclase spectra in the FHT-a, which contrasts with more frequent plagioclase detections in the central peaks of craters sampling the crust in younger lunar terranes using identical spectroscopic techniques [Martinot et al., 2018b], as a possible effect of terrane maturation, or of mixing with mafic components that mask their signature in the visible near-infrared. Overall, the FHT-a appears homogeneous laterally. However, data hint at a pyroxene compositional change with increasing depth, from high-calcium content in the upper crust towards less calcic compositions with increasing depth, which is consistent with prior studies of the architecture of the lunar crust.

Keywords:
Feldspathic Highlands Terrane, Moon Mineralogy Mapper, Spectroscopy

3.1. Introduction

Studying the lunar surface composition and mineralogy can provide constraints on the Moon's magmatic and thermal evolution [e.g., Jaumann et al., 2012, Shearer et al., 2006]. An asymmetry between the nearside and the farside surface was first observed on the images retrieved from the early Luna missions. Analyses of the Lunar Prospector geochemical data showed that there is a geographic link between the surface abundance of heat-producing elements and the location of basaltic maria [Lawrence et al., 1998]. Jolliff et al. [2000] divided the lunar surface into three major terranes based on Clementine multispectral data and global geochemical data provided by the Lunar Prospector gamma-ray probe (Fig. 3.1). The Procellarum KREEP Terrane (PKT) includes the nearside high-thorium region; the South-Pole Aitken Terrane (SPAT) comprises the farside high average FeO non-mare material. The Feldspathic Highlands Terrane (FHT) is anorthositic, and characterized by low FeO and thorium abundances. It is subdivided into two sub-terranes, based on their geochemical signature: the anorthositic FHT (FHT-a), highly anorthositic and covering most of the lunar farside outside the SPAT, and the outer FHT (FHT-o), including cryptomare and impact basins ejecta.

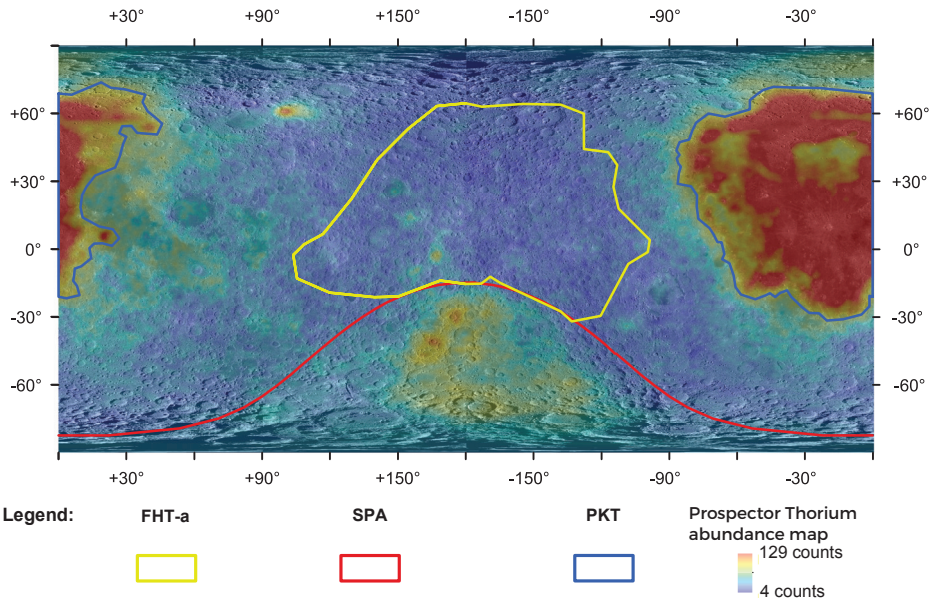

Figure 3.1: Outline of the three major terranes as defined by Jolliff et al. [2000]. The PKT is in blue, the SPAT is in red, and the FHT-a is in yellow. The surface that is not comprised in the PKT, SPAT or FHT-a is the FHT-o. Prospector's qualitative Thorium abundance map is color-coded from high (red) to low (blue) abundances is displayed in transparency over the Lunar Reconnaissance Orbiter Wide Angle Camera global mosaic.

The lunar nearside-farside asymmetry is not limited to the lunar surface. A 2 km offset towards the Earth of the Moon center of mass relative to the center of figure was observed [Bills and Ferrari, 1977, Kaula, 1979]. The crustal thickness models derived from the Clementine mission data suggested that the farside had a higher average crustal thickness (68 km) than the nearside crust (60 km) [Zuber et al., 1994]. More recently, data from the Gravity Recovery and Interior Laboratory (GRAIL, Wieczorek et al. [2013]) show that the FHT has a higher average crustal thickness than the SPAT and the PKT (36 km for the FHT and 27 km for the SPAT and the PKT).

Different lunar evolution models were proposed to explain the nearside-farside asymmetry. Hypotheses include: an asymmetric crystallization of the magma ocean [Charlier et al., 2018, Ohtake et al., 2012, Wasson and Warren, 1980]; the asymmetric accumulation of a liquid iron alloy, resulting in the displacement of the colder, undifferentiated core upwards [Stevenson, 1980]; or the result of a gravitational instability that triggered the preferential emplacement of lunar mare on the nearside [Parmentier et al., 2002]. Yamamoto et al. [2016] proposed that a two-stage crustal growth could explain the observed discrepancy between thorium abundance and crustal thickness.

They proposed that low-thorium floating plagioclase plateaus crystallized and aggregated to form a lid on the surface of the magma ocean, followed by a downward growth of the lunar crust. More recently, Laneuville et al. [2018] proposed a thermal evolution model in which the mantle beneath the PKT is moderately enriched in heat producing elements compared to the mantle beneath the highlands, resulting in a slower cooling of some parts of the PKT. This influences the temperature of the mantle, thus able to sustain a volcanic activity on the nearside for longer than on the farside.

A number of remote sensing studies have surveyed the mineralogy of the farside-centered FHT to further elucidate the nearside-farside asymmetry. Lucey and Cahill [2006] and Arai et al. [2008] combined geochemical data with remote sensing studies, and proposed that the lunar nearside crust is composed of ferroan anorthosites, whereas the farside crust (and presumably the FHT-a) is composed of more magnesian material. As a consequence, and based on the cumulate sequence where high-Mg rocks crystallize before lower Mg rocks, Arai et al. [2008] proposed a two-stage crystallization for the Lunar Magma Ocean with the crystallization of the troctolitic farside crust prior to that of the noritic nearside. Their suggestion could explain the observed extended age range and overlap between lunar anorthosites and magnesian suite plutonic rocks [e.g., Borg et al., 1999, 2015, Gross et al., 2014, Papanastassiou and Wasserburg, 1971a,b]).

Several remote sensing surveys have investigated the composition of the lunar crust at depth using impact craters as natural, vertical probes in the lunar interior. Several remote sensing surveys used visible near-infrared (VNIR) observations in order to study the global distribution of anorthosite, and concluded that there is a global, but discrete, ≈30 to 50 km thick layer of anorthosite buried under a 3 to 10 km thick more pyroxene-rich mixed layer resulting from impact events, depositing a thickness ejecta material on top of the anortositic layer [Donaldson Hanna et al., 2014, Hawke et al., 2003, Ohtake et al., 2009, Yamamoto et al., 2012a]. Hawke et al. [2003] described pure anorthosites (PAN) as rocks with over 95 vol.% plagioclase. Donaldson Hanna et al. [2014], Ohtake et al. [2009], Yamamoto et al. [2012a] reported the presence of PAN exposures in the FHT.

Farside crust studies however need to take into account the effects of the formation of the South-Pole Aitken basin, which is the largest impact structure on the Moon [e.g., Stuart-Alexander, 1978, Wilhelms et al., 1979]. According to Arai et al. [2008], the FHT was significantly resurfaced by the SPA basin formation, and subsequent post-magma ocean magmatism.
The SPA basin itself shows geochemical and mineralogical signatures [e.g., Jolliff et al., 2000, Moriarty and Pieters, 2018]. Yamamoto et al. [2012b] studied the distribution of olivine in the SPA basin with spectroscopic data, and reported a paucity of olivine exposures in the SPA basin. Moriarty et al. [2013] and Moriarty and Pieters [2018] stud-

ied the SPA basin with spectroscopic data from M^3 and showed that the composition of the basin is organized in concentric annuli, from pyroxene-rich signatures in its center to more anorthositic-rich signatures towards the SPA exterior. Melosh et al. [2017] modeled the formation of the SPA basin, and showed that it must have sampled the lunar upper mantle. The lack of olivine detections in and around SPA, combined with the abundance of Low-Calcium Pyroxene (LCP) led them to conclude that the upper mantle of the Moon is LCP-rich.

According to the Lunar Magma Ocean (LMO) concept, the lunar crust was formed by flotation of plagioclase after half of the magma ocean crystallized, whereas denser, mafic cumulates of olivine and pyroxene minerals sank to the bottom of the magma ocean, forming the lunar mantle [e.g., Smith et al., 1970, Warren, 1985, Wood, 1970]. This concept is supported by a range of recent experimental studies of LMO crystallization [Charlier et al., 2018, Lin et al., 2017a,b, Rapp and Draper, 2018]. Some authors proposed that the mafic content of the crust builds up with increasing depth [Cahill et al., 2009, Ryder and Wood, 1977, Spudis and Davis, 1986, Tompkins and Pieters, 1999], while observations from other authors debate this conclusion [Lemelin et al., 2015, Song et al., 2013]. Martinot et al. [2018b] found in their study of craters located in the PKT and FHT terranes that crustal pyroxene composition changes with increasing depth, from HCP to LCP. However, they did not find a clear mineralogical change between crustal and mantle material, as they detected plagioclase occurrences (implying the presence of > 95 % plagioclase, Cheek et al. [2013]) in craters supposedly sampling mantle material. In the present study, the mineralogical diversity specifically of the FHT-a crustal column is constrained. The goal of this work is to find out whether the FHT-a crust becomes more mafic with increasing depth, which could provide further constraints to lunar evolution models. The central peak or peak ring of 75 impact craters located within the FHT-a were studied with spectroscopic data from M^3.

3.2. Material and Methods

3.2.1. Reflectance Data and Crater Selection

Reflectance data from the Moon Mineralogy Mapper (M^3) were used in order to derive the mineralogic diversity of the craters central peak or peak ring. M^3 is a hyperspectral imager that orbited the Moon between 2008 and 2009. It acquired VNIR images of the lunar surface. M^3 data span 85 spectral channels, from 430 to 3000 nm [Pieters et al., 2009]. The M^3 data used here were archived in the Planetary Data System (PDS, version 1 of Level 2). These data are calibrated, and were corrected for radiometry, geometry, thermal effects and geometry [Besse et al., 2013, Boardman et al., 2011, Clark et al., 2011, Green et al., 2011]. The mosaics were made with data from the same optical period OP2C2. The same optical period was used in order to keep similar detector conditions (temperature, beta angle, spacecraft altitude). The optical period OP2C2 was selected because it covers the maximum number of central

peak or peak ring craters in the FHT-a. Data from the OP2C2 optical period have a spatial resolution of 280 m/pixel. The Lunar Impact Crater Database (LICD) Losiak et al. [2009] (revised by Ohman at LPI) provides a list of lunar impact craters. To maximize the retrieval of information about the vertical and lateral architecture of the FHT-a crust, all complex craters located in the FHT-a, and which central peak or peak ring is partially or completely covered by the M^3 OP2C2 optical period data, were selected for mineralogical study. A total of 75 craters were selected (Figure 3.2, Table 3.3). Because of their low signal-to-noise ratio, wavelengths below 620 nm were discarded [Green et al., 2011]. Thermal effects due to the contribution of the lunar surface are significant at wavelengths beyond 2700 nm [Clark et al., 2011]. Therefore, reflectance data beyond 2700 nm were not analyzed.

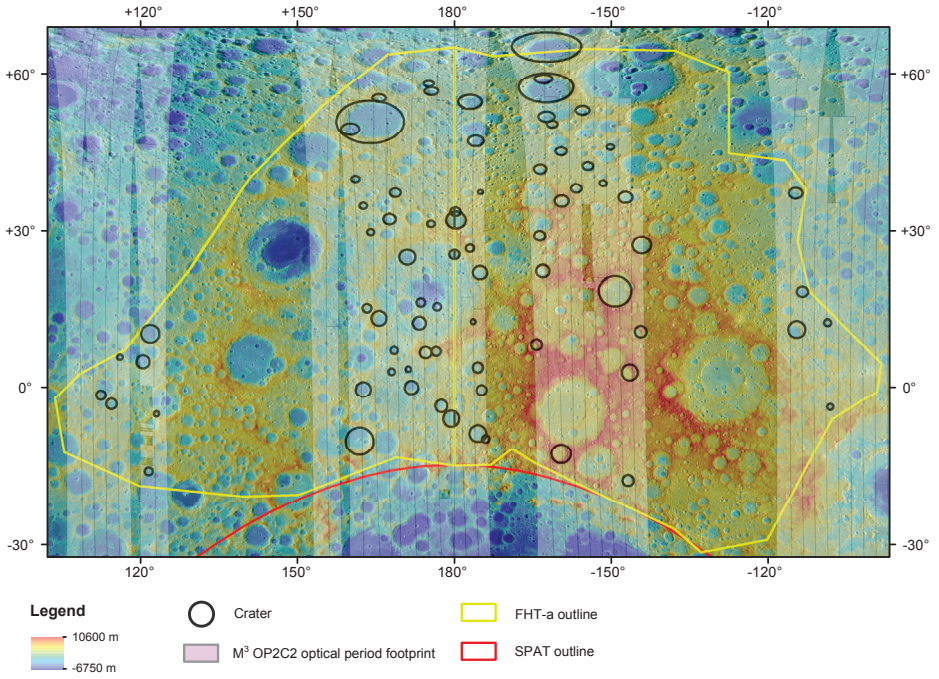

Figure 3.2: LOLA global digital elevation model [Smith et al., 2010] of the selection of craters, centered on the FHT-a (yellow outline). The transparent white strips represent the M^3 OP2C2 optical period footprints. The black circles outline the craters selected in this study. The SPA basin is outlined in red.

The global Lunar Reconnaissance Orbiter (LRO) Wide Angle Camera (WAC) mosaic (spatial resolution of 100 m/pixel) was used in order to visualize the geological context of the central peaks. The LRO Lunar Orbiter Laser Altimeter (LOLA) global digital elevation model (horizontal precision: 118 m at the Equator, vertical precision: 1 m)

was used in order to provide information on the topography and elevation of the central peaks or peak rings [Smith et al., 2010].

The GRAIL mission acquired gravimetric data from the Moon between 2011 and 2012. Wieczorek et al. [2013] derived four crustal thickness models, assuming different crustal porosities and constraining the crustal thickness with Apollo 12 and 14 landing sites' seismic data. Here, the GRAIL crustal thickness model 1 was used in order to constrain crustal thickness values at each crater location as in our previous studies Martinot et al. [2018a,b], see Table 3.3.

3.2.2. Data Processing and Pyroxene Composition Analysis

M^3 data were processed using the continuum-removal algorithm and output spectral parameter maps developed by Martinot et al. [2018a]. With this algorithm, the continuum is found by maximizing the absorption band area of lunar mafic minerals at 1000 and 2000 nm. Tie points to the spectrum continuum are searched for in fixed intervals (620–1100 nm; 1100–1660 nm) on a smoothed spectrum, in order to limit the influence of noise on the tie point positions. A third tie point is fixed at 2700 nm. Output parameter maps (e.g., band 1 and 2 position, depth, area, asymmetry) are stretched in order to highlight the central peak or peak ring diversity. In this study, the band 1 position and the band 2 position and band 2 depth maps are primarily used. Only spectra with a band 2 depth stronger than 2 % were considered for pyroxene compositional analyses, in order to limit the effect of noise. Pixels located in shadowed areas were also discarded, due to their low reflectance (which could lead to a mis-interpretation of the mineralogical signature).

This specific continuum-removal algorithm is optimized for spectra displaying two absorption bands (e.g., pyroxene). Minerals displaying a single absorption band (e.g., plagioclase) can also be processed correctly by the continuum-removal algorithm, if the absorption band is strong. However, the spectra observed on the FHT-a terrane generally have high slopes, and shallow absorption bands. The maximum absorption band depth does not exceed 20 % in any of the surveyed central peak or peak ring craters. This explains why some plagioclase occurrences previously described in Donaldson Hanna et al. [2014] were not detected using this algorithm. For the purpose of this study, spectral parameters developed specifically for the detection of plagioclase were therefore used in order to identify plagioclase occurrences on the selected central peaks. Two spectral parameters were used: the band depth at 1250 nm (BD1250, developed by Donaldson Hanna et al. [2014]), and the 1250 nm integrated band depth (IBD1250). The BD1250 parameter calculates the band depth at 1250 nm, by using continuum boundaries at 749 and 1579 nm. It calculates the band depth between 1030 and 1700 nm. This spectral parameter highlights plagioclase spectra with band depth exceeding 1-2 % [Donaldson Hanna et al., 2014].

The number and position of absorption bands in M^3 VNIR reflectance spectra enable the identification of several minerals. In this survey, plagioclase, High-Calcium

Pyroxene (HCP) and featureless spectra were detected. Detailed descriptions distinguishing features of these spectra can be found in Martinot et al. [2018b] (see their Fig. 4).

Moriarty et al. [2013] used scatter plots presenting band depth values as a function of band positions in order to assess pyroxene compositional variations within a central peak, and to obtain the degree of homogeneity in a central peak. We used a similar method to study pyroxene compositional variations. In each central peak or peak ring crater, all spectra displaying a pyroxene signature (a band 1 center centered between 850 nm and 1100 nm, and a band 2 center centered between 1700 nm and 2400 nm) were selected. These output pixels are further referred to as the pixels in the central peak having a pyroxene signature.
In some craters, less than 10 % of the pixels covering the central peak surface had a pyroxene signature, leading us to question whether these occurrences are representative of the central peak.For craters with more than 10 % of central peak pixels showing pyroxene signature, the spectral dispersion of the pyroxene composition was assessed using the median position of the 200 pixels in each central peak having the strongest band depth. The number 200 was determined empirically. In order to show the spread of data against wavelength, the minimum and maximum positions of the band 1 and 2 center are extracted from the data, as well as the minimum and maximum values of the band 1 and 2 depth values, and the distribution of those values (Table 3.1).

3.2.3. SPA Ejecta Thickness Calculation

Given its large size, the SPA basin formation probably ejected material over the whole Moon; it is thus important to take the SPA basin ejecta into account when investigating the composition of the nearby FHT-a province. Several material transport models predict the thickness of ejected material at a given distance to an impact basin. Equations *(1)* and *(2)* describe the models from McGetchin et al. [1973] and Housen et al. [1983], respectively.

$T = 0.14 \times R^{0.74} \times (r/R)^{-3}$ *(1)* , and

$T = 0.0078 \times R \times (r/R)^{-2.61}$ *(2)*

Estimates of SPA ejecta thickness at the location of the selected craters are noted T (Table 3.3). In both equations, the distance to SPA, noted r was measured from the center of the SPA basin, in meters. The SPA basin diameter is noted R, in meters, and is taken to be 2600 km [Melosh, 2011]. The model from McGetchin et al. [1973] gives an ejecta thickness that is 2 times lower than that of Housen et al. [1983]. We favor equation *(1)* in our final discussion in order to have a lower estimate (and possibly, a more realistic one) for the thickness of ejecta.

3.2.4. Proximity Value to an Interface

The proximity value to an interface, introduced by Cahill et al. [2009], compares the distance of origin of the material emplaced in a crater central peak to a given

interface (e.g., the crust-mantle interface). [Cintala and Grieve, 1998] proposed that the maximum depth of melting (D_m) can be approximated as the minimum depth of origin of central peak material. Two proximity values were calculated in this study (Table 3.3): the proximity value to the interface between the SPA ejecta and the FHT-a crust, and the proximity value to the crust-mantle interface (referred to as P_{cmi} value). The proximity value to the interface between the SPA ejecta and the FHT-a crust (*i.e.*, depth in the SPA ejecta) is noted D^{*}_{SPA} when calculated using Equation 1, and D^{**}_{SPA} when calculated using Equation 2. The thickness of the crust before the impact event was calculated following the method in Flahaut et al. [2012]. The crustal thickness of an annulus around the impact crater was averaged, at a distance of one crater diameter, ± 10 % of the crater diameter. The GRAIL crustal thickness model 1 was used to provide crustal thickness values [Wieczorek et al., 2013] for the proximity value to the crust-mantle interface. If the P_{cmi} value is positive, only crustal material should be chemically represented in the central peak; if the P_{cmi} value is negative, then material from below the crust-mantle interface is potentially emplaced in the central peak material.

3.3. Results

3.3.1. Mineralogical Detections

This study's mineralogical detections are shown in Fig. 3.3a.

Fig. 3.3 b, c and d show previous work on the lithology and mineralogy of central peak craters located in the FHT-a from Tompkins and Pieters [1999], Lemelin et al. [2015], and Donaldson Hanna et al. [2014]. The mineralogical detections from all studies are in general agreement.

In the craters selected here (Fig. 3.3a), HCP, featureless spectra and plagioclase occurrences are detected. HCP is detected in the vast majority of studied craters (61 out of 75 craters). Featureless spectra are observed at all latitudes in the FHT-a (39 out of 75 craters), and some plagioclase occurrences are detected (7 out of 75 craters). HCP spectra are observed in a wide range of P_{cmi} values (between 45.7 and −1.5 km, see Table 3.3). Featureless spectra are observed in craters spanning the whole range of P_{cmi} values (between 48.9 and −1.5 km). Plagioclase is detected in craters having a positive P_{cmi} value (between 39.2 and 12.1 km). Featureless spectra occurrences span across all crater ages (ages taken from the LICD, Losiak et al. [2009], revised by Ohman at LPI), whereas plagioclase occurrences appear more concentrated in younger craters (Copernican to Eratosthenian in age). The plagioclase detections reported here are concentrated in the center of the FHT-a (5 out of 7 detections), and the South of FHT-a (2 out of 7 detections). Featureless occurrences span a wider range of latitude, from the South to the North of the FHT-a (Fig. 3.3a).

The band 1 and 2 positions for all 60 craters where HCP was detected are shown

in Table 3.1.

In the craters present in both Tompkins and Pieters [1999] and this study's selections, pyroxene was detected where Tompkins and Pieters [1999] detected pyroxene-compatible lithologies (anorthositic troctolite, anorthositic gabbronorite, anorthositic gabbro and gabbroic-noritic-troctilitic anorthosite containing less than 90 % plagioclase). Plagioclase or featureless spectra were detected in the craters where Lemelin et al. [2015] reported between 88 and 95 % plagioclase, and locations of the highest plagioclase contents from Lemelin et al. [2015] (Fig. 3.3c) are in agreement with the most anorthositic detections from Tompkins and Pieters [1999]. There is also a good agreement between the anorthositic detections by Tompkins and Pieters [1999] and the plagioclase occurrences detected by Donaldson Hanna et al. [2014] (Fig. 3.3d). No plagioclase was detected in the craters where Lemelin et al. [2015] estimated less than 79 % plagioclase. Pyroxene-compatible lithologies were detected by Tompkins and Pieters [1999] in the 2 craters that are in both Tompkins and Pieters [1999] and Donaldson Hanna et al. [2014] craters selection. In craters that are part of both Donaldson Hanna et al. [2014] and this study's selections, pyroxene detections are in good agreement. In some cases, Donaldson Hanna et al. [2014] reported plagioclase in central peaks where it was not detected in this study.

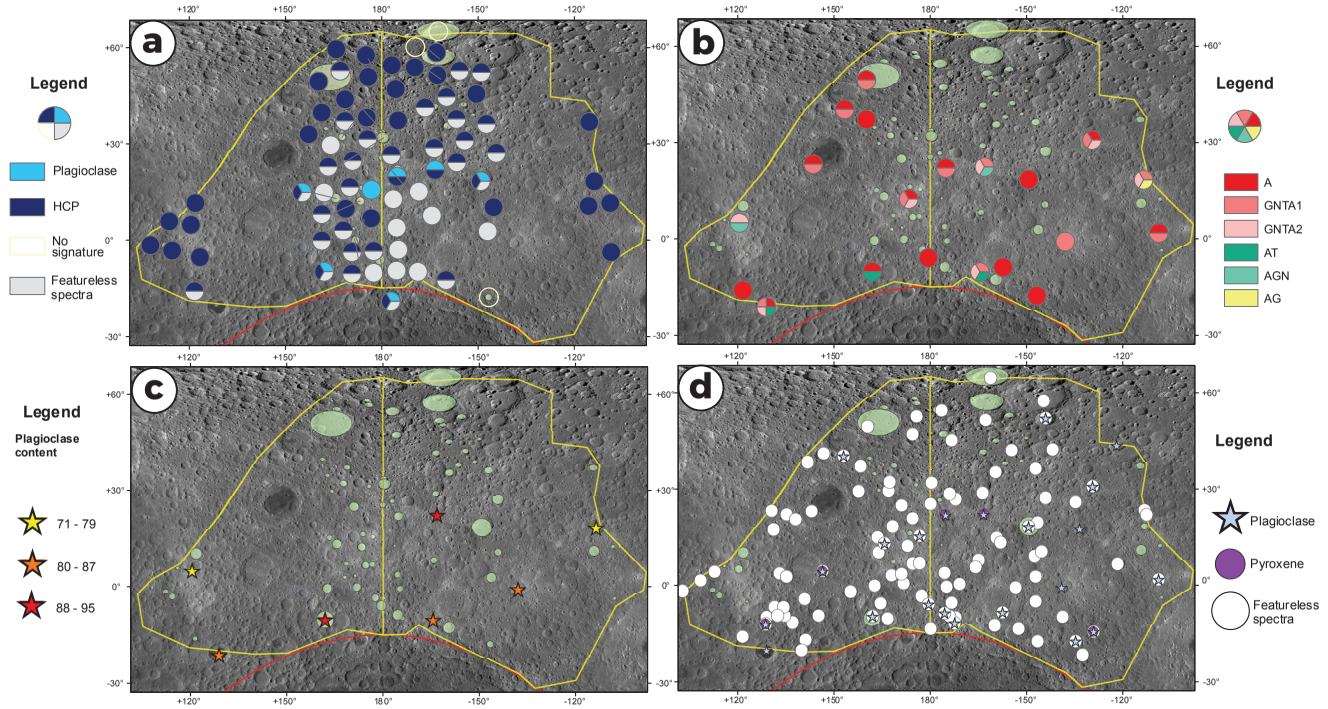

Figure 3.3: LRO WAC mosaics of the FHT. The outlines of the FHT-a and SPA as defined by Jolliff et al. [2000] are show in yellow and red, respectively. The green circles represent this study's crater selection. **a**. This study's plagioclase (pale blue), featureless spectra (gray), and HCP (dark blue) detections. The craters where no dominant mineralogic signature was detected are symbolized with a yellow hollow circle. **b**. Lithology detections from Tompkins and Pieters [1999] in central peak craters located in the FHT-a. High to low plagioclase contents are coded from dark red to light pink. The dark red symbol points to an anorthositic detection (A), the middle red symbol codes for a gabbroic-noritic-troctolitic anorthosite with 85-90 % plagioclase (GTA1), and the light pink symbol materializes a gabbroic-noritic-troctolitic anorthosite with 80-85 % plagioclase (GTA2). The dark green symbol signals the anorthositic troctolites (AT), the pale green symbol signals the anorthositic gabbronorites (AGN), and the yellow symbol represents the anorthositic gabbro detections (AG). **c**. Lemelin et al. [2015] plagioclase content in their selected central peak craters located in the FHT-a. The redder the symbol, the higher the plagioclase content. **d**. Donaldson Hanna et al. [2014] plagioclase (blue star), featureless spectra (white circle) and pyroxene (purple circle) occurrences in central peak craters located in the FHT-a.

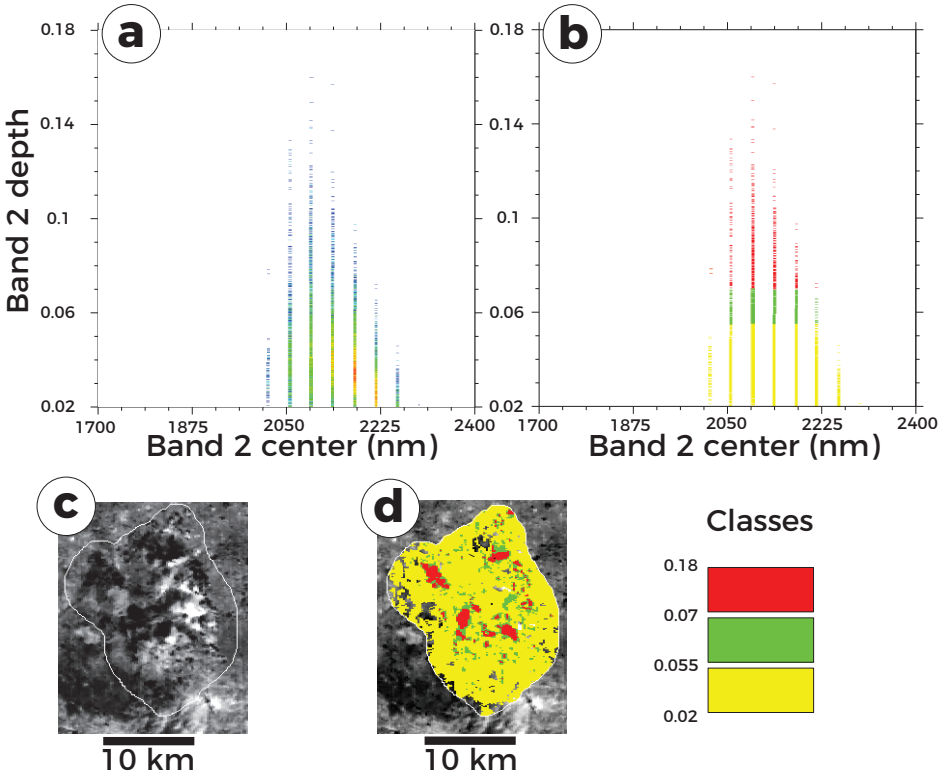

Figure 3.4: Spectral dispersion of the band 2 center in King central peak. **a**. Scatter plot presenting band 2 depth values as a function of band 2 center positions. The colors represent the density of points, from blue to red. The redder the color, the higher the density of points. **b**. Scatter plot presenting the positions of the band 2 center as a function of the band 2 depths. The colors represent the classes, projected in **d**. **c**. M^3 2896 nm band of King crater central peak, outlined in white. **d**. M^3 2896 nm band of King crater central peak. The colored pixels have the characteristics (band 2 center and depth) of the classes drawn in **b**.

Table 3.1: Study of the band 1 and 2 positions for all 60 craters where HCP was identified. The craters are ranked according to increasing crater diameter. The number of pixels having a pyroxene signature in the central peak is indicated, along with the median band 1 and 2 positions of all studied spectra in the central peak; the standard deviation associated to the band 1 and 2 positions of all studied spectra in the central peak (σ_{B1} global and σ_{B2} global, respectively); the median band 1 and 2 positions of the 200 pixels with the strongest band 2 depth; the standard deviation associated to the band 1 and 2 positions of the 200 pixels with strongest band 2 depth (σ_{B1} 200 px and σ_{B2} 200 px, respectively); the minimum and maximum of the band 1 and 2 center; the minimum and maximum of the band 1 and 2 depth; and the percentage of the central peak having a pyroxene signature. Band positions are in nm. - denotes occurrences where the standard deviations could not be calculated because only one pixel in the central peak has a band 2 depth superior to 2 %.

Crater	Nr pixels	Median B1 global	Median B2 global	σ_{B1} global	σ_{B2} global	Median B1 200 px	Median B2 200 px	σ_{B1} 200 px	σ_{B2} 200 px	B1 min	B1 max	B2 min	B2 max	BD1 min	BD1 max	BD2 min	BD2 max	% CP covered
Moore F	2491	990	2258	22	38	970	2218	16.52	25.80	890	1070	2098	2377	0.010	0.125	0.020	0.067	86.7
Necho	8886	950	2138	25	74	950	2098	13.97	43.23	850	1090	1818	2377	0.017	0.138	0.020	0.106	87.6
Coriolis Y	15	890	2018	47	242	890	2018	47.00	241.81	850	990	1739	2337	0.008	0.042	0.020	0.023	0.3
Fowler W	112	890	2218	39	75	890	2218	39.37	74.64	850	1050	1978	2377	0.003	0.029	0.020	0.037	0.9
Tsinger Y	4027	910	2098	26	153	950	2098	16.30	115.16	850	1050	1739	2337	0.011	0.231	0.020	0.152	13.7
Katchalsky	1553	950	2138	64	56	910	2178	59.70	35.46	850	1090	1898	2297	0.007	0.055	0.020	0.038	7.5
Kulik L	6	930	2258	10	21	930	2258	10.31	20.62	910	930	2218	2258	0.013	0.014	0.021	0.024	0.2
Grachev	8	970	2178	0	30	970	2178	0.00	29.70	970	970	2098	2178	0.039	0.051	0.020	0.028	0.1
Stearns	332	930	2178	32	37	930	2178	28.35	36.75	850	1050	2098	2337	0.009	0.069	0.020	0.043	5.2
Coriolis W	602	930	2058	22	46	930	2018	15.76	30.84	850	1070	1898	2218	0.008	0.091	0.020	0.049	8.7
Golovin	503	930	2138	69	102	930	2178	71.26	87.13	850	1090	1818	2377	0.003	0.034	0.020	0.041	15.8
Shayn H	45	990	2218	40	26	990	2218	40.11	26.37	870	1090	2178	2297	0.001	0.013	0.020	0.026	0.8
Butlerov	83	970	2178	10	64	970	2178	10.09	63.98	950	990	2138	2337	0.035	0.054	0.020	0.030	1.1
Montgolfier Y	166	910	2138	24	149	910	2138	23.51	149.49	850	970	1739	2218	0.009	0.065	0.020	0.046	4
Dufay X	26	930	2018	18	28	930	2018	18.13	27.66	890	930	1978	2058	0.024	0.055	0.020	0.032	0.8
Dante E	30	910	2258	60	52	910	2258	60.32	52.35	850	1010	2218	2377	0.008	0.023	0.020	0.030	0.4
d'Alembert Z	1493	890	2058	30	128	930	2058	18.12	116.29	850	1010	1739	2218	0.003	0.120	0.020	0.095	17.3
Tsinger	675	910	1898	31	158	910	2058	31.38	150.28	850	1070	1739	2297	0.001	0.165	0.021	0.097	2.7
Delporte	572	950	2138	61	109	950	2138	55.40	98.94	850	1090	1898	2337	0.011	0.048	0.020	0.044	7.1
Kulik J	709	910	2218	66	180	910	2218	67.83	71.12	850	1090	1739	2377	0.020	0.343	0.020	0.050	1.9
Woltjer	1147	910	2218	53	63	930	2178	44.18	58.46	850	1090	2018	2337	−0.001	0.124	0.020	0.049	4.4
Evershed C	823	930	2258	75	44	990	2258	72.10	51.81	850	1090	2018	2377	0.001	0.035	0.020	0.041	4.9
Anderson F	75	1030	2218	25	29	1030	2218	24.61	28.88	950	1070	2178	2297	0.006	0.040	0.021	0.050	1
Larmor Z	5187	930	2218	42	62	950	2138	28.79	29.97	850	1090	1739	2377	0.000	0.114	0.020	0.073	27.5
Rowland J	3652	910	2178	41	90	930	2178	22.90	86.84	850	1090	1739	2337	0.001	0.174	0.020	0.103	7.6
Hutton	34	990	2258	49	163	990	2258	48.93	163.34	850	1050	1818	2377	0.005	0.028	0.020	0.023	0.2
Tiselius	30	990	2178	11	39	990	2178	11.10	39.34	970	1010	2098	2218	0.038	0.067	0.021	0.043	0.1
Rowland Y	460	910	2058	30	81	930	2098	17.52	65.61	850	1050	1778	2178	0.009	0.156	0.020	0.061	4
Schneller	16	950	2058	14	77	950	2058	14.35	77.44	910	950	2018	2258	0.011	0.119	0.021	0.072	0.3
Buisson	2815	970	2178	52	50	950	2178	52.28	41.92	850	1090	2018	2377	0.004	0.242	0.020	0.081	4
Cockcroft N	136	990	2297	54	31	990	2297	53.52	31.09	850	1050	2178	2337	0.003	0.035	0.020	0.026	1.1
Rowland M	34	930	2058	23	154	930	2058	22.92	153.86	910	990	1739	2098	0.025	0.095	0.021	0.053	0.2
Nusl	93	930	2138	15	24	930	2138	15.45	24.21	910	990	2098	2218	0.019	0.088	0.020	0.050	1.6
Vesalius	3161	950	2178	42	52	950	2138	20.84	30.53	850	1090	2018	2377	0.003	0.081	0.020	0.077	7.4
Perkin	37	930	2098	58	166	930	2098	57.70	165.51	850	1070	1739	2337	0.001	0.079	0.021	0.051	0.3
Petropavlovskiy	294	930	2138	25	48	930	2138	22.92	40.89	870	1090	2058	2337	0.007	0.061	0.020	0.040	4.4
Ohm	8051	990	2258	15	35	970	2218	10.10	36.50	890	1010	2098	2297	0.018	0.155	0.020	0.098	69.3
Gadomski	2	910	2337	0	0	910	2337	0.00	0.00	910	910	2337	2337	0.004	0.004	0.020	0.020	0
Evershed	180	910	2218	35	73	910	2218	35.38	73.13	870	1090	1978	2337	0.000	0.026	0.020	0.038	3.6
Artem'ev	30	990	2178	7	29	990	2178	6.90	29.06	970	990	2138	2218	0.032	0.063	0.020	0.049	0.6
Slipher	2027	930	2098	72	89	910	2138	67.10	66.31	850	1090	1739	2377	0.001	0.062	0.020	0.042	13.5

Continued on next page

Table 3.1 – *Continued from previous page*

Crater	Nr pixels	Median B1 global	Median B2 global	σ B1 global	σ B2 global	Median B1 200 px	Median B2 200 px	σ B1 200 px	σ B2 200 px	B1 min	B1 max	B2 min	B2 max	BD1 min	BD1 max	BD2 min	BD2 max	% CP covered
Daedalus W	1	970	2138	-	-	970	2138	-	-	970	970	2138	2138	0.044	0.044	0.023	0.023	0
Jackson	1166	970	2138	21	92	970	2058	13.44	50.94	910	1050	1898	2337	0.010	0.131	0.020	0.078	6.3
Sharonov	395	970	2218	34	56	970	2218	23.99	51.54	850	1050	2058	2297	0.009	0.074	0.020	0.049	1.8
King	22913	950	2138	16	52	970	2098	9.98	24.85	870	1030	2018	2297	0.014	0.208	0.020	0.180	91
Morse	72	950	2178	59	49	950	2178	59.25	48.88	850	1050	2138	2297	0.009	0.096	0.020	0.037	0.3
Coriolis	2	950	2138	0	0	950	2138	0.00	0.00	950	950	2138	2138	0.023	0.023	0.021	0.021	0
Chappell	14	870	1739	13	230	870	1739	13.23	229.99	850	890	1739	2258	0.020	0.037	0.020	0.027	0
Freundlich	2	910	2178	0	0	910	2178	0.00	0.00	910	910	2178	2178	0.019	0.019	0.020	0.020	0
Spencer Jones	2	950	2138	0	0	950	2138	0.00	0.00	950	950	2138	2138	0.035	0.035	0.024	0.024	0
Vening Meinesz	270	890	2178	45	92	890	2178	33.49	83.41	850	1050	1739	2337	0.004	0.032	0.020	0.035	0.3
Daedalus	2	950	2018	0	0	950	2018	0.00	0.00	950	950	2018	2018	0.055	0.055	0.022	0.022	0
Joule	171	970	2138	32	63	970	2138	32.02	63.08	870	1030	2058	2297	0.005	0.037	0.020	0.036	1.4
Kolhorster	55	970	2138	4	26	970	2138	3.77	26.25	970	990	2098	2178	0.034	0.099	0.021	0.057	0.5
Larmor	185	990	2258	60	64	990	2258	59.75	64.42	850	1070	2058	2377	0.001	0.091	0.020	0.051	1.9
Ostwald	6	930	2098	10	62	930	2098	10.31	61.85	930	950	2098	2218	0.039	0.055	0.020	0.023	0.1
Doppler	161	970	2218	48	34	970	2218	47.51	34.03	870	1070	2138	2337	0.005	0.027	0.020	0.045	1
Keeler	2	970	2258	0	0	970	2258	0.00	0.00	970	970	2258	2258	0.033	0.033	0.025	0.025	0
Mach	159	970	2218	47	40	970	2218	47.43	39.95	701	1030	2178	2377	0.005	0.061	0.020	0.037	0.4
d'Alembert	19634	930	1978	72	147	950	2058	77.58	119.86	850	1090	1739	2377	0.000	0.212	0.020	0.071	6.2

3.3.2. Pyroxene Compositional Variations

As discussed in section 3.2.2, we used a method similar to that described in the study by Moriarty et al. [2013], to evaluate the pyroxene compositional variations in these craters. The global median and the median of the 200 pixels with strongest band depth were calculated for three classes: spectra with band depth values between 2 and 5.5 % in a first class, spectra with band depth values between 5.5 and 7 % in a second class, and spectra with band depth values larger than 7 % in a third class. These classes were defined in order to check if the composition of pyroxene remains the same with increasing band depth values. The results are presented in Table 3.2. In general, the band depth values are homogeneous in the different band depth classes: in all cases, the band 2 position difference between the classes does not exceed 2 spectral channels (about 80 nm).

Table 3.2: Results of band 2 center global median and median of the 200 pixels with strongest absorption band calculations for 3 band depth classes. These medians were calculated in craters where more than 10 percent of the central peak surface has a pyroxene signature. The crater, percentage of the central peak having a pyroxene signature, and P_{cmi} value are indicated. The number of pixel, global median and median of the 200 pixels with the strongest absorption band is given for each class: all pixels having a pyroxene signature; pixels with band depth values comprised between 2 and 5.5 %; pixels with band depth values comprised between 5.5 and 7 %; and pixels with band depth values superior to 7 %.

Name	Percent_CP	P_{cmi} value	Global class			Band 2 depth from 2 to 5.5 % class			Band 2 depth from 5.5 to 7 % class			Band 2 depth superior to 7 % class		
			Nr pixels	Median global	First 200 median	Nr pixels	Median global	First 200 median	Nr pixels	Median global	First 200 median	Nr pixels	Median global	First 200 median
Slipher	13.5	32.0	1853	2098	2098	1853	2098	2098	-	-	-	-	-	-
Tsinger Y	13.7	35.2	1255	2138	2138	1085	2138	2138	54	2138	2138	116	2098	2098
Golovin	15.8	40.0	405	2178	2178	405	2178	2178	-	-	-	-	-	-
d'Alembert Z	17.3	35.7	817	2058	2058	626	2058	2058	121	2058	2058	70	2058	2058
Larmor Z	27.5	38.9	2241	2178	2138	2201	2178	2138	38	2138	2138	2	2138	2138
Ohm	69.3	32.9	7817	2258	2218	6975	2258	2218	632	2218	2218	210	2218	2218
Moore F	86.7	45.3	2418	2258	2258	2355	2258	2218	56	2178	2178	-	-	-
Necho	87.6	39.6	8842	2138	2098	8400	2138	2098	381	2098	2098	61	2098	2098
King	91.0	28.2	22913	2138	2098	19154	2178	2138	2332	2138	2138	1427	2098	2098

Fig. 3.5a shows the position of the band 2 center (median per central peak as outlined in the Methods section) as a function of the distance to the SPA basin center. The band 2 position spans between 2018 and 2337 nm in the whole investigated range (1200 to 3400 km from the SPA basin center), compatible with a HCP composition [e.g., Cloutis and Gaffey, 1991, Klima et al., 2011]. Fig. 3.5b shows the position of the band 2 center as a function of the depth within the SPA basin ejecta blanket. The depth in the SPA basin ejecta was calculated by subtracting the depth of melting (depth of origin of the material emplaced in a central peak, Cintala and Grieve [1998]) to the ejecta thickness at the center of the considered crater (calculated with McGetchin et al. [1973] equation *(1)*). Positive values represent depths within the SPA ejecta, while negative values represent depths below the SPA ejecta, *i.e.*, in the lunar crust.

No significant trend with depth within the SPA ejecta or distance to SPA appears in the band 2 positions. There is a hint of a decrease in median band 2 position between −20 and −40 km in Fig. 3.5b, but the low number of craters in this range of depth below the SPA ejecta preclude a definitive conclusion.

3.3.3. Evolution of the Pyroxene Composition With Depth

Fig. 3.6 shows the distribution of craters where more than 10 % of the central peak has a pyroxene signature as a function of distance to the crust-mantle interface. A weak linear regression suggests that the position of the band 2 band center shifts towards shorter wavelength with increasing depth as the distance to the crust-mantle interface decreases.

3.4. Discussion

3.4.1. Mineralogy

The mineralogical detections presented in this study are generally in good agreement with results from previous remote sensing surveys. [Cheek et al., 2013] showed that pyroxene can spectrally dominate a rock composed of < 95 % plagioclase, which is consistent with the lack of plagioclase detections in craters where Lemelin et al. [2015] estimated less than 79 % plagioclase.

In some cases, Donaldson Hanna et al. [2014] reported plagioclase occurrences in central peaks where it was not detected in this study (even when using the spectral parameters developed for the detection of plagioclase, BD1250 and IBD1250). This can be explained by the fact that Donaldson Hanna et al. [2014] used M^3 observations in all optical periods, whereas only optical period OP2C2 was considered in this study. This choice was made in order to keep similar detector conditions (temperature, beta angle, spacecraft altitude), to allow for data comparison between craters.

The featureless spectra occurrences from Donaldson Hanna et al. [2014] and this study are generally in good agreement. In some craters (24 out of 33 craters in common), Donaldson Hanna et al. [2014] detected only featureless spectra, while pyroxene

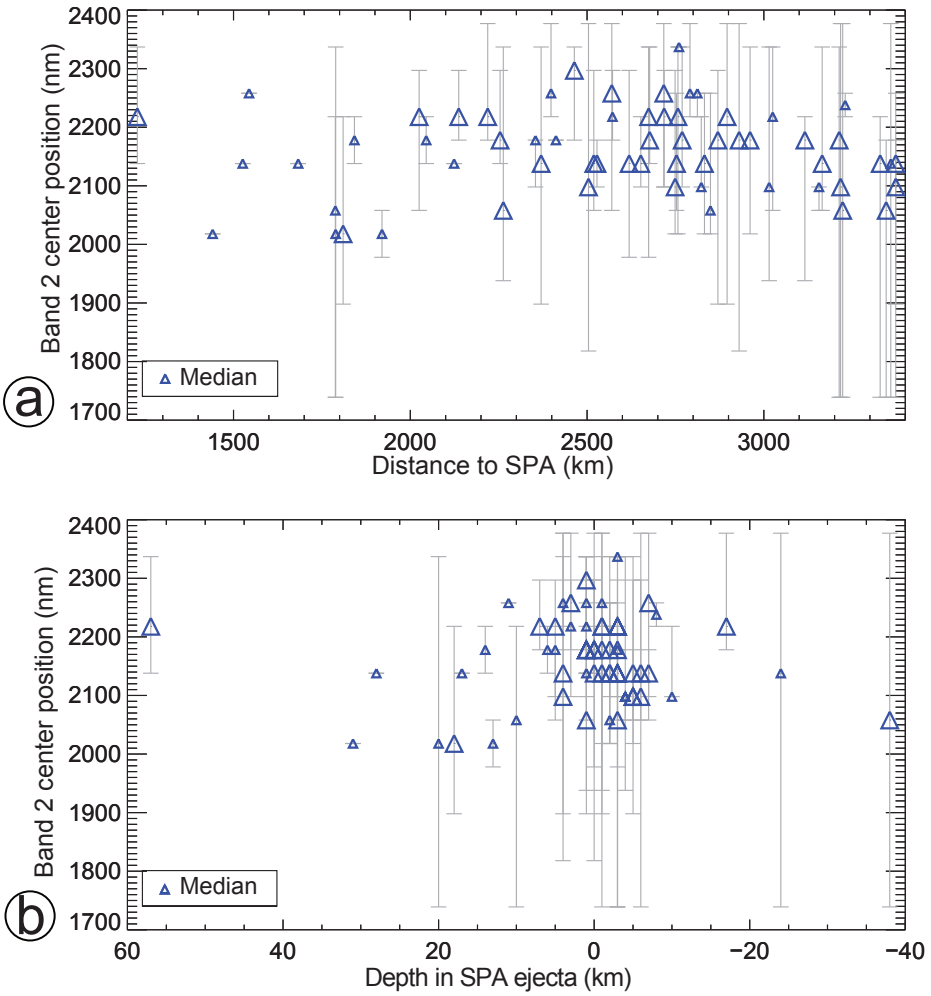

Figure 3.5: **a**. Position of the median band 2 center as a function of the distance to the SPA basin center. Blue triangles represent the median of the 200 central peak pixels with strongest band depth that 1/ have a band depth stronger than 2 %, 2/ which band 2 center position fall between 1700 and 2400 nm. When less than 200 pixels were represented in the central peak, the median of all pixels was calculated. Symbol size depend on the number of central peak pixels having a pyroxene signature. The symbol is small if there are fewer than 50 pixels; large if there are more than 50 pixels. Vertical error bars indicate the minimum and maximum band 2 center position. **b**. Position of the median band 2 center as a function of the depth in the SPA basin ejecta (calculated with Equation 1).

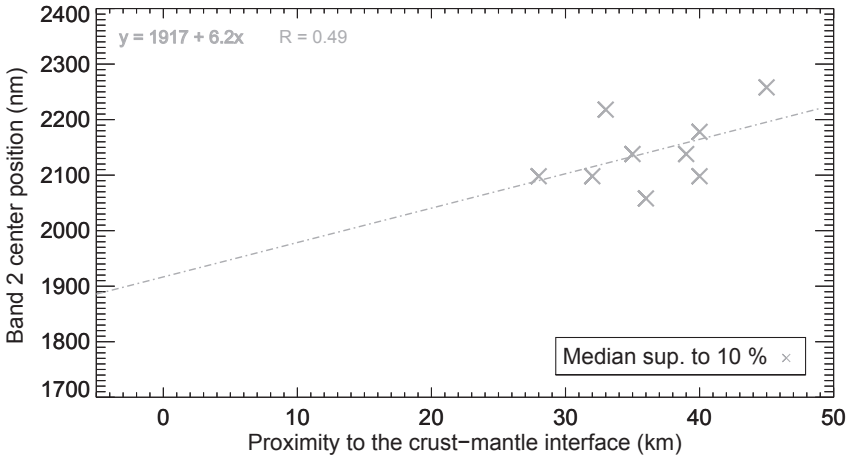

Figure 3.6: Position of the band 2 center as a function of the P_{cmi} value for all craters in which more than 10 percent of the central peak surface has a pyroxene signature (grey crosses). The linear regression is shown as a dotted line.

and/or featureless spectra were detected using our method.

The age of craters where featureless detections are observed in this study span a wide range of ages, from Pre-Nectarian ages to Copernican ages, therefore we cannot link their occurrence to terrain maturation. Plagioclase occurrences from this study are concentrated in younger craters (Copernican to Eratosthenian in age). However, Donaldson Hanna et al. [2014] detected plagioclase both in young and old craters (the oldest is pre-Nectarian Mach crater). Therefore, no clear link between plagioclase, featureless spectra occurrences and crater age is observed.

In the craters selected for this study, plagioclase occurrences are concentrated in the center and South of the FHT-a, and featureless spectra detections are mainly concentrated in the center of the FHT-a. HCP occurrences are dispersed throughout the whole FHT-a, and the periphery of FHT-a seems to be richer in HCP than its center. This could be explained by a mixing with PKT, mare or cryptomare material. The locations of the plagioclase and featureless spectra detections from Donaldson Hanna et al. [2014] show that plagioclase and featureless spectra are widely dispersed throughout the FHT-a.

3.4.2. Central Peak Pyroxene Compositional Variation

The mineralogical detections presented here have spectra with shallow band depths: the strongest band depth of all surveyed spectra in the craters selection was equal to 18 %. When looking at band depth classes, it is worth noting that the strongest classes

are generally located on topographic highs. In the case of King, Moore F and Tsinger Y craters, the position of the band 2 center shifts towards longer wavelength with decreasing band depth. Moriarty et al. [2013] interpreted this to be caused by the development of soil post-impact, rather than significant changes in composition. This is supported by the fact that the difference between the minimum and maximum band 2 position as a function of band depth does not exceed 2 spectral channels (about 80 nm) in all craters where HCP was identified, suggesting that pyroxene composition does not vary significantly within individual central peaks. Thus, the pyroxene composition of the surveyed central peak is fairly homogeneous within each central peak.

Hawke et al. [2003] introduced the idea of a mixed layer, formed during the LMO crystallization, and resulting from impact events depositing pyroxene-bearing, mafic material on top of the pure anorthositic crust formed by flotation. They also proposed that the SPA impact event deposited ejecta material on top of the crust, in thick pile close to SPA, and thinning as the distance to SPA increases. Moriarty and Pieters [2018] recently described four compositionally different units in the SPA basin, organized radially. The SPA center has a HCP signature. It is surrounded by a Mg-pyroxene annulus, then a heterogeneous annulus where more anorthositic-rich material is observed, and finally a highly feldspathic, mafic-free SPA exterior.

We attempted to identify if a significant SPA basin ejecta signature exists, and if it changes with distance from the SPA basin center. We observe no link between the position of the band 2 center and the distance to SPA, or the depth within the SPA ejecta (Fig. 3.5). This hints that the material ejected by the SPA impact event was probably reworked by the numerous subsequent impact events, and the material ejected by the SPA-forming event is no longer discernible from the FHT-a material. An alternative explanation would be that the mineralogical composition of the SPA ejecta material is very similar to that of the FHT-a crust.

Several studies pointed at the existence of a global anorthositic layer, buried under a shallow (3 to 10 km thick) layer of more pyroxene-rich material [Donaldson Hanna et al., 2014, Hawke et al., 2003, Ohtake et al., 2009, Yamamoto et al., 2012a]. The results from Tompkins and Pieters [1999] and Lemelin et al. [2015] point at a highly plagioclase-rich FHT-a crust. Only seven plagioclase occurrences were detected in this study. However, Lucey [2002] discussed that space weathering of plagioclase can cause featureless spectra, and the study of shocked plagioclase reflectance spectra showed that shock pressures can trigger the weakening or disappearance of plagioclase absorption band [Adams et al., 1979, Bruckenthal and Pieters, 1984]. The numerous featureless spectra occurrences reported here could therefore have formed from space weathered or shocked anorthositic material.

The plagioclase detections reported here are too scarce to draw any conclusions on the evolution of the plagioclase abundance with depth, so we are unable to con-

firm the proposed decrease in plagioclase abundance with increasing depth in the crust [Spudis and Davis, 1986, Tompkins and Pieters, 1999]. However, the observation of plagioclase over a wide range of depth in the FHT-a crust is consistent with the existence of a thick anorthositic crust.

Craters where plagioclase and featureless spectra are detected do not cluster in a specific P_{cmi} values range, which implies the existence of a thick plagioclase-rich, anorthositic crust. The anorthosite crust is estimated to be 27 km thick if only craters where plagioclase is detected are taken into account; 50 km thick if both plagioclase and featureless spectra are considered. Donaldson Hanna et al. [2014], Ohtake et al. [2009], Yamamoto et al. [2012a], respectively speculate the existence of a 27 km, 50 km and at least 30 km thick, discrete PAN-rich layer. The numerous HCP detections presented in this study at all investigated crustal depths are not in agreement with the existence of a discrete PAN-rich layer, but do not negate the existence of a thick (27 to 50 km) plagioclase-rich, anorthositic crust. The numerous HCP detections in the FHT-a crust at all crustal depths support the presence of a thick anorthositic crust that is mingled with the mixed layer introduced by Hawke et al. [2003], where pyroxene-bearing material is mixed with anorthositic material through impact events.

3.4.3. Link Between Pyroxene Composition and Crustal Depth

Fig. 3.6 shows that a weak positive correlation between the position of the band 2 center and the proximity to the crust-mantle interface was observed. Craters tapping upper crustal material seem to have a pyroxene signature that is more calcic than craters tapping material originating from closer to the crust-mantle interface. The change in pyroxene calcium content with depth is consistent with the results from Martinot et al. [2018b], who observed that the pyroxene signatures changes from HCP to LCP at the crust-mantle interface on the basis of the analysis of 36 craters spreading the FHT (anorthositic and outer part as described by Jolliff et al. [2000]), and with the conclusions from Melosh et al. [2017], who proposed that the lunar upper mantle is LCP-rich.

It would be helpful to add craters tapping material closer to the crust-mantle interface in order to assess the validity of this trend. The detection of pyroxene with low-calcium composition in craters tapping material originating from close to the crust-mantle interface would confirm the trend, whereas the detection of pyroxene with high-calcium composition would invalidate the trend. In the latter case, perhaps pyroxene compositions reflect the widespread emplacements of plutonic intrusions in the crust [e.g., Head and Wilson, 1992]. Unfortunately, there are no craters tapping closer to the crust-mantle interface that are covered by M^3 data from the optical period OP2C2 used in this study.

It is worth noting that pyroxene is spectrally dominant over plagioclase: Cheek and Pieters [2014] showed that as little as 2 vol.% of pyroxene in a plagioclase-rich rock could hide a potential plagioclase signature. Therefore, the detection of pyroxene

does not preclude the presence of plagioclase in a rock. Consequently, the detection of HCP in the FHT-a means that the mafic component of the FHT-a is spectrally dominated by HCP, but does not exclude that the rock petrologically fits the definition of an anorthosite.

Finally, to further analyze the compositional variations in pyroxenes detected in this study, we incorporate band 1 position analyses. The pyroxene compositions obtained from the pyroxene composition analysis in the central peaks was compared with the positions of the band 1 and 2 centers obtained by Adams [1974]'s study of orthopyroxene and clinopyroxene (Fig. 3.7). Fig. 3.7a presents Adams [1974]'s study of orthopyroxene and clinopyroxene band 1 and 2 centers with all studied impact craters where pyroxene was detected (61 out of 75). Fig. 3.7b, c and d show the band 1 and 2 centers of the selected craters where more than 10 % of the central peak (respectively, 3 to 10 % in c, and 0 to 3 % in d) has a pyroxene signature compared to the pyroxene selection from Adams [1974].

Error bars in Fig. 3.7d are bigger than in Fig. 3.7b and c, because there are only a few spectra having a pyroxene signature in the central peak, so a potential difference in pyroxene composition within the central peak has a strong effect on the standard deviation. Moreover, in the case of craters where fewer than 200 pixels in the central peak have a pyroxene signature, all spectra are taken into account in the median band center calculations, which means anomalous pyroxene compositions will strongly affect the resulting median and standard deviation of the pixel population.

The compositions of pyroxene observed in the studied central peaks are generally consistent with clinopyroxene (e.g., diopside, augite, or HCP), and a small number of pyroxene compositions is compatible with orthopyroxene (e.g., ferrosilite, enstatite, or LCP), within error bars. This is consistent with the fact that the pyroxene calcium content changes with depth. The band 2 center of studied craters stretches until 2340 nm, so the pyroxenes observed in this study are probably less calcic than the calcic endmember studied in Adams [1974].

Overall, the data again hint at a decrease in pyroxene calcium content with depth.

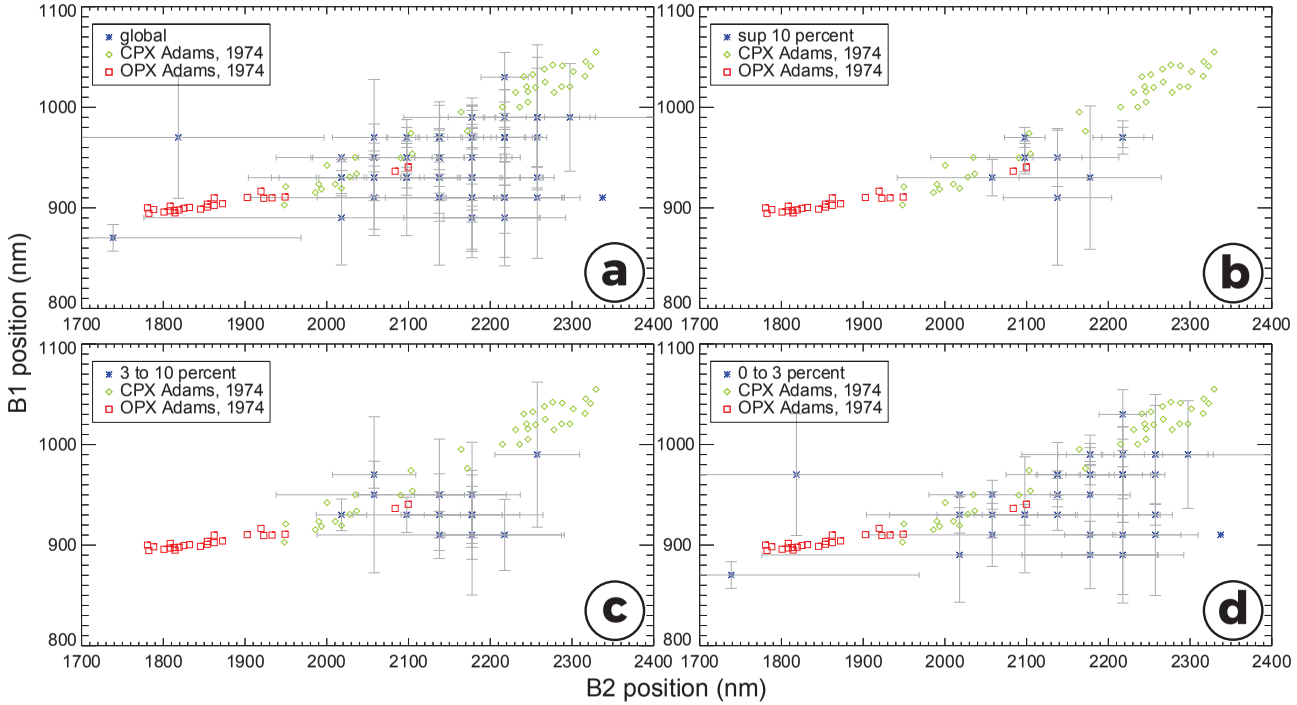

Figure 3.7: [Adams, 1974] study's orthopyroxene and clinopyroxene band 1 and 2 centers (respectively, red square and green diamond). This study's pyroxene band 1 and 2 centers are coded with blue stars. They correspond to the median of the 200 pixels having the strongest band depth. Error bars were calculated as the standard deviation of the 200 pixels having the strongest band depth. **a** All studied central peak craters where pyroxene was detected. **b** Pyroxene compositions derived from the studied central peak craters where more than 10 % of the central peak has a pyroxene signature. **c** Pyroxene compositions derived from the studied central peak craters where 3 to 10 % of the central peak has a pyroxene signature. **d** Pyroxene compositions derived from the studied central peak craters where less than 3 % of the central peak has a pyroxene signature.

3.5. Conclusions

The analysis of 75 impact craters' central peaks with spectroscopic data showed that HCP and featureless spectra are widely detected in the FHT-a.

The plagioclase detections reported here are consistent with the existence of an anorthositic crust at least 27 km thick, which is probably mixed with pyroxene-bearing material emplaced during the LMO crystallization through impact events [Hawke et al., 2003].

Data hint at a pyroxene compositional change with depth. The composition of pyroxene is more calcic far from the crust-mantle interface than closer to the crust-mantle interface. This result is compatible with the conclusions from Martinot et al. [2018b], who proposed that there is a transition from HCP to LCP around the crust-mantle interface. A transition from HCP to LCP at the crust-mantle interface is also consistent with the conclusions from Melosh et al. [2017], who proposed that the upper mantle is LCP-rich.

At the time of the SPA formation, the ejecta from the SPA basin probably overprinted the FHT-a material (and the lunar surface more broadly). Yet, no significant SPA signature was detected, and no link between the position of the band 2 center and the distance to SPA of the depth in the SPA ejecta was observed. This suggests that the material ejected by the SPA-forming event was reworked by subsequent impact craters and mixed with the FHT-a material, or that the ejected crust from the SPA impact event formation and the FHT-a crust were petrologically similar.

Acknowledgments

The authors would like to thank K. Donaldson-Hanna for kindly sharing her data, J.-F. Blanchette-Guertin for helping with the proximity calculations, L. Mandon for sharing useful data, and C. Brustel for helpful discussions. This work was supported by a Netherlands Organization for Scientific Research (NWO) Vici grant and a User Support Space Research grant from the Netherlands Space Office (NSO) to W.v.W. J.F. is supported by a CNES APR LIS-Luna funding. C.Q.N. is supported by European Research Council through the FP7/2007-2013/ERC grant agreement 280168. M^3 and LRO WAC data can be accessed in the PDS Geoscience Node, Lunar Orbital Data Explorer (`http://ode.rsl.wustl.edu/`). The GRAIL crustal thickness models archive is hosted at `https://zenodo.org/record/997347`. LRO LOLA digital elevation model can be downloaded from `https://astrogeology.usgs.gov/search/details/Moon/LRO/LOLA/Lunar_LRO_LOLA_Global_LDEM_118m_Mar2014/cub`. The Lunar Impact Crater Database is available at `https://www.lpi.usra.edu/lunar/surface/Lunar_Impact_Crater_Database_v08Sep2015.xls`.

3.6. Supporting Information

Table 3.3: Craters selected for this survey, ranked according to the crater diameter; crater age; the GRAIL crustal thickness model 1 (M1); the depth of melting (Dm); the distance to SPA; the thickness of SPA ejecta calculated with the method from McGetchin et al. [1973] and from Housen et al. [1983] (SPA ejecta thick.* and SPA ejecta thick.**, respectively); depth within the SPA ejecta, calculated respectively with McGetchin et al. [1973] and Housen et al. [1983] estimates of the SPA thickness (D^{*}_{SPA} and D^{**}_{SPA}, respectively); and P_{cmi} value are indicated. Some craters ages were not reported in the LICD, they were marked - in the table. The central peak material depth of origin was approximated with the D_m [Cintala and Grieve, 1998].

Crater	Age	LON	LAT	Diam. (km)	GRAIL M1 (km)	Dm (km)	Distance to SPA (km)	SPA ejecta thick.* (km)	SPA ejecta thick.** (km)	D^{*}_{SPA} (km)	D^{**}_{SPA} (km)	P_{cmi} (km)
Moore F	-	−175.0	37.4	24	49	3	2717	7	18	3	15	45.3
Hayford	-	−176.4	12.7	27	45	4	1975	18	42	14	38	41.5
Necho	Copernican	123.1	−5.0	30	44	4	2504	9	22	4	18	39.6
Coriolis Y	Nectarian	171.2	3.6	31	41	4	1789	24	54	20	49	36.7
Fowler W	-	−150.2	46.0	31	45	4	3025	5	14	1	9	40.9
Tsinger Y	Eratosthenian	175.1	58.1	31	40	4	3373	4	10	−1	6	35.2
Katchalsky	Upper Imbrian	116.1	5.9	32	37	5	2870	6	16	1	11	32.9
Kulik L	-	−151.6	39.1	33	46	5	2812	6	17	1	12	40.9
Grachev	Eratosthenian	−108.2	−3.7	35	45	5	2354	11	26	5	21	39.7
Stearns	Eratosthenian	162.6	34.8	36	43	5	2769	6	17	1	12	37.7
Trumpler V	Nectarian	164.0	29.8	36	42	5	2608	8	20	3	15	36.6
Coriolis W	-	168.0	3.1	37	40	5	1810	23	52	18	47	34.3
Golovin	Upper Imbrian	161.1	39.9	37	45	5	2930	5	15	0	9	40.0
Shayn H	Nectarian	175.5	31.4	38	44	6	2572	8	21	3	15	38.0
Butlerov	Upper Imbrian	−108.7	12.5	40	40	6	2677	7	19	1	13	34.2
Montgolfier Y	Upper Imbrian	−161.3	50.5	40	46	6	3116	5	13	−1	7	40.0
Dufay X	-	168.5	7.2	42	40	6	1920	19	45	13	39	33.6
Amici T	Eratosthenian	−174.0	−9.7	43	50	6	1291	64	126	58	120	43.4
Dante E	Eratosthenian	−177.0	26.7	43	47	6	2398	10	25	4	19	40.4
d'Alembert Z	Upper Imbrian	165.6	55.4	44	42	6	3346	4	10	−3	4	35.7
Tsinger	Nectarian	175.6	56.7	44	41	6	3329	4	11	−3	4	34.1
Virtanen	Copernican	176.7	15.5	44	30	6	2098	15	36	8	29	23.3
Delporte	Upper Imbrian	121.6	−16.0	45	43	7	2370	10	26	4	19	35.9
Kulik J	-	−154.5	42.4	46	46	7	2896	6	15	−1	8	38.8
Woltjer	Upper Imbrian	−159.6	45.2	46	46	7	2961	5	14	−2	8	38.8
Evershed C	Nectarian	−156.7	38.1	48	49	7	2757	7	17	−1	10	41.9
Anderson F	Nectarian	173.6	16.3	49	26	7	2137	14	34	7	27	19.1
Larmor Z	Upper Imbrian	−179.8	33.7	49	46	7	2619	8	20	0	13	38.9
Rowland J	Eratosthenian	−155.5	53.1	49	45	7	3213	4	12	−3	4	37.4
Hutton	Nectarian	168.7	37.3	50	43	7	2791	6	17	−1	9	35.8
Spencer Jones W	Nectarian	163.3	15.2	50	39	7	2204	13	31	5	24	31.3
Tiselius	Upper Imbrian	176.5	7.0	53	46	8	1842	22	50	14	42	37.8
Dante	Upper Imbrian	180.0	25.5	54	46	8	2367	10	26	2	18	38.2
Rowland Y	Nectarian	−163.0	59.1	54	42	8	3373	4	10	−5	2	33.5

Continued on next page

Table 3.3 – *Continued from previous page*

Crater	Age	LON	LAT	Diam. (km)	GRAIL M1 (km)	Dm (km)	Distance to SPA (km)	SPA ejecta thick.* (km)	SPA ejecta thick.** (km)	D^{*}_{SPA} (km)	D^{**}_{SPA} (km)	P_{cmi} (km)
Schneller	Nectarian	−163.6	41.8	54	46	8	2849	6	16	−2	8	38.3
Buisson	-	112.5	−1.4	56	43	8	2832	6	16	−2	8	34.3
Cockcroft N	-	−163.7	29.1	56	51	8	2464	9	23	1	15	42.2
Krasovskiy L	-	−174.8	−0.4	58	46	9	1571	35	76	27	67	37.6
Rowland M	Nectarian	−162.4	51.9	58	45	9	3156	4	12	−4	3	35.9
Krasovskiy	Upper Imbrian	−175.5	3.9	59	48	9	1704	28	61	19	52	38.8
Nusl	Upper Imbrian	167.6	32.3	61	42	9	2652	7	19	−2	10	32.9
Vesalius	Nectarian	114.5	−3.1	61	42	9	2753	7	17	−3	8	32.8
Lebedinskiy	Nectarian	−164.3	8.3	62	58	9	1817	23	52	14	42	48.9
Lodygin	Nectarian	−146.8	−17.7	62	52	9	1241	72	140	63	130	42.6
Perkin	Nectarian	−175.9	47.2	62	40	9	3015	5	14	−4	4	30.9
Petropavlovskiy	Nectarian	−114.8	37.2	63	41	10	3165	4	12	−5	3	31.9
Ohm	Copernican	−113.5	18.4	64	43	10	2718	7	18	−3	8	32.9
Gadomski	Nectarian	−147.3	36.4	65	49	10	2760	7	17	−3	7	38.9
Evershed	-	−159.5	35.7	66	51	10	2674	7	19	−3	9	40.9
Artem'ev	Lower Imbrian	−144.4	10.8	67	56	10	2045	16	38	6	28	45.7
Valier	Nectarian	174.5	6.8	67	43	10	1845	22	50	12	39	33.0
Slipher	Lower Imbrian	160.1	49.5	69	43	11	3217	4	12	−6	1	32.0
Daedalus W	-	177.5	−3.5	70	42	11	1526	39	81	28	71	31.5
Jackson	Copernican	−163.1	22.4	71	50	11	2263	12	29	1	18	39.2
Sharonov	Copernican	173.3	12.4	74	38	11	2025	17	39	5	28	26.7
King	Copernican	120.5	5.0	76	40	12	2749	7	18	−5	6	28.2
Morse	Eratosthenian	−175.1	22.1	77	45	12	2254	12	29	0	18	33.4
Coriolis	Pre-Nectarian	171.8	0.1	78	40	12	1683	29	63	17	51	27.5
Chappell	-	−177.0	54.7	80	41	12	3230	4	12	−8	−1	28.3
Schliemann	Nectarian	155.2	−2.1	80	40	12	1864	21	48	9	36	27.5
Freundlich	Nectarian	171.0	25.0	85	42	13	2412	10	25	−3	11	28.8
Spencer Jones	Lower Imbrian	165.6	13.3	85	40	13	2124	14	34	1	21	26.9
Vening Meinesz	Nectarian	162.6	−0.3	87	40	14	1788	24	54	10	40	26.2
Kibal'chich	Nectarian	−146.5	3.0	92	56	14	1780	24	55	10	40	42.0
Daedalus	Lower Imbrian	179.4	−5.9	93	43	15	1441	46	95	31	80	28.1
Amici U	-	−175.5	−8.7	96	48	15	1321	60	119	45	104	32.8
Joule	Nectarian	−144.2	27.3	96	54	15	2519	9	22	−6	7	38.8
Kolhorster	Nectarian	−114.6	11.2	97	44	15	2528	9	22	−7	7	28.7
Larmor	Nectarian	−179.7	32.1	97	46	15	2570	8	21	−7	6	30.5
Ostwald	-	121.9	10.4	104	37	16	2823	6	16	−10	0	20.8
Doppler	Lower Imbrian	−159.6	−12.6	110	52	17	1228	74	144	57	126	34.4
Keeler	Lower Imbrian	161.9	−10.2	160	38	26	1544	37	79	11	53	12.1
Sommerfeld	Nectarian	−162.4	65.2	169	39	28	3359	4	10	−24	−17	11.2
Rowland	Nectarian	−162.5	57.4	171	43	28	3299	4	11	−24	−17	14.4

Continued on next page

Table 3.3 – *Continued from previous page*

Crater	Age	LON	LAT	Diam. (km)	GRAIL M1 (km)	Dm (km)	Distance to SPA (km)	SPA ejecta thick.* (km)	SPA ejecta thick.** (km)	D^{*}_{SPA} (km)	D^{**}_{SPA} (km)	P_{cmi} (km)
Mach	Pre-Nectarian	−149.3	18.5	180	54	30	2219	13	31	−17	1	24.3
d'Alembert	Nectarian	163.9	50.8	248	41	42	3223	4	12	−38	−30	−1.5

* SPA ejecta thickness calculated with McGetchin et al. [1973] method.
** SPA ejecta thickness calculated with Housen et al. [1983] method.

Table 3.4: Overview of craters where Donaldson Hanna et al. [2014] detected plagioclase occurrences, with crater diameter (km); age of the crater; GRAIL crustal thickness model 1 (km); depth of melting (km); and P_{cmi} value (km). Craters where no age is provided by the LICD (Losiak et al. [2009], revised by Ohman at LPI) are signaled with -.

Name	Age	LON	LAT	Diam (km)	GRAIL M1 (km)	Dm (km)	P_{cmi} (km)
Amici N	Nectarian	−172.5	−11.8	39	52	6	46
Stromgren X	Nectarian	−134.6	−17.4	42	52	6	46
Virtanen	Copernican	176.7	15.5	44	30	6	23
Leuschner	Eratosthenian	−108.8	1.8	49	45	7	38
Shirakatsi	Nectarian	128.6	−12.1	51	43	8	35
Korolev M	Nectarian	−157.3	−8.8	58	55	9	46
Jackson	Copernican	−163.1	22.4	71	50	11	39
Morse	Eratosthenian	−175.1	22.1	77	45	12	33
Wood	Nectarian	−120.8	43	78	44	12	32
Spencer Jones	Lower Imbrian	165.6	13.3	85	40	13	27
Ioffe	Nectarian	−129.2	−14.4	86	53	13	40
Daedalus	Lower Imbrian	179.4	−5.9	93	43	15	28
Amici U	-	−175.5	−8.7	96	48	15	33
Vavilov	-	−137.9	−0.8	98	57	15	42
Schuster	Nectarian	146.5	4.2	108	39	17	22
Kovalevskaya	Upper Imbrian	−129.6	30.8	115	48	18	30
Carnot	Nectarian	−143.5	52.3	126	45	20	24
Poynting	Nectarian	−133.4	18.1	128	52	21	31
Keeler	Lower Imbrian	161.9	−10.2	160	38	26	12
Mach	Pre-Nectarian	−149.3	18.5	180	54	30	24
Tsiolkovskiy	Upper Imbrian	128.9	−21.2	185	40	31	9

Bibliography

Adams, J.B., 1974. Visible and near-infrared diffuse reflectance spectra of pyroxenes as applied to remote sensing of solid objects in the solar system. Journal of Geophysical Research 79, 4829. doi:10.1029/JB079i032p04829.

Adams, J.B., Hörz, F., Gibbons, R.V., 1979. Effects of shock-loading on the reflectance spectra of plagioclase, pyroxene, and glass, in: Proceedings of the 10th Lunar and Planetary Science Conference, pp. 5–7.

Arai, T., Takeda, H., Yamaguchi, A., Ohtake, M., 2008. A new model of lunar crust: asymmetry in crustal composition and evolution. Earth, Planets and Space 60, 433–444.

Besse, S., Sunshine, J., Staid, M., Boardman, J., Pieters, C., Guasqui, P., Malaret, E., McLaughlin, S., Yokota, Y., Li, J.Y., 2013. A visible and near-infrared photometric correction for Moon Mineralogy Mapper (M^3). Icarus 222, 229–242. doi:10.1016/j.icarus.2012.10.036.

Bills, B.G., Ferrari, A.J., 1977. A lunar density model consistent with topographic, gravitational, librational, and seismic data. Journal of Geophysical Research 82, 1306–1314.

Boardman, J.W., Pieters, C.M., Green, R.O., Lundeen, S.R., Varanasi, P., Nettles, J., Petro, N.E., Isaacson, P., Besse, S., Taylor, L.A., 2011. Measuring moonlight: An overview of the spatial properties, lunar coverage, selenolocation, and related Level 1B products of the Moon Mineralogy Mapper. Journal of Geophysical Research E: Planets 116, 1–15. doi:10.1029/2010JE003730.

Borg, L., Norman, M., Nyquist, L., Bogard, D., Snyder, G., Taylor, L., Lindstrom, M., 1999. Isotopic studies of ferroan anorthosite 62236: A young lunar crustal rock from a light rare-earth-element-depleted source. Geochimica et Cosmochimica Acta 63, 2679–2691. doi:10.1016/S0016-7037(99)00130-1.

Borg, L.E., Gaffney, A.M., Shearer, C.K., 2015. A review of lunar chronology revealing a preponderance of 4.34-4.37 Ga ages. Meteoritics and Planetary Science 50, 715–732. doi:10.1111/maps.12373.

Bruckenthal, E.A., Pieters, C.M., 1984. Spectral effects of natural shock on plagioclase felsdpar, in: Lunar and Planetary Institute. Cambridge, pp. 96–97.

Cahill, J.T.S., Lucey, P.G., Wieczorek, M.A., 2009. Compositional variations of the lunar crust: Results from radiative transfer modeling of central peak spectra. Journal of Geophysical Research E: Planets 114, 1–17. doi:10.1029/2008JE003282.

Charlier, B., Grove, T.L., Namur, O., Holtz, F., 2018. Crystallization of the lunar magma ocean and the primordial mantle-crust differentiation of the Moon. Geochimica et Cosmochimica Acta 234, 50–69. URL: https://doi.org/10.1016/j.gca.2018.05.006, doi:10.1016/j.gca.2018.05.006.

Cheek, L.C., Donaldson Hanna, K.L., Pieters, C.M., Head, J.W., Whitten, J.L., 2013. The distribution and purity of anorthosite across the Orientale basin: New perspectives from Moon Mineralogy Mapper data. Journal of Geophysical Research: Planets 118, 1805–1820. doi:10.1002/jgre.20126.

Cheek, L.C., Pieters, C.M., 2014. Reflectance spectroscopy of plagioclase-dominated mineral mixtures: Implications for characterizing lunar anorthosites remotely. American Mineralogist 99, 1871–1892. doi:10.2138/am-2014-4785.

Cintala, M.J., Grieve, R.A.F., 1998. Scaling impact melting and crater dimensions: Implications for the lunar cratering record. Meteoritics & Planetary Science 33, 889–912. doi:10.1111/j.1945-5100.1998.tb01695.x.

Clark, R.N., Pieters, C.M., Green, R.O., Boardman, J.W., Petro, N.E., 2011. Thermal removal from near-infrared imaging spectroscopy data of the Moon. doi:10.1029/2010JE003751.

Cloutis, E.A., Gaffey, M.J., 1991. Pyroxene Spectroscopy Revisited: Spectral-Compositional Correlations and Relations to Geothermometry. Journal of Geophysical Research 96, 22809–22826.

Donaldson Hanna, K.L., Cheek, L.C., Pieters, C.M., Mustard, J.F., Greenhagen, B.T., Thomas, I.R., Bowles, N.E., 2014. Global assessment of pure crystalline plagioclase across the Moon and implications for the evolution of the primary crust. Journal of Geophysical Research: Planets 119, 1516–1545. doi:10.1002/2013JE004476.

Flahaut, J., Blanchette-Guertin, J.F., Jilly, C., Sharma, P., Souchon, A., Van Westrenen, W., Kring, D.A., 2012. Identification and characterization of science-rich landing sites for lunar lander missions using integrated remote sensing observations. Advances in Space Research 50, 1647–1665. doi:10.1016/j.asr.2012.05.020.

Green, R.O., Pieters, C., Mouroulis, P., Eastwood, M., Boardman, J., Glavich, T., Isaacson, P., Annadurai, M., Besse, S., Barr, D., Buratti, B., Cate, D., Chatterjee, A., Clark, R., Cheek, L., Combe, J., Dhingra, D., Essandoh, V., Geier, S., Goswami, J.N., Green, R., Haemmerle, V., Head, J., Hovland, L., Hyman, S., Klima, R., Koch, T., Kramer, G., Kumar, A.S.K., Lee, K., Lundeen, S., Malaret, E., McCord, T., McLaughlin, S., Mustard, J., Nettles, J., Petro, N.E., Plourde, K., Racho, C., Rodriquez, J., Runyon, C., Sellar, G., Smith, C., Sobel, H., Staid, M.I., Sunshine, J.M., Taylor, L., Thaisen, K., Tompkins, S., Tseng, H., Vane, G., Varanasi, P., White, M., Wilson, D., 2011. The Moon Mineralogy Mapper (M^3) imaging spectrometer for lunar science: Instrument description, calibration, on-orbit measurements, science data calibration and on-orbit validation. Journal of Geophysical Research E: Planets 116, 1–31. doi:10.1029/2011JE003797.

Gross, J., Treiman, A.H., Mercer, C.N., 2014. Lunar feldspathic meteorites: Constraints on the geology of the lunar highlands, and the origin of the lunar crust. Earth and Planetary Science Letters 388, 318–328. doi:10.1016/j.epsl.2013.12.006.

Hawke, B.R., Peterson, C.A., Blewett, D.T., Bussey, D.B.J., Lucey, P.G., Taylor, G.J., Spudis, P.D., 2003. Distribution and modes of occurrence of lunar anorthosite. Journal of Geophysical Research 108, 1–16. doi:10.1029/2002JE001890.

Head, J.W.I., Wilson, L., 1992. Lunar mare volcanism - Stratigraphy, eruption conditions, and the evolution of secondary crusts. Geochim. Cosmochim. Acta 56, 2155–2175. doi:10.1016/0016-7037(92)90183-J.

Housen, K.R., Schmidt, R.M., Holsapple, K.A., 1983. Crater ejecta scaling laws: fundamental forms based on dimensional analysis. Journal of Geophysical Research 88, 2485–2499. doi:10.1029/JB088iB03p02485.

Jaumann, R., Hiesinger, H., Anand, M., Crawford, I.A., Wagner, R., Sohl, F., Jolliff, B.L., Scholten, F., Knapmeyer, M., Hoffmann, H., Hussmann, H., Grott, M., Hempel, S., Köhler, U., Krohn, K., Schmitz, N., Carpenter, J., Wieczorek, M.A., Spohn, T., Robinson, M.S., Oberst, J., 2012. Geology, geochemistry, and geophysics of the Moon: Status of current understanding. Planetary and Space Science 74, 15–41. doi:10.1016/j.pss.2012.08.019.

Jolliff, B.L., Gillis, J.J., Haskin, L.A., Korotev, R.L., Wieczorek, M.A., 2000. Major lunar crustal terranes: Surface expressions and crust-mantle origins. Journal of Geophysical Research 105, 4197. doi:10.1029/1999JE001103.

Kaula, W.M., 1979. Thermal evolution of earth and moon growing by planetesimal impacts. Journal of Geophysical Research 84, 999–1008. doi:10.1029/JB084iB03p00999.

Klima, R.L., Pieters, C.M., Isaacson, P.J., Head, J.W., Petro, N.E., Staid, M., Sunshine, J.M., Taylor, L.A., 2011. Spectroscopic evidence of Mg-rich Low-Ca Pyroxenes on the nearside of the Moon. Lunar Planetary Science Conference 42. doi:10.1029/2006JE002868.

Laneuville, M., Taylor, J., Wieczorek, M.A., 2018. Distribution of Radioactive Heat Sources and Thermal History of the Moon. Journal of Geophysical Research: Planets doi:10.1029/2018JE005742.

Lawrence, D.J., Feldman, W.C., Barraclough, B.L., Binder, A.B., Elphic, R.C., Maurice, S., Thomsen, D.R., 1998. Global elemental maps of the Moon: The Lunar Prospector gamma-ray spectrometer. Science 281, 1484–1489.

Lemelin, M., Lucey, P.G., Song, E., Taylor, G.J., 2015. Lunar central peak mineralogy and iron content using the Kaguya Multiband Imager: Reassessment of the compositional structure of the lunar crust. Journal of Geophysical Research: Planets 120, 869–887. doi:10.1002/2014JE004778.

Lin, Y., Tronche, E.J., Steenstra, E.S., van Westrenen, W., 2017a. Evidence for an early wet Moon from experimental crystallization of the lunar magma ocean. Nature Geoscience 1, 1–6. doi:10.1038/ngeo2845.

Lin, Y., Tronche, E.J., Steenstra, E.S., van Westrenen, W., 2017b. Experimental constraints on the solidification of a nominally dry lunar magma ocean. Earth and Planetary Science Letters 471, 104–116. URL: http://dx.doi.org/10.1016/j.epsl.2017.04.045, doi:10.1016/j.epsl.2017.04.045.

Losiak, A., Wilhelms, D.E., Byrne, C.J., Thaisen, K., Weider, S.Z., Kohout, T., O'Sullivan, K., Kring, D.A., 2009. A new lunar impact crater database, in: Lunar and Planetary Science Conference.

Lucey, P.G., 2002. Radiative transfer model constraints on the shock state of remotely sensed lunar anorthosites. Geophysical Research Letters 29, 1–3. doi:10.1029/2001GL014655.

Lucey, P.G., Cahill, J., 2006. Magnesian rock types in the lunar highlands: remote sensing using data from Lunar Prospector and Clementine, in: Lunar and Planetary Institute Science Conference.

Martinot, M., Besse, S., Flahaut, J., Quantin-Nataf, C., Lozac'h, L., van Westrenen, W., 2018a. Mineralogical Diversity and Geology of Humboldt Crater Derived Using Moon Mineralogy Mapper Data. Journal of Geophysical Research: Planets 123. doi:10.1002/2017JE005435.

Martinot, M., Flahaut, J., Besse, S., Quantin-Nataf, C., van Westrenen, W., 2018b. Compositional variations in the vicinity of the lunar crust-mantle interface from Moon Mineralogy Mapper data. Journal of Geophysical Research: Planets 123. doi:10.1029/2018JE005744.

McGetchin, T.R., Settle, M., Head, J.W., 1973. Radial Thickness Variation in Impact Crater Ejecta: Implications for lunar basin deposits. Earth and Planetary Science Letters 20, 226–236.

Melosh, H.J., 2011. Planetary Surface Processes. doi:10.1017/CBO9780511977848.

Melosh, H.J., Kendall, J., Horgan, B., Johnson, B.C., Bowling, T., Lucey, P.G., Taylor, G.J., 2017. South Pole-Aitken basin ejecta reveal the Moon's upper mantle. Geology 45, 1063–1066. doi:10.1130/G39375.1.

Moriarty, D.P., Pieters, C.M., 2018. The Character of South Pole-Aitken Basin: Patterns of Surface and Subsurface Composition. Journal of Geophysical Research: Planets , 729–747doi:10.1002/2017JE005364.

Moriarty, D.P., Pieters, C.M., Isaacson, P.J., 2013. Compositional heterogeneity of central peaks within the south pole-aitken basin. Journal of Geophysical Research E: Planets 118, 2310–2322. doi:10.1002/2013JE004376.

Ohtake, M., Matsunaga, T., Haruyama, J., Yokota, Y., Morota, T., Honda, C., Ogawa, Y., Torii, M., Miyamoto, H., Arai, T., Hirata, N., Iwasaki, A., Nakamura, R., Hiroi, T., Sugihara, T., Takeda, H., Otake, H., Pieters, C.M., Saiki, K., Kitazato, K., Abe, M., Asada, N., Demura, H., Yamaguchi, Y., Sasaki, S., Kodama, S., Terazono, J., Shirao, M., Yamaji, A., Minami, S., Akiyama, H., Josset, J.L., 2009. The global distribution of pure anorthosite on the Moon. Nature 461, 236–240. doi:10.1038/nature08317.

Ohtake, M., Takeda, H., Matsunaga, T., Yokota, Y., Haruyama, J., Morota, T., Yamamoto, S., Ogawa, Y., Hiroi, T., Karouji, Y., Saiki, K., Lucey, P.G., 2012. Asymmetric crustal growth on the Moon indicated by primitive farside highland materials. Nature Geoscience 5, 384–388. URL: http://dx.doi.org/10.1038/ngeo1458, doi:10.1038/ngeo1458.

Papanastassiou, D.A., Wasserburg, G.J., 1971a. Lunar chronology and evolution from RbSr studies of Apollo 11 and 12 samples. Earth and Planetary Science Letters 11, 37–62. doi:10.1016/0012-821X(71)90139-7.

Papanastassiou, D.A., Wasserburg, G.J., 1971b. RbSr ages of igneous rocks from the Apollo 14 mission and the age of the Fra Mauro formation. Earth and Planetary Science Letters 12, 36–48. doi:10.1016/0012-821X(71)90052-5.

Parmentier, E.M., Zhong, S., Zuber, M.T., 2002. Gravitational differentiation due to initial chemical stratification: Origin of lunar asymmetry by the creep of dense KREEP? Earth and Planetary Science Letters 201, 473–480. doi:10.1016/S0012-821X(02)00726-4.

Pieters, C.M., Boardman, J., Buratti, B., Chatterjee, A., Clark, R., Glavich, T., Green, R., Head, J.W.I., Isaacson, P., Malaret, E., Mccord, T., Mustard, J., Petro, N.E., Runyon, C., Staid, M.I., Sunshine, J.M., Taylor, L., Tompkins, S., Varanasi, P., White, M., 2009. The Moon Mineralogy Mapper (M^3) on Chandrayaan-1. Current Science 96, 1–6.

Rapp, J.F., Draper, D.S., 2018. Fractional crystallization of the lunar magma ocean : Updating the dominant paradigm. Meteoritics & Planetary Science 24, 1–24. doi:10.1111/maps.13086.

Ryder, G., Wood, J.A., 1977. Serenitatis and Imbrium impact melts - Implications for large-scale layering in the lunar crust. Proc. Lunar Planet. Sci. Conf. , 655–668.

Shearer, C.K., Hess, P.C., Wieczorek, M.A., Pritchard, M.E., Parmentier, E.M., Borg, L.E., Longhi, J., Elkins-Tanton, L.T., Neal, C.R., Antonenko, I., Canup, R.M., Halliday, A.N., Grove, T.L., Hager, B.H., Lee, D.C., Wiechert, U., 2006. Thermal and Magmatic Evolution of the Moon. Reviews in Mineralogy and Geochemistry 60, 365–518. doi:10.2138/rmg.2006.60.4.

Smith, D.E., Zuber, M.T., Neumann, G.A., Lemoine, F.G., Mazarico, E., Torrence, M.H., McGarry, J.F., Rowlands, D.D., Head, J.W., Duxbury, T.H., Aharonson, O., Lucey, P.G., Robinson, M.S., Barnouin, O.S., Cavanaugh, J.F., Sun, X., Liiva, P., Mao, D.D., Smith, J.C., Bartels, A.E., 2010. Initial observations from the Lunar Orbiter Laser Altimeter (LOLA). Geophysical Research Letters 37, 1–6. doi:10.1029/2010GL043751.

Smith, J.V., Anderson, A.T., Newton, R.C., Olsen, E.J., Wyllie, P.J., Crewe, A.V., Isaacson, M.S., Johnson, D., 1970. Petrologic history of the moon inferred from petrography, mineralogy, and petrogenesis of Apollo 11 rocks. Proceedings of the Apollo 11 Lunar Science Conference 1, 897–925.

Song, E., Bandfield, J.L., Lucey, P.G., Greenhagen, B.T., Paige, D.A., 2013. Bulk mineralogy of lunar crater central peaks via thermal infrared spectra from the Diviner Lunar Radiometer: A study of the Moon's crustal composition at depth. Journal of Geophysical Research E: Planets 118, 689–707. doi:10.1002/jgre.20065.

Spudis, P.D., Davis, P.A., 1986. A chemical and petrological model of the lunar crust and implications for lunar crustal origin. Journal of Geophysical Research 91, E84–E90. doi:10.1029/JB091iB13p00E84.

Stevenson, D.J., 1980. Lunar asymmetry and palaeomagnetism. Nature 287, 520–521. doi:10.1038/287520a0.

Stuart-Alexander, D.E., 1978. Geologic map of the central far side of the Moon. URL: http://pubs.er.usgs.gov/publication/i948.

Tompkins, S., Pieters, C.M., 1999. Mineralogy of the Lunar Crust - Results From Clementine. Meteoritics & Planetary Science 34, 25–41.

Warren, P.H., 1985. The magma ocean concept and lunar evolution. Annual Review of Earth and Planetary Science 13, 201–40. doi:10.1146/annurev.earth.13.1.201.

Wasson, J.T., Warren, P.H., 1980. Contribution of the mantle to the lunar asymmetry. Icarus 771, 752–771. doi:10.1016/0019-1035(80)90142-6.

Wieczorek, M.A., Neumann, G.A., Nimmo, F., Kiefer, W.S., Taylor, G.J., Melosh, H.J., Phillips, R.J., Solomon, S.C., Andrews-Hanna, J.C., Asmar, S.W., Konopliv, A.S., Lemoine, F.G., Smith, D.E., Watkins, M.M., Williams, J.G., Zuber, M.T., 2013. The crust of the Moon as seen by GRAIL. Science (New York, N.Y.) 339, 671–5. doi:10.1126/science.1231530.

Wilhelms, D.E., Howard, K.A., Wilshire, H.G., 1979. Geologic maps of the South side of the Moon. US Geol. Surv. Misc. Invest. Ser., I-1162 .

Wood, J.A., 1970. Petrology of the lunar soil and geophysical implications. Journal of Geophysical Research 75, 6497–6513. URL: http://doi.wiley.com/10.1029/JB075i032p06497, doi:10.1029/JB075i032p06497.

Yamamoto, S., Nakamura, R., Matsunaga, T., Ogawa, Y., Ishihara, Y., Morota, T., Hirata, N., Ohtake, M., Hiroi, T., Yokota, Y., Haruyama, J., 2012a. Massive layer of pure anorthosite on the Moon. Geophysical Research Letters 39, 1–6. doi:10.1029/2012GL052098.

Yamamoto, S., Nakamura, R., Matsunaga, T., Ogawa, Y., Ishihara, Y., Morota, T., Hirata, N., Ohtake, M., Hiroi, T., Yokota, Y., Haruyama, J., 2012b. Olivine-rich exposures in the South Pole-Aitken Basin. Icarus 218, 331–344. doi:10.1016/j.icarus.2011.12.012.

Yamamoto, S., Nakamura, R., Matsunaga, T., Ogawa, Y., Ishihara, Y., Morota, T., Hirata, N., Ohtake, M., Hiroi, T., Yokota, Y., Haruyama, J., 2016. GLOBAL DISTRIBUTION OF GLASS-RICH MATERIAL SITES ON THE MOON, in: Lunar and Planetary Institute Science Conference, pp. 12–13.

Zuber, M.T., Smith, D.E., Lemoine, F.G., Neumann, G.A., 1994. The shape and internal structure of the moon from the clementine mission. Science (New York, N.Y.) 266, 1839–1843. doi:10.1126/science.266.5192.1839.

4

Application of the developed tools to future science exploration Science-rich sites for future lunar exploration (Chang'E-4 mission)

The chance to apply the continuum removal and spectral study tools for future lunar exploration presented itself, and I had the opportunity to contribute to the characterization of the soon to be launched Chinese Chang'E-4 and 5 landing sites. Two scientific article were published as part of this collaboration, in preparation to the missions launch:

- Geological Characteristics of Von Kármán Crater, Northwestern South Pole-Aitken Basin: Chang'E-4 Landing Site Region, J. Huang, Z. Xiao, J. Flahaut, M. Martinot, J. Head, X. Xiao, M. Xie, L. Xiao, JGR-Planets, https://doi.org/10.1029/2018JE005577 (chapter 4).

- Geology and Scientific Significance of the Rümker Region in Northern Oceanus Procellarum: China's Chang'E-5 Landing Region, Y. Qian, L. Xiao, S. Zhao, J. Zhao, J. Huang, J. Flahaut, M. Martinot, J. W. Head, H. Hiesinger, and G. X. Wang, JGR-Planets, https://doi.org/ 10.1029/2018JE005595 (chapter 5).

The two following chapters are the reproduction of both articles.

4.1. Geological Characteristics of the Chang'E-4 Landing Site Region: Von Kármán Crater, Northwestern South Pole-Aitken Basin

Jun Huang[1], Zhiyong Xiao[1], Jessica Flahaut[2,3], Mélissa Martinot[4,5], James Head[6], Xiao Xiao[1], Minggang Xie[7], Long Xiao[1]

[1] State Key Laboratory of Geological Processes and Mineral Resources, Planetary Science Institute, School of Earth Sciences, China University of Geosciences, Wuhan 430074, China
[2] CRPG-CNRS/Université de Lorraine, 54500 Vandœuvre-lès-Nancy, France
[3] IRAP-CNRS-CNES/Université Paul Sabatier, 31400 Toulouse, France
[4] Faculty of Science, Vrije Universiteit Amsterdam, Amsterdam, The Netherlands
[5] Université Lyon 1, ENS-Lyon, CNRS, UMR 5276 LGL-TPE, Villeurbanne, France
[6] Department of Earth, Environmental and Planetary Sciences, Brown University, Providence, RI, 02912 USA
[7] Space Science Institute, Macau University of Science and Technology, Macau, China

Corresponding author: Jun Huang (junhuang@cug.edu.cn)

Keypoints:

- We report a detailed 3-D geological analysis of the nature and history of pre-Nectarian aged Von Kármán crater in the lunar South Pole-Aitken basin
- The region contains farside mare basalts affected by linear features and ejecta material from a wide range of surrounding craters
- Our geological analysis provides a framework for the Chang'E-4 mission to carry out in situ exploration

Abstract

Von Kármán crater (diameter = ~186 km), lying in the northwestern South Pole-Aitken (SPA) basin, was formed in the pre-Nectarian. The Von Kármán crater floor was subsequently flooded with one or several generations of mare basalts during the Imbrian period. Numerous subsequent impact craters in the surrounding region delivered ejecta to the floor, together forming a rich sample of the SPA basin and farside geologic history. We studied in details the targeted landing region (45.0–46.0°S, 176.4–178.8°E) of the 2018 Chinese lunar mission Chang'E-4, within the Von Kármán

crater. The topography of the landing region is generally flat at a baseline of ~60 m. Secondary craters and ejecta materials have covered most of the mare unit and can be traced back to at least four source craters (Finsen, Von Kármán L, Von Kármán L', and Antoniadi) based on preferential spatial orientations and crosscutting relationships. Extensive sinuous ridges and troughs are identified spatially related to *Ba Jie* crater (diameter = ~4 km). Reflectance spectral variations due to difference in both composition and physical properties are observed among the ejecta from various-sized craters on the mare unit. The composition trends were used together with crater scaling relationships and estimates of regolith thickness to reconstruct the subsurface stratigraphy. The results reveal a complex geological history of the landing region and set the framework for the in situ measurements of the CE-4 mission, which will provide unique insights into the compositions of farside mare basalt, SPA compositional zone including SPA compositional anomaly and Mg-pyroxene annulus, regolith evolution, and the lunar space environment.

4.1.1. Introduction

The farside South Pole-Aitken (SPA) basin is the largest known impact structure on the Moon (Stuart-Alexander, 1978; Wilhelms et al., 1987). Its geology provides insights into the composition of the lower crust and upper mantle, the impact flux in early lunar history, the nature and evolution of basin-scale impact melt deposits, and the nature of large impact basins and their formation and modification processes (Garrick-Bethell & Zuber, 2009; Head et al., 1993; Moriarty & Pieters, 2018; Potter et al., 2012; Spudis et al., 1994; Vaughan & Head, 2014). The SPA basin has been studied with spectral observations (e.g., Ohtake et al., 2014; Pieters et al., 2001) and recently been subdivided into four distinct compositional zones based on Moon Mineralogy Mapper (M^3) data (Moriarty & Pieters, 2018): (1) a central ~700-km-wide SPA compositional anomaly (SPACA), which exhibits a strong Ca-pyroxene signature, which is different from typicalmare basalts; (2) a Mg-Pyroxene Annulus, which is characterized by Mg-rich pyroxenes; (3) a Heterogeneous Annulus, which exhibits mixing of localized pyroxene-rich units and feldspathic materials; and (4) the SPA Exterior, which is mafic-free and dominated by feldspathic materials. Pyroxene compositions in both the Heterogeneous Annulus and Mg-Pyroxene Annulus are similar. Moriarty and Pieters (2018) have indicated that the Mg-pyroxene unit is beneath the SPACA Ca-pyroxene unit from the stratigraphic relationships and central peak exposures among craters within SPACA. The material of Mg-Pyroxene Annulus was the main material excavated and melted by the SPA-forming event due to the relatively uniform composition and the great area, depth, and thickness of the Mg-Pyroxene Annulus. The extremely large size of the SPA basin strongly suggests that it has excavated subcrustal and mantle material (e.g., Melosh et al., 2017); however, the lack of evidence for widespread dunite or olivine-dominated mineral assemblages, and the dominance

of Mg-pyroxenes in the basin interior, suggests that lunar mantle must include a significant Mg-pyroxene component (Moriarty & Pieters, 2018).

Von Kármán crater (diameter D = 186 km; central coordinates as 44.4°S, 176.2°E; Fig. 4.1a) lies within the Mg-Pyroxene Annulus, just northwest of the SPACA terrain. This crater is a pre-Nectarian crater (Losiak et al., 2009; Yingst et al., 2017), younger than the Von KármánMbasin (D = 219 km; central coordinates as 49.4°S, 174.9°E), and older than the Leibnitz crater (diameter D = 236 km; central coordinates as 38.2°S 179.3°E: Fig. 4.1b and 4.1c; Yingst et al., 2017). Mare basalts flooded parts of the Von Kármán crater floor during the Imbrian Period (Pasckert et al., 2018; Wilhelms et al., 1979; Yingst & Head, 1997; Yingst et al., 2017), but a portion of the central peak remains exposed near the center of the crater (Fig. 4.1d). Finsen crater (diameter D = 73 km; central coordinates as 42.3°S, 182.3°E), Von Kármán L crater (diameter D = 29 km; central coordinates as 47.8°S 177.9°E), and a similar-sized unnamed crater nearby (we informally denote it as Von Kármán L' in this study) were formed subsequent to the Von Kármán crater (Wilhelms et al., 1979; Fig. 4.1c). Relatively higher albedo linear features on the mare basalt of Von Kármán crater converge toward the crater Finsen (Fig. 4.1b), which is located within the SPACA, suggesting that the SPACA material has been derived from Finsen crater.

In 2018, the Chinese lunar mission Chang'E-4 (CE-4; Wu et al., 2017) will explore the SPA basin. It will be the first in situ exploration of the farside of the Moon. The selected landing region for CE-4 (45°S–46°S, 176.4°E-178.8°E; Wu et al., 2017) is located on the southern floor of the Von Kármán crater. In situ exploration within the Von Kármán landing region will bring unprecedented imaging, spectral, radar, and low-frequency radio spectral data for the landing region, and it will greatly improve our understanding about the compositions of farside mare basalt, SPA compositional zones including SPA compositional anomaly and Mg-pyroxene annulus, regolith evolution, and the lunar space environment. Indeed, the U.S. National Research Council (2007) has identified key scientific priorities for future lunar exploration that can be addressed from the Von Kármán crater, including the possibility to study the existence and extent of differentiation of the SPA melt sheet (Morrison, 1998; Nakamura et al., 2009; Vaughan & Head, 2014) and possible exposed upper mantle materials (Melosh et al., 2017; Moriarty & Pieters, 2018). In this study, we have (1) investigated the geological characteristics of the landing region using available remote sensing data including topography, high-resolution imaging, and reflectance spectral data; (2) identified targets of high scientific interests; and (3) proposed testable hypothesis for the CE-4 mission.

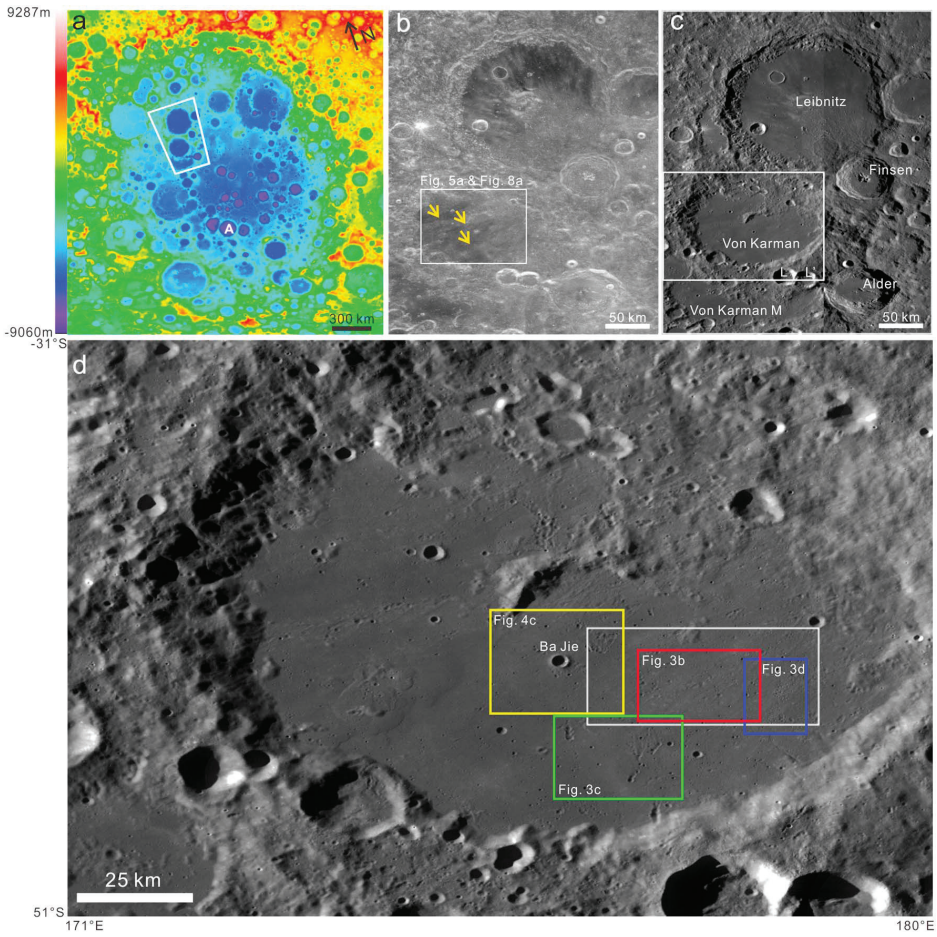

Figure 4.1: **a** Color-coded Lunar Orbiter Laser Altimeter (LOLA) digital elevation model of the South Pole-Aitken Basin (altitude scale on the left). The polygon shows the location of subsets b and c. Letter "A" indicates the location of the Antoniadi crater. **b** Global normalized reflectance (incidence = 30, emission = 0, phase = 30) of the 643 nm Lunar Reconnaissance Orbiter Camera (LROC) Wide-Angle Camera (WAC) mosaic of the Von Kármán area. The rectangle shows the location of Fig. 4.5a and 4.8a. The yellow arrows indicate the ray materials on the floor of Von Kármán crater, and they are converged to Finsen crater. **c** LROC WAC mosaic of the same area. The white box shows the location of subset **d**. **d** LRO WAC mosaic of Von Kármán crater. The white box shows the selected landing region, which shows the locations of Fig. 4.2a and 4.2b, red box in Fig. 4.3a, black boxes in Fig. 4.5c and 4.5d, 4.7, and 4.9a–4.9d. The red, green, blue and yellow rectangles show the locations of Fig. 4.3b–4.3d and 4.4c, respectively. We informally named the unnamed impact crater (diameter D = 3.6 km; central coordinates as 43.3°S 176.1°E) near the landing region as *Ba Jie*, which we use in italics to indicate its informal designation. North is toward the top in subsets **b**–**d**.

4.1.2. Methods

Data Sets

We analyzed the local geology using the Lunar Reconnaissance Orbiter Camera (LROC) Wide Angle Camera (WAC) mosaic (100 m/pixel) for regional context (Robinson et al., 2010), Kaguya Multiband Imager (MI) 750 nm reflectance mosaic (14 m/pixel) for albedo variations (Ohtake et al., 2008), Terrain Camera (TC) morning mosaic (7 m/pixel) for local context (Kato et al., 2010), and LROC Narrow Angle Camera (NAC) images (0.5–1.6 m/pixel) for small geological feature identification. Topographic analyses were performed using the merged digital elevation model (DEM) that is derived from the LRO Lunar Orbiter Laser Altimeter (LOLA; Smith et al., 2010) and Kaguya TC data (SLDEM: 59 m/pix; Barker et al., 2016). We produced a slope map for the landing region using SLDEM at a 59 m scale.

Regolith and Ejecta Thicknesses

We estimated the thickness of the regolith within the proposed landing area using NAC images that have incidence angles less than 55° following the method described in Quaide and Oberbeck (1968). Quaide and Oberbeck (1968) found that relatively fresh concentric craters with diameters less than 250 m could be used to estimate the thickness of the regolith with the equation: thickness = (k - DF/DA) * DA * tan (α)/2, where DA is the rim-to-rim diameter of a crater, DF is the diameter of the inner concentric ring, k is an empirically constant, and α is the angle of repose of materials on the surface of the Moon. The angle of repose of lunar regolith (α) is 31°, so the corresponding k is 0.86 and the corresponding slope of inner walls of fresh craters is 31° ± 2° (Quaide & Oberbeck, 1968). It is considered more robust to identify concentric craters using images with smaller incidence angle; otherwise, the flat bottomed craters and concentric craters could be misrecognized as normal craters and flat-bottomed craters, respectively (Fa et al., 2014). Thus, we conservatively chose these LROC NAC images with incidence angles less than 55°. Only relatively well-preserved craters with diameters less than 250 m were used to estimate the regolith thickness (Oberbeck & Quaide, 1967) due to the difficulties in diameter identification and measurements using degraded craters (Soderblom, 1970).

The thickness of ejecta deposits (i.e., the mixture of ejecta and excavated local material) that were transported from craters outside of the landing region are estimated using the empirical scaling laws estimated by Xie and Zhu (2016). Local geological context suggests that the Finsen, Von Kármán L, and Von Kármán L' craters have contributed most of the ejecta deposits within the proposed landing region (McGetchin et al., 1973; Oberbeck et al., 1975; Petro & Pieters, 2006; Sharpton, 2014). We have a detailed description of the model in section 4.4.

Absolute Model Ages

The absolute model age of the landing region is derived from crater statistics. Since obvious secondary craters (i.e., secondaries) that occur in chains and clusters have almost covered the entire landing region (see section 3.2), we employed two independent methods to estimate the model age. (1) The mare surface on the floor of Von Kármán was interpreted to be emplaced by one episode of basaltic volcanism based on the uniform reflectance spectral characteristics (Yingst & Head, 1999). Therefore, the model age for the mare surface is derived via craters that are substantially larger than the largest obvious secondaries (diameter D > ~2 km; see section 3.1) on the LROC WAC mosaic. (2) There are a few subareas, including two within the proposed landing region of CE-4, where craters larger than ~300–400 m are not heavily modified by obvious secondaries. The model ages for these subareas are derived by studying the size-frequency distributions of craters larger than 300–400 m in diameter using Kaguya TC mosaics. During analysis of the crater statistics, the CraterTools toolbox in ArcMap was employed to collect the craters by fitting circles based on three points on the crater rims. The crater chronology and production functions proposed by Neukum et al. (2001) were used to derive the model ages based on the Poisson Possibility analyses method advocated by Michael et al. (2016).

Compositional Aspects

In order to distinguish geological units of different composition, age, or texture, a RGB composite mosaic of MI data was built (R = 750 nm/415 nm, G = 950 nm/750 nm, B = 415 nm/750 nm (e.g., Huang et al., 2011; Weitz & Head, 1999). Observed variations in this RGB composite that mimic the Clementine false color ratio are commonly due to variations of the titanium and iron contents and the maturity of the surface materials (Pieters et al., 1993). We marked locations representative of different spectral units in the MI RGB composite. The mineralogy of these locations was derived from spectroscopic data from Chandrayaan-1 M^3 instrument (Pieters et al., 2009). M^3 is a visible to near-infrared hyperspectral imager, with 85 spectral channels spanning from 430 to 3,000 nm. The data used in this study are archived in the Planetary Data System (PDS, version 1 of Level 2), radiometrically corrected (Green et al., 2011), geometrically corrected (Boardman et al., 2011), thermally corrected (Clark et al., 2011), and photometrically corrected (Besse et al., 2013). The optical period used in this study is the OP2C2, with a resolution of 280 m/pixel. We selected this optical period because it covers the entire landing site region. The continuum of the spectra was removed with the algorithm developed by Martinot et al. (2018), and a suite of band parameters were calculated. The continuum is modeled as linear segments connected to the original M^3 spectrum in points called tie points, defined in fixed intervals. The algorithm maximized the 1 and 2 μm absorption band areas and automatically extracted the continuum. After continuum removal, a suite of spectral parameters is calculated (e.g., band center position, band area, and band depth) and exported as

maps.

4.1.3. Results

Surface Morphology and Terrain Characteristics

The selected landing region is located on the mare units within Von Kármán crater. The average elevation of this area is about -5926 m, with a standard deviation of 20.4 m. The elevation ranges over about 321 m. The highest geological feature in the region is the mound located near the north boundary (Fig. 4.2a). The proposed landing region is generally flat at a scale length of 59 m, as nearly 99% of the area has a slope less than 15°, and the slopes of about 94% of the area are less than 5° at a 59 m scale length (Fig. 4.2b). Local steep slopes (>15°) are mostly associated with craters larger than ~1 km diameter (Fig. 4.2b). The northeastern and southwestern portions of the landing area are lower in elevation compared with the northwestern and southeastern portions (Fig. 4.2a). NE-SW linear features with elevated topography are visible across the landing region (Fig. 4.2) and correspond to the ejecta deposits and secondary craters that originated from the Finsen crater (Fig. 4.1b).

Obvious secondary craters are widespread within the entire landing region (Fig. 4.3a). With irregular planar morphology, secondaries are recognized by their spatial occurrences in chains and/or clusters that exhibit herringbone-shaped morphology. Secondaries within a given chain and cluster have similar preservation states and their elevated crater rims all point in the same direction. Based on the preferential spatial orientation of secondaries within the landing region (Fig. 4.1d and 4.3), we have identified at least four sets of various-sized secondary craters that have different preservation states. The NE-SW trending secondary craters (Fig. 4.3a) are larger than 500min diameter, and they converge toward the Finsen crater (Fig. 4.1b and 4.3a). These secondaries are heavily degraded because their rims now occur as subparallel ridges (Fig. 4.3b) and the original shallow cavity has been gradually filled by mass wasting and subsequent ejecta deposition. The second set of secondaries generally trend north to south and are larger than 1 km in diameter. The secondaries overlap those formed by Finsen and have a better preservation state (Fig. 4.3c and S1). The steepened crater walls are located at the southern part of the secondaries, suggesting that the source crater is located to the south of Von Kármán. The minimum diameter of the parent crater should be at least 20 km considering that the maximum ratio between continuous secondaries and primaries is ~5% on terrestrial planets (Melosh, 1989) and that distant secondaries are much smaller than those on continuous secondaries facies (Xiao, 2016). Tracing southward along a great ellipse circle in ArcMap, we noticed that the Antoniadi crater (D = 138 km; central coordinates as 69.3°S, 186.9°E) is the most likely source crater that fulfills the above criteria (Figure S1). Judging by the same criteria, the freshest secondaries within the proposed landing region are the east-northeast and south-southwest trending secondaries that are located on top of the secondaries formed by Finsen and Antoniadi. These secondaries (e.g., Fig. 4.3d) are much smaller,

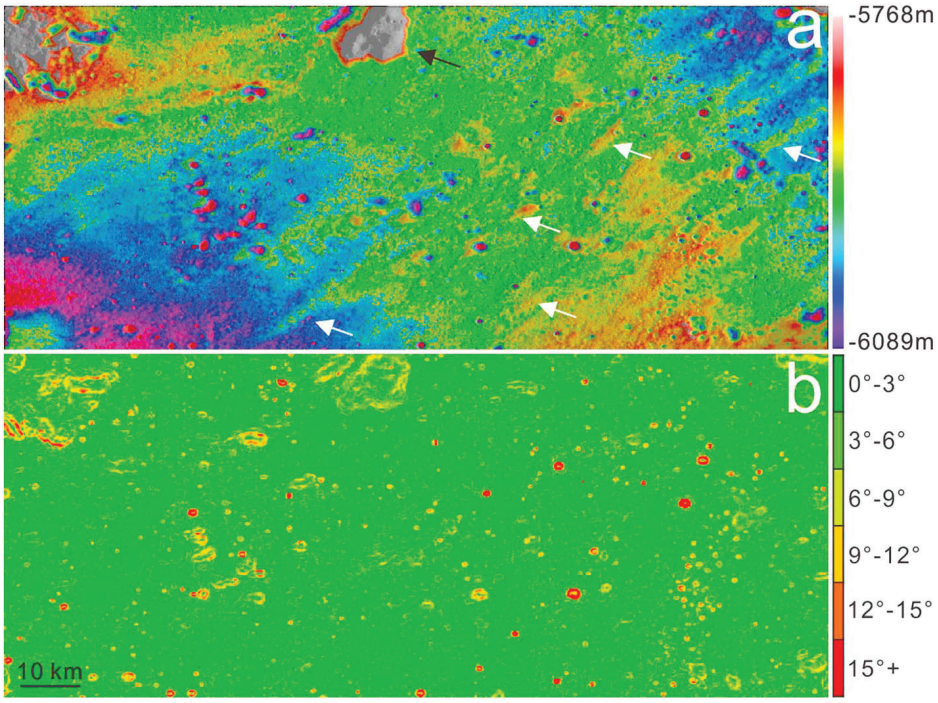

Figure 4.2: **a** Colorized SLDEM topography overlain in transparency over the TC morning mosaic of the landing region. The black arrow points to the mound with the highest altitude in this region. The white arrows indicate NE-SW linear features with elevated topography. **b** Slope map of the landing region calculated with a baseline of 59 m. The location of **a** and **b** is indicated in Fig. 4.1d.

and they are ~250–500 m in diameter (Fig. 4.3d). Tracing along the secondaries, we find that the Von Kármán L and Von Kármán L' craters to the south of the landing region are the possible source craters (Figure S2).

Notably, we have identified extensive sinuous ridges within the landing region, which are different from wrinkle ridges (e.g., Binder, 1982) and degraded secondary crater chains (e.g., Lucchitta, 1977) on the Moon. The ridges are asymmetric in shape and extend in a sinusoidal-like shape (Fig. 4.4a): the widths of the ridges are tens of meters. Sinuous troughs are formed between the ridges (Fig. 4.4b), and both the troughs and ridges are spatially associated with *Ba Jie* crater, which is to the west of the landing region (Fig. 4.4c).

Compositional Diversity

Variations in composition are identified in the reflectance spectra of the proposed landing area (Fig. 4.5). Spectrally, the entire region is dominated by pyroxene signatures (Fig. 4.5b, 4.5d, and 4.5e). Pyroxene reflectance spectra are characterized by the presence of diagnostic, broad absorption bands located around 1 and 2 μm, shifting toward longer wavelengths with increasing iron or calcium content (e.g., Klima et al., 2007). The 1 and 2 μm absorption band center positions, displayed on the parameter maps, show that the mare itself is rather homogenous (Fig. 4.5b). Minor variations of the 1 and 2 μm absorption band center positions of pyroxene spectra are observed within impact crater ejecta located on the mare floor, suggesting variations in chemistry with depth (Fig. 4.5b). On the MI color composite (Fig. 4.5d), relatively fresh small craters (diameter ~66 to 324 m; Fig. 4.6a) show blue-toned ejecta (e.g., site 1 in Fig. 4.5d) and higher albedo in the MI 750 nm reflectance data (Fig. 4.5c). Their reflectance spectra are consistent with that of Low-Calcium Pyroxene (LCP)-bearing material (Fig. 4.5e). The orange-toned ejecta (e.g., site 2 in Fig. 4.5d) are related to larger craters (diameter 252–950 m; Fig. 4.6b), with spectra consistent with Higher-Calcium Pyroxene (HCP)-bearing materials (Fig. 4.5e). The spectra of the ejecta of *Ba Jie* crater are similar to the spectra of the orange-toned ejecta (sites 4, 5, 6, and 7 in Fig. 4.5d). The ejecta on the rim of *Ba Jie* crater presents HCP signatures, but with larger spectral contrast (site 5 in Fig. 4.5d). The mare itself (site 3 in Fig. 4.5d) has a spectral signature consistent with these HCP-rich materials with weaker absorption bands.

Regolith Thickness

We analyzed relatively fresh concentric impact craters using LROC NAC images with incidence angle less than 55° to estimate the regolith thickness using the method of Quaide and Oberbeck (1968). These images have solar angles greater than 35°, which are larger than the repose angle of the regolith (31°). Therefore, we can clearly determine the morphology of the impact craters with these NAC images (Fa et al., 2014). The estimated thickness of the regolith in this area varies from ~2.5 to 7.5 m (Fig. 4.7). It appears that the regolith in the northeastern portion of the region is thicker

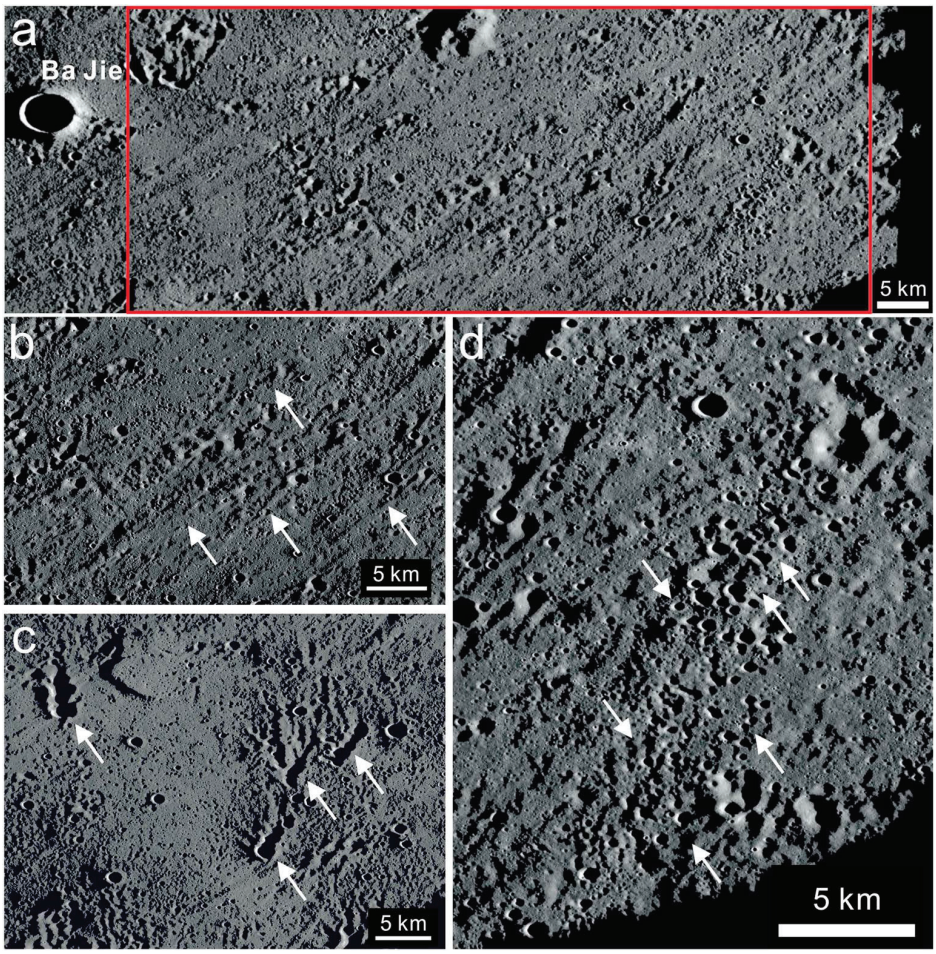

Figure 4.3: **a** TC morning mosaic shows secondary craters occurrence all over the landing region (indicated by the red box). The red box is the same location of the white box in Fig. 4.1d. **b** NE-SW trending linear features formed by Finsen, which are interpreted as highly degraded secondary craters with diameters >500 m. **c** N-S trending secondary craters (D > 1 km) overlapping the previous NE-SW trending linear features formed by Finsen. The source crater is most likely Antoniadi crater. **d** NE-SW relatively fresh secondary craters superposing the NE-SW trending linear features. The source craters are most likely the Von Kármán L and Von Kármán L' craters. North is up in all the panels. The locations of **b**–**d** are indicated in Fig. 4.1d.

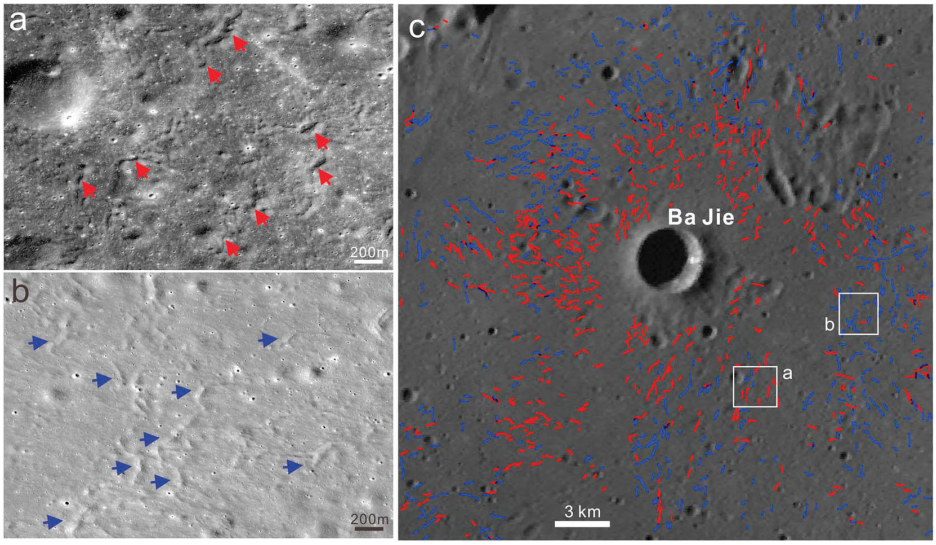

Figure 4.4: **a** LRO NAC image (M1100060445RE) of a region west of the landing region. The red arrows indicate the position of asymmetric sinuous ridges. **b** LRO NAC image (M1183658592RE) of an area in the western part of the landing region. The blue arrows indicate the position of sinuous troughs. **c** The spatial relationships between sinuous ridges and sinuous troughs observed in the vicinity *Ba Jie* crater. The red lines indicate sinuous ridges, and the blue lines indicate sinuous troughs. North is toward the top in all the panels.

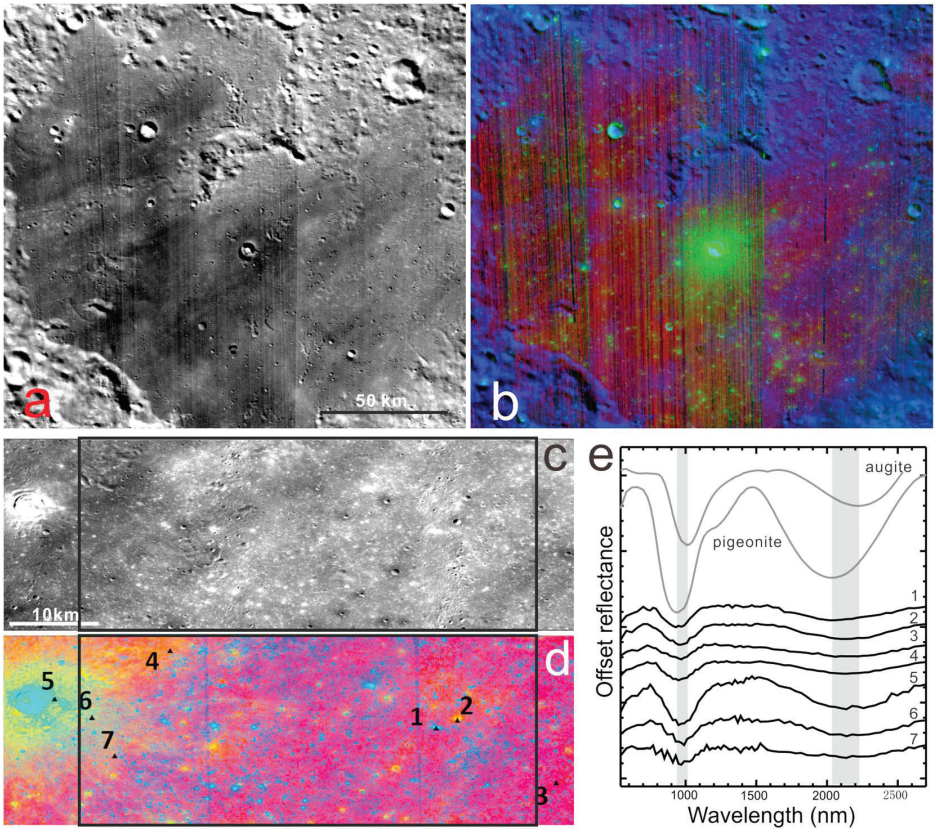

Figure 4.5: **a**. M^3 750 nm reflectance mosaic of Von Kármán crater (stretch: 0.044-0.082). High albedo linear features oriented WSW-ENE are visible on the crater floor. The landing area is indicated as a white rectangle. **b**. M^3 color composite of Von Kármán crater. R = 2 micron band center (2000-2500); G = 2 micron band depth (0.04-0.17); B = reflectance at 1580 nm (0.085-0.15). Stretch values are indicated in brackets. LCP-bearing material appears in light blue, and HCP-bearing material is displayed in green. Spectral parameters were calculated using the method described in Martinot et al. (2018). **c**. MI 750 nm reflectance mosaic of the landing area outlined as a rectangle. High albedo features are mostly associated with ejecta deposits of small fresh craters, and impact rays from the Finsen crater, whereas low albedo features are mostly associated with mare basalts and ejecta deposits of large craters. The landing area is indicated as a white rectangle. **d**. RGB composite of MI data. R: 750 nm/415 nm (1.797-1.925), G: 950 nm/750 nm (0.877-1.034), B: 415 nm/750 nm (0.515-0.564). The blue-toned ejecta are associated with smaller craters of higher albedo. The orange-toned ejecta are associated with larger craters of lower albedo. **e**. Continuum-removed M^3 spectra of locations (1 to 7) in **b**. Each spectrum corresponds to a single pixel. Spectra were processed with the method described in Martinot et al. (2018). A pigeonite (LCP) and an augite (HCP) spectrum from the RELAB database are displayed above the observed spectra (respective RELAB-ID: DL-CMP-008 and AG-TJM-010). Shaded areas represent the diversity of values of the 1 and 2 micron bands.

than that of the southwestern portion, which is consistent with a larger contribution of ejecta deposits (Fig. 4.10), as well as a strong gardening effect of secondary crater chains (Fig. 4.2a) formed as a result of the Finsen crater-forming event.

Stratigraphic Ages of the Landing Area

Obvious secondary crater chains have dominated the entire mare unit on the floor of Von Kármán (Fig. 4.3a). Most of the secondaries are less than 2 km in diameter (section 3.2). Therefore, we studied the size-frequency distribution of craters larger than 2 km in diameter to estimate the model age of the mare unit. The absolute model age derived by probability analyses (Michael et al., 2016) is 3.6 (+0.09, -0.2) Ga, which falls in the Imbrian period. This result is consistent with the recent geological mapping (Yingst et al., 2017), and crater statistics (Haruyama et al., 2009). We also selected three sub-regions on the mare units that have been less affected by large secondary craters in order to verify the model age. Fig. 4.8a shows the locations of the counting areas. The surface morphology of the sub-regions shows that craters larger than ~300–400 m are not obvious secondary craters (e.g., Fig. 4.8c, 4.8e, and 4.8g), and model ages derived from the crater counts are identical with those estimated from craters larger than 2 km in diameter.

4.1.4. Discussion

Context of CE-4 Mission

CE-4 is scheduled to launch in 2018 and will be the first lunar farside in situ exploration mission. The CE-4 mission will be carried out in two phases. First, a relay satellite with two microsatellites will be launched by a CZ-4C rocket from Xichang, China. The relay satellite will be sent to the Earth-Moon Lagrange Point 2. A Dutch-made low-frequency radio spectrometer (0.1–80 MHz) is carried by the relay satellite to perform space physics measurements. In addition, the relay satellite will carry several laser reflectors for assisting orbital determination. This mission will also include two microsatellites that will orbit the Moon, and they will be equipped with very-long-baseline interferometry instruments to conduct radio science experiments. One of the microsatellites will have a visible wavelength microcamera contributed from Saudi Arabia. Six months after the launch, the second part of the CE-4 mission, which is composed of a lander and a rover, will be launched by a CZ-3B rocket launched from Xichang, China. Since both the lander and the rover were designed as a backup for the Chang'E-3 (CE-3) mission, some of the science payloads on CE-4 are similar to those on CE-3 (Jia et al., 2018), which include a landing camera, a terrain camera, a panorama camera on the lander and a visible/near infrared imaging spectrometer (He et al., 2014), and two ground penetrating radars (Fang et al., 2014) on the rover. Additional instruments on the lander (Jia et al., 2018) include (1) a low-frequency radio spectrometer (0.1–40 MHz) to perform joint space physics observations with the low-frequency radio spectrometer on the relay satellite, (2) a German lunar neutron

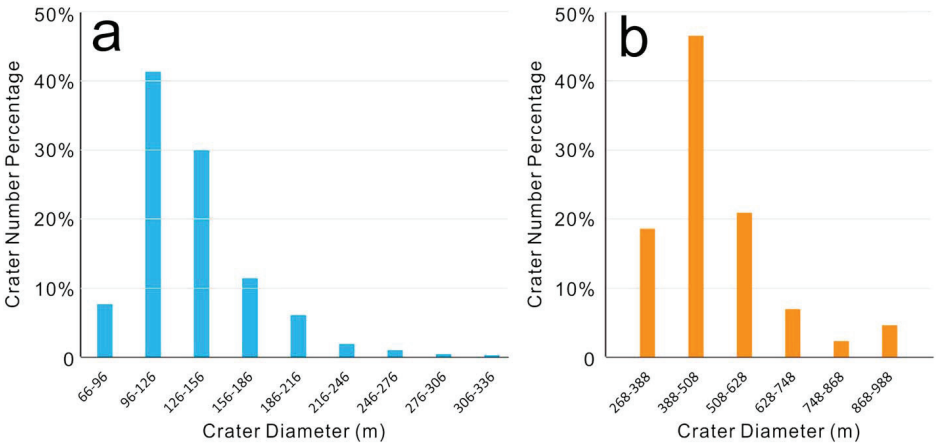

Figure 4.6: Diameter distribution of craters with **a** low-Ca pyroxene bearing ejecta (blue) and **b** high-Ca pyroxene bearing ejecta (orange) within the landing region (see Fig. 4.5d).

and radiation dose detector to explore the farside surface radioactive environment, and (3) a lunar micro-ecosystem for astrobiology experiments and public outreach. A new instrument on the rover (Jia et al., 2018) is the Swedish neutral atom detector designed to study the interaction between the solar wind and lunar surface materials. However, the CE-4 will not be equipped with the alpha particle X-ray spectrometer that was previously used by CE-3 to detect elemental abundances within surface material (Jia et al., 2018; Wu et al., 2017). Still the lander and rover together should be able to perform imaging, spectral, radar, and low-frequency radio spectral measurements.

Geological Features

Several features of interest have been identified within the landing region, including farside mare basalts, sinuous linear features, and ejecta rays. Non-nearside mare basalts will be investigated in situ for the first time at Von Kármán and may bring new clues about the farside and SPA volcanism. Spectral data show HCP signatures associated with the mare unit, which is consistent with most lunar mare (e.g., Staid et al., 2011). However, in contrast to the CE-3 landing site, olivine has not yet been detected at Von Kármán (Ling et al., 2015; Zhang et al., 2015), which suggests that the farside mare might be of slightly different composition. The mare unit is homogeneous and likely to represent a single eruptive episode during the lunar peak volcanic period that occurred in the Late Imbrian (3.80–3.20 Ga; e.g., Yingst & Head, 1999). A single eruptive episode was one in which the mechanism of emplacement did not significantly vary over the period of activity, meaning that the rock unit left in place should share generally similar morphological and compositional characteristics, making it a viable geologic unit.

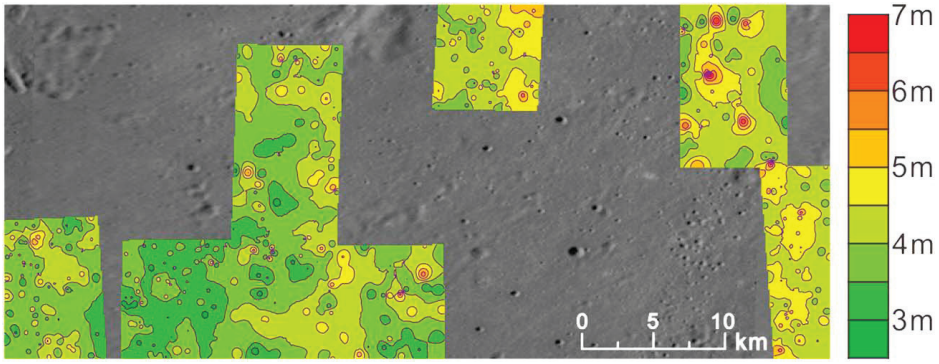

Figure 4.7: Estimated thickness contour of regolith in the landing region based on available LROC NAC images with incidence angle inferior to 55°. The background image is WAC mosaic, and the location is indicated in Fig. 4.1d. The IDs of NAC images used are M143453659RE, M143453659LE, M143460468RE, M143460468LE, M156434145RE, M156434145LE, M189435642RE, M189435642LE, M1133052548RE, M1133052548LE, M1145979809RE, M1145979809LE, and M1163658519LE.

Sinuous linear features, ridges and troughs, have been identified in the vicinity of *Ba Jie* crater. They are distinct from lunar wrinkle ridges, but their origin remains controversial. For example, Oberbeck (1975) proposed these to be ejecta deposits typical of small craters in which the ejecta is emplaced at relatively low velocity, and Atwood-Stone et al. (2016) suggested that these structures are likely the results of Kelvin-Helmholtz instabilities within the ejecta flows. The key information to understand their formation mechanism is the subsurface structure of these features, that is, the depth and structural disturbance of the ejecta deposits of the *Ba Jie* crater, and whether or not fractures deeper than *Ba Jie*'s ejecta exist. The ground penetrating radars onboard CE-4 could reveal the subsurface structure of these linear features and provide clues to their possible formation mechanism.

The secondary craters produced by the Finsen crater-forming event, and associated with relatively high albedo linear features, are heavily degraded but also of interest (Fig. 4.1b and 4.3). Hawke et al. (2004) proposed four different mechanisms to explain the formation of impact rays: (1) immature primary ejecta emplacement, (2) secondary craters immature local material deposition, (3) the action of debris surges downrange of secondary clusters, and (4) immature interior. Reflectance spectra for the landing region show that the rays formed by Finsen appear to have distinct composition compared with the buried mare basalts (Fig. 4.5b), indicating that the rays are composed of primary ejecta deposits. With the aid of the CE-4 cameras and radar system, the thickness and spatial distribution of impact ejecta from the Finsen crater could be more well constrained. This would be the first in situ constraint for the subsurface structure of compositional rays, which will serve as an observational basis for

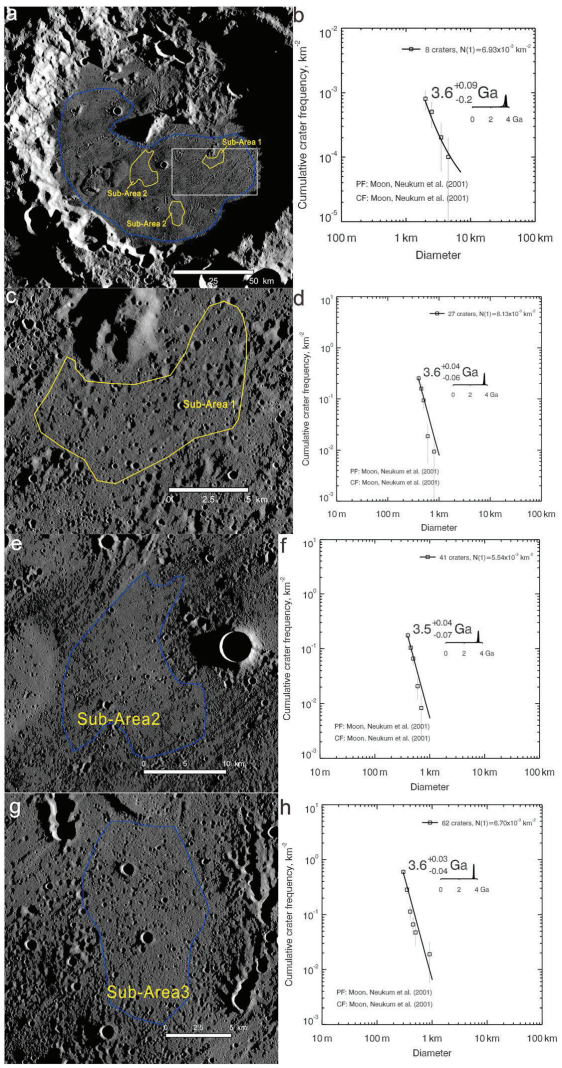

Figure 4.8: Absolute model ages derived from crater statistics for the mare unit located within the floor of Von Kármán crater. **a** Counting areas on the crater floor based on Kaguya TC mosaic. The mare units on the crater floor were classified as a single geological unit based on recent geological mapping (Yingst et al., 2017). The blue area shows the counting area where only craters larger than 2 km in diameter are used in deriving the model age. The locations of the three subareas are shown in yellow polygons. These regions were selected as they are less affected by obvious secondaries in comparison to the rest of the crater floor. **b** Model age for the mare unit derived from probability analysis (Michael et al., 2016). **c** Detailed surface morphology of the subarea 1 shown in Kaguya TC mosaic. This area is located within the selected landing area, where the population of obvious secondary craters is smaller. Degraded secondary craters within this subarea are less than 400 m in diameter. **d** Model age for the subarea 1 on the mare surface derived from probability analysis (Michael et al., 2016). **e** Context of subarea 2 shown by Kaguya TC mosaic and the location of the counting area (blue polygon). **f** Model ages derived for the crater population in subarea 2. **g** Context of subarea 3 shown by Kaguya TC mosaic and the counting area (blue polygon). **h** Model ages derived for the crater population in subarea 3. North is to the top in **a**, **c**, **e**, and **g**.

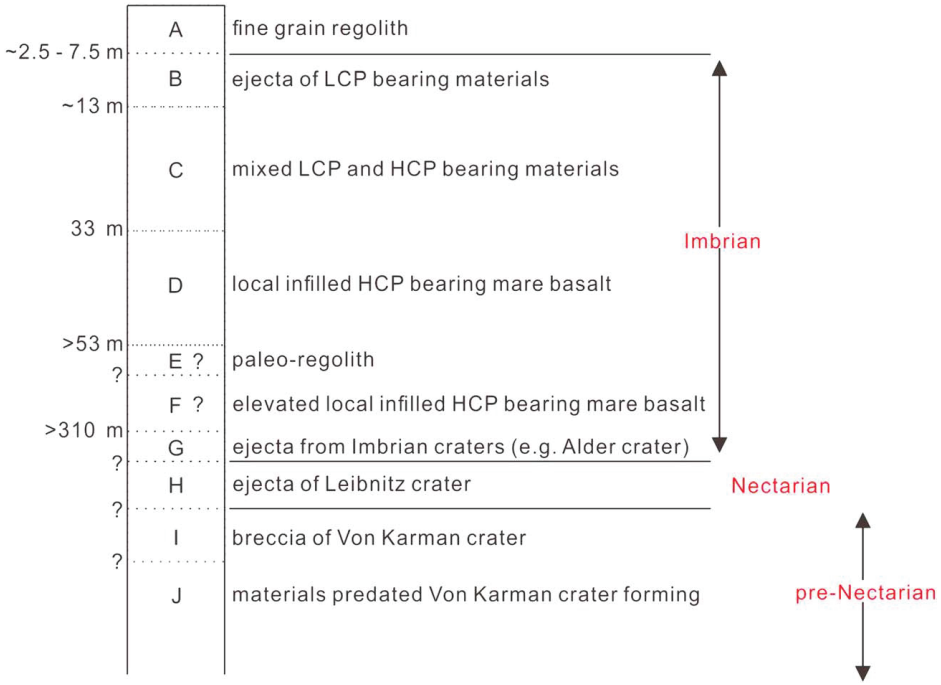

Figure 4.9: Proposed stratigraphy of the landing region. The thickness of the layers is not to scale.

understanding the efficiency of material transport by impact cratering on the Moon.

Stratigraphy of the Landing Region

Impact craters are probes of local stratigraphy (Melosh, 1989). Variations of reflectance spectra of crater ejecta deposits indicate vertical variations in composition/mineralogy in the landing area (section 3.3). We used the geometric relationship between the diameter of impact craters and the depth from which the ejecta was excavated to reconstruct the regional stratigraphy (Fig. 4.9). The maximum depth of excavation is approximately 1/10 of the transient crater diameter, which equals to 0.84 times final crater rim-to-rim diameter for simple craters (Melosh, 1989). Therefore, we used this relationship for the diameter measured on the image to calculate the excavation depth of each of the simple craters located upon the mare unit. Note that most of the small craters less than 2 km in diameter are probably secondary craters; thus, they have smaller excavation depths than similar-sized primary craters (McEwen & Bierhaus, 2006; Oberbeck, 1975), indicating that the calculated excavation depths are the upper bound for the actual values.

The regolith constitutes the uppermost layer of the reconstructed stratigraphic col-

umn (A in Fig. 4.9), with a thickness of ~2.5 to 7.5 m (the regolith in the northeastern part is thicker than in the southwestern part in the landing region; Fig. 4.7). The main uncertainties in the regolith thickness estimates come from LROC NAC images with the necessary illumination geometry (incidence angle less than 55°), the determination of rim-to-rim diameter of craters, and the limitations of the estimation method (Quaide & Oberbeck, 1968).

Beneath the regolith is the Finsen LCP-bearing ejecta layer (B in Fig. 4.9; which might be discontinuous or variable in thickness). Represented in blue tones in the MI color composite (Fig. 4.5d), this layer is excavated by craters ~66 to 336 m in diameter (Fig. 4.6a). The majority of these craters is 96 to 156 m in diameter (Fig. 4.6a), suggesting that the LCP-bearing material is at least ~8 to 13 m deep.

The HCP-bearing layer (D + E + F in Fig. 4.9) is exposed in the orange-toned ejecta in the MI color composite (Fig. 4.5d) of larger craters with diameters ranging from 268 to 988 m (Fig. 4.6b) as well as *Ba Jie* crater. The majority of orange toned ejecta craters fall in the 388 to 628 m range in diameter (Fig. 4.6b), indicating that the HCP-bearing materials (D) are at least ~33 to 53 m deep. *Ba Jie* crater is ~3.7 km in diameter, suggesting that local minimal depth of the HCP-bearing materials (and hence mare unit) is greater than 310 m. The spectrum extracted from the site 5 of *Ba Jie* crater's ejecta has a deeper absorption band than the spectra of sites 6 and 7 (Fig. 4.5e). This absorption band depth difference could indicate that the material of site 5 is slightly distinct compared to material of sites 6 and 7, possibly more enriched in HCP or with a different grain size or texture (or less mature). Alternatively, the ejecta could be thicker at site 5 and less mixed with the underlying likely space-weathered layer, resulting in a more intense signature. Spectral variations within the ejecta of *Ba Jie* crater (Fig. 4.5d and 4.5e) could hint at a subtle vertical compositional difference in the layer of HCP-bearing materials. The material located at site 5 (layer F) are from deeper portions of the preimpact stratigraphy than the material located at sites 6 and 7, due to the fact that the deeper seated material tends to be ejected closer to the crater rim (Stöffler et al., 1975). Therefore, there is probably a layer of enriched HCP-bearing material (F) under the HCP-bearing-material layer, and could imply a possible paleo-regolith layer (E) between layers D and F if there were at least two episodes of basalt emplacement. The paleo-regolith thickness (if such a layer exists) could be studied with the radar instrument onboard the CE-4 rover, similarly to the detections made at the CE-3 landing site (Xiao et al., 2015). It appears reasonable to speculate that there could be somewhere in the stratigraphy a layer of mixed LCP and HCP-bearing material (C) due to collision of these two types of materials. However, we are not able to constrain the thickness of this mixed layer. The main uncertainties of the reconstructed stratigraphy come from ejecta of unidentified impact craters, mixing of ejecta of local materials, and products of uncertain geological events between stratigraphic layers.

We propose a stratigraphic column with several layers beneath the HCP-bearing-material layer/mare unit based on the regional setting and previous geological maps

(Wilhelms et al., 1979; Yingst et al., 2017). However, the thickness of these layers cannot be constrained using available data and previous mapping results. We expect a layer G made of ejected material from Imbrian-aged craters (e.g., Alder) resurfacing HCP-bearing basalts. Layer B to G were formed during the Imbrian epoch. Ejecta of Leibnitz crater (H) occurred as the layer beneath, and this impact event occurred in Nectarian. Then there should be a layer (I) of breccia from Von Kármán crater forming event lying above the target materials (J) of Von Kármán crater. Layer I and J are of pre-Nectarian age (Fig. 4.9), likely to be part of the SPA basin Mg-Pyroxene Annulus (Moriarty & Pieters, 2018).

The two ground penetrating radars onboard the CE-4 rover will be able to reveal the subsurface structure of the landing area and test the stratigraphy predicted in this study. In a manner similar to the CE-3 Yutu rover, the radar system of the CE-4 rover has two frequency channels with different penetrating depths and vertical resolutions: Channel 1 has a frequency of 40.80 MHz, whereas Channel 2 has a frequency of 250.750 MHz (Jia et al., 2018). The radar system on the CE-3 mission demonstrated that the Channel 2 radar could detect details of the subsurface structures up to a depth of ~12 m, and the Channel 1 radar could reveal subsurface structures up to ~400 m (Xiao et al., 2015). Therefore, the ground penetrating radars Channel 1 can detect layers A, B, C, D, E, and F, and it could detect layer G, H, I, and J depending on their thickness. Channel 2 could detect detailed structures within layers A and B, and the upper portion of the layer C.

The Origin of the LCP Bearing Materials

The LCP-bearing materials have relatively higher albedo compared to the relatively lower albedo mare basalts in the landing region. Regional geological context suggests that the LCP-bearing materials are part of the ejecta of the Finsen crater forming event (section 3.1). Besides Finsen crater, we have surveyed the nearby regions for younger craters that might have contributed ejecta over the landing region. Von Kármán L and Von Kármán L' adjacent to the landing region are the two large craters that are younger than the mare units, and they have inevitably launched ejecta into the landing region. We estimate the thickness of ejecta deposits formed by the impact of ejecta from Finsen, Von Kármán L, and Von Kármán L' craters. First, we estimate the ejecta thickness distribution. Then, the thickness of local material excavated by the impact of ejecta is derived from empirical equation. Finally, the ejecta deposit thickness is the sum of ejecta from other craters and local material. Assuming a power law distribution of ejecta with slope of -3 (McGetchin et al., 1973) and using the scaling relationship between ejecta thickness at final crater rim crest and final crater radius given by Sharpton (2014), we estimate the ejecta thickness distribution by using this relationship $T = 3.95R^{0.399}(r/R)^{-3}$, where r is the distance from crater center in meters and R is the final crater radius (all in meters). Therefore, the amount of ejecta contributed from Finsen (Fig. 4.10a; diameter D = 73 km) is the largest among the three craters, followed

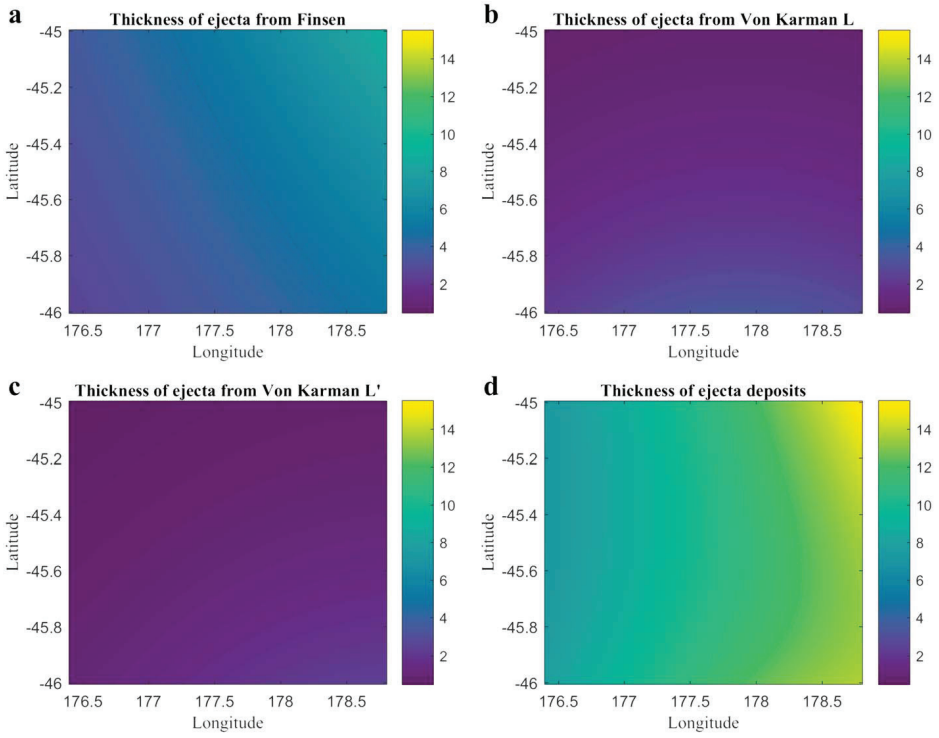

Figure 4.10: The thickness of ejecta from **a** Finsen crater, **b** Von Kármán L crater, and **c** Von Kármán L' crater. **d** Thickness of all ejecta deposits consisting of excavated local material and accumulated ejecta from Finsen, Von Kármán L, and Von Kármán L'. The locations of **a**–**d** are labeled in Fig. 4.1d.

by Von Kármán L (Fig. 4.10b; diameter D = 29 km) and Von Kármán L' (Fig. 4.10c; diameter D = 29 km). Assuming the incident angle of ejecta was 75°, Oberbeck et al. (1975) established an empirical model that can estimate the excavation efficiency (μ) of crater ejecta for given thickness of ejecta and the distance from crater center based on the analysis of Copernicus secondary craters (i.e., $\mu = 4.5 \times 10^{-5} r^{0.87}$, all in meters). However, recent works (e.g., Petro & Pieters, 2006; Xie & Zhu, 2016) suggested that the authors may have overestimated the excavation efficiency. Here we adopt half of excavation efficiency of Oberbeck et al. (1975) (i.e., $\mu = 2.25 \times 10^{-5} r^{0.87}$) according to the result of Petro and Pieters (2006). The thickness of local material excavated by the ejecta from either Von Kármán L or Von Kármán L' is predicted to be smaller than 1 m, whereas the thickness of Finsen ejecta is larger than 2.5 m (Fig. 4.10a). In addition, Finsen crater is older than both Von Kármán L and Von Kármán L' (Wilhelms et al., 1979; Yingst et al., 2017). Therefore, the ejecta from Von Kármán L or Von Kármán L' is expected to rework the ejecta deposits formed by Finsen crater ejecta. The thickness of ejecta deposits including the excavated local material and the total accumulated ejecta is predicted to vary from about 7.2 to 15.5 m (Fig. 4.10d), which is consistent with the depth of LCP bearing materials discussed previously. This is independent evidence that the LCP-bearing materials were likely from Finsen crater, Von Kármán L, and Von Kármán L'.

LCP-bearing materials are pervasive across the SPA basin, including the central peak of Finsen crater (Moriarty et al., 2013; Moriarty & Pieters, 2018; Pieters et al., 2001). However, the origin of the LCP bearing materials is still under debate. The LCP-bearing material could correspond to exposed KREEP-related Mg-suite rocks (Pieters et al., 1997; Klima et al., 2011) or the differentiated upper layer of the hypothesized SPA melt sheet (Nakamura et al., 2009; Uemoto et al., 2017). Alternatively, the LCP-bearing materials could come from a LCP-dominated lunar upper mantle (Melosh et al., 2017; Moriarty & Pieters, 2018).

The hypotheses can be evaluated using geological context, but it is challenging to use orbital remote sensing data to pin down the origin of the LCP bearing materials due to lack of detailed geochemical data. The definitive way to establish the origin of the LCP-bearing materials is by sample return (e.g., Jolliff et al., 2010), and the current payloads onboard the CE-4 mission are not designed to reveal element distribution for surface materials. However, we point out that the penetrating radar onboard the CE-4 rover can test and help verify the stratigraphy of the landing area, which might be used to indirectly infer the composition (e.g., by backward modeling for the dielectric constant) and provide additional clues about the origin of the LCP-bearing materials. These LCP-bearing materials could help to better constrain the history of the SPA region (Moriarty & Pieters, 2018) and might represent high priority targets for future sample return missions, for example, Chang'E-6.

4.1.5. Conclusions

The Chinese CE-4 lunar mission will be the first in situ exploration to explore the surface of the Moon and study its environment on the farside. The selected landing area is located in the southern portion of the Von Kármán crater, on the top of the infilling mare unit, and within the SPA basin (Fig. 4.1). We characterized the terrain and geological characteristics of the landing region using multisource remote sensing data sets. The main conclusions are as follows:

1 The landing region (45°S–46°S, 176.4°E–178.8°E) is generally flat at a length scale of 59 m and located within a rather homogenous mare unit.

2 The absolute model age of the mare unit within Von Kármán crater is 3.6 Ga (+0.09, -0.2), based on multiple crater size-frequency distribution measurements.

3 Secondary craters have almost covered the entire landing area. The oldest secondary craters (NE-SW direction) look degraded and converge to Finsen crater. N-S direction secondary craters are superposing on them, and they are converging to Antoniadi crater. The youngest secondary craters are NE-SW, and they are likely from Von Kármán L and Von Kármán L'.

4 The thickness of the regolith is estimated to be ~2.5 to 7.5 m in the landing area.

5 Extensive sinuous ridges and sinuous troughs are identified in the landing area. They are related to *Ba Jie* crater spatially, but the origin is controversial. The ground penetrating radar onboard CE-4 rover will reveal the subsurface structure and provide clues to the origin of these linear features.

6 Spectral variations among the ejecta of craters of various sizes reveal the subsurface structures. Along with the estimated thickness of the regolith, crater size-frequency distribution absolute model age, and previously geological mapping results, we proposed a stratigraphic profile of the landing area that can be tested with CE-4 ground penetrating radar data.

7 LCP-bearing material, probably excavated from the nearby Finsen crater from a depth <7 km, are widespread in the landing region and could bring more clues about SPA history.

8 The detailed stratigraphy and the diversity of farside geologic units sampled by impact craters in the region (in both the vertical and lateral sense) and delivered to the landing and traverse area to form secondary craters ensure that the Von Kármán landing site will be an excellent candidate for the first sample return mission to the lunar farside by Chang'E-6. Soils in the Von Kármán regolith are very likely to contain samples of farside lunar maria, a diversity of farside highland rock types, and samples of the SPA basin Mg-Rich Annulus (impact melt

and possible mantle of the SPA basin). The Change'E-4 mission and surface traverses will provide the surface and three-dimensional stratigraphic information necessary to help refine the lateral and vertical stratigraphy to ensure optimal sample return.

Acknowledgements

Reviews by Daniel Moriarty, Aileen Yingst, and an anonymous reviewer were incredibly helpful to help clarify the paper, and much appreciated. We thank the Editor Steven A. Hauck II for comments and editorial help. LRO NAC and WAC data, Chandrayaan-1 M^3 data, were downloaded from the PDS (https://pds.nasa.gov/). MI and TC data were downloaded from the SELENE archive (`http://darts.isas.jaxa.jp/planet/pdap/selene/`). The data of regolith estimation, subsurface reconstruction and crater count are available in the supporting information. J. H. was supported by National Natural Science Foundation of China (41773061), the Fundamental Research Funds for the Central Universities, MOST Special Fund from the State Key Laboratory of Geological Processes and Mineral Resources China University of Geosciences (Wuhan) (CUGL160402, CUG2017G02, and MSFGPMR05). Z. X. was supported by National Natural Science Foundation of China (41773063). The work of J. F. is supported by the CNES (Luna/ExoMars APR). The work of M. M. was supported by a Netherlands Organization for Scientific Research (NWO) grant. The authors also thank Qiong Wang for the discussion of the landing region.

Bibliography

– Atwood-Stone, C., Bray, V. J., & McEwen, A. S. (2016). A new study of crater concentric ridges on the Moon. Icarus, 273, 196–204. `https://doi.org/10.1016/j.icarus.2016.03.012`

– Barker, M., Mazarico, E., Neumann, G., Zuber, M., Haruyama, J., & Smith, D. (2016). A new lunar digital elevation model from the Lunar Orbiter Laser Altimeter and SELENE Terrain Camera. Icarus, 273, 346–355. `https://doi.org/10.1016/j.icarus.2015.07.039`

– Besse, S., Sunshine, J., Staid, M., Boardman, J., Pieters, C., Guasqui, P., et al. (2013). A visible and near-infrared photometric correction for Moon Mineralogy Mapper (M^3). Icarus, 222(1), 229–242. `https://doi.org/10.1016/j.icarus.2012.10.036`

– Binder, A. B. (1982). Post-Imbrian global lunar tectonism: Evidence for an initially totally molten Moon. The Moon and the Planets, 26(2), 117–133. `https://doi.org/10.1007/BF00929277`

– Boardman, J. W., Pieters, C., Green, R., Lundeen, S., Varanasi, P., Nettles, J., et al. (2011). Measuring moonlight: An overview of the spatial properties, lunar coverage, selenolocation, and related Level 1B products of the Moon Mineralogy Mapper. Journal of Geophysical Research, 116, E00G14. `https://doi.org/10.1029/2010JE003730`

– Clark, R. N., Pieters, C. M., Green, R. O., Boardman, J., & Petro, N. E. (2011). Thermal removal from near-infrared imaging spectroscopy data of the Moon. Journal of Geophysical Research, 116, E00G16. `https://doi.org/10.1029/2010JE003751`

– Fa, W., Liu, T., Zhu, M. H., & Haruyama, J. (2014). Regolith thickness over Sinus Iridum: Results from morphology and size-frequency distribution of small impact craters. Journal of Geophysical

Research: Planets, 119, 1914. https://doi.org/10.1002/2013JE004604\T1\textendash1935

– Fang, G.-Y., Zhou, B., Ji, Y.-C., Zhang, Q.-Y., Shen, S.-X., Li, Y.-X., et al. (2014). Lunar penetrating radar onboard the Chang'e-3 mission. Research in Astronomy and Astrophysics, 14(12), 1607–1622. https://doi.org/10.1088/1674-4527/14/12/009

– Garrick-Bethell, I., & Zuber, M. T. (2009). Elliptical structure of the lunar South Pole-Aitken basin. Icarus, 204(2), 399–408. https://doi.org/10.1016/j.icarus.2009.05.032

– Green, R., Pieters, C., Mouroulis, P., Eastwood, M., Boardman, J., Glavich, T., et al. (2011). The Moon Mineralogy Mapper (M3) imaging spectrometer for lunar science: Instrument description, calibration, on-orbit measurements, science data calibration and on-orbit validation. Journal of Geophysical Research, 116, E00G19. https://doi.org/10.1029/2011JE003797

– Haruyama, J., Ohtake, M., Matsunaga, T., Morota, T., Honda, C., Yokota, Y., et al. (2009). Long-lived volcanism on the lunar farside revealed by SELENE Terrain Camera. Science, 323(5916), 905–908. https://doi.org/10.1126/science.1163382

– Hawke, B. R., Blewett, D. T., Lucey, P. G., Smith, G. A., Bell, J. F., Campbell, B. A., & Robinson, M. S. (2004). The origin of lunar crater rays. Icarus, 170(1), 1–16. https://doi.org/10.1016/j.icarus.2004.02.013

– He, Z.-P., Wang, B.-Y., Lü, G., Li, C.-L., Yuan, L.-Y., Xu, R., et al. (2014). Operating principles and detection characteristics of the Visible and Near-Infrared Imaging Spectrometer in the Chang'e-3. Research in Astronomy and Astrophysics, 14(12), 1567–1577. https://doi.org/10.1088/1674-4527/14/12/006

– Head, J. W., Murchie, S., Mustard, J. F., Pieters, C. M., Neukum, G., McEwen, A., et al. (1993). Lunar impact basins: New data for the western limb and far side (Orientale and South Pole-Aitken basins) from the first Galileo flyby. Journal of Geophysical Research, 98(E9), 17,149–17,181. https://doi.org/10.1029/93JE01278

– Huang, J., Xiao, L., He, X., Qiao, L., Zhao, J., & Li, H. (2011). Geological characteristics and model ages of Marius Hills on the Moon. Journal of Earth Science, 22(5), 601–609. https://doi.org/10.1007/s12583-011-0211-8

– Jia, Y. Z., Zou, Y. L., Xue, C. B., Ping, J. S., Yan, J., & Ning, Y. M. (2018). Scientific objectives and payloads of Chang'E-4 Missionormalsize [in Chinese]. Chinese Journal of Space Science, 38(1), 118–130.

– Jolliff, B. L., Shearer, C. K., Papanastassiou, D. A., Alkalai, L., & Team, M. (2010). MOONRISE: South Pole-Aitken Basin sample return mission for solar system science. In Annual Meeting of the Lunar Exploration Analysis Group (Vol. 1595, p. 31).

– Kato, M., Sasaki, S., & Takizawa, Y. (2010). The Kaguya mission overview. Space Science Reviews, 154(1–4), 3–19. https://doi.org/10.1007/s11214-010-9678-3

– Klima, R. L., Pieters, C. M., Boardman, J. W., Green, R. O., Head, J. W., Isaacson, P. J., et al. (2011). New insights into lunar petrology: Distribution and composition of prominent low-Ca pyroxene exposures as observed by the Moon Mineralogy Mapper (M^3). Journal of Geophysical Research, 116, E00G06. https://doi.org/10.1029/2010JE003719

– Klima, R. L., Pieters, C. M., & Dyar, M. D. (2007). Spectroscopy of synthetic Mg-Fe pyroxenes I: Spin-allowed and spin-forbidden crystal field bands in the visible and near-infrared. Meteoritics & Planetary Science, 42(2), 235–253.

– Ling, Z., Jolliff, B. L., Wang, A., Li, C., Liu, J., Zhang, J., et al. (2015). Correlated compositional and mineralogical investigations at the Chang' e-3 landing site. Nature Communications, 6(1), 8880. https://doi.org/10.1038/ncomms9880

– Losiak, A., Wilhelms, D., Byrne, C., Thaisen, K., Weider, S., Kohout, T., et al. (2009). A new lunar impact crater database. Paper presented at the Lunar and Planetary Science Conference. Lucchitta, B. K. (1977). Crater clusters and light mantle at the Apollo 17 site: A result of secondary impact from Tycho. Icarus, 30(1), 80–96. https://doi.org/10.1016/0019-1035(77)90123-3

– Martinot, M., Besse, S., Flahaut, J., Quantin-Nataf, C., Lozac'h, L., & Westrenen, W. V. (2018). Mineralogical diversity and geology of Humboldt crater derived using Moon Mineralogy Mapper data. Journal of Geophysical Research: Planets, 123, 612–629. https://doi.org/10.1002/2017JE005435

– McEwen, A. S., & Bierhaus, E. B. (2006). The importance of secondary cratering to age constraints on planetary surfaces. Annual Review of Earth and Planetary Sciences, 34(1), 535–567. https://doi.org/10.1146/annurev.earth.34.031405.125018

– McGetchin, T. R., Settle, M., & Head, J. (1973). Radial thickness variation in impact crater ejecta: Implications for lunar basin deposits. Earth and Planetary Science Letters, 20(2), 226–236. https://doi.org/10.1016/0012-821X(73)90162-3

– Melosh, H. J. (1989). Impact cratering: A geologic process. Research supported by NASA. New York, Oxford Univ. Press (Oxford Monographs on Geology and Geophysics, No. 11), 253 p., 11.

– Melosh, H. J., Kendall, J., Horgan, B., Johnson, B., Bowling, T., Lucey, P., & Taylor, G. (2017). South Pole–Aitken basin ejecta reveal the Moon's upper mantle. Geology, 45(12), 1063–1066. https://doi.org/10.1130/G39375.1

– Michael, G. G., Kneissl, T., & Neesemann, A. (2016). Planetary surface dating from crater size-frequency distribution measurements: Poisson timing analysis. Icarus, 277, 279–285. https://doi.org/10.1016/j.icarus.2016.05.019

– Moriarty, D. P., & Pieters, C. M. (2018). The character of south pole - Aitken Basin: Patterns of surface and sub-surface composition. Journal of Geophysical Research: Planets, 123, 729–747. https://doi.org/10.1002/2017JE005364

– Moriarty, D. P., Pieters, C. M., & Isaacson, P. J. (2013). Compositional heterogeneity of central peaks within the South Pole-Aitken Basin. Journal of Geophysical Research: Planets, 118, 2310–2322. https://doi.org/10.1002/2013JE004376

- Morrison, D. A. (1998). Did a thick South Pole-Aitken Basin melt sheet differentiate to form cumulates? Lunar and Planetary Science Conference (Vol. 29). Nakamura, R., Matsunaga, T., Ogawa, Y., Yamamoto, S., Hiroi, T., Saiki, K., et al. (2009). Ultramafic impact melt sheet beneath the South Pole–Aitken basin on the Moon. Geophysical Research Letters, 36, L22202. https://doi.org/10.1029/2009GL040765

- National Research Council (2007). The scientific context for exploration of the Moon. National Academies Press. Neukum, G., Ivanov, B. A., & Hartmann, W. K. (2001). Cratering Records in the Inner Solar System in Relation to the Lunar Reference System. Space Science Reviews, 12,55–86. https://doi.org/10.1007/978-94-017-1035-0_3

- Oberbeck, V. R. (1975). The role of ballistic erosion and sedimentation in lunar stratigraphy. Reviews of Geophysics, 13(2), 337–362. https://doi.org/10.1029/RG013i002p00337

- Oberbeck, V. R., Hörz, F., Morrison, R., Quaide, W., & Gault, D. (1975). On the origin of the lunar smooth-plains. The Moon, 12(1), 19–54. https://doi.org/10.1007/BF02626332

- Oberbeck, V. R., & Quaide, W. L. (1967). Estimated thickness of a fragmental surface layer of Oceanus Procellarum. Journal of Geophysical Research, 72(18), 4697–4704. https://doi.org/10.1029/JZ072i018p04697

- Ohtake, M., Haruyama, J., Matsunaga, T., Yokota, Y., Morota, T., & Honda, C. (2008). Performance and scientific objectives of the SELENE (KAGUYA) Multiband Imager. Earth, Planets and Space, 60(4), 257–264. https://doi.org/10.1186/BF03352789

- Ohtake, M., Uemoto, K., Yokota, Y., Morota, T., Yamamoto, S., Nakamura, R., et al. (2014). Geologic structure generated by large-impact basin formation observed at the South Pole-Aitken basin on the Moon. Geophysical Research Letters, 41, 2738–2745. https://doi.org/10.1002/2014GL059478

- Pasckert, J. H., Hiesinger, H., & van der Bogert, C. H. (2018). Lunar farside volcanism in and around the South Pole–Aitken basin. Icarus, 299, 538–562. https://doi.org/10.1016/j.icarus.2017.07.023

- Petro, N. E., & Pieters, C. M. (2006). Modeling the provenance of the Apollo 16 regolith. Journal of Geophysical Research, 111, E09005. https:// doi.org/10.1029/2005JE002559

- Pieters, C., Head, J., Gaddis, L., Jolliff, B., & Duke, M. (2001). Rock types of South Pole-Aitken basin and extent of basaltic volcanism. Journal of Geophysical Research, 106(E11), 28,001–28,022. https://doi.org/10.1029/2000JE001414

- Pieters, C. M., Boardman, J., Buratti, B., Chatterjee, A., Clark, R., Glavich, T., et al. (2009). The Moon Mineralogy Mapper (M^3) on Chandrayaan-1. Current Science, 500–505.

- Pieters, C. M., Head, J., Sunshine, J., Fischer, E., Murchie, S., Belton, M., et al. (1993). Crustal diversity of the Moon: Compositional analyses of Galileo solid state imaging data. Journal of Geophysical Research, 98(E9), 17,127–17,148. https://doi.org/10.1029/93JE01221

– Pieters, C. M., Tompkins, S., Head, J. W., & Hess, P. C. (1997). Mineralogy of the mafic anomaly in the South Pole-Aitken Basin: Implications for excavation of the lunar mantle. Geophysical Research Letters, 24(15), 1903–1906. https://doi.org/10.1029/97GL01718

– Potter, R. W. K., Collins, G. S., Kiefer, W. S., McGovern, P. J., & Kring, D. A. (2012). Constraining the size of the South Pole-Aitken basin impact. Icarus, 220(2), 730–743. https://doi.org/10.1016/j.icarus.2012.05.032

– Quaide, W. L., & Oberbeck, V. R. (1968). Thickness determinations of the lunar surface layer from lunar impact craters. Journal of Geophysical Research, 73(16), 5247–5270. https://doi.org/10.1029/JB073i016p05247

– Robinson, M. S., Brylow, S. M., Tschimmel, M., Humm, D., Lawrence, S. J., Thomas, P. C., et al. (2010). Lunar Reconnaissance Orbiter Camera (LROC) instrument overview. Space Science Reviews, 150(1–4), 81–124. https://doi.org/10.1007/s11214-010-9634-2

– Sharpton, V. L. (2014). Outcrops on lunar crater rims: Implications for rim construction mechanisms, ejecta volumes and excavation depths. Journal of Geophysical Research: Planets, 119, 154–168. https://doi.org/10.1002/2013JE004523

– Smith, D. E., Zuber, M. T., Neumann, G. A., Lemoine, F. G., Mazarico, E., Torrence, M. H., et al. (2010). Initial observations from the lunar orbiter laser altimeter (LOLA). Geophysical Research Letters, 37, L18204. https://doi.org/10.1029/2010GL043751

– Soderblom, L. A. (1970). A model for small-impact erosion applied to the lunar surface. Journal of Geophysical Research, 75(14), 2655–2661. https://doi.org/10.1029/JB075i014p02655

– Spudis, P. D., Gillis, J. J., & Reisse, R. A. (1994). Ancient multiring basins on the Moon revealed by Clementine laser altimetry. Science, 266(5192), 1848–1851. https://doi.org/10.1126/science.266.5192.1848

– Staid, M. I., Pieters, C. M., Besse, S., Boardman, J., Dhingra, D., Green, R., et al. (2011). The mineralogy of late stage lunar volcanism as observed by the Moon Mineralogy Mapper on Chandrayaan-1. Journal of Geophysical Research, 116, E00G10. https://doi.org/10.1029/2010JE003735

– Stöffler, D., Gault, D., Wedekind, J., & Polkowski, G. (1975). Experimental hypervelocity impact into quartz sand: Distribution and shock metamorphism of ejecta. Journal of Geophysical Research, 80(29), 4062–4077. https://doi.org/10.1029/JB080i029p04062

– Stuart-Alexander, D. E. (1978). Geologic map of the central far side of the Moon. Washington, DC: US Geological Survey. Uemoto, K., Ohtake, M., Haruyama, J., Matsunaga, T., Yamamoto, S., Nakamura, R., et al. (2017). Evidence of impact melt sheet differentiation of the lunar South Pole-Aitken basin. Journal of Geophysical Research: Planets, 122, 1672–1686. https://doi.org/10.1002/2016JE005209

– Vaughan, W. M., & Head, J. W. (2014). Impact melt differentiation in the South Pole-Aitken basin: Some observations and speculations. Planetary and Space Science, 91, 101–106. https://doi.org/10.1016/j.pss.2013.11.010

- Weitz, C. M., & Head, J. W. (1999). Spectral properties of the Marius Hills volcanic complex and implications for the formation of lunar domes and cones. Journal of Geophysical Research, 104(E8), 18,933–18,956. https://doi.org/10.1029/1998JE000630

- Wilhelms, D. E., Howard, K. A., & Wilshire, H. G. (1979). Geologic map of the south side of the Moon. Wilhelms, D. E., John, F., & Trask, N. J. (1987). The geologic history of the Moon. Wu, W. R., Wang, Q., Tang, Y. H., Yu, G. B., Liu, J. Z., Zhang, W., et al. (2017). Design of Chang'E-4 lunar farside soft-landing mission (in Chinese). Journal of Deep Space Exploration, 4(2), 111–117.

- Xiao, L., Zhu, P., Fang, G., Xiao, Z., Zou, Y., Zhao, J., et al. (2015). A young multilayered terrane of the northern Mare Imbrium revealed by Chang'E-3 mission. Science, 347(6227), 1226–1229. https://doi.org/10.1126/science.1259866

- Xiao, Z. (2016). Size-frequency distribution of different secondary crater populations: 1. Equilibrium caused by secondary impacts. Journal of Geophysical Research, Planets, 121, 2404–2425. https://doi.org/10.1002/2016JE005139

- Xie, M., & Zhu, M.-H. (2016). Estimates of primary ejecta and local material for the Orientale basin: Implications for the formation and ballistic sedimentation of multi-ring basins. Earth and Planetary Science Letters, 440,71–80. https://doi.org/10.1016/j.epsl.2016.02.012

- Yingst, R., Chuang, F., Berman, D., & Mest, S. (2017). Geologic Mapping of the Planck Quadrangle of the Moon (LQ-29). Paper presented at the Lunar and Planetary Science Conference.

- Yingst, R. A., & Head, J. W. (1997). Volumes of lunar lava ponds in South Pole-Aitken and Orientale basins: Implications for eruption conditions, transport mechanisms, and magma source regions. Journal of Geophysical Research, 102(E5), 10,909–10,931. https://doi.org/10.1029/97JE00717

- Yingst, R. A., & Head, J. W. (1999). Geology of mare deposits in South Pole-Aitken basin as seen by Clementine UV/VIS data. Journal of Geophysical Research, 104(E8), 18,957–18,979. https://doi.org/10.1029/1999JE900016

- Zhang, H., Yang, Y., Yuan, Y., Jin, W., Lucey, P. G., Zhu, M. H., et al. (2015). In situ optical measurements of Chang'E-3 landing site in Mare Imbrium: 1. Mineral abundances inferred from spectral reflectance. Geophysical Research Letters, 42, 6945–6950. https://doi.org/10.1002/2015GL065273

5

Application of the developed tools to future science exploration Science-rich sites for future lunar exploration (Chang'E-5 mission)

5.1. Geology and Scientific Significance of the Rümker Region in Northern Oceanus Procellarum: China's Chang'E-5 Landing Region

Y. Q. Qian[1], L. Xiao[1], S. Y. Zhao[1], J. N. Zhao[1], J. Huang[1], J. Flahaut[2,3], M. Martinot[4,5], J. W. Head[6], H. Hiesinger[7], and G. X. Wang[8]

[1] State Key Laboratory of Geological Processes and Mineral Resources, Planetary Science Institute, School of Earth Sciences, China University of Geosciences, Wuhan, China

[2] Centre de Recherches Pétrographiques et Géochimiques, CNRS/UMR 7358, Université de Lorraine, Vandoeuvre-lès-Nancy, France

[3] Institut de Recherche en Astrophysique et Planétologie, CNRS/UMR 5277, Université Paul Sabatier, Toulouse, France

[4] Faculty of Science, Vrije Universiteit Amsterdam, Amsterdam, Netherlands

[5] Université Lyon 1, ENS-Lyon, CNRS, UMR 5276 LGL-TPE, Villeurbanne, France

[6] Department of Earth, Environmental and Planetary Sciences, Brown University, Providence, RI, USA

[7] Institut für Planetologie, Westfälische Wilhelms-Universität Münster, Münster, Germany
[8] Beijing Spacecrafts, China Academy of Space Technology, Beijing, China

Corresponding author: L. Xiao (longxiao@cug.edu.cn)

Keypoints:

- The Rümker region is located in the northwest of the Procellarum KREEP Terrane, experiencing a long and complex geological history
- We carried out a detailed geological study and defined and dated 14 geological units
- The Em4 is the science-richest unit and suitable for landing. It is proposed as the first priority for sample return

Abstract

The Rümker region (41–45°N, 49–69°W) is located in northern Oceanus Procellarum of the Moon. Mons Rümker is the most distinctive geological feature in the area. The region is characterized by prolonged lunar volcanism (Late Imbrian Period to Eratosthenian Period), forming multiple geologic units in the area, including very low-Ti to low-Ti mare basalts, high-Ti mare basalts, and volcanic complexes. Each geologic unit has distinct element composition and mineral assemblages. The Rümker region, overlying the Procellarum KREEP Terrain, was selected as the landing region for China's Chang'E-5 lunar sample return mission. Prelanding analyses of the geologic context and scientific potential are reported in this contribution. We conducted detailed geological mapping using image, spectral, and altimetry data. Fourteen geological units were defined, a geologic map was constructed, and the geologic history was outlined. The western mare units (Im1, Im2, and Im3) are Imbrian-aged (~3.4–3.5 Ga) representing the major stage of lunar mare eruptive volcanism. The eastern young mare units (Em3 and Em4; <2 Ga) are among the youngest mare basalts on the Moon. They have never been explored in situ or studied in the laboratory. We suggest that samples returned from the eastern mare unit (Em4) could answer many fundamental questions and that this unit should be listed as the top priority landing site for Chang'E-5 sample return mission.

5.1.1. Introduction

The Procellarum KREEP Terrane (PKT) is one of the most prominent geochemically anomalous areas on the Moon (Haskin, 1998; Jolliff et al., 2000). It is characterized

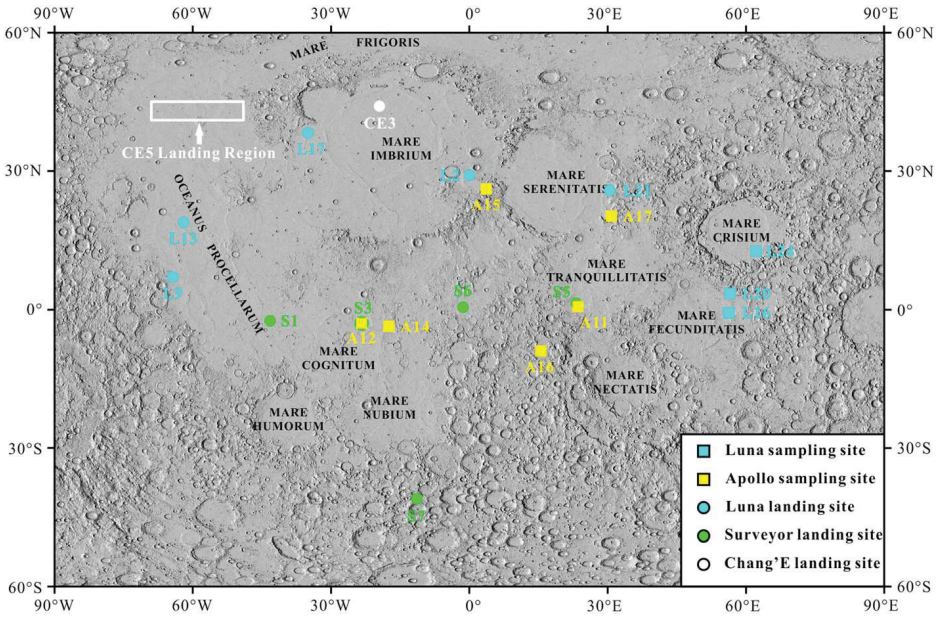

Figure 5.1: Location of the Rümker region and previous landing sites. The Rümker region is located in northern Oceanus Procellarum, away from previous sampling sites. The basemap is a Lunar Orbiter Laser Altimeter and Kaguya Terrain Camera merged hillshade map (simple cylindrical projection; Barker et al., 2016).

by high concentrations of heat producing elements (Th, U, and K; e.g., Haskin et al., 2000; Lawrence et al., 2000; Prettyman et al., 2006), a thin crust (Wieczorek et al., 2013), a complex thermal evolution history (Laneuville et al., 2013; Wieczorek & Phillips, 2000), and a long duration of lunar volcanism relative to most of the rest of the Moon (Hiesinger et al., 2000, 2003, 2010, 2011; Morota et al., 2011).

Located in northern Oceanus Procellarum (Fig. 5.1), the Rümker region is in the northwest part of the PKT (Fig. 5.2; Haskin, 1998; Jolliff et al., 2000). Its extended and complex geologic history includes multiple volcanic episodes, each differing in element composition and mineral assemblages (e.g., Hiesinger et al., 2003, 2011; Morota et al., 2011; Pieters, 1978; Zhang et al., 2016).

Earliest geological mapping (Wilhelms & McCauley, 1971; 1:5 million) defined two mare units in the Rümker region, that is, Imbrian-aged and Eratosthenian-aged mare units (Im and Em). Scott et al. (1977) combined these into an Imbrian-Eratosthenian-aged mare unit (EIm). Scott and Eggleton (1973) subdivided two nonmare units (Ith and If) and two mare units (Im and Em) in their 1:1 million geological map. The authors concluded that the Ith unit resembles the Alpes Formation and that the If unit

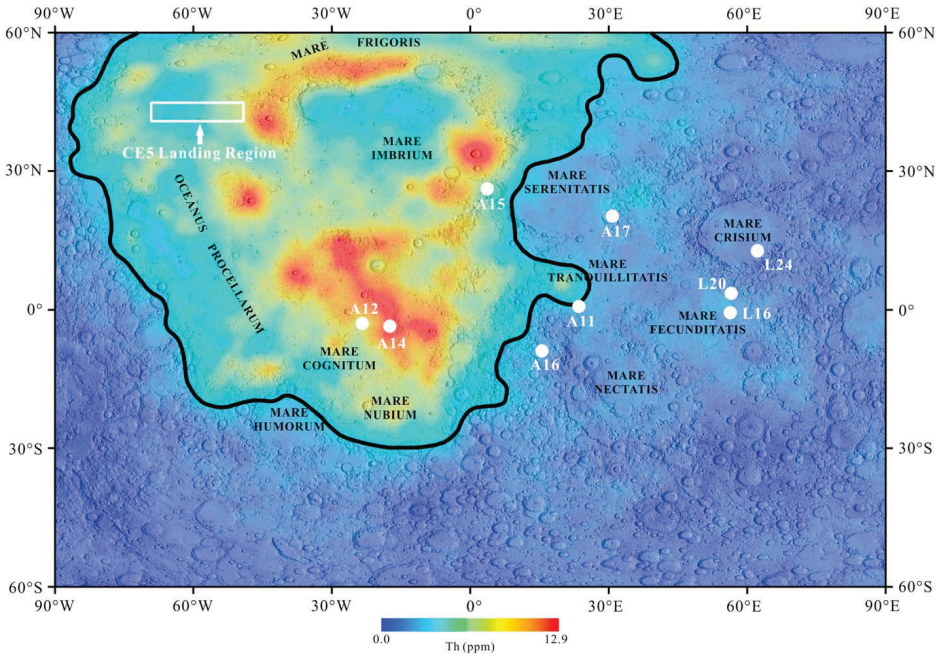

Figure 5.2: Thorium abundance map of the lunar nearside. The thick black line denotes the boundary of the Procellarum KREEP Terrane (Th > 3.5 ppm). "A" represents the Apollo sampling sites; "L" represents the Luna sampling sites. The white box indicates the CE5 designated landing region. The basemap is a Lunar Orbiter Laser Altimeter and Kaguya Terrane Camera merged hillshade map (Barker et al., 2016) superposed on the Lunar Prospector thorium data (Prettyman et al., 2006).

is part of the Fra Mauro Formation, both of which are interpreted as ejecta materials from the Imbrium impact basin (Page, 1970; Scott & Eggleton, 1973).

Whitford-Stark and Head (1980) later subdivided four lithostratigraphic formations in Oceanus Procellarum according to surface morphology and spectral characteristics. Three of them occur in the Rümker region, including the Telemann Formation (the western part), the Sharp Formation (the eastern part), and the Hermann Formation (the central southern part). Three basalt end-members were identified (Dechen Basalt, Lavoisier Basalt, and Roris Basalt), and their sources and emplacement styles were studied in detail (Whitford-Stark & Head, 1980).

More recent stratigraphic works were based on Clementine data. Hiesinger et al. (2003, 2011) used Clementine color ratio data (750–400 nm/750 + 400 nm as red, 750/990 nm as green, and 400/750 nm as blue) to map the mare units in Oceanus Procellarum. Three spectrally homogeneous units in the Rümker region were defined and dated by crater size-frequency distribution (CSFD) methods (P9, 3.47 Ga; P10,

3.44 Ga; P58, 1.33 Ga; Hiesinger et al., 2003, 2011). Using Clementine false-color mosaics (750 nm/415 nm as red, 750 nm/950 nm as green, and 415 nm/750 nm as blue), titanium and iron data, Boroughs and Spudis (2001) mapped six lava flows in northern Oceanus Procellarum. Four of them are located within the Rümker region (Flow2, Flow3, Flow5, and Flow6).

Mons Rümker (i.e., Rümker Hills), the most distinctive topographic feature in northern Oceanus Procellarum, has long been recognized as one of the three major volcanic complexes in Oceanus Procellarum (Whitford-Stark & Head, 1977). Its morphology, composition, mineralogy, and formation mechanism have been well studied (Campbell et al., 2009; Dmitrovsky et al., 2017; Farrand et al., 2015; Smith, 1974; Whitford-Stark & Head, 1977; Wöhler et al., 2007; Zhao et al., 2017). A comprehensive analysis using recent lunar orbital data (Zhao et al., 2017) identified three geologic units at Mons Rümker and further obtained their model ages by CSFD methods (IR1, 3.71 Ga; IR2, 3.58 Ga; IR3, 3.51 Ga). Zhao et al. (2017) concluded that the steep-sided domes and shallow domes on Mons Rümker are probably formed at different stages of evolution of this volcanic complex.

China's first lunar sample return mission, Chang'E-5 (CE5) mission, is scheduled to launch in 2019, following the successful Chang'E-3 (CE3) soft landing and roving exploration of northern Mare Imbrium (44.12°N, 19.51°W; Ling et al., 2015; Xiao, 2014; Xiao et al., 2015; Zou et al., 2016). The Rümker region in northern Oceanus Procellarum (41–45°N, 49–69°W, ~58,000 km2 in area) is the landing region selected for the CE5 mission (Zeng et al., 2017). Up to 2 kg of lunar samples from the surface and subsurface (up to 2 m in depth) are planned to be collected and returned to the Earth (Wang & Xiao, 2017; Zou & Li, 2017), providing an opportunity to study new lunar samples in terrestrial laboratories since Luna-24 (1976).

The Rümker region remains unexplored by robotic or human landing missions carried out earlier by the United States (Surveyor, Apollo) or the Soviet Union (Luna), and no samples have ever been returned from this broad area (Figures 1 and 2). Understanding its geological context and evaluating the scientific value of materials from this region are key to the further exploration and preparation for sample return and analysis. A detailed study of Mons Rümker was carried out, and several candidate landing sites were proposed by Zhao et al. (2017). However, the extensive mare areas to the north, making up the majority of the landing region (Fig. 5.3), have not been well studied using newly obtained orbital remote sensing data. herefore, the goals of this study are (1) to characterize the geological context of the Rümker region, (2) to assess their science potential for understanding and resolving outstanding lunar science questions, and (3) to propose the most scientifically significant landing and sampling sites for the CE5 mission. To understand better the context of the Rümker region, we extend our study area to 39–46°N, 48–70°W (Fig. 5.3).

5.1.2. Data and Methods

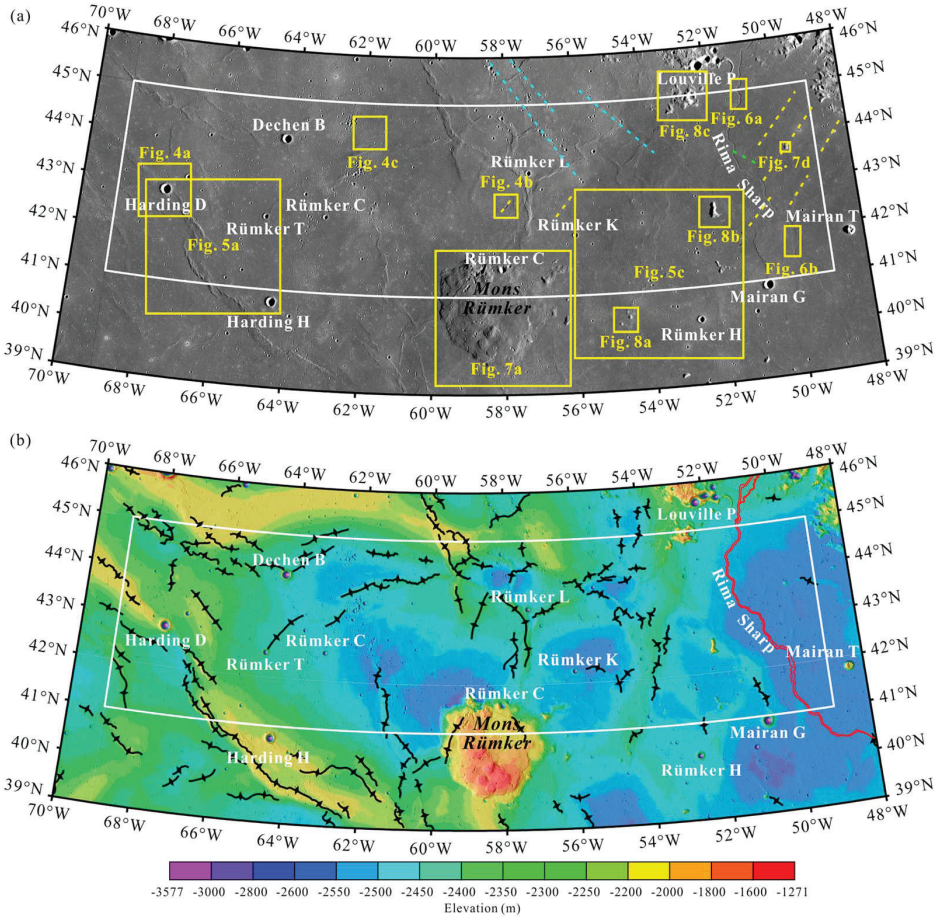

Figure 5.3: **a** Terrane camera (TC) morning map of the Rümker region (Lambert conformal conic projection). The white box denotes the CE5 landing region. The yellow boxes represent the locations of other figures in this paper. The yellow dashed lines denote the ejecta from Harpalus carter. The blue dashed lines denote ejecta from Pythagoras crater. The green dashed lines denote ejecta probably from Copernicus crater. **b** Topography of the Rümker region. The image is a Lunar Orbiter Laser Altimeter and Kaguya TC merged hillshade map superposed on the TC DTM data (Lambert conformal conic projection). The white box denotes the CE5 landing region. The black lines denote wrinkle ridges. The red lines denote Rima Sharp.

Topography and Geomorphology

A Kaguya Terrain Camera (TC) global image mosaic with uniform morning illumination (TC Morning Map data) and TC DTM data, with a spatial resolution of ~10 m/pixel (Haruyama et al., 2008, 2014), were mosaicked to analyze topographic and geomorphologic features. TC Morning Map data were used to perform the CSFD measurements on the major mare units to determine their absolute model ages. TC Morning Map and TC DTM data were downloaded from the SELENE Data Archive (http://darts.isas.jaxa.jp/planet/pdap/selene/). Lunar Reconnaissance Orbiter (LRO) wide-angle camera (WAC) DTM data (~118 m/pixel; Scholten et al., 2012) were applied at a baseline length of 354 m to survey surface slopes. LRO narrow-angle camera (NAC) data were used for more detailed studies of local features, due to their high spatial resolution (up to ~0.5 m/pixel) and more variable illumination conditions (Robinson et al., 2010). WAC DTM data and NAC data were downloaded from the LROC website (http://lroc.sese.asu.edu/).

Composition

TiO_2 and FeO Contents Kaguya Multiband Imager (MI) data were downloaded from the SELENE Data Archive (http://darts.isas.jaxa.jp/planet/pdap/selene/). MI has five visible bands (415, 750, 900, 950, and 1,000 nm) and a spatial resolution of 20 m (Ohtake et al., 2008). TiO_2 and FeO abundances were calculated from MI data using the algorithms described by Otake et al. (2012):

$$\theta\mathrm{Ti} = \arctan[(\mathrm{R415{=}R750}) - 0.208]{=}(\mathrm{R750} + 0.108) \quad (1)$$

$$\mathrm{wt\%TiO_2} = 0.72 \times \theta\mathrm{Ti}^{14.964} \quad (2)$$

$$\theta\mathrm{Fe} = \arctan[(\mathrm{R950{=}R750}) - 1.250]/(\mathrm{R750} - 0.037) \quad (3)$$

$$\mathrm{wt\%FeO} = 20.527 \times \theta\mathrm{Fe} - 12.266 \quad (4)$$

where R415, R750, and R950 are the reflectance at each corresponding band. The standard deviation of the TiO_2 and FeO contents are 0.43 and 0.81 wt%, respectively. Caution should be exercised in interpretations when the TiO_2 content is lower than 2 wt%, at which point the linear correlation between UV/VIS (321 nm/415 nm) and TiO_2 content tends to break down (Coman et al., 2018; Sato et al., 2017).

A false color composite map was produced from MI data by assigning 750 nm/415 nm as red, 750 nm/950 nm as green, and 415 nm/750 nm as blue (Pieters et al., 1994). Because of its sensitivity to surface maturity and composition, and its ability to highlight subtle spectral differences (Eliason et al., 1999; Pieters et al., 1994), the false color composite map, together with titanium and iron variation and crater distribution data, was used to determine the nature and boundaries of geologic units.

Mineralogy Moon Mineralogy Mapper (M^3) reflectance data acquired from the optical period OP2C were selected because of their full spatial coverage over the

Rümker region. M^3 OP2C data have a spatial resolution of 280 m/pixel, with 85 bands, spanning from 430 to 3,000 nm (Pieters et al., 2009). The M^3 data used in this study are calibrated data archived in the Planetary Data System (version 1 of Level 2), radiometrically corrected (Green et al., 2011), geometrically corrected (Boardman et al., 2011), thermally corrected (Clark et al., 2011), and photometrically corrected (Besse et al., 2013).

To decrease the effects of space weathering and to permit a more robust spectral study, we removed the continuum following the method of Horgan et al. (2014) and Martinot et al. (2018). These authors defined the continuum by maximizing the 1 and 2 micron absorption bands. Spectral parameters such as band centers, band depths, band areas, and band asymmetries were calculated for the 1 and 2 micron absorption bands of each spectrum. M^3 RGB composite maps using these criteria were produced to highlight the mineralogical diversity of the Rümker region (Martinot et al., 2018; Mustard et al., 2011). Both M^3 original and continuum-removed spectra were visually analyzed for definitive mineral identification, performed by comparison of the M^3 spectra with the RELAB reference library (http://www.planetary.brown.edu/relab/).

5.1.3. Results

Topography

The Rümker region is located within the relatively smooth mare plains of northern Oceanus Procellarum (Kreslavsky et al., 2013; Rosenburg et al., 2011; Fig. 5.3a). This area is covered by widespread mare basalts and is generally flat. The mean slope of the area is 1.1° (at a baseline length of 354 m), with only 10% of the area exceeding a slope of 2°. The average elevation of the mare area is ~-2,145 m. The western maria is 200–300 m higher than the eastern maria (Fig. 5.3b). The highest point is in the south of Mons Rümker (-1,271 m), and the lowest point is at the bottom of Mairan G crater (-3,571 m). The regional topography is largely influenced by mare ridges, along which the mare surface is locally raised, up to 100–200 m. Mons Rümker, ~70 km in diameter, stands up to 1,300 m above the surrounding mare. It has a mean slope of 2.7°. The individual domes on Mons Rümker are slightly steeper than the plateau.

Geomorphology

Impact Craters Most of the craters in the area are simple primary craters smaller than 2 km in diameter, characterized by bowl-shaped floors, only few with flat bottoms. Almost all craters larger than 2 km in diameter are found in the western maria. It is also apparent that the western maria has a much higher crater density than the eastern maria. Harding D (centered at 42.8°N, 67.6°W; Fig. 5.4a) is the largest crater in the area. It has a diameter of 6.3 km and a bowl-shaped floor. Its rim is ~250 m higher than the surrounding mare. This crater formed on a NE-orientated wrinkle ridge.

Secondary crater clusters formed by ejecta from the crater Copernicus (NW trend), Harpalus (NE trend), and Pythagoras (NW trend) are distributed in the area (Fig. 5.3a;

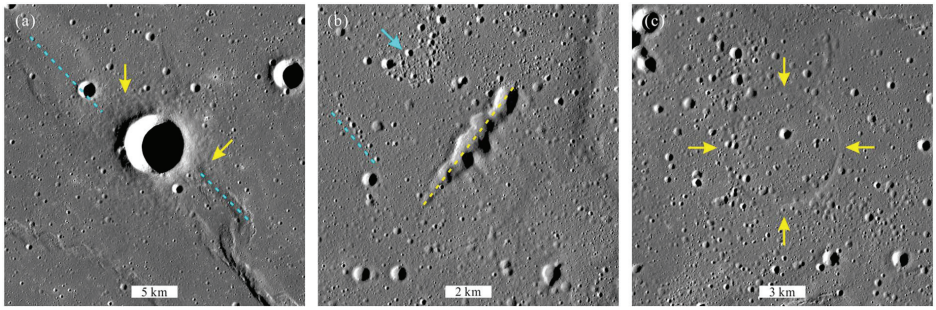

Figure 5.4: Typical impact crater-related structures in the Rümker region. **a** Harding D crater (centered at 42.8°N, 67.6°W; Fig. 5.3a). This crater formed on a NW oriented wrinkle ridge (blue dashed lines). Its ejecta (yellow arrow) buries a portion of the wrinkle ridge. **b** Secondary crater clusters (centered at 42.9°N, 58.0°W; Fig. 5.3a). The yellow dashed line denotes Harpalus secondaries (Scott & Eggleton, 1973). The secondary craters denoted by the blue dashed line are radial to Copernicus crater and are thus probably formed by Copernicus crater ejecta. The blue arrow denotes secondaries without any dominant orientations. **c** A buried crater (centered at 44.4°N, 61.9°W; Fig. 5.3a). The yellow arrows denote the exposed rim crest of the preexisting crater. This preexisting crater is almost completely buried by the later lavas. The subsequent lava flooding is estimated to be less than 800 m, using the depth/diameter relationships of fresh craters (Pike, 1974).

Scott & Eggleton, 1973). For example, the NE-oriented clusters to the north of Mons Rümker are formed by Harpalus crater ejecta (Fig. 5.4b; Scott & Eggleton, 1973). However, the sources of the secondaries that are not characterized by any preferred orientations are mostly unknown.

There are at least 35 buried craters in the study area (39–46°N, 48–70°W) and 15 buried craters that lie within the Rümker region (41–45°N, 49–69°W), mostly in the eastern maria. These premare craters were partially filled by lava flows, leaving only the raised rim crests visible on the surface (Fig. 5.4c).

Wrinkle Ridges Lunar wrinkle ridges are abundant in the study area (Fig. 5.3b). Most of the wrinkle ridges have typical shapes as described by Strom (1972) and Sharpton and Head (1988) (i.e., a gently sloping, broad arch at the base, and a sharper but irregular ridge at the top; Fig. 5.5). The dimensions of the wrinkle ridges are variable in the Rümker region. In the western maria, the wrinkle ridges range up to 6 km in width and 110 km in length and are 200 m above the surrounding mare. In the eastern maria, the wrinkle ridges are smaller than those in the western maria, mostly less than 1.5 km in width and 20 km in length, and are seldom much higher than 50 m above the surrounding mare.

The wrinkle ridges in the Rümker region have three preferred orientations (NW, NNW, and NE, respectively). In the western maria, most wrinkle ridges are oriented NW or NNW, consistent with the preferred orientation of those in Oceanus Procel-

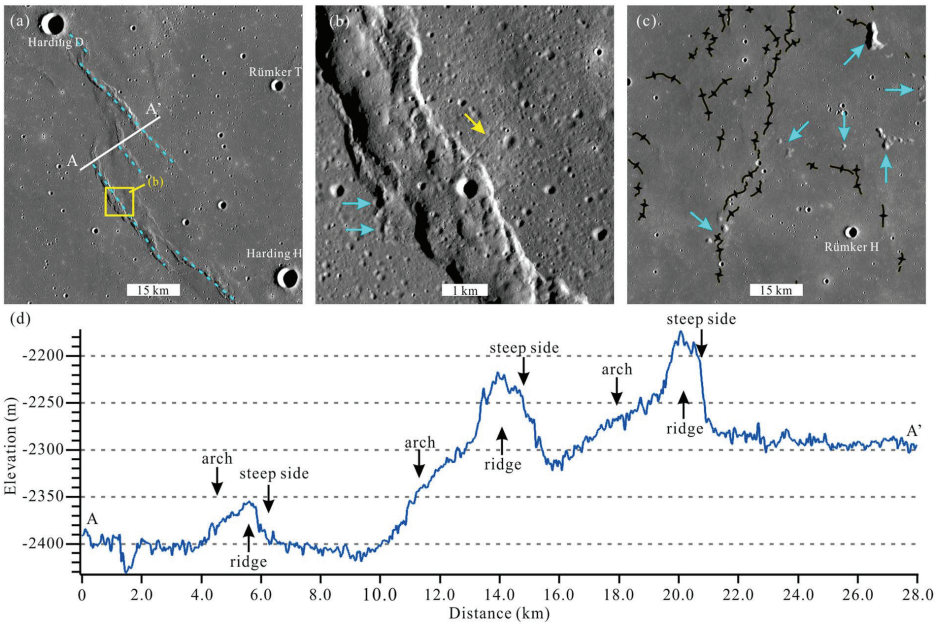

Figure 5.5: Wrinkle ridges. **a** NW-orientated parallel wrinkle ridges (centered at 41.7°N, 66.3°W; Fig. 5.3a). The blue dashed lines denote parallel wrinkle ridges. AA' shows the location of the profile in **d**. The yellow box denotes the location of **b**. **b** A southwest trending fault cuts the wrinkle ridge in the area (the yellow arrow). The craters denoted by blue arrows are cross-cut by the ridge front. **c** Wrinkle ridges in the eastern maria (centered at 41.3°N, 53.9°W; Fig. 5.3a). They are oriented NE along the outer ring marked by kipukas (see section 3.2.5). **d** Topographic profile across wrinkle ridges (AA' in **a**). The wrinkle ridges in the area display the typical broad arches (2–3°) and sharp ridges (up to 8°; Sharpton & Head, 1988; Strom, 1972).

larum as a whole (Yue et al., 2015). For example, the wrinkle ridges between Harding D and Harding H craters in the western maria are parallel and have a distinct NW trend (Fig. 5.5a). Five independent wrinkle ridges are parallel with each other, with variable lengths (10 to 100 km) but similar morphologies and slopes. In the vicinity of these parallel wrinkle ridges, a linear fault vertically cuts a wrinkle ridge (Fig. 5.5b).

In the eastern maria, the wrinkle ridges have a prominent NE trend along the outer ring of the Imbrium basin marked by the shoreline of Mare Frigoris (Spudis et al., 1988; Wilhelms & McCauley, 1971). This trend suggests that the wrinkle ridge formation in the eastern maria was affected by the ring system of the Imbrium basin (Head, 1982; Maxwell et al., 1975).

Sinuous Rilles In the eastern maria, a sinuous rille (Rima Sharp) is incised into the mare plains along the mare/highland boundary (Fig. 5.3b). Rima Sharp is even the longest sinuous rille on the Moon (Hurwitz et al., 2013). It originates in Sinus Roris, to the north of the Rümker region, at an elevation of -2,300 m, and fades into the mare surface to the south at an elevation of -2,500 m(Fig. 5.6). Rima Sharp is 566 km long, 257 km of which are within the study area. The width of Rima Sharp varies from 0.8 to 3 km. Its depth varies from 20 to 50 m, and the narrowest parts of the channel have greater depths than those of the wider parts. The channel wall slopes of Rima Sharp fluctuate between 8 and 12°. The regional slope of Rima Sharp (defined as the gradient of the material surrounding the sinuous rille) is -0.02° as measured by Hurwitz et al. (2013). A thermal erosion formation mechanism is favored for such sinuous rilles (Hurwitz et al., 2012).

Volcanic Domes Volcanic domes are relatively common in the lunar maria (Head & Gifford, 1980; Smith, 1973). They are often observed in clusters, as in the case of Mons Rümker (Smith, 1974; Whitford-Stark & Head, 1977), where most of the volcanic domes in the study area are located. Zhao et al. (2017) identified 22 volcanic domes on the Rümker plateau and divided them into two groups: steep-sided domes and shallow domes (Fig. 5.7a). The steep-sided domes usually have relatively steep flank slopes (>5°) and greater heights, with associated volcanic features such as possible summit pits and flow features (Fig. 5.7b). The shallow domes have gentle topographic relief and lower heights (<200 m); only two domes have associated volcanic features. Both dome groups are interpreted to have formed by extrusion of basaltic magma to form small shield volcanoes similar to those in Marius Hills (Head & Gifford, 1980; Head & Wilson, 2017; Lawrence et al., 2013; Zhao et al., 2017).

Another possible volcanic dome (named East Dome in this study; 49.85°W, 43.68°N) is located near the Mairan domes, close to the mare/highland boundary. The East Dome is circular in shape (Fig. 5.7d), with a diameter of ~3 km, and is up to 205 m higher than the mare (Fig. 5.7e). The flank slope is up to 9°, less than those of the Mairan domes (Glotch et al., 2011; Head & McCord, 1978). This dome is cratered,

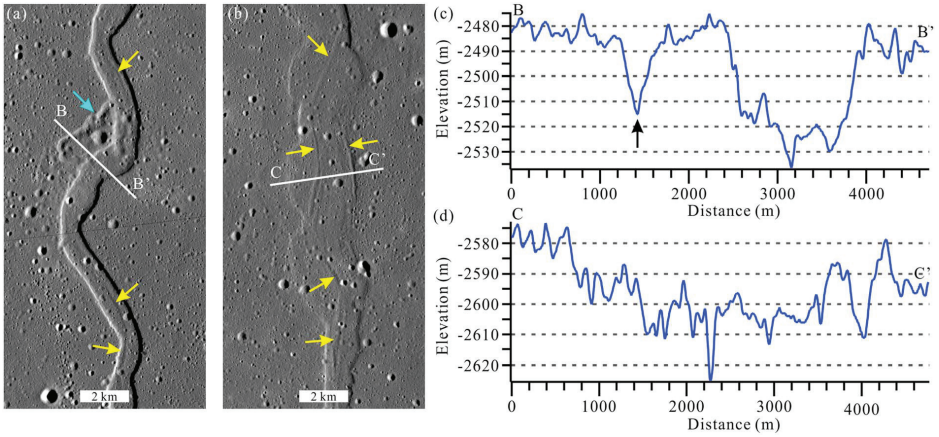

Figure 5.6: Sinuous rilles. **a** The narrow and deep parts of Rima Sharp (centered at 45.0°N, 51.0°W; Fig. 5.3a). Rima Sharp is ~1.3 km wide and 40–50 m deep in this part. The yellow arrows denote small channels within Rima Sharp. The blue arrow denotes a shallow (~30 m in depth) branch of Rima Sharp. The white line (BB') shows the location of the profile in **c**. (b) The wide and shallow part of Rima Sharp (centered at 41.7°N, 50.0°W; Fig. 5.3a). Rima Sharp is 3.1 km wide and ~20 m deep in this part. The yellow arrows denote small channels within Rima sharp. The white line (CC') shows the location of the profile in **d**. **c** Topographic profile of the narrow part of Rima Sharp. The black arrow denotes a branch of Rima Sharp. **d** Topographic profile of the wide part of Rima Sharp.

but most of the craters appear to be fresh secondaries that not highly degraded. A circular depression (~1.3 km in diameter) which may be a volcanic depression is outlined in the northwest (the yellow dashed line in Fig. 5.7d). The East Dome was first described as a silica-rich dome by Glotch et al. (2011). Similar features in the vicinity (the Gruithuisen and Mairan domes) are interpreted to have formed from high viscosity silica-rich magmas of rhyolitic or dacitic composition (Glotch et al., 2010, 2011; Head & Wilson, 2017; Ivanov et al., 2016; Wilson & Head, 2003).

Kipukas Kipukas are islands or exposures of earlier structures or units that have been surrounded by later units. Numerous isolated kipukas are identified within the eastern maria. They are hilly to hummocky highland materials of various shapes and are up to 500 m higher than the surrounding surface. The kipukas have relatively smooth surfaces with fewer craters than the maria, and the few remaining craters are all heavily degraded (Figures 8a and 8b). At the base of the kipukas, debris from the upper slopes encircles the kipukas and forms a 200 to 300-m wide deposit zone (Head, 1977). Although the kipukas usually display a scattered distribution in the eastern maria, the highlands in the northeastern part of the study area near Louville P crater have similar morphologies (Fig. 5.8c). Both the isolated kipukas and highlands

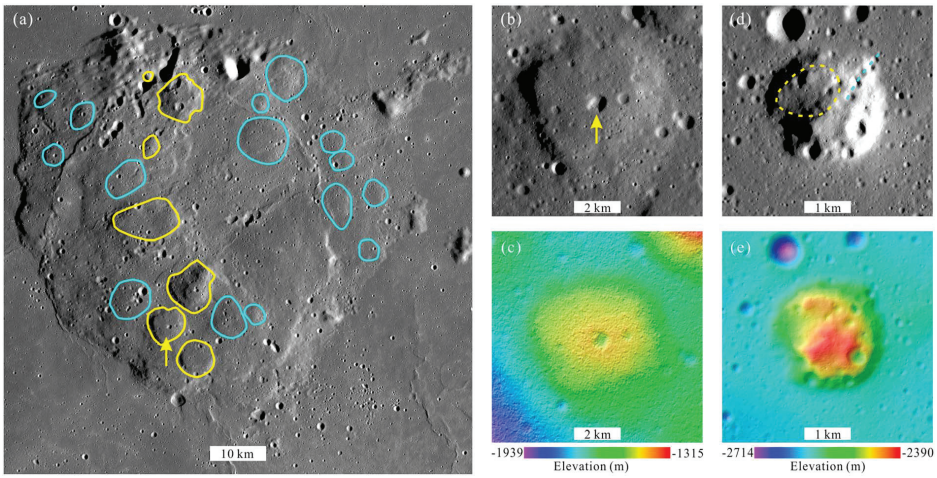

Figure 5.7: Volcanic domes in the Rümker region. **a** Volcanic domes on Mons Rümker. The yellow lines denote steep-sided domes (flank slopes >5°). The blue lines denote shallow domes (flank slopes <5°). The yellow arrow denotes the steep-sided dome in Fig. 5.7b. **b** Steep-sided dome in the southwest of Mons Rümker. The yellow arrow denotes a summit pit, which may be a volcanic crater (Zhao et al., 2017). **c** Topography of the steep-sided dome in Fig. 5.7b. The image is a Lunar Orbiter Laser Altimeter and Kaguya Terrane Camera (TC) merged hillshade map superposed on TC DTM data. **d** The East Dome (centered at 49.85°W, 43.68°N; Fig. 5.3a). The yellow dashed line denotes a circular structure that may be a volcanic depression. The blue line denotes NE trending secondary craters. **e** Topography of the volcanic dome in Fig. 5.7d. The image is a narrow-angle camera (NAC) hillshade map superposed on NAC DTM data.

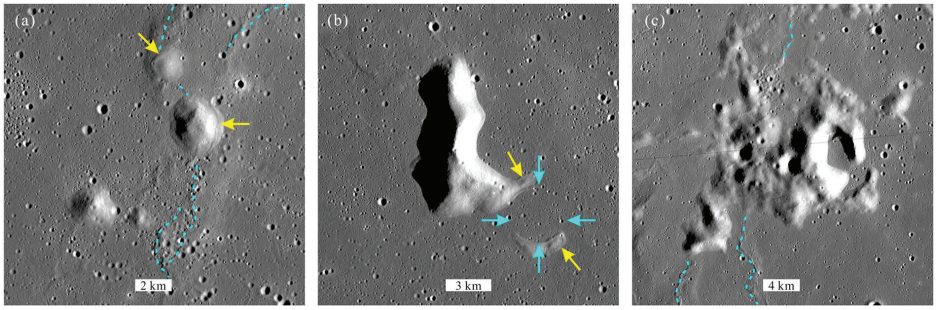

Figure 5.8: Kipukas in the Rümker region. **a** Isolated kipukas (centered at 40.4°N, 54.8°W; Fig. 5.3a). These kipukas are reshaped by wrinkle ridges (the blue dashed lines), especially in the places denoted by the yellow arrows. **b** The largest isolated kipuka (centered at 42.6°N, 52.1°W; Fig. 5.3a). The yellow arrows denote debris. The blue arrows denote a buried crater (~3.9 km in diameter). **c** Highlands near Louville P crater, with a morphology that is similar to the kipukas scattered in the eastern maria. The blue dashed lines denote wrinkle ridges.

near Louville P crater are characterized by subdued shapes and heavily degraded superposed craters, lying on the possible Imbrium basin ring (Wilhelms & McCauley, 1971).

Composition

TiO_2 and FeO Concentrations TiO_2 and FeO abundance maps (Fig. 5.9) were used to estimate the surface TiO_2 and FeO contents. The results show that both the TiO_2 and FeO abundances vary significantly across the area. The TiO_2 contents range up to 7.5 wt % (Fig. 5.9a), and the FeO contents vary from 10 to 18.0 wt % (Fig. 5.9b). The western and the eastern maria are dominated by two different types of mare basalts, with distinctly different TiO_2 contents, and varying FeO contents. However, it should be noted that about 45% of the study area has TiO_2 contents lower than 2 wt %, a value at which the specific TiO_2 contents are probably not accurate (Coman et al., 2018).

The western maria are characterized by very low-Ti to low-Ti basalts (up to 5.0 wt %, TiO_2 content; Neal & Taylor, 1992). The mean content of TiO_2 is 1.6 wt %. About 80% of the area has TiO_2 contents lower than 1%. The northwestern part of the western maria exhibits the lowest TiO_2 contents in the study area (1.3 wt %, mean content). The TiO_2 contents increase from north to south in the western maria and reach an average of 2.4 wt % to the south of Harding D crater. The FeO contents of the western maria are lower than of the eastern maria. The FeO contents range from 14 to 17 wt % (15.8 wt %, mean content), increasing toward the south.

The western maria are characterized by very low-Ti to low-Ti basalts (up to 5.0 wt %, TiO_2 content; Neal & Taylor, 1992). The mean content of TiO_2 is 1.6 wt %. About 80%

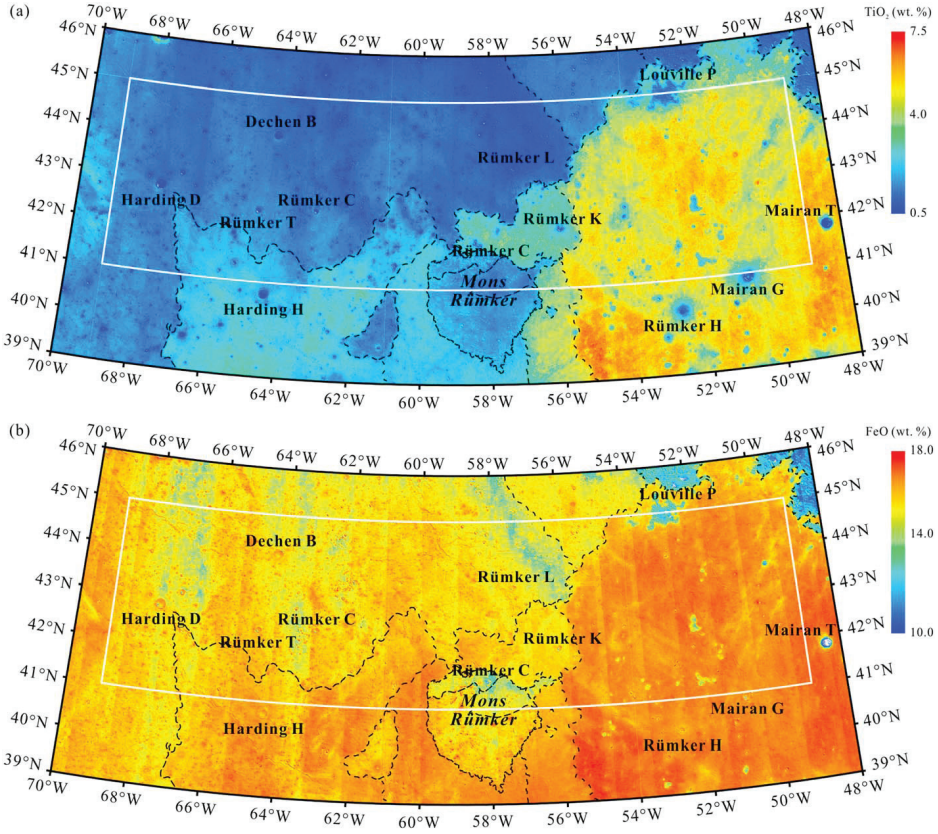

Figure 5.9: TiO_2 and FeO abundance maps of the Rümker region (Lambert conformal conic projection). **a** TiO_2 abundance map of the study area. **b** FeO abundance map of the study area. The white boxes denote the CE5 landing region. The black dashed lines denote geologic boundaries discussed in section 3.4.

of the area has TiO_2 contents lower than 1%. The northwestern part of the western maria exhibits the lowest TiO_2 contents in the study area (1.3 wt %, mean content). The TiO_2 contents increase from north to south in the western maria and reach an average of 2.4 wt % to the south of Harding D crater. The FeO contents of the western maria are lower than of the eastern maria. The FeO contents range from 14 to 17 wt % (15.8 wt %, mean content), increasing toward the south.

A very low-FeO zone occurs in the northeast of the western maria, without variation of TiO_2 abundances, suggesting an origin due to the emplacement of ejecta from Pythagoras crater (low-Fe and very low-Ti), rather than due to the composition of local bedrock or regolith. Large craters and their surrounding ejecta in the western maria have even lower TiO_2 contents than the mare surface (<1 wt %); we interpret this to be due to the excavation of underlying very low-Ti lava flows or underlying fresh rocks of the same lithology. This relationship between lava flows and their compositions can be used to obtain the thickness of lava flows (Thomson et al., 2009; Weider et al., 2010), which is discussed in section 4.1.1. The eastern maria are clearly more enriched in TiO_2 (4.7 wt %, mean content) and FeO (16.7 wt %, mean content) than the western maria. About 65% of the eastern area has TiO_2 contents between 4 and 7 wt % and about 80% of the area has FeO contents greater than 16%. Most of the eastern maria are covered by bright (high albedo) ray materials radiating from Copernican-aged Harpalus crater (Fig. 5.3a), whose bedrock target is low-Ti mare basalts. These materials clearly decrease the surface TiO_2 contents in the eastern maria. Except for these areas covered by ejecta, rocks in the region are classified as high-Ti basalts (TiO_2 contents between 6 and 7 wt %; Neal & Taylor, 1992).

The underlying older low-Ti materials are clearly excavated by superposed impact craters, as shown in the nature of the ejecta from relatively large and fresh craters. This ejecta has TiO_2 contents close to those of the western maria (1.9 wt %, mean content). The kipukas are expected to show very low TiO_2 and FeO contents due to their origin as highlands (Spudis et al., 1988), but mixture with the surrounding high-Ti basalts by impacts has commonly raised their titanium and iron abundance.

Mons Rümker is dominated by low-Ti basalts (1.8 wt %, mean content; Neal & Taylor, 1992). The mean content of FeO is 15.6 wt %. The FeO content is lower in the northeastern Rümker plateau, due to admixing of highland and basaltic materials (Zhao et al., 2017).

Mineralogy The color composite maps shown in Fig. 5.10 highlight the presence of distinct spectral units, represented by different colors. The area is dominated by pyroxene signatures, characterized by broad absorption bands centered around 1 and 2 microns (Adams, 1974). Other common lunar minerals such as olivine or plagioclase have not been detected throughout the study area. Although several parameters, such as surface physical properties and rock texture, may also influence the band shape, band center positions are often indicative of the pyroxene cation content (Adams,

1974; Burns et al., 1973; Cloutis & Gaffey, 1991).

The western maria spectra (Fig. 5.10c) are characterized by greater band depths and band centers at shorter wavelengths than the eastern maria spectra. Spectra from the eastern maria (Fig. 5.10d) are quite homogenous, with the exception of those taken from the interiors of impact craters with diameters exceeding 900 m, where the spectra have band centers located at shorter wavelengths, consistent with the western maria spectra. It is therefore likely that the impact craters of the eastern maria have excavated material from an older, buried unit, spectrally similar to the western maria. Spectra of the western maria show 1 and 2 micron bands centered around 990 and 2,180 nm, consistent with a pyroxene of intermediate-Ca composition such as pigeonite (Fig. 5.10e). Spectra of the eastern maria have 1 and 2 micron bands centered at ~1,010 and 2,260 nm, consistent with high-Ca pyroxene such as augite (Fig. 5.10e). Ling et al. (2017) also conducted spectral observation of the Rümker region. Both Ling et al. (2017) and this survey suggest that there is little low-Ca pyroxenes in the mare area.

Mons Rümker, the Mairan T dome, and the highlands in Montes Jura to the east of the study area are all characterized by weaker pyroxene absorptions bands, which likely indicate a lower mafic component, or more mature regolith (Fischer & Pieters, 1994). The pyroxene component of the highlands is slightly more variable, with absorption bands shifted toward shorter wavelengths (~950 and 2,140 nm), suggesting the presence of low-Ca pyroxene rather than the intermediate to high-Ca pyroxene detected in the mare units. The Mons Rümker pyroxene component is closer in composition to the older, western maria in composition (intermediate-Ca pyroxene). The Mairan T dome, Mons Rümker, and the highlands in Montes Jura have higher average reflectance values than the mare units, which may indicate the presence of a less mafic component, such as silica or feldspar, which cannot easily be detected in the VNIR domain when mixed with pyroxene (e.g., Adams & McCord, 1972; Pieters, 1986).

Geologic Units

Fourteen geologic units were defined and mapped in this study, including seven mare units (Im1, Im2, IM^3, Em1, Em2, EM^3, and Em4), three Rümker plateau units (IR1, IR2, and IR3), one nonmare highland units (Ith), and three dome units (ld, sd, and Idm; Fig. 5.11). In order to define the geologic units, we followed the assumption by Hiesinger et al. (2000) that spectrally and compositionally homogeneous units are formed within a short period and each unit represents a single volcanic eruptive phase. Therefore, each spectrally and compositionally homogeneous unit is regarded as a geologic unit. We used TiO_2 and FeO contents and a false color composite from Kaguya MI data to define spectral and compositional units. The boundaries revealed by TiO_2 and FeO abundance data (Fig. 5.9) correlate well with those revealed by M^3 color composite data (Fig. 5.10). Boundaries are shown as black lines in Fig. 5.11 and black dashed lines in Fig. 5.9.

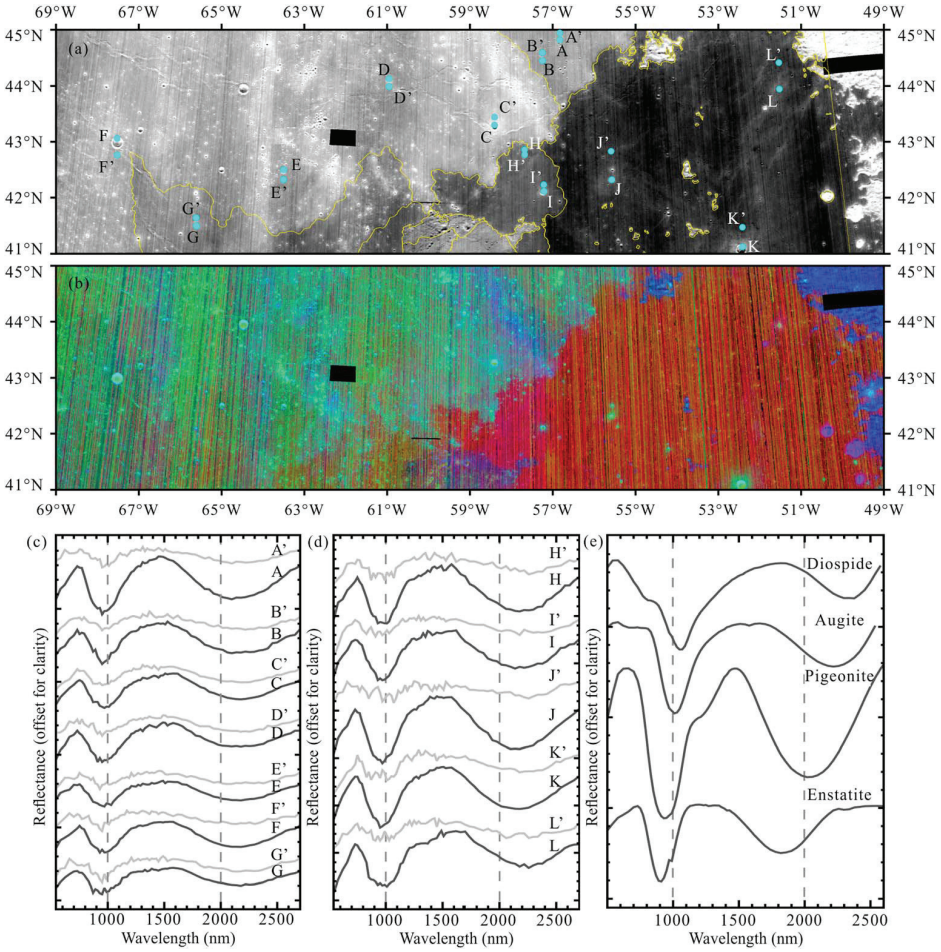

Figure 5.10: M^3 spectral analysis of the Rümker region. **a**. M^3 2900 nm mosaic. **b**. M^3 RGB composite of spectral parameters (R = 2 micron band center, stretched values: 2000-2500; G = 2 micron band depth, stretched values: 0.04-0.13; B = reflectance at 1580 nm, stretched values: 0.085-0.15). **c**. M^3 original spectra averaged over the entire units defined in next section (see yellow outlines on **a**). **d**. M^3 continuum-removed spectra of the same units (using the method of Martinot et al., 2018. **e**. M^3 continuum-removed 3x3 pixel average spectra of selected impact craters (A through E) and of the nearby mare (A' through E') within the eastern mare (see positions on a). **f**. M^3 continuum-removed 3x3 pixel average spectra of selected impact craters (F through L) and of the nearby mare (F' through L') within the western mare (see positions on **a**). **g**. RELAB database pyroxene spectra processed using the method of Martinot et al., 2018 (respective RELAB-IDs: PD-CMP-006, AG-TJM-010, DL-CMP-008 and DH-MBW-005 for diopside, augite, pigeonite and enstatite).

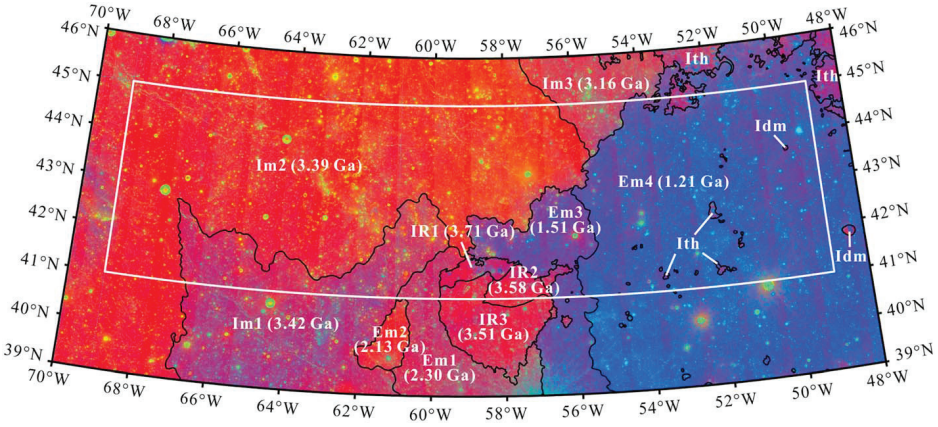

Figure 5.11: Geologic units of the Rümker region. The black lines denote the geological boundaries. The white box denotes the CE5 landing region. Im1, Im2, and Im3 are Imbrian-aged mare units. Em1, Em2, Em3, and Em4 are Eratosthenian-aged mare units. IR1, IR2, and IR3 are Rümker plateau units. Ith is a highland unit. Idm is an Imbrian-aged dome unit.

Crater size-frequency distribution methods were carried out to analyze the homogeneous units using TC Morning Map data to determine their absolute model ages. The results are shown in Table 5.1 together with optical maturity values, TiO_2 and FeO contents, and their uncertainties (shown as standard deviation). The cumulative crater frequency plots are shown in Fig. 5.12. Mons Rümker was mapped, and surface ages were determined by Zhao et al. (2017), and we used their results in this study.

Im1, Im2, and IM^3 are Imbrian-aged mare units (referred to as western maria above), adopting the lunar stratigraphy system by Stöffler and Ryder (2001). Im1 is the oldest mare unit (~3.42 Ga) in the area. It is dark bluish-purple in color with a red hue in the false color map (Fig. 5.11), dominated by low-Ti basalts (2.4 wt %, mean content of TiO_2). Im2 (~3.39 Ga) is the largest mare unit in the area, containing five large craters (>3 km in diameter), Eratosthenian-aged Pythagoras secondaries, and large wrinkle ridges. It is orange-red in the false color map (Fig. 5.11), and the TiO_2 content (1.3 wt %, mean content) is apparently lower than that of Im1. IM^3 is located in the northeast near Louville P crater (~3.16 Ga; Fig. 5.11), with a low TiO_2 content (1.4 wt %, mean content). It is the smallest Imbrian-aged unit in the area, embaying some of the highlands near Louville P. Most of the unit is covered by NE-orientated Pythagoras secondary ejecta, resulting in the largest OMAT value (0.184) in the area. Our mapping results of Imbrian-aged mare units correlate well with previous stratigraphic studies by Whitford-Stark and Head (1980) and Hiesinger et al. (2003).

Em1, Em2, EM^3, and Em4 (EM^3 and Em4 are referred to as eastern maria above) are Eratosthenian-aged mare units. Em1 (~2.30 Ga) embays Mons Rümker in the

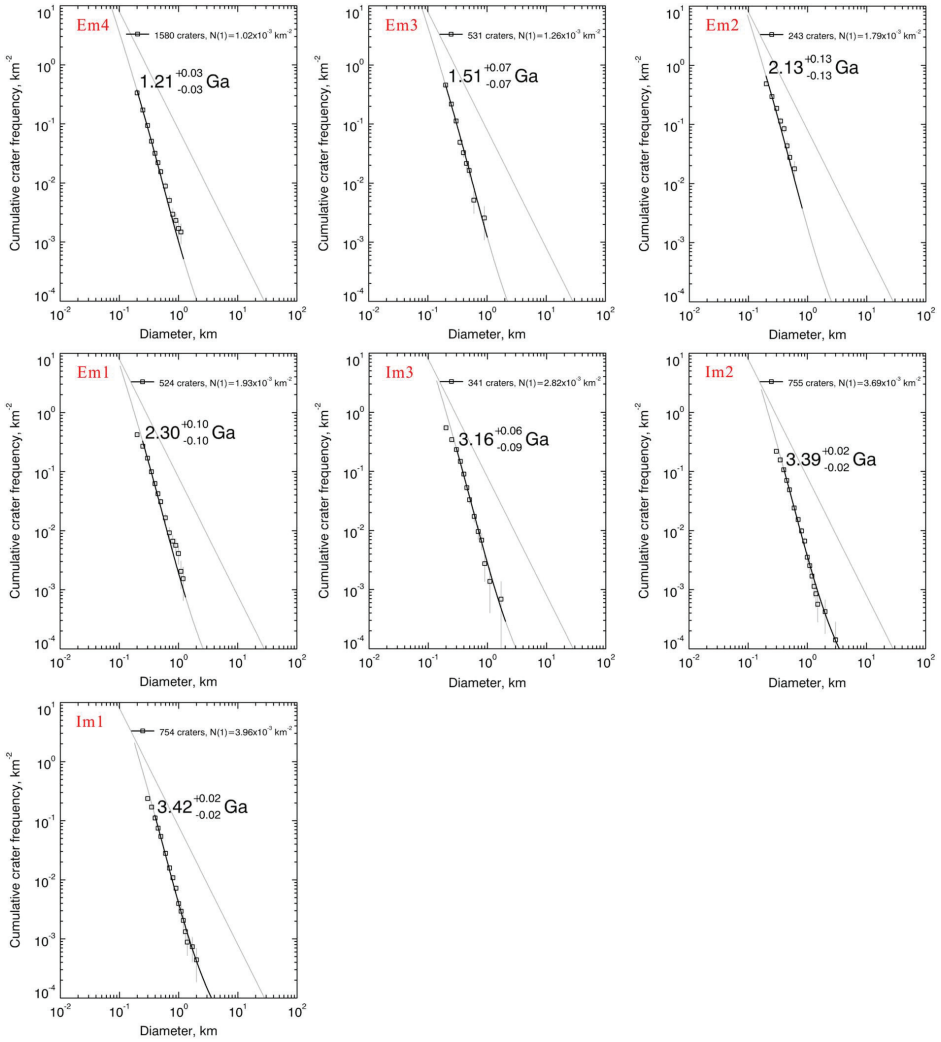

Figure 5.12: Cumulative crater frequency plots and absolute model ages of the mare units analyzed. See Table 5.1 for details. The lunar production function and the chronology function are given by Neukum et al. (2001).

southwest. It has similar color ratios and TiO_2 contents as the neighboring unit, Im1, but it is different in its relatively high FeO contents and lower crater density. Em2 (~2.13 Ga) has the lowest TiO_2 contents (1.6 wt %, mean content) among the Eratosthenian units. It has an orange-red hue in the false color map (Fig. 5.11) similar to the Im2 unit, but it has fewer craters and a younger model age. EM^3 (~1.51 Ga) is located to the east of Mons Rümker. It is purple in the false color map (Fig. 5.11), characterized by a low-Ti composition (3.6 wt %, mean content of TiO_2). This unit embays a portion of Mons Rümker in the east.

Em4 (~1.21 Ga) is the youngest mare unit in the area. This unit has a high TiO_2 (6–7%) content, except for the areas covered by Copernican-aged secondary ejecta, as discussed in section 3.2.1. The FeO contents of Em4 are also high (16.7 wt %, mean). This unit is purple-blue in the false color map (Fig. 5.11) and embays dozens of highland kipukas. The wrinkle ridges are smaller than those of western maria, trending NE along the outer ring of the Imbrium basin. Rima Sharp incises this unit at its boundary with Montes Jura.

IR1, IR2, and IR3 are Rümker plateau units, according to the definition and crater counting results of Zhao et al. (2017) (Table 5.1). IR1 (~3.71 Ga) is a lineated terrain in the north of Mons Rümker, formed by a mixing of Iridum crater ejecta and basaltic materials. IR2 (~3.58 Ga) occurs northeast of Mons Rümker, exhibiting lower TiO_2 contents. IR3 (~3.51 Ga) covers the main portion of Mons Rümker, characterized by higher TiO_2 and FeO contents than IR2 (Zhao et al., 2017).

Three dome units are identified in the area. Two of them (ld, ~3.5 Ga; sd, active until ~3.0 Ga) were defined by Zhao et al. (2017) on the basis of their flank slopes. The silica-rich domes including the East Dome and the Mairan domes (Idm) are mapped as another independent unit with a highland volcanism formation mechanism in the Imbrian Period (Head & McCord, 1978).

Kipukas/highlands are informally defined as massif materials (Wilhelms, 1970) that resemble the Alpes Formation (Page, 1970), interpreted to have been formed by the ejecta of the Imbrium basin in previous studies (Scott & Eggleton, 1973; Spudis et al., 1988). In the current study, we defined it as the Ith unit after Scott and Eggleton (1973). It is the oldest unit in the area, contemporary with the Imbrium basin impact (~3.93 Ga; Snape et al., 2016).

5.1.4. Discussion

Volcanic Events and Geologic History

Volcanic Events The oldest recognizable mare basaltic unit in Oceanus Procellarum is the Repsold Formation (medium to high TiO_2 content). At present it is only exposed in northwestern Oceanus Procellarum near the Rümker region (Whitford-Stark & Head, 1980). It is inferred to be beneath the uppermost mare basalts defined in this study, on the basis of superposition relationships and its extensive coverage (Whitford-Stark & Head, 1980). The Repsold Formation was emplaced around 3.75 ±

Table 5.1: Geologic Units in the Study Area

Unit	Area (km^2)	Model age (this study)[a] (Ga)	Hiesinger et al.[b] (2003) (Ga)	OMAT[cf]	TiO_2^{df} (wt. %)	FeO^{df} (wt. %)
Em4	35905	1.21 (+0.03/-0.03)	1.33, P58	0.174	4.9	16.7
Em3	5396	1.51 (+0.07/-0.07)		0.169	3.6	16.1
Em2	915	2.13 (+0.13/-0.13)		0.164	1.6	16.2
Em1	3928	2.30 (+0.10/-0.10)		0.170	2.4	16.7
Im3	3454	3.16 (+0.06/-0.09)	3.40, P13	0.184	1.4	15.3
Im2	44327	3.39 (+0.02/-0.02)	3.44, P10	0.167	1.3	15.6
Im1	13749	3.42 (+0.02/-0.02)	3.47, P9	0.167	2.4	16.3
IR1	2912	3.71 (+0.04/-0.05)[e]		0.157	2.0	15.1
IR2	727	3.58 (+0.03/-0.04)[e]		0.156	1.5	14.8
IR3	747	3.51 (+0.04/-0.06)[e]		0.157	1.9	15.8

[a] Absolute model ages. Absolute model ages of each unit were calculated using CraterstatsII (http://www.geo.fu-berlin.de/). Uncertainties are reported by Michael and Neukum (2010). [b] Geologic units and their model ages defined by Hiesinger et al.(2003). [c] Mean optical maturity (OMAT) values. OMAT values were obtained from Kaguya MI data, using the method described by Lucey et al. (2000) and Lemelin et al. (2016).[d] Mean TiO2 and FeO contents. [e] The CSFD results by Zhao et al. (2017). [f] The values in parentheses of OMAT, TiO_2, and FeO indicate standard deviation values of each unit.

0.05 Ga (Boyce & Jonnson, 1978) or 3.72 Ga (P28; Hiesinger et al., 2003, 2011) ago.

The basaltic unit IR1 formed ~3.71 Ga during the same period or shortly after the emplacement of the Repsold Formation, followed by IR2 (3.58 Ga) and IR3 (3.51 Ga; Zhao et al., 2017). Shallow domes (ld) formed around 3.5 Ga ago (Zhao et al., 2017). Extrusive steep-sided domes formed later by relatively high viscosity magma, and volcanic activity continued until ~3.0 Ga ago (Zhao et al., 2017). The basaltic eruptions in the Mons Rümker region are similar to the western maria flows in elemental composition (low TiO_2), mineralogy (intermediate pyroxene composition), and emplacement ages (Imbrian-aged), suggesting that they may be from the same mantle source region but have different eruption styles.

Although the small silica-rich East Dome has not been dated in this study due to its small area, it most likely formed in the Imbrian Period, contemporary with the Mairan domes (Head & McCord, 1978) and other silica-rich domes, for example, the Gruithuisen domes (3.7–3.85 Ga, Wagner et al., 2002) and the Hansteen domes (3.65–3.74 Ga, Wagner et al., 2010). On the other hand, its relatively shallow slopes (9°), low thorium abundance (8.6 ppm), and lower silica content compared with other Mairan domes (Glotch et al., 2011) might indicate that it is not completely similar to typical red spots that are formed by more viscous, silica-rich magmas (Glotch et al., 2010, 2011; Head & Wilson, 2017; Ivanov et al., 2016; Wilson & Head, 2003).

The Imbrian-aged mare basalts (Im1, Im2, and IM^3) defined in the current study comprise the major mare eruption phase during the Late Imbrian Period (3.2–3.8 Ga; Hiesinger et al., 2000, 2003, 2010, 2011). This eruption phase has a very low-Ti to low-Ti and intermediate pyroxene composition (e.g., pigeonite), suggesting early magma source regions without ilmenite. The materials excavated from the largest crater (Harding D, 6.3 km diameter) have similar mineral, TiO_2, and FeO contents as those in the surface of the mare, unlike the underlying Repsold Formation materials, as do other impact craters. This implies that the thickness of the Imbrian mare units is at least 700 m. The sources of the Imbrian-aged basalt units are hard to trace, but the sinuous rilles in Mons Rümker and Aristarchus regions were probably the source of some of these materials (Whitford-Stark & Head, 1980).

The Eratosthenian-aged mare basalts (Em1, Em2, EM^3, and Em4) represent the young phase of volcanism, characterized by high titanium content (Blewett et al., 1997; Elphic, 2002; Pieters, 1978) and high olivine content (Pieters, 1978; Staid et al., 2011; Staid & Pieters, 2001; Zhang et al., 2016). The Eratosthenian-aged mare basalts in this area are also rich in iron, especially the EM^3 and Em4 units. The Em1 and Em2 units are not as high in TiO_2 and FeO content as the early Late Eratosthenian Period aged EM^3 and Em4 units. The spectra from these units have band center positions shifted toward shorter wavelengths from EM^3 to Em4 (Fig. 5.10d), suggesting a slight change in the pyroxene compositions (decrease of calcium) of the eruptive high-Ti mare basalts with time.

Em4 comprises the main member of the Eratosthenian mare units in the area.

Table 5.2: Basalt Thickness of the Young Mare Units (Em3 and Em4) and Craters Used to Calculate the Thickness

No	Latitude (^{o})	Longitude (^{o})	Diameter (km)	Dt (km)	R_{base} (km)	H_b (m)
1	40.9	50.8	6.1	5.1	5.0	228 (±105)
2	42.1	52.2	1.6	1.4	0.9	119 (±7)
3	40.3	52.8	4.3	3.6	4.4	78 (±78)
4	39.8	53.2	2.0	1.7	1.4	106 (±22)
5	42.6	54.1	1.7	1.4	1.7	50 (±39)
6	43.2	55.5	1.2	1.0	0.7	97 (±3)
7	42.1	55.6	1.8	1.5	1.0	137 (±5)
8	42.3	56.0	3.3	2.8	2.6	132 (±53)

Note. The applied method is described in Thomson et al. (2009). Dt is the transient crater diameter. R_{base} is the radius of ejecta. H_b is basalt thickness.

Rima Sharp is the longest sinuous rille on the Moon and feeds most of the lavas of Em4 from the north in Sinus Roris with the assistance of Rima Mairan from the south-east (Whitford-Stark & Head, 1980). The Em4 lava flow boundaries are undetectable in WAC low solar illumination image data, although Eratosthenian-aged lava flow fronts can be readily observed in Mare Imbrium (Chen et al., 2018; Wu et al., 2018). This observation suggests that the Em4 lava flow unit thickness is too small to be recognized. Spectroscopic observations by M^3 show that materials excavated by craters with diameter greater than 900 min the eastern maria (EM^3 and Em4) are different from surface materials associated with EM^3 and Em4 and similar to the older western maria. This observation indicates that the eastern Eratosthenian-aged mare units (EM^3 and Em4) are superposed on the old western Imbrian-aged mare units (Im1, Im2, and IM^3). Thus, we estimated the thickness of the eastern mare basalt to be less than 90 m using depth/diameter relationships (Pike, 1974). Further constraints on basalt thickness were provided by crater penetrating measurements (Thomson et al., 2009), yielding a thickness of 50–100 m for the young basalts (EM^3 and Em4; Table 5.2), comparable to the 30–60 m estimated by Hiesinger et al. (2002).

In summary, the Imbrian-aged and Eratosthenian-aged mare units in the study area have a significant variation in age, mineralogy, composition, and volume, which are interpreted to originate from different mantle source regions or depths (Kato et al., 2017; Staid et al., 2011).

Geological History The sequence of geologic events in the area, including volcanic activity, tectonism (wrinkle ridge formation), and impact cratering, are now summarized. A geologic map (Fig. 5.13) was produced, and we interpret the geological evolutionary history of the Rümker region as follows:

1 The Imbrium impact at 3.92 Ga ago generated a complex multiring system (Snape et al., 2016) and the outer ring materials formed the Ith unit in the area (Scott & Eggleton, 1973; Spudis et al., 1988). Ejecta of the Iridum impact (3.84–3.7 Ga; Wagner et al., 2002) formed the lineated terrain in the north of Mons Rümker before 3.71 Ga (Zhao et al., 2017).

2 The earliest detectable basaltic volcanism in the area erupted around 3.72 Ga ago (Hiesinger et al., 2003), forming medium to high-titanium mare basalts belonging to the Repsold Formation (Whitford-Stark & Head, 1980).

3 Basaltic volcanism was active from 3.71 to 3.51 Ga ago in Mons Rümker, forming plateau basalts IR1 (3.71 Ga), IR2 (3.58 Ga), and IR3 (3.51 Ga; Zhao et al., 2017).

4 Silica-rich domes (Idm) formed contemporaneously to, or a little earlier than, Mons Rümker by silica/felsite volcanic activity (Glotch et al., 2010, 2011; Head & McCord, 1978; Head & Wilson, 2017; Ivanov et al., 2016; Wilson & Head, 2003).

5 The major phase of basaltic volcanism occurred during the Late Imbrian Period, forming very low-Ti to low-Ti mare basalts (Im1, 3.42 Ga; Im2, 3.39 Ga; IM^3, 3.16 Ga).

6 NW-oriented wrinkle ridges in Oceanus Procellarum were tectonically generated around 3.35 Ga ago (Yue et al., 2017).

7 The youngest phase of mare volcanism started at ~2.30 Ga ago and ceased at ~1.21 Ga ago, forming four episodes of mare units (Em1, 2.30 Ga; Em2, 2.13 Ga; EM^3, 1.51 Ga; Em4, 1.21 Ga). The youngest mare volcanism (with elevated titanium content) formed the Em4 unit.

Potential Science Outcomes From Sample Return

Laboratory studies of lunar samples from Apollo and Luna missions (landing sites shown in Figures 1 and 2) solved numerous fundamental scientific issues of selenology and heralded the beginning of a golden age of lunar research that continues to this day (e.g., Hiesinger, 2006; Jaumann et al., 2012; Neal, 2009; Taylor, 2014; Taylor et al., 2006). However, most of the Moon remains unexplored and there are still many unanswered scientific questions (National Research Council, 2007) that remain to be addressed by returned samples (e.g., Crawford et al., 2007, 2012; Crawford & Joy, 2014; Flahaut et al., 2012; Kring & Durda, 2012). China's CE5 lunar sample return mission to the Rümker region provides a great opportunity to solve some of the significant outstanding questions of lunar science. Samples from each geologic unit in the area have specific scientific importance, which should be ranked to maximize the science outcomes.

The Young Mare Units On the Moon, the phase of mare basalt volcanism that records internal mantle evolution began (cryptomaria; Whitten & Head, 2015) prior to the end of impact basin formation (Orientale basin, ~3.68 Ga; Whitten et al., 2011) peaked between 3 and 4 Ga and subsequently declined with time, with only a few extrusive mare basalt deposits, widely spaced in the last 50% of the lunar history (Head & Wilson, 2017; Hiesinger et al., 2000, 2003, 2010, 2011; Morota et al., 2011). Where is the youngest mare basalt volcanism, what is its exact radiometric age, and what does its mineralogy and geochemistry tell us about the lunar mantle in the last half of lunar history?

Remote sensing data and counts of superposed impact craters on mare basalt units show that the youngest mare basalts could be as young as 1.2 Ga (Hiesinger et al., 2003, 2011). The youngest mare basalts are concentrated in the northern Oceanus Procellarum region, centrally located in the PKT, characterized by elevated abundances of radioactive heat-producing elements such as U, Th, and K (e.g., Haskin, 1998; Jolliff et al., 2000; Prettyman et al., 2006).

One (P58, 1.33 Ga) of the five young mare units (others are P56, P57, P59, and P60) occurs in the Rümker region (Hiesinger et al., 2003, 2011). P58 nearly corresponds with EM^3 (1.51 Ga) and Em4 (1.21 Ga) in the current study. These two mare units have extremely young model ages, especially Em4, which is one of the youngest mare units on the Moon revealed by crater counting methods (Hiesinger et al., 2000, 2003, 2010, 2011; Morota et al., 2011). These high-Ti basalts (EM^3 and Em4) are younger than any existing lunar samples, including the youngest lunar meteorites (NWA032, 2.8 Ga; Fagan et al., 2002).

These factors led scientists to place the return of samples from these young mare basalt units as a top priority for future lunar exploration (National Research Council, 2007). Analysis of these samples in Earth laboratories will (1) provide exact radiometric dates for the extrusive events and thereby improve our knowledge of lunar chronology, (2) provide new knowledge of the nature of the geochemistry and mineralogy of basaltic source regions and their isotopic and trace element characteristics, (3) permit the testing of the role of the radioactive PKT in the generation of late-stage mare volcanism, and (4) improve understanding of the thermal state of the lunar interior in late lunar history, thereby testing and constraining models for the thermal evolution of the Moon.

Finally, the ages of these young basalts are currently determined by impact CSFD of the craters superposed on the units, calibrated by counts of craters on geologic units radiometrically dated in Earth laboratories from samples collected by Apollo and Luna missions. However, no samples have currently been returned from such young lunar units, and, thus, there is a high level of uncertainty in the size-frequency distribution ages in the last half of lunar impact chronology (Crawford et al., 2007; Stöffler et al., 2006; Stöffler & Ryder, 2001). Return of samples from these young basalts would thus serve to provide an absolute calibration for the cratering flux, an accomplishment

that will assist in our understanding of the geological evolution of planetary bodies throughout the Solar System (Crawford et al., 2007; Kring & Durda, 2012; National Research Council, 2007).

Other Geological Units The Imbrian-aged mare basalts in the area are low-Ti (Im1) to very low-Ti (Im2 and IM[3]) and dominated by intermediate composition pyroxene such as pigeonite. Samples from the Imbrian-aged mare basalts are similar in age (Imbrian-aged) and composition (very low-Ti to low Ti) to Apollo and Luna samples (Apollo 12 and 15 missions collected low-Ti basalts, and Apollo 17 and Luna 24 missions collected very low-Ti basalts). Samples from these units can provide important ground truth to help evaluate the low-Ti and VLT basalt petrogenesis models (Neal & Taylor, 1992) and reveal mantle source region properties (Snyder et al., 1992).

Steep-sided lunar domes and volcanic complexes have not been sampled in previous lunar missions. Samples from the domes on Mons Rümker and the silica-rich East Dome can reveal the elemental and mineral compositions of these surface materials, providing ground truth for remote sensing data/methods. Geochemical analysis can constrain the nature of magma source regions and test the existing models and mechanism of dome formation (Head & Wilson, 2017; Wilson & Head, 2003; Wilson & Head, 2017). Samples from the silica-rich East Dome can reveal the nature of silica-rich volcanism on the Moon, the effects of thorium concentration on red spot formation, and lead to further understanding of the late stage magmatic evolution of the Moon (Glotch et al., 2010, 2011; Hagerty et al., 2006).

Proposed Sampling Sites

Comparing the potential science return of each of the geologic units, we suggest that the Em4 unit has the richest scientific value and should be the top priority landing unit for the CE5 mission. Sampling anywhere in the Em4 unit could return young mare materials and fulfill the desired scientific goals. Thus, we propose the entire Em4 unit as a candidate from which to choose a specific landing site (proposed landing site A). Our suggestion to land in the young mare unit is supported by Ling et al. (2017) and Jolliff et al. (2017).

Furthermore, sampling the regolith developed on the Em4 unit could readily return samples of the underlying older materials (i.e., Imbrian-aged mare basalts) excavated by impacts. In addition, the secondary clusters and crater rays in the area indicate that material in the soils is likely to contain admixed ejecta from distant craters, such as Copernicus, Harpalus, and Pythagoras. Finally, ejecta from craters superposed on the exposed kipukas in the Em4 unit may provide fragments from the underlying Imbrium basin ejecta unit. In contrast, landing in the western maria is likely to return only the Imbrian-aged mare deposits and possible ejecta and fragments (similar in age and composition to Apollo and Luna samples) that could also be sampled in Em4 unit.

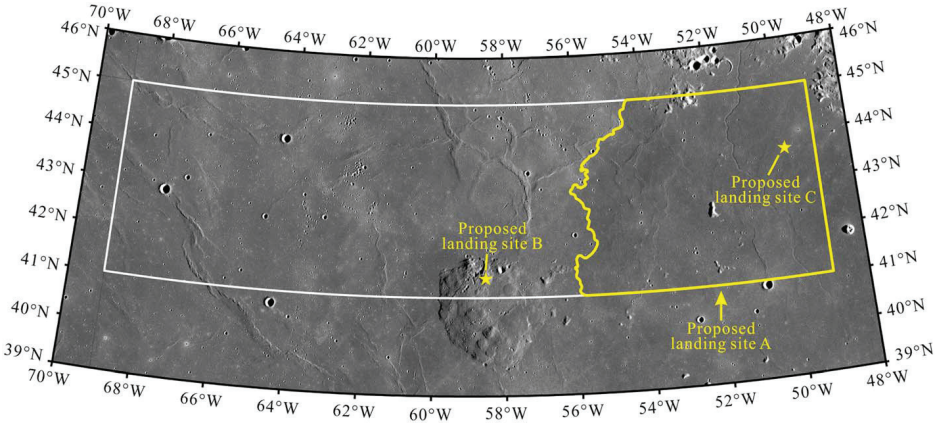

Figure 5.13: The location of proposed landing sites in this study. Landing site A indicates the region of the Em4 mare unit.

Mons Rümker and the silica-rich East Dome are also valuable sampling units of significant scientific interest. We list these as the second and third priority landing sites for the CE5 mission and propose two landing sites within each unit (proposed landing sites B and C). Proposed landing site B is at a steep-sided dome on Mons Rümker (centered at 58.53°W, 41.41°N). This steep-sided dome is ~7.5 km in diameter. The top of this dome is flat and may be suitable for landing (<2°). The third proposed landing site is on the silica-rich East Dome (centered at 49.85°W, 43.68°N), which is discussed in detail in sections 3.2.4 and 4.1.1.

These three proposed landing sites (Fig. 5.14 and Table 5.3) can be further evaluated to assess the engineering requirements (e.g., surface slopes, rock abundance, and crater density) in a future study.

Engineering Advantages of Sampling the Em4 Unit

The proposed landing site A (Em4) is not only the very highest scientific priority but also very favorable from an engineering and landing safety point of view. It offers a relatively safe landing site, which is regionally flat, young, and is really homogeneous and so does not require pin-point landing. These benefits are listed:

1 The Em4 unit is regionally flat (1.1°, mean slope) and very similar to the topography and slopes observed at the CE3 landing site. CE3 landing data can be used to simulate the nature of the landing region.

2 The Em4 unit is very young (1.21 Ga), which means it contains fewer large impact craters and has smoother topography.

3 The Em4 unit is very widely distributed and continuous in the CE5 landing region (Figures 11 and 14), making up almost one third of the total landing region. Landing and sampling anywhere in the Em4 unit would fulfill the primary scientific objectives of the mission.

4 The Em4 unit is a mare unit very similar in age and surface characteristics to that explored by CE3 (Qiao et al., 2014; Zhao et al., 2014) and suited for soft landing by CE5. Ground penetrating radar data from the CE3 landing site (Fa et al., 2015; Xiao et al., 2015; Yuan et al., 2017; Zhang et al., 2015) show the type of vertical structure to be expected in the CE5 Em4 unit.

5.1.5. Conclusions

We systematically studied the topography, geomorphology, composition, and surface properties of the Rümker region, the target region for the CE5 sample return mission. Principle results include the following:

1 The Rümker region is an unexplored and unsampled area in northern Oceanus Procellarum. It is located within the unusual PKT, characterized by levels of high heat producing elements.

2 Fourteen geologic units were defined and mapped, including seven mare units (Im1, Im2, IM^3, Em1, Em2, EM^3, and Em4), three Rümker plateau units (IR1, IR2, and IR3), one nonmare highland units (Ith), and three dome units (ld, sd, and Idm).

3 The Rümker region experienced long (~3.7 to ~1.2 Ga) and complex volcanic activity, forming multiple volcanic units with distinct composition and mineralogy.

4 Three candidate landing sites are proposed for the CE5 mission. We interpret the Em4 unit (proposed landing site A) to be the most scientifically valuable and also the safest from a landing and engineering point of view and should be listed as the top priority for the CE5 mission.

Acknowledgments

This study is supported by the National Natural Science Foundation of China (41772050 and 41773061), the Fundamental Research Funds for the Central Universities, and the China University of Geosciences, Wuhan (CUGL160402 and CUG2017G02), MOST Special Fund from the State Key Laboratory of Geological Processes and Mineral Resources, China University of Geosciences (MSFGPMR05). Wang is supported by the National Natural Science Foundation of China (11502277). The work of Flahaut is supported by the CNES (Luna/ExoMars APR). Martinot is supported by the Netherlands Organization for

Table 5.3: Proposed Landing Sites and Their Scientific Values

Landing site	Center coordinates	Unit	Local feature	Scientific values
A	58.53°W, 41.41°N	Em4	Young mare	1. Unsampled new rock type 2. Extent of lunar volcanism duration 3. Properties of late stage lunar volcanism 4. Deep mantle properties 5. Concentration mechanism of Th and its role in late stage volcanism 6. Precise isotopic age of young volcanism 7. Impact cratering flux history 8. Improving CSFD dating method and chronology
B	49.85°W, 43.68°N	sd	Mons Rümker	1. Origin of lunar domes 2. Property of the magma source 3. The duration of Mons Rümker volcanism 4. Impact cratering flux history 5. Improve CSFD dating method and chronology
C		ldm	Silica dome	1. Rock-type characteristic of the dome 2. Origin of the silica-rich domes 3. Properties of the magma source 4. Evolution of magmas 5. Influence of Th in silica dome formation 6. The mechanism of Th concentration

Scientific Research (NWO) grant. The Kaguya TC Morning Map data, TC DTM data, and Multiband Imager (MI) data are available from the SELENE Data Archive (http://darts.isas.jaxa.jp/planet/pdap/selene/). The LRO WAC Data and NAC data are available from the LROC website (http://lroc.sese.asu.edu/). The LOLA and Kaguya TC merged hillshade map are available from USGS Astrogeology Science Center https://astrogeology.usgs.gov/). The M^3 Level 2 data are archived in the Planetary Data System. Spectra for lunar minerals are available from RELAB reference library (http://www.planetary.brown.edu/relab/). The thorium abundance data by Prettyman et al. (2006) are available from the Planetary Data System Geoscience Node (http://pds-geosciences.wustl.edu/lunar/lp-l-grs-5-elem-abundancev1/). The crater counting files (.scc) are in Data Set S1 in the supporting information. Crater counting was carried using CraterTools (Kneissl et al., 2011). Statistics on CSFD based on crater counting files (.scc) were performed on CraterstatsII (Michael & Neukum, 2010). CraterTools, CraterstatsII, and the introduction on how to use these software are available from http://www.geo.fuberlin.de/en/geol/fachrichtungen/planet/software/index.html. The geologic map of the Rümker region (Fig. 5.13) has been uploaded individually to Figure S1 in the supporting information.

Bibliography

- Adams, J. B. (1974). Visible and near-infrared diffuse reflectance spectra of pyroxenes as applied to remote sensing of solid objects in the solar system. Journal of Geophysical Research, 79, 4829–4836. https://doi.org/10.1029/JB079i032p04829

- Adams, J. B., & McCord, T. B. (1972). Electronic spectra of pyroxenes and interpretation of telescopic spectral reflectivity curves of the Moon. Proceedings of 3rd Lunar Science Conference, 3 (pp. 3021–3024).

- Barker, M. K., Mazarico, E., Neumann, G. A., Zuber, M. T., Haruyama, J., & Smith, D. E. (2016). A new lunar digital elevation model from the Lunar Orbiter Laser Altimeter and SELENE Terrain Camera. Icarus, 273, 346–355. https://doi.org/10.1016/j.icarus.2015.07.039

- Besse, S., Sunshine, J., Staid, M., Boardman, J., Pieters, C., Guasqui, P., et al. (2013). A visible and near-infrared photometric correction for Moon Mineralogy Mapper (M3). Icarus, 222(1), 229–242. https://doi.org/10.1016/j.icarus.2012.10.036

- Blewett, D. T., Lucey, P. G., Hawke, B. R., & Jolliff, B. L. (1997). Clementine images of the lunar sample-return stations: Refinement of FeO and TiO2 mapping techniques. Journal of Geophysical Research, 102, 16,319–16,325. https://doi.org/10.1029/97JE01505

- Boardman, J. W., Pieters, C. M., Green, R. O., Lundeen, S. R., Varanasi, P., Nettles, J., et al. (2011). Measuring moonlight: An overview of the spatial properties, lunar coverage, selenolocation, and related level 1B products of the Moon Mineralogy Mapper. Journal of Geophysical Research, 116, E00G14. https://doi.org/10.1029/2010JE003730

- Boroughs, L. L., & Spudis, P. D. (2001). The stratigraphy of lava flows in northern Oceanus Procellarum, Moon. Paper Presented at 32nd Lunar and Planetary Science Conference, Lunar and Planetary Institute, Houston.

– Boyce, J. M., & Jonnson, D. A. (1978). Ages of flow units in the far eastern maria and implications for basin-filling history. Proceedings of 9th Lunar and Planetary Science Conference (pp. 2717–2728).

– Burns, R. G., Vaughan, D. J., Abu-Eid, R. M., Witner, M., & Morawski, A. (1973). Spectral evidence for Cr3+, Ti3+, Fe2+ rather than Cr2+ and Fe3+ in lunar ferromagnesian silicates. Proceedings of 4th Lunar Science Conference, 1 (pp. 983-994).

– Campbell, B. A., Hawke, B. R., & Campbell, D. B. (2009). Surface morphology of domes in the Marius Hills and Mons Rümker regions of the Moon from Earth-based radar data. Journal of Geophysical Research, 114, E01001. https://doi.org/10.1029/2008JE003253

– Chen, Y., Li, C., Ren, X., Liu, J., Wu, Y., Lu, Y., et al. (2018). The thickness and volume of young basalts within Mare Imbrium. Journal of Geophysical Research: Planets, 123, 630–645. https://doi.org/10.1002/2017JE005380

– Clark, R. N., Pieters, C. M., Green, R. O., Boardman, J. W., & Petro, N. E. (2011). Thermal removal from near-infrared imaging spectroscopy data of the Moon. Journal of Geophysical Research, 116, E00G16. https://doi.org/10.1029/2010JE003751

– Cloutis, E. A., & Gaffey, M. J. (1991). Pyroxene spectroscopy revisited: Spectral-compositional correlations and relationship to geothermometry. Journal of Geophysical Research, 96(E5), 22,809–22,826. https://doi.org/10.1029/91JE02512

– Coman, E. O., Joliff, B. L., & Carpenter, P. (2018). Mineralogy and chemistry of Ti-bearing lunar soils: Effects on reflectance spectra and remote sensing observations. Icarus, 306, 243–255. https://doi.org/10.1016/j.icarus.2018.02.008

– Crawford, I.A., Anand, M., Cockell, C. S., Falcke, H., Green, D.A., Jaumann, R., & Wieczorek, M. A. (2012). Backtothe Moon: The scientific rationale for resuming lunar surface exploration. Planetary and Space Science, 74(1), 3–14. https://doi.org/10.1016/j.pss.2012.06.002

– Crawford, I. A., Fagents, S., & Joy, K. (2007). Full Moon exploration. Astronomy & Geophysics, 48, 3.18–3.21. https://doi.org/10.1111/j.1468-4004.2007.48318.x

– Crawford, I. A., & Joy, K. H. (2014). Lunar exploration: Opening a window into the history and evolution of the inner solar system. Philosophical Transactions of the Royal Society A, 372(2024), 20130315. https://doi.org/10.1098/rsta.2013.0315

– Dmitrovsky, A. A., Zacharova, M. A., & Slyuta, E. N. (2017). Preliminary data on the age ofthe Mons Rumker Volcanic Province. Paper Presented at 48th Lunar and Planetary Science Conference, Lunar and Planetary Institute, The Woodlands.

– Eliason, E. M., McEwen, A. S., Robinson, M. S., Lee, E. M., Becker, T., Gaddis, L., et al. (1999). Digital processing for a global multispectral map of the Moon from the Clementine UVVIS Imaging Instrument. Paper presented at 30th Lunar and Planetary Science Conference, Lunar and Planetary Institute, Houston.

- Elphic, R. C. (2002). Lunar Prospector Neutron Spectrometer constraints on TiO2. Journal of Geophysical Research, 107(E4), 5024. https://doi.org/10.1029/2000JE001460

- Fa, W., Zhu, M.-H., Liu, T., & Plescia, J. B. (2015). Regolith stratigraphy at the Chang'E-3 landing site as seen by lunar penetrating radar. Geophysical Research Letters, 42, 10,179–10,187. https://doi.org/10.1002/2015GL066537

- Fagan, T. J., Taylor, G. J., Keil, K., Bunch, T. E., Wittke, J. H., Korotev, R. L., et al. (2002). Northwest Africa 032: Product of lunar volcanism. Meteoritics & Planetary Science, 37(3), 371–394. https://doi.org/10.1111/j.1945-5100.2002.tb00822.x

- Farrand, W. H., Kramer, G. Y., Gaddis, L. R., & Videen, G. (2015). Spectral and photometric examination of pyroclastic mantles over Mons Rumker. Paper Presented at 46th Lunar and Planetary Science Conference, Lunar and Planetary Institute, The Woodlands.

- Fischer, E. M., & Pieters, C. M. (1994). Remote determination of exposure degree and iron concentration of lunar soils using VIS-NIR spectroscopic methods. Icarus, 111(2), 475–488. https://doi.org/10.1006/icar.1994.1158

- Flahaut, J., Blanchette-Guertin, J.-F., Jilly, C., Sharma, P., Souchon, A., van Westrenen, W., & Kring, D. A. (2012). Identification and characterization of science-rich landing sites for lunar lander missions using integrated remote sensing observations. Advances in Space Research, 50(12), 1647–1665. https://doi.org/10.1016/j.asr.2012.05.020

- Glotch, T. D., Hagerty, J. J., Lucey, P. G., Hawke, B. R., Giguere, T. A., Arnold, J. A., et al. (2011). The Mairan domes: Silicic volcanic constructs on the Moon. Geophysical Research Letters, 38, L21204. https://doi.org/10.1029/2011GL049548

- Glotch, T. D., Lucey, P. G., Bandfield, J. L., Greenhagen, B. T., Thomas, I. R., Elphic, R. C., et al. (2010). Highly silicic compositions on the Moon. Science, 329(5998), 1510–1513. https://doi.org/10.1126/science.1192148

- Green, R. O., Pieters, C., Mouroulis, P., Eastwood, M., Boardman, J., Glavich, T., et al. (2011). The Moon Mineralogy Mapper (M^3) imaging spectrometer for lunar science: Instrument description, calibration, on-orbit measurements, science data calibration and on-orbit validation. Journal of Geophysical Research, 116, E00G19. https://doi.org/10.1029/2011JE003797

- Hagerty, J. J., Lawrence, D. J., Hawke, B. R., Vaniman, D. T., Elphic, R. C., & Feldman, W. C. (2006). Refined thorium abundances for lunar red spots: Implications for evolved, nonmare volcanism on the Moon. Journal of Geophysical Research, 111, E06002. https://doi.org/10.1029/2005JE002592

- Haruyama, J., Matsunaga, T., Ohtake, M., Morota, T., Honda, C., Yokota, Y., et al. (2008). Global lunar-surface mapping experiment using the Lunar Imager / Spectrometer on SELENE. Earth, Planets and Space, 60(4), 243–255. https://doi.org/10.1186/bf03352788

- Haruyama, J., Ohtake, M., Matsunaga, T., Otake, H., Ishihara, Y., Masuda, K., et al. (2014). Data products ofSELENE (Kaguya) Terrain Camera for future lunar missions. Paper presented at 45th Lunar and Planetary Science Conference, Lunar and Planetary Institute, The Woodlands.

– Haskin, L. A. (1998). The Imbrium impact event and the thorium distribution at the lunar highlands surface. Journal of Geophysical Research, 103, 1679–1689. https://doi.org/10.1029/97JE03035

– Haskin, L. A., Gillis, J. J., Korotev, R. L., & Jolliff, B. L. (2000). The materials of the lunar Procellarum KREEP Terrane: A synthesis of data from geomorphological mapping, remote sensing, and sample analyses. Journal of Geophysical Research, 105, 20,403–20,415. https://doi.org/10.1029/1999JE001128

– Head, J. W. (1977). Regional distribution of Imbrium Basin deposits: Relationship to pre-Imbrian topography and mode of emplacement. In The Imbrium Consortium (Ed.), Interdisciplinary studies by the Imbrium Consortium (pp. 120–125). Cambridge: The Imbrium Consortium.

– Head, J. W. (1982). Lava flooding of ancient planetary crusts: Geometry, thickness, and volumes of flooded lunar impact basins. The Moon and the Planets, 26(1), 61–88. https://doi.org/10.1007/bf00941369

– Head, J. W., & Gifford, A. (1980). Lunar mare domes: Classification and modes of origin. The Moon and the Planets, 22(2), 235–258. https://doi.org/10.1007/bf00898434

– Head, J. W., & McCord, T. B. (1978). Imbrian-age highland volcanism on the Moon: The Gruithuisen and Mairan domes. Science, 199(4336), 1433–1436. https://doi.org/10.1126/science.199.4336.1433

– Head, J. W., & Wilson, L. (2017). Generation, ascent and eruption of magma on the Moon: New insights into source depths, magma supply, intrusions and effusive/explosive eruptions (part 2: Predicted emplacement processes and observations). Icarus, 283, 176–223. https://doi.org/10.1016/j.icarus.2016.05.031

– Hiesinger, H. (2006). New views of lunar geoscience: An introduction and overview. Reviews in Mineralogy and Geochemistry, 60(1), 1–81. https://doi.org/10.2138/rmg.2006.60.1

– Hiesinger, H., Head, J. W., Wolf, U., Jaumann, R., & Neukum, G. (2002). Lunar mare basalt flow units: Thicknesses determined from crater size-frequency distributions. Geophysical Research Letters, 29(8), 1248. https://doi.org/10.1029/2002GL014847

– Hiesinger, H., Head, J. W., Wolf, U., Jaumann, R., & Neukum, G. (2003). Ages and stratigraphy of mare basalts in Oceanus Procellarum, Mare Nubium, Mare Cognitum, and Mare Insularum. Journal of Geophysical Research, 108(E7), 5056. https://doi.org/10.1029/2002JE001985

– Hiesinger, H., Head, J. W., Wolf, U., Jaumann, R., & Neukum, G. (2010). Ages and stratigraphy of lunar mare basalts in Mare Frigoris and other nearside maria based on crater size-frequency distribution measurements. Journal of Geophysical Research, 115, E03003. https://doi.org/10.1029/2009JE003380

– Hiesinger, H., Head, J. W., Wolf, U., Jaumann, R., & Neukum, G. (2011). Ages and stratigraphy of lunar mare basalts: A synthesis. Geological Society of America Special Papers, 477,1–51. https://doi.org/10.1130/2011.2477(01

- Hiesinger, H., Jaumann, R., Neukum, G., & Head, J. W. (2000). Ages of mare basalts on the lunar nearside. Journal of Geophysical Research, 105, 29,239–29,275. https://doi.org/10.1029/2000JE001244

- Horgan, B. H. N., Cloutis, E. A., Mann, P., & Bell, J. F. (2014). Near-infrared spectra of ferrous mineral mixtures and methods for their identification in planetary surface spectra. Icarus, 234, 132–154. https://doi.org/10.1016/j.icarus.2014.02.031

- Hurwitz, D. M., Head, J. W., & Hiesinger, H. (2013). Lunar sinuous rilles: Distribution, characteristics, and implications for their origin. Planetary and Space Science, 79-80,1–38. https://doi.org/10.1016/j.pss.2012.10.019

- Hurwitz, D. M., Head, J. W., Wilson, L., & Hiesinger, H. (2012). Origin of Lunar Sinuous Rilles: Modeling effects of gravity, surface slope, and lava composition on erosion rates during the formation of Rima Prinz. Journal of Geophysical Research, 117, E00H14. https://doi.org/10.1029/2011JE004000

- Ivanov, M. A., Head, J. W., & Bystrov, A. (2016). The lunar Gruithuisen silicic extrusive domes: Topographic configuration, morphology, ages, and internal structure. Icarus, 273, 262–283. https://doi.org/10.1016/j.icarus.2015.12.015

- Jaumann, R., Hiesinger, H., Anand, M., Crawford, I. A., Wagner, R., Sohl, F., et al. (2012). Geology, geochemistry, and geophysics of the Moon: Status of current understanding. Planetary and Space Science, 74(1), 15–41. https://doi.org/10.1016/j.pss.2012.08.019

- Jolliff, B. L., Gillis, J. J., Haskin, L. A., Korotev, R. L., & Wieczorek, M. A. (2000). Major lunar crustal terranes: Surface expressions and crust-mantle origins. Journal of Geophysical Research, 105, 4197–4216. https://doi.org/10.1029/1999JE001103

- Jolliff, B. L., Wang, A., Ling, Z., & Zhang, J. (2017). Scientific context and objectives for Chang'E-4 and Chang'E-5 missions. Paper Presented at the 3rd Beijing International Forum on Lunar and Deep-Space Exploration, Chinese Academy of Sciences, Beijing, China.

- Kato, S., Morota, T., Yamaguchi, Y., Watanabe, S., Otake, H., & Ohtake, M. (2017). Magma source transition of lunar mare volcanism at 2.3 Ga. Meteoritics & Planetary Science, 52(9), 1899–1915. https://doi.org/10.1111/maps.12896

- Kneissl, T., Gasselt, S. v., & Neukum, G. (2011). Map-projection-independent crater size-frequency determination in GIS environments-New software tool for ArcGIS. Planetary and Space Science, 59(11-12), 1243–1254. https://doi.org/10.1016/j.pss.2010.03.015

- Kreslavsky, M. A., Head, J. W., Neumann, G. A., Rosenburg, M. A., Aharonson, O., Smith, D. E., & Zuber, M. T. (2013). Lunar topographic roughness maps from Lunar Orbiter Laser Altimeter (LOLA) data: Scale dependence and correlation with geologic features and units. Icarus, 226(1), 52–66. https://doi.org/10.1016/j.icarus.2013.04.027

- Kring, D. A., & Durda, D. D. (Eds.) (2012). A Global Lunar Landing Site study to provide the scientific context for exploration ofthe Moon. Houston: Lunar and Planetary Institute.

– Laneuville, M., Wieczorek, M. A., Breuer, D., & Tosi, N. (2013). Asymmetric thermal evolution of the Moon. Journal of Geophysical Research: Planets, 118, 1435–1452. https://doi.org/10.1002/jgre.20103

– Lawrence, D. J., Feldman, W. C., Barraclough, B. L., Binder, A. B., Elphic, R. C., Maurice, S., et al. (2000). Thorium abundances on the lunar surface. Journal of Geophysical Research, 105(E8), 20,307–20,331. https://doi.org/10.1029/1999JE001177

– Lawrence, S. J., Stopar, J. D., Hawke, B. R., Greenhagen, B. T., Cahill, J. T. S., Bandfield, J. L., et al. (2013). LRO observation of morphology and surface roughness of volcanic cones and lobate lava flows in the Marius Hills. Journal of Geophysical Research: Planets, 118, 615–634. https://doi.org/10.1002/jgre.20060

– Lemelin, M., Lucey, P. G., Gaddis, L. R., Hare, T., & Ohtake, M. (2016). Global map products from the Kaguya Multiband Imager at 512 ppd: Minerals, FeO, and OMAT. Paper Presented at 47th Lunar and Planetary Science Conference, Lunar and Planetary Institute, The Woodlands.

– Ling, Z., Jolliff, B. L., Wang, A., Li, C., Liu, J., Zhang, J., et al. (2015). Correlated compositional and mineralogical investigations at the Chang'e-3 landing site. Nature Communications, 6(1), 8880. https://doi.org/10.1038/ncomms98805

– Ling, Z., Liu, C., Jolliff, B. L., Zhang, J., Li, B., Sun, L., Chen, J., et al. (2017). Spectral and mineralogical analysis of Chang'E-5 candidate landing site in northern Oceanus Procellarum. Paper presented at 48th Lunar and Planetary Science Conference, Lunar and Planetary Institute, The Woodlands.

– Lucey, P. G., Blewett, D. T., Taylor, G. J., & Hawke, B. R. (2000). Imaging of lunar surface maturity. Journal of Geophysical Research, 105, 20, 377–20,386. https://doi.org/10.1029/1999JE001110

– Martinot, M., Besse, S., Flahaut, J., Quantin-Nataf, C., Lozac'h, L., & Westrenen, W. v. (2018). Mineralogical diversity and geology of Humboldt crater derived using Moon Mineralogy Mapper data. Journal of Geophysical Research: Planets, 123, 612–629. https://doi.org/10.1002/2017JE005435

– Maxwell, T. A., El-Baz, F., & Ward, S. H. (1975). Distribution, morphology, and origin of ridges and arches in Mare Serenitatis. Geological Society ofAmerica Bulletin, 86(9), 1273–1278. https://doi.org/10.1130/0016-7606(1975)86%3C1273:DMAOOR%3E2.0.CO;2

– Michael, G. G., & Neukum, G. (2010). Planetary surface dating from crater size-frequency distribution measurements: Partial resurfacing events and statistical age uncertainty. Earth and Planetary Science Letters, 294(3–4), 223–229. https://doi.org/10.1016/j.epsl.2009.12.041

– Morota, T., Haruyama, J., Ohtake, M., Matsunaga, T., Honda, C., Yokota, Y., et al. (2011). Timing and characteristics of the latest mare eruption on the Moon. Earth and Planetary Science Letters, 302(3–4), 255–266. https://doi.org/10.1016/j.epsl.2010.12.028

– Mustard, J. F., Pieters, C. M., Isaacson, P. J., Head, J. W., Besse, S., Clark, R. N., et al. (2011). Compositional diversity and geologic insights of the Aristarchus crater from Moon Mineralogy Mapper data. Journal of Geophysical Research, 116, E00G12. https://doi.org/10.1029/2010JE003726

- National Research Council (2007). The scientific context for exploration of the Moon. Washington DC: National Academies Press. Neal, C. R. (2009). The Moon 35 years after Apollo: What's left to learn? Chemie der Erde - Geochemistry, 69(1), 3–43. https://doi.org/10.1016/j.chemer.2008.07.002

- Neal, C. R., & Taylor, L. A. (1992). Petrogenesis of mare basalts: A record of lunar volcanism. Geochimica et Cosmochimica Acta, 56(6), 2177–2211. https://doi.org/10.1016/0016-7037(92)90184-k

- Neukum, G., Ivanov, B. A., & Hartmann, W. K. (2001). Cratering records in the inner solar system in relation to the lunar reference system. Space Science Reviews, 96(1/4), 55–86. https://doi.org/10.1023/A:1011989004263

- Ohtake, M., Haruyama, J., Matsunaga, T., Yokota, Y., Morota, T., & Honda, C. (2008). Performance and scientific objectives of the SELENE (KAGUYA) Multiband Imager. Earth, Planets and Space, 60(4), 257–264. https://doi.org/10.1186/bf03352789

- Otake, H., Ohtake, M., & Hirata, N. (2012). Lunar iron and titanium abundance algorithms based on SELENE (Kaguya) Multiband Imager data. Paper Presented at 43rd Lunar and Planetary Science Conference, Lunar and Planetary Institute, The Woodlands.

- Page, N. J. (1970). Geologic map of the Cassini quadrangle of the Moon (Map I-666). Flagstaff: USGS Astrogeology Science Center. Pieters, C. M. (1978). Mare basalt types on the front side of the Moon—A summary of spectral reflectance data. Preceedings of 9th Lunar and Planetary Science Conference (pp. 2825–2849).

- Pieters, C. M. (1986). Composition of the lunar highland crust from near-infrared spectroscopy. Reviews of Geophysics, 24, 557–578. https://doi.org/10.1029/RG024i003p00557

- Pieters, C. M., Boardman, J., Buratti, B., Chatterjee, A., Clark, R., Glavich, T., et al. (2009). The Moon Mineralogy Mapper (M^3) on Chandrayaan-1. Current Science, 96(4), 500–505.

- Pieters, C. M., Staid, M. I., Fischer, E. M., Tompkins, S., & He, G. (1994). A sharper view of impact craters from Clementine data. Science, 266(5192), 1844–1848. https://doi.org/10.1126/science.266.5192.1844

- Pike, R. J. (1974). Depth/diameter relations of fresh lunar craters: Revision from spacecraft data. Geophysical Research Letters, 1, 291–294. https://doi.org/10.1029/GL001i007p00291

- Prettyman, T. H., Hagerty, J. J., Elphic, R. C., Feldman, W. C., Lawrence, D. J., McKinney, G. W., & Vaniman, D. T. (2006). Elemental composition of the lunar surface: Analysis of gamma ray spectroscopy data from Lunar Prospector. Journal of Geophysical Research, 111, E12007. https://doi.org/10.1029/2005JE002656

- Qiao, L., Xiao, L., Zhao, J., Huang, Q., & Haruyama, J. (2014). Geological features and evolution history of Sinus Iridum, the Moon. Planetary and Space Science, 101,37–52. https://doi.org/10.1016/j.pss.2014.06.007

– Robinson, M. S., Brylow, S. M., Tschimmel, M., Humm, D., Lawrence, S. J., Thomas, P. C., et al. (2010). Lunar Reconnaissance Orbiter Camera (LROC) instrument overview. Space Science Reviews, 150(1–4), 81–124.
https://doi.org/10.1007/s11214-010-9634-2

– Rosenburg, M. A., Aharonson, O., Head, J. W., Kreslavsky, M. A., Mazarico, E., Neumann, G. A., et al. (2011). Global surface slopes and roughness of the Moon from the Lunar Orbiter Laser Altimeter. Journal of Geophysical Research, 116, E02001. https://doi.org/10.1029/2010JE003716

– Sato, H., Robinson, M. S., Lawrence, S. J., Denevi, B. W., Hapke, B., Joliff, B. L., & Hiesinger, H. (2017). Lunar mare TiO_2 abundances estimated from UV/Vis reflectance. Icarus, 296, 216–238. https://doi.org/10.1016/j.icarus.2017.06.013

– Scholten, F., Oberst, J., Matz, K. D., Roatsch, T., Wählisch, M., Speyerer, E. J., & Robinson, M. S. (2012). GLD100: The near-global lunar 100 m raster DTM from LROC WAC stereo image data. Journal of Geophysical Research, 117, E00H17. https://doi.org/10.1029/2011JE003926

– Scott, D. H., & Eggleton, R. E. (1973). Geologic map of the Rümker quadrangle of the Moon (Map I805). Flagstaff: USGS Astrogeology Science Center.

– Scott, D. H., McCauley, J. F., & West, M. N. (1977). Geologic map of the west side of the Moon (Map I-1034). Flagstaff: USGS Astrogeology Science Center. Sharpton, V. L., & Head, J. W. (1988). Lunar mare ridges: Analysis of ridge-crater intersections and implications for the tectonic origin of mare ridges. Proceedings of 18th Lunar and Planetary Science Conference (pp. 307–317).

– Smith, E. I. (1973). Identification, distribution and significance of lunar volcanic domes. The Moon, 6(1-2), 3–31. https://doi.org/10.1007/bf02630650

– Smith, E. I. (1974). Rümker hills: A lunar volcanic dome complex. The Moon, 10(2), 175–181. https://doi.org/10.1007/bf00655718 Snape, J. F., Nemchin, A. A., Grange, M. L., Bellucci, J. J., Thiessen, F., & Whitehouse, M. J. (2016). Phosphate ages in Apollo 14 breccias: Resolving multiple impact events with high precision U-Pb SIMS analyses. Geochimica et Cosmochimica Acta, 174,13–29. https://doi.org/10.1016/j.gca.2015.11.005

– Snyder, G. A., Taylor, L. A., & Neal, C. R. (1992). A chemical model for generating the sources of mare basalts: Combined equilibrium and fractional crystallization of the lunar magmasphere. Geochimica et Cosmochimica Acta, 56(10), 3809–3823. https://doi.org/10.1016/0016-7037(92)90172-F

– Spudis, P. D., Hawke, B. R., & Lucey, P. G. (1988). Materials and formation of the Imbrium basin. Proceedings of 18th Lunar and Planetary Science Conference (pp. 155–168).

– Staid, M. I., & Pieters, C. M. (2001). Mineralogy of the last lunar basalts: Results from Clementine. Journal of Geophysical Research, 106, 27,887–27,900. https://doi.org/10.1029/2000JE001387 Staid, M. I., Pieters, C. M., Besse, S., Boardman, J., Dhingra, D., Green, R., et al. (2011). The mineralogy of late stage lunar volcanism as observed by the Moon Mineralogy Mapper on Chandrayaan-1. Journal of Geophysical Research, 116, E00G10. https://doi.org/10.1029/2010JE003735

- Stöffler, D., & Ryder, G. (2001). Stratigraphy and isotope ages of lunar geologic units: Chronological standard for the inner solar system. In R. Kallenbach, J. Geiss, & W. K. Hartmann (Eds.), Chronology and evolution of Mars (pp. 9–54). Dordrecht: Springer.

- Stöffler, D., Ryder, G., Ivanov, B. A., Artemieva, N. A., Cintala, M. J., & Grieve, R. A. F. (2006). Cratering history and lunar chronology. Reviews in Mineralogy and Geochemistry, 60(1), 519–596. https://doi.org/10.2138/rmg.2006.60.05

- Strom, R. G. (1972). Lunar mare ridges, rings and volcanic ring complexes. In S. K. Runcorn & H. C. Urey (Eds.), The Moon (pp. 187–215). Dordrecht: Springer. https://doi.org/10.1007/978-94-010-2861-5_19

- Taylor, S. R. (2014). The Moon re-examined. Geochimica et Cosmochimica Acta, 141, 670–676. https://doi.org/10.1016/j.gca.2014.06.031

- Taylor, S. R., Taylor, G. J., & Taylor, L. A. (2006). The Moon: A Taylor perspective. Geochimica et Cosmochimica Acta, 70(24), 5904–5918. https://doi.org/10.1016/j.gca.2006.06.262

- Thomson, B. J., Grosfils, E. B., Bussey, D. B. J., & Spudis, P. D. (2009). A new technique for estimating the thickness of mare basalts in Imbrium Basin. Geophysical Research Letters, 36, L12201. https://doi.org/10.1029/2009GL037600

- Wagner, R., Head, J. W., Wolf, U., & Neukum, G. (2002). Stratigraphic sequence and ages of volcanic units in the Gruithuisen region of the Moon. Journal of Geophysical Research, 107(E11), 5104. https://doi.org/10.1029/2002JE001844

- Wagner, R., Head, J. W., Wolf, U., & Neukum, G. (2010). Lunar red spots: Stratigraphic sequence and ages of domes and plains in the Hansteen and Helmet regions on the lunar nearside. Journal of Geophysical Research, 115, E06015. https://doi.org/10.1029/2009JE003359

- Wang, Q., & Xiao, L. (2017). China's Lunar Exploration Programme. Paper presented at Lunar Exploration Analysis 2017, Lunar and Planetary Institute, The Woodlands.

- Weider, S. Z., Crawford, I. A., & Joy, K. H. (2010). Individual lava flow thicknesses in Oceanus Procellarum and Mare Serenitatis determined from Clementine multispectral data. Icarus, 209(2), 323–336. https://doi.org/10.1016/j.icarus.2010.05.010

- Whitford-Stark, J. L., & Head, J. W. (1977). The Procellarum volcanic complexes-Contrasting styles of volcanism. Proceedings of 8th Lunar Science Conference (pp. 2705–2724).

- Whitford-Stark, J. L., & Head, J. W. (1980). Stratigraphy of Oceanus Procellarum basalts: Sources and styles of emplacement. Journal of Geophysical Research, 85, 6579–6609. https://doi.org/10.1029/JB085iB11p06579

- Whitten, J., Head, J. W., Staid, M., Pieters, C. M., Mustard, J., Clark, R., et al. (2011). Lunar mare deposits associated with the Orientale impact basin: New insights into mineralogy, history, mode of emplacement, and relation to Orientale Basin evolution from Moon Mineralogy Mapper (M^3)

data from Chandrayaan-1. Journal of Geophysical Research, 116, E00G09. https://doi.org/10.1029/2010JE003736

– Whitten, J. L., & Head, J. W. (2015). Lunar cryptomaria: Physical characteristics, distribution, and implications for ancient volcanism. Icarus, 247, 150–171. https://doi.org/10.1016/j.icarus.2014.09.031

– Wieczorek, M. A., Neumann, G. A., Nimmo, F., Kiefer, W. S., Taylor, G. J., Melosh, H. J., et al. (2013). The crust of the Moon as seen by GRAIL. Science, 339(6120), 671–675. https://doi.org/10.1126/science.1231530

– Wieczorek, M. A., & Phillips, R. J. (2000). The "Procellarum KREEP Terrane": Implications for mare volcanism and lunar evolution. Journal of Geophysical Research, 105, 20,417–20,430. https://doi.org/10.1029/1999JE001092

– Wilhelms, D. E. (1970). Summary of lunar stratigraphy—Telescopic observations (599F). Washington DC: United States Government Office. Wilhelms, D. E., & McCauley, J. F. (1971). Geologic map of the near side of the Moon (Map I-703). Flagstaff: Astrogeology Science Center.

– Wilson, L., & Head, J. W. (2003). Lunar Gruithuisen and Mairan domes: Rheology and mode of emplacement. Journal of Geophysical Research, 108(E2), 5012. https://doi.org/10.1029/2002JE001909

– Wilson, L., & Head, J. W. (2017). Generation, ascent and eruption of magma on the Moon: New insights into source depths, magma supply, intrusions and effusive/explosive eruptions (part 1: Theory). Icarus, 283, 146–175. https://doi.org/10.1016/j.icarus.2015.12.039

– Wöhler, C., Lena, R., & Pau, K. C. (2007). The lunar dome complex Mons Rümker: Morphometry, rheology, and mode of emplacement. Paper Presented at 38th Lunar and Planetary Science Conference, Lunar and Planetary Institute, League City, USA.

– Wu, Y., Li, L., Luo, X., Lu, Y., Chen, Y., Pieters, C. M., et al. (2018). Geology, tectonism and composition of the northwest Imbrium region. Icarus, 303,67–90. https://doi.org/10.1016/j.icarus.2017.12.029

– Xiao, L. (2014). China's touch on the Moon. Nature Geoscience, 7(6), 391–392. https://doi.org/10.1038/ngeo2175

– Xiao, L., Zhu, P., Fang, G., Xiao, Z., Zou, Y., Zhao, J., et al. (2015). A young multilayered terrane of the northern Mare Imbrium revealed by Chang'E-3 mission. Science, 347(6227), 1226–1229. https://doi.org/10.1126/science.1259866

– Yuan, Y., Zhu, P., Zhao, N., Xiao, L., Garnero, E., Xiao, Z., et al. (2017). The 3-D geological model around Chang'E-3 landing site based on lunar penetrating radar channel 1 data. Geophysical Research Letters, 44, 6553–6561. https://doi.org/10.1002/2017GL073589

- Yue, Z., Li, W., Di, K., Liu, Z., & Liu, J. (2015). Global mapping and analysis of lunar wrinkle ridges. Journal of Geophysical Research: Planets, 120, 978–994. https://doi.org/10.1002/2014JE004777

- Yue, Z., Michael, G. G., Di, K., & Liu, J. (2017). Global survey of lunar wrinkle ridge formation times. Earth and Planetary Science Letters, 477, 14–20. https://doi.org/10.1016/j.epsl.2017.07.048

- Zeng, X., Zuo, W., Zhang, Z., Liu, Y., & Li, C. (2017). Topographic and geologic analysis of the pre-selection landing sites for Chang'E 5 (CE-5) lunar sample returning mission of China. Paper Presented at 19th EGU General Assembly, EGU, Vienna, Austria.

- Zhang, J., Yang, W., Hu, S., Lin, Y., Fang, G., Li, C., et al. (2015). Volcanic history of the Imbrium basin: A close-up view from the lunar rover Yutu. Proceedings of the National Academy of Sciences of the United States ofAmerica, 112(17), 5342–5347. https://doi.org/10.1073/pnas.1503082112

- Zhang, X., Wu, Y., Ouyang, Z., Bugiolacchi, R., Chen, Y., Zhang, X., et al. (2016). Mineralogical variation of the late stage mare basalts. Journal of Geophysical Research: Planets, 121, 2063–2080. https://doi.org/10.1002/2016JE005051

- Zhao, J., Huang, J., Qiao, L., Xiao, Z., Huang, Q., Wang, J., et al. (2014). Geologic characteristics of the Chang'E-3 exploration region. Science China - Physics Mechanics & Astronomy, 57(3), 569–576. https://doi.org/10.1007/s11433-014-5399-z

- Zhao, J., Xiao, L., Qiao, L., Glotch, T. D., & Huang, Q. (2017). The Mons Rümker volcanic complex of the Moon: A candidate landing site for the Chang'E-5 mission. Journal of Geophysical Research: Planets, 122, 1419–1442. https://doi.org/10.1002/2016JE005247

- Zou, Y. L., & Li, W. (2017). Scientific visions of lunar research-station from China. Paper Presented at 48th Lunar and Planetary Science Conference, Lunar and Planetary Institute, The Woodlands.

- Zou, Y. L., Xu, L., & Wang, Q. (2016). Progress in China's lunar exploration program. Chinese Journal of Space Science, 36(5), 610–619. https://doi.org/10.11728/cjss2016.05.610

6

Conclusions and Recommendations

During this PhD, several questions related to the architecture of the lunar crust were tackled using remote sensing data.

First, the mineralogical nature of the lunar crust as a function of depth, of the crust-mantle interface, and of the upper mantle were investigated using data from the Moon Mineralogy Mapper (M^3) instrument. We struggle to detect olivine occurrences in craters supposedly sampling mantle material. Moreover, while pyroxene composition changes from high-calcium (HCP) to low-calcium (LCP) with increasing depth, plagioclase occurrences are detected in craters that allegedly sample mantle material (chapter 2). The detection of plagioclase in reflectance spectra is possible only in cases where it is extremely abundant: Cheek and Pieters [2014] showed that as little as 2 vol. % of olivine or pyroxene in a plagioclase-rich rock would completely mask the plagioclase signal. The observation of plagioclase in the central peak of craters that are thought to sample mantle material indicates that the crust-mantle interface in the Moon is likely not equal to the depth at which plagioclase is not present anymore. Significant reservoirs of almost pure plagioclase seem to occur across a substantial depth range in the Moon.

A change in pyroxene composition (from HCP to LCP) from crustal to mantle material is consistent with Melosh et al. [2017]'s work. They proposed that the lunar upper mantle is dominated by LCP and not olivine, contrary to the more traditional concept of olivine-dominated planetary upper mantle composition.

The lack of a sharp transition from crustal to mantle material led us to question, in chapter 3, whether the lunar crust becomes more mafic with depth. To study this, we focused on the architecture of the anorthositic part of the Feldspathic Highlands

Terrane (FHT-a), highly anorthositic and covering most of the lunar farside outside the South-Pole Aitken Terrane (SPAT) as defined by Jolliff et al. [2000]. The FHT-a is removed from the maria deposits influence, unlike the Procellarum Kreep Terrane or the outer Feldspathic Highlands Terrane. The approach was more automated than the one used for the crust-mantle interface study. Data hint at a pyroxene compositional change, from highly calcic to lesser calcic contents with increasing depth in the crustal column. However, plagioclase occurrences are still detected at depth, and are consistent with the existence of an anorthositic crust at least 27 km thick.

Several key questions related to lunar science still need to be addressed in light of the results of this thesis. This work shows that remote sensing of crater central peaks provides a useful method to give insight into the architecture of the lunar crust and upper mantle. However, limitations of the visible near-infrared (VNIR) spectroscopic techniques mean that this insight is not always complete. When analysing spectroscopic data, it is important to consider the spatial resolution: the analysis of a spectrum from a footprint covering several hundred squared meters (M^3 has a spatial resolution of 140 or 280 m/pixel) has different implications on the mineralogy than the analysis of the spectrum from a single rock or mineral. Some minerals having a stronger spectroscopic signature than others, this can result in a biased conclusion of the mineralogy and ultimately inferred rock petrology. Moreover, a mixture between two minerals will result in different spectra depending on how they are mixed. An areal mixture (a pixel contains separate patches of pure mineralogic occurrences) results in a linear combination of the two minerals spectra, whereas an intimate mixture (a pixel contains the two minerals mixed in the same rock) is non-linear. Therefore, deconvolving spectra remains difficult and the approach is rarely used for quantitative assessments. Another important aspect of spectroscopic data is the sampling depth: VNIR spectroscopy samples the top few microns on the surface of a planetary surface, which on the Moon always limits us to the regolith upper layer.

The interpretation of spectroscopic data could be improved by performing more Earth-based analogue measurements on mineral mixtures, key to the understanding of how reflectance spectra of mineral mixtures change as a function of mineral proportions and grain size. Combining datasets from several instruments over the same footprint (for instance, spectroscopic, X-ray and thermal data) may help characterizing minerals or rocks based on a series of key absorption or emission features located at different wavelengths.

With the benefit of hindsight, it is apparent that the criteria for crater selection of the study on the FHT-a crust architecture (chapter 3) were suboptimal. Indeed, some plagioclase occurrences reported in previous surveys using spectroscopic data from the M^3 instrument were not detected using our approach. For instance, it may be easier to detect plagioclase occurrences with a higher spatial resolution or a lower detector temperature. The optical period OP2C2, retained for the study discussed in

chapter 3, has a spatial resolution of 280 m/pixel, whereas the optical periods OP1A, OP1B, OP2A and OP2B have a spatial resolution of 140 m/pixel. Additionally, the optical period used for this study has a sensor temperature that is higher than that of other optical periods (optical periods OP1B, OP1A and OP2C3).

The detection of plagioclase occurrences may be further improved using a different continuum removal algorithm. The algorithm developed and used here is able to process plagioclase spectra with strong absorption bands. However, it does not process continuum removal ideally in the cases where the absorption band is weak. Using a continuum removal algorithm specifically developed for the detection of plagioclase in the FHT-a will improve detection of the plagioclase occurrences and yield better agreement with detections that were reported in previous studies.

Studying the cratering process further is necessary to provide better constraints on scaling relationships. Pike [1980] observed that the transition from simple crater to complex crater on the Moon is different in mare material than in highland material, suggesting an effect of the target properties on the final impact crater morphology. Target properties may in turn influence the central peak material depth of origin. It is important keep these limitations in mind when working on establishing a more detailed crustal stratigraphy.

Remote sensing surveys have greatly expanded our catalogue of mineralogical detections, but also allowed the identification of new geological features. In order to obtain ground truth, it becomes obvious that many surface and sample return missions will become necessary in the next years. The complementary nature of remote sensing datasets and sample analysis should not be underestimated: remote sensing datasets, and more specifically, spectroscopy, clearly advanced our knowledge of the diversity of lunar petrography beyond what was learned from the samples. Moreover, remote sensing data offer a global view of a planetary surface, and allow us to study the geological context of the areas sampled, whereas sample analysis provides ground truth for spectroscopy trough quantification of a rock composition, and a more complete understanding of the rock formation conditions than spectroscopy allows for. Techniques like the one we used (spectroscopic mapping) may be used in order to locate and target the most promising sites and samples.

To further advance our knowledge of the lunar crust architecture specifically, obtaining more lunar samples from key locations would enable perfecting the incomplete picture provided by the Apollo and Luna samples.

Collecting highlands samples in particular, which are poorly represented in the Apollo and Luna samples, could help determine how the lunar farside crust was formed, a topic that cannot be solved solely with the type of data used in this thesis.

Obtaining samples from the South-Pole Aitken basin would bring crucial constraints to the understanding of the lower crust and perhaps upper mantle of the

Moon. Providing an absolute age for the South-Pole Aitken basin formation would also improve crater density age calibration, as well as clarify its influence on lunar crustal formation. The current Chang'E-4 mission on the lunar farside (chapter 4) may help us understand the geology of the South-Pole Aitken basin.

Unlike the Earth, where there is no direct evidence of the magma ocean episode because of secondary or tertiary processes, the Moon provides a classic example of a planetary body influenced by a magma ocean episode. However, our current laboratory models of lunar evolution during the magma ocean phase are still too simple to account for the observed complexity of the lunar geological history. For instance, secondary processes like post-magma ocean magmatic activity are not resolved by current laboratory models. What is more, examination of recently acquired data enabled the detection of new features on the lunar surface: from irregular mare patches (Braden et al. [2014]) to the discovery of volatiles in permanently shadowed regions (Spudis et al. [2010]), as well as a new rock type, Mg-spinel anorthosite (Pieters et al. [2011]), also not accounted for in current lunar evolution models. The detection of these new features proves yet again that remote sensing datasets are complementary to lunar samples. Collecting new datasets would undoubtedly shed more light on lunar science.

In 2022, the Luna 27 mission, led by Russia, and in collaboration with the European Space Agency, is planned to land on the lunar South pole. It will carry on the PROSPECT (Package for Resource Observation and in-Situ Prospecting for Exploration, Commercial exploitation and Transportation) instrument package, which aim is to collect and analyse volatile elements from the lunar subsurface, and evaluate their potential as resource for future lunar missions. Moreover, the upcoming Chang'E-5 mission will bring back up to 2 kg of lunar samples from a young maria deposit with intermediate TiO_2 contents (chapter 5), for which we have only a small number of samples. Samples returned by Chang'E-5 could therefore fill a gap in the sample suite, a first step towards advancing lunar science this decade.

Bibliography

Braden, S. E., Stopar, J. D., Robinson, M. S., Lawrence, S. J., van der Bogert, C. H., and Hiesinger, H. (2014). Evidence for basaltic volcanism on the Moon within the past 100 million years. *Nature Geoscience*, 7(11):787–791.

Cheek, L. C. and Pieters, C. M. (2014). Reflectance spectroscopy of plagioclase-dominated mineral mixtures: Implications for characterizing lunar anorthosites remotely. *American Mineralogist*, 99(10):1871–1892.

Jolliff, B. L., Gillis, J. J., Haskin, L. A., Korotev, R. L., and Wieczorek, M. A. (2000). Major lunar crustal terranes: Surface expressions and crust-mantle origins. *Journal of Geophysical Research*, 105(E2):4197.

Melosh, H. J., Kendall, J., Horgan, B., Johnson, B. C., Bowling, T., Lucey, P. G., and Taylor, G. J. (2017). South Pole-Aitken basin ejecta reveal the Moon's upper mantle. *Geology*, 45(12):1063–1066.

Pieters, C. M., Besse, S., Boardman, J., Buratti, B., Cheek, L., Clark, R. N., Combe, J. P., Dhingra, D., Goswami, J. N., Green, R. O., Head, J. W., Isaacson, P., Klima, R., Kramer, G., Lundeen, S., Malaret, E., McCord, T., Mustard, J., Nettles, J., Petro, N., Runyon, C., Staid, M., Sunshine, J., Taylor, L. A., Thaisen, K., Tompkins, S., and Whitten, J. (2011). Mg-spinel lithology: A new rock type on the lunar farside. *Journal of Geophysical Research E: Planets*, 116(4).

Pike, R. J. (1980). Control of crater morphology by gravity and target type: Mars, Earth, Moon. *Proceedings Lunar Planetary Science Conference*, pages 2159–2189.

Spudis, P. D., Bussey, D. B. J., Baloga, S. M., Butler, B. J., Carl, D., Carter, L. M., Chakraborty, M., Elphic, R. C., Gillis-Davis, J. J., Goswami, J. N., Heggy, E., Hillyard, M., Jensen, R., Kirk, R. L., Lavallee, D., Mckerracher, P., Neish, C. D., Nozette, S., Nylund, S., Palsetia, M., Patterson, W., Robinson, M. S., Raney, R. K., Schulze, R. C., Sequeira, H., Skura, J., Thompson, T. W., Thomson, B. J., Ustinov, E. A., and Winters, H. L. (2010). Initial results for the north pole of the Moon from Mini-SAR, Chandrayaan-1 mission. *Geophys. Res. Lett.*, 37(L06204):6–11.

A

Remote sensing and in situ mineralogic survey of the Chilean salars: An analog to Mars evaporate deposits?

This chapter is the reproduction of an article published in Icarus.

J. Flahaut[a,b,*], M. Martinot[a,b], J.L. Bishop[c], G.R. Davies[a], N.J. Potts[a,d]

[a] Faculty of Earth and Life Sciences, Vrije University Amsterdam, The Netherlands
[b] Univ Lyon, Université Lyon 1, ENS-Lyon, CNRS, UMR 5276 LGL-TPE, F-69622, Villeurbanne, France
[c] Carl Sagan Center, The SETI Institute, Mountain View, CA 94043, USA
[d] School of GeoSciences, University of Edinburgh, King's Buildings, Edinburgh, EH9 3FE, UK

Corresponding author: Laboratoire de Géologie de Lyon: Terre, Planètes, Environnement, Université Lyon1, 2, rue Raphaël Dubois, 69622 Villeurbanne cedex, France.
E-mail address: jessica.flahaut@ens-lyon.org (J. Flahaut).

Keypoints: Atacama; Mars; Chile; Analog; Spectroscopy; XRD; Sulfates; Chlorides; Salts

Abstract

The identification and characterization of hydrated minerals within ancient aqueous environments on Mars are high priorities for determining the past habitability of the planet. Few studies, however, have focused on characterizing the entire mineral assemblage, even though it could aide our understanding of past environments. In this study we use both spaceborne and field (VNIR spectroscopy) analyses to study the mineralogy of various salt flats (salars) of the northern region of Chile as an analog for Martian evaporites. These data are then compared to laboratory based Raman and XRD analyses for a complete overview on mineral assemblages. Central (core) and marginal zones within the salars are easily distinguished on the Landsat 8 band color composites. These areas host different mineral assemblages that often result in different landscapes. The lower elevation Salar de Atacama, located in the Andean pre-depression, is characterized by a unique thick halite crust at its center, whereas various assemblages of calcium sulfates (gypsum, bassanite, anhydrite) and sodium sulfates (mirabilite, thenardite, blodite, glauberite), borates (ulexite, pinnoite), Al/Fe-clays and carbonates (calcite, aragonite) were found at its margin. Sulfates form the main crust of the Andean salars to the east, although various compositions are observed. These compositions appear controlled by the type of feeder brine (Ca, SO_4 or mixed), a result of the local geology among other factors. Sulfate crusts were found to be generally thin (< 5 cm) with a sharp transition to the underlying clay, silt, or sand-rich alluvial deposits. Coupled with morphologic analyses, VNIR spectroscopy provides a powerful tool to distinguish different salt crusts. XRD analysis allowed us to quantify the mineral assemblages and assess the limitations of VNIR techniques in the presence of hydrated sulfates, which tend to mask the signatures of other minerals such as clays, chlorides, and carbonates. We found that the Atacama's unique arid and volcanic environment, coupled with the transition recorded in some of the salars has a strong Mars analog potential. Characterizing the outcrop mineralogy at a variety of environments from alkaline, lake waters to more acidic salar brines may help in constraining geochemical environments on Mars.

A.1. Introduction

Remote sensing and in situ data from past and current Mars orbiter and lander missions have provided extensive evidence for the presence of water-lain sedimentary rocks on Mars (Carr and Head, 2010, and references therein). Infrared technology has been utilized to detect hydrated minerals, including phyllosilicates, carbonates, sulfates, and chlorides in specific areas of the Martian surface (Poulet et al., 2005; Gendrin et al., 2005; Osterloo et al., 2008; Murchie et al., 2009; Ehlmann et al., 2008, 2011; Carter et al., 2010, 2013). These minerals are generally found in Noachian (~4.1–~3.7 Gy) and Hesperian-aged (~3.7–~3.0 Gy) terrains, although younger, more localized

outcrops have also been detected (e.g., Murchie et al., 2009; Carter et al., 2013). Coupled with morphological evidence for ancient lakes and valleys (e.g., Fassett and Head, 2008; Hynek et al., 2010), this key observation has led to the hypothesis that Mars likely underwent major climate change, and could have experienced warmer, wetter, and more habitable conditions in its past (< 3.7 Gy) (Bibring et al., 2006). The nature and timing of this potential, planetary-scale, climate change is a major outstanding question in current Mars studies. In an attempt to better interpret the exact environmental conditions for the formation of hydrated minerals on the Martian surface, terrestrial analogs were examined.

The region of northern Chile/Central Andes (including the Atacama desert) is characterized by a succession of north-south trending mountain ranges and closed basins. The central parts of the basins are infilled by evaporate deposits or occupied by saline lagoons, collectively referred to as salars. Receiving only a few millimeters of rain per year, and being spread along a volcanic ridge, this region appears similar to some Martian paleo-environments (Ericksen, 1983; Stoertz and Ericksen, 1974). Martian sulfate and chloride-rich deposits may have formed through similar processes to those that formed the salars salts and appear to share common features and mineralogy (e.g., Sutter et al., 2007). Future Mars research should benefit from a detailed terrestrial analog survey that permits a full understanding of the geological context, mineralogical assemblages, and the geochemical and environmental processes responsible for the formation of evaporate deposits in enclosed settings, under arid conditions.

To that end, we performed an in-depth combined remote sensing and in situ analytical study of five salars located within the Antofagasta region of Northern Chile. Our site selection includes the largest salar, the Salar de Atacama, formed at intermediate elevations (2500 m) under dry and hot conditions, and located on sedimentary basement, as well as various salars located at higher elevations (> 4000 m) within the slightly wetter Andean volcanic highlands. We report the mineralogy and morphological characteristics of each salar as observed from space and in the field and discuss the mineral zonation and intra-salar variations as a function of environmental parameters (source type, temperature, elevation, evaporation rate etc.). The ultimate objective of this study is to correlate the remote and field observations made in the salars and interpret their variations in term of the overall geochemical and sedimentary environment. By comparing features and assemblages with observations made on Mars we aim to be able to place constraints on past Martian environments and their habitability potential.

A.2. Regional context

The subduction of the Nazca Plate below the South American Plate resulted in the formation of north-south trending compressional features, including the Andean orogenic belt. The high topography of the Andes has a major impact on the climate of South America, referred to as the rain-shadow effect. Whereas lands to the north

are wet and warm, lands on the western side of the Andes barrier (including the Atacama desert) are extremely hot and dry. This effect is enhanced by the action of the upwelling, northwest-flowing, cold Pacific Humboldt current that inhibits the moisture capacity of onshore winds and prevents precipitations (e.g., Houston and Hartley, 2003; Armijo et al., 2015). The Atacama Basin is estimated to have a mean annual precipitation below 50 mm and an average temperature of about 11°C (Stoertz and Ericksen, 1974). It is one of the oldest deserts on Earth and has experienced extremely arid conditions for at least 15 My (Houston and Hartley, 2003). The presence of water in the Atacama desert and surrounding regions is rare, only occuring as near-surface groundwater or occasional transient rivers draining from the Andes (Houston, 2006). The semi-arid high Andean reliefs contain > 100 basins with interior drainage; most contain salt-encrusted playas referred to as salars. The Atacama desert is defined as the plateau of northern Chile located between the Andes and the Pacific coast. Hills and valleys in the Atacama desert are covered with extensive saline crusts of diverse types (Stoertz and Ericksen, 1974). Because it is the driest non-polar desert on Earth, the Atacama desert has been used as an analog for martian and lunar environments over the past two decades (e.g., Wettergreen et al., 1999; Navarro-Gonzales et al, 2003; Piatek et al., 2007; Wynne et al., 2008).

The present study area is located in the Antofagasta region of Chile, north of the Atacama region, south and east of the San Pedro de Atacama village, between -23 and -24° latitude, and -68.8 and -67.3°longitude (Fig. A.1). This area of northern Chile is underlain by marine Cretaceous rocks, as well as rhyolitic to basaltic rocks in the Andean highlands (Stoertz and Ericksen, 1974). The main morpho-structural units in this region of Chile, are, from west to east: (1) the Coast Range, (2) the Central Depression or Central Valley, (3) the Precordillera (also referred to as the Domeyko Range), (4) the pre-Andean Depression, (5) the Western Cordillera, (6) the Altiplano, and (7) the Eastern Cordillera (Risacher et al., 2003; Fig. A.1). Most of the major reliefs formed as a result of the late Tertiary to Holocene faulting, accompanied by the uplift of Cordillera Domeyko Range. Our study area includes portions of the pre-Andean Depression (Atacama basin) and of the Andean highlands (also called the Western Cordillera) and encompasses the main salar, the Salar de Atacama, as well as several high elevation, smaller scale salars (including the Salar de Quisquiro, Laguna Tuyajto, Salar de Laco, Salar de Aguas Calientes 3), (Fig. A.1). The study area is predominantly underlain by Tertiary and Quaternary rhyolotic and dacitic ignimbrite sheets and covered by numerous andesitic stratovolcanoes, reaching up to 6500 m in elevation. Native sulfur deposits are found throughout the area and were mined at the Cerro Toco (white arrow on Fig. A.2 a). The Atacama basin is filled with Tertiary to Quaternary (or Cenozoic) alluvium and lacustrine sediments (Stoertz and Ericksen, 1974; Risacher et al., 2003) and represents the largest structural basin in the area. The basin is fringed to the west by the Cordillera de la Sal, a former evaporate body that was faulted and folded as a result of compression during the Cenozoic (Dingman, 1962, 1967), and

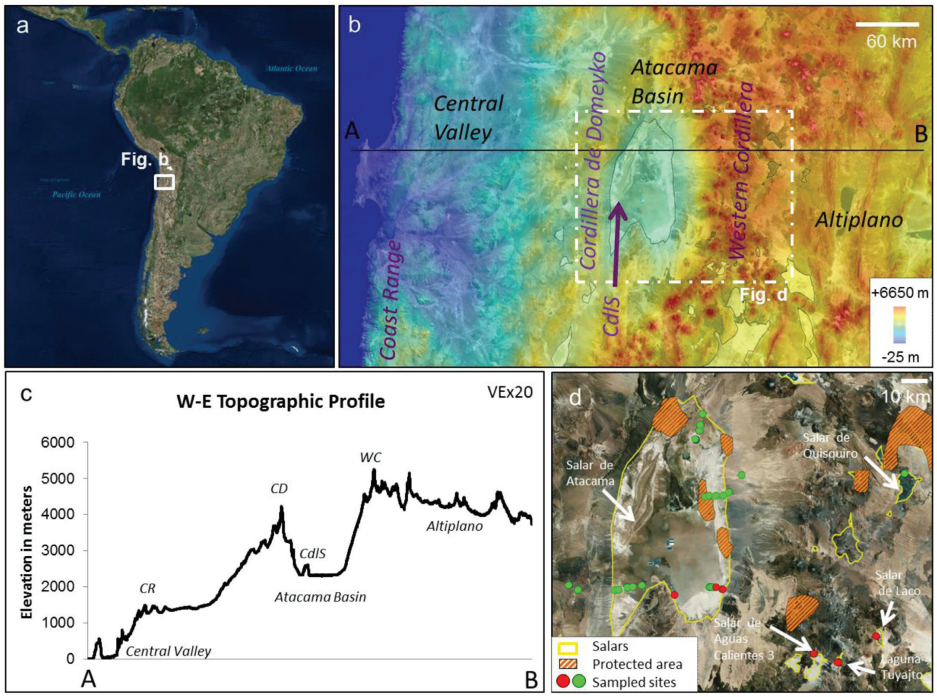

Figure A.1: a) Location of the study area (ArcGIS world imagery maps, ESRI/TerraColor), b) ASTER global digital elevation model (GDEM) of the study area. The ASTER GDEM is a product of METI and NASA. c) AB East-west Topographic profile highlighting the succession of mountain ranges (CR: Coastal Range; CD: Cordillera de Domeyko; CdlS: Cordillera de la Sal, WC: Western Cordillera) and basins/plateaus. d) Location of the sampling sites (green and red circles, red circles locations where sterile sampling was performed for astrobiological analyses (see companion paper by Monaghan et al., 2016), main salars (yellow outlines) and protected areas (Flamingo reserve, orange hatch) on DigitalGlobe 1 m/pixel satellite imagery (ArcGIS world imagery maps, ESRI/DigitalGlobe).

that includes the famous Lunar Valley and Death Valley sites.

Our study area differs from previous Mars analogs studies that focused on the Central Depression, between the Coast Range and the Domyeko Range, near the ghost town of Yungay (e.g., Navarro-Gonzales et al, 2003; McKay et al., 2003; Sutter et al., 2007; Piatek et al.,2007; Fig. A.1). The Central Valley, which is comprised of a thick fill of Tertiary to Holocene detrital and lacustrine sediments, was not considered in the present study as multiple authors (Eriksen, 1981; Berger and Cooke, 1998; Rech et al., 2003; Bao et al., 2004; Michalski et al., 2004) have pointed out the possible influence of an oceanic source on the formation of local evaporate deposits; this is not thought to be applicable to martian environments.

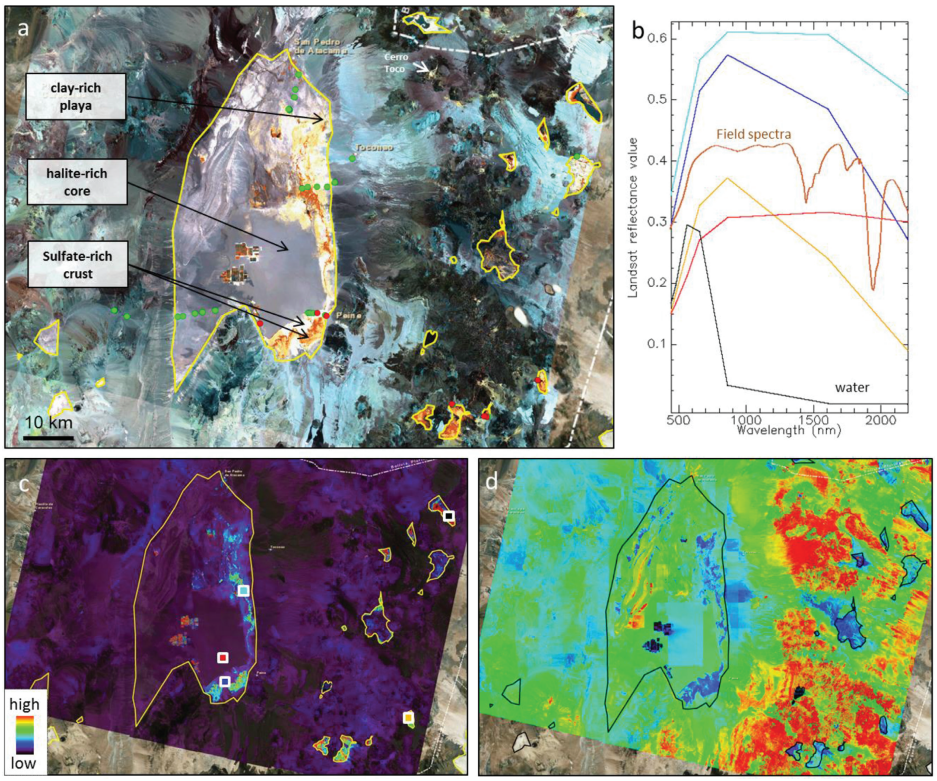

Figure A.2: Landsat observations of the study area. a) RGB color composite of Landsat 8 reflectance bands 5, 6, 7. Distinct zones are highlighted within the salars, which correlate with mineralogical variations (see text for more details). Green and red circles indicate the location of sampling sites, yellow lines delimit the location of the main salars (see Fig. A.1.b) Landsat reflectance spectra collected on the Salar de Atacama halite-rich core (red), sulfate-rich margin (dark blue), clay-rich margin (cyan), on the water in the Salar de Tara (black) and on the sulfate-rich margin of the Salar de Laco (orange). A field spectrum (gypsum) collected at the Salar de Laco (brown) is shown for comparison. Field observations suggest that the lower average reflectance level at the Salar de Laco is due to the mixture of sulfates with a high proportion of detrital silicate material. c) The ratio between band 5 and band 7 can be utilized to highlight sulfate-rich areas, such as the Andean salars located along the Paso Sico road (south east). Colored squares indicate the location of the spectra shown in Fig.A.2 b. d) The ratio between band 4 and band 2 can be utilized to infer the effect of salt dilution on soils. High values (red tones) are attributed to iron-rich terrains (volcanic highlands), whereas the sedimentary bedrock of the Atacama basin as well as the Andean salars are characterized by lower values (blue tones).

A.3. Method

A.3.1. GIS setting

Available remote sensing datasets and maps were gathered into a geographic information system (GIS) that enables management of the data and also supports simultaneous visualization and analyses of various data of diverse types. Field data were collected on a tablet using the GIS pro application (Garafa) and later integrated into our GIS.

Remote sensing data from imaging satellites were used to map and characterize the Atacama salars from space. ArcGIS (ESRI) world imagery maps (including 15 m/pixel TerraColor imagery at small and mid-scales, and DigitalGlobe 1 m/pixel imagery at large scale) and data (boundaries, places) were used as a background (more information is available at `http://www.arcgis.com/home/item.html?id=10df2279f9684e4a9f6a7f08febac2a9`; Source: Esri, DigitalGlobe, GeoEye, Earthstar Geographics, CNES/Airbus DS, USDA, USGS, AEX, Getmapping, Aerogrid, IGN, IGP, swisstopo, HERE, DeLorme, MapmyIndia, ©OpenStreetMap contributors, and the GIS user community). Landsat imagery has previously been demonstrated to be efficient at mapping salar zonation (e.g., Chapman et al., 1989) and was, therefore, used to survey the terrain diversity from space and select representative field sites. The recent Landsat 8 reflectance data provide full coverage of the area at multiple wavelengths (Fig. A.1). The Landsat 8 satellite is equipped with two push broom sensors, the Operational Land Imager (OLI), that covers nine VNIR channels at 15–30 m spatial resolution, and the Thermal Infrared Sensor (TIRS), whose two thermal bands enable thermal wavelength atmospheric correction at a resolution of 100 m (Irons et al., 2012). Orthorectified and terrain corrected Level 1T OLI imagery was obtained from the USGS EarthExplorer (`http://earthexplorer.usgs.gov/`). VNIR bands 1 to 7 were converted to surface reflectance using the USGS L8SR on demand tool, that produces provisional Landsat 8 Surface Reflectance (SR) product (USGS, 2015).

A.3.2. Field sampling and field VNIR spectroscopy

Field sites were first selected based on their spectral diversity as suggested by Landsat imagery, then refined based on their accessibility, in terms of available roads or tracks, protected natural areas, and potential landmines. A total of ~50 sites in 5 different salars were visited during a field campaign that was carried out in February-March 2015 with the local support of ESO/APEX (Table A.1). Several E-W and N-S transects were undertaken in the main salar, the Salar de Atacama (mixed brines), which lies at relatively low elevation (2500 m) on a sedimentary basement (Fig. A.1). In addition, four salars were visited at higher elevations (> 4000 m) in the Andean highlands: the Salar de Quisquiro (Ca-brines), the Laguna Tuyajto (SO_4-brines), the Salar de Laco (SO_4-brines), and the Salar de Aguas Calientes 3 (mixed brines) (Fig. A.1 d). For each salar, we performed (where possible) transects out from the center towards margins

to collect spectroscopy measurements and samples. The location and morphology of the outcrops was documented with the GIS pro application including field pictures, while the in situ mineralogy was derived from VNIR reflectance spectra measured with an Analytical Spectral Devices (ASDinc) field spectrometer. The ASDinc Fieldspec 4 Hi-Res instrument collects visible and near-infrared (VNIR) spectra in the 350–2500 nm spectral domain with three detectors (VNIR: 300–1000, SWIR-1: 1000–1800, SWIR-2: 1800–2500 nm) and has a spectral resolution of 3 nm in the 350–1000 nm range, and 8 nm in the 1000–2500 nm range. All spectra were acquired in the field at a distance of ~10 cm from the outcrops, using the bare fiber inserted directly in the pistol grip, which produces a 25° field of view (FOV). As the atmospheric water vapor content is very low (< a few %) in the Atacama there was no need for a contact probe. A 100% white panel was used for calibration prior to every set of measurements. From each outcrop a set of 5 to 10 spectra were acquired from different locations to assess the outcrop homogeneity. Spectra were converted from radiance to reflectance using the ASDinc software and compared with the VNIR spectra of reference minerals from the USGS and CRISM spectral libraries (Clark et al., 2007; Murchie et al., 2007). All field VNIR spectra correspond to single measurements and are presented unsmoothed, in units of absolute reflectance, and uncorrected for atmospheric gases, as their effect is only minor.

Samples were collected in sealed tubes and bags at each site to be further characterized by Raman spectroscopy and X-Ray diffraction in the laboratory. Additional samples were collected and preserved in sterile conditions for a complementary astrobiologic investigation performed jointly with Leiden University and the European Space Agency (Martini et al., 2016; Monaghan et al., 2016). For this purpose eight samples were also collected at a 20 cm depth below salar crusts at 7 different sites.

A.3.3. Raman spectroscopy

Selected samples, collected from the field, were taken from sealed containers under a nitrogen atmosphere (to avoid atmospheric water contamination) and measured with a Renishaw InVia Reflex confocal Raman microscope (Wotton-under-Edge, United Kingdom) at the Vrije University Amsterdam, the Netherlands. Spectra were recorded using a 80 mW, 532-nm frequency doubled Nd:YAG excitation source in combination with a 1800-l/mm grating and a Peltier cooled CCD detector (203 K). The 521 cm^{-1} Raman shift of an internal silicon standard was used to verify the spectral calibration of the system. Spectra were compared with the Raman spectra of reference minerals present in the RUFF libraries and in the WURM database (Downs and Hall-Wallace, 2003; Caracas et al., 2011).

A.3.4. X-ray diffraction

Semi-Quantitative X-ray diffraction (XRD) analyses were conducted to determine the composition and relative abundance of the various salts. Selected samples were dried

Table A.1: List of investigated salars and collected samples at each location. The corresponding brine types and salar properties were extracted from Risacher et al. (2003). No information were available for the Laguna Cejar, de la Piedra and Chaxa specifically, but as they are located in the eastern part of the Atacama salar, they are all inferred to be fed by mixed to SO_4-rich brines.

Salar name	Brine type	Mean elevation (m)	Mean temperature (°C)	Evaporation (mm/yr)	Area salar (km^2)	Corresponding samples	Corresponding figures
Salar de Aguas Calientes 3	Mixed	3950	1	1500	46	J5L1R3 (center), J5L1R4 (margin)	3e, 4p,q
Laguna Tuyajto	SO_4	4010	1	1500	2.9	J2L1R1 (far margin), J2L2R2 (water pond, margin), J2L2R3 (center), J2L2R4 (margin)	3f, 4e,f,k,o
Salar de Laco	SO_4	4250	1	1500	16.2	J2L1R1 (center), J2L1R2 (margin)	3g, 4h,i
Salar de Quisquiro	Ca	4150	1	1500	80	J11L1R1, J11L1R2 (margins), J11L1R3 (water pond, margin), J11L1R4 (center)	3c, 4g,l
Salar de Atacama	mixed	2300	14	1800	3000	J8L1 (N margin), J7L4, J7L5, J7L6 (E margin), J7L7, J7L8, J7L9, J7L10, margin)	3h, 4a,b,c,d,m,n
Salar de Atacama - Laguna Cejar	SO_4				J9L1R1, JEL1R2, J9L1R3 (center), J9L1R4, J9L1R5 (margin)	4j	
Salar de Atacama - Laguna Piedra	SO_4				J9L2R1 (pond), J9L2R2, J9L2R3 (center), J9L1R4, J9L1R5 (margin)	3i	
Salar de Atacama - Laguna Chaxa	SO_4				J1L1R1, J1L1R2 (center), J1L1R3, J1L1R4, J1L1R5 (margin)		

at 70°C for 48 hours, ground in an agate mortar, dry sieved to < 100 $\mu$and measured using a Bruker D8 Advance diffractometer equipped with an X-ray Cu source at the Centre de Diffractométrie of the University Lyon 1, France. Disoriented measurements were made over a 2Theta range of 3° to 70°. XRD patterns were analyzed using the Bruker DIFFRAC.SUITE EVA software. Mineralogical fits were performed by comparing D-spacing values to those of minerals listed in the International Center for Diffraction Data database and the Crystallography Open Database (Kabekkodu et al., 2002; Grazulis et al., 2009). Basic mineralogy and crystallinity were derived from the analyses, with the exception of clay mineralogy, which would require a different technique of XRD analysis. Mineral abundance was determined as weight percent (wt. %) using the Rietveld method, with a 10 to 20% accuracy.

A.4. Results

A.4.1. Remote sensing observations

Salars in the study area are easily mapped from space due to their high albedo and being confined within topographic lows. In Landsat imagery, salars are also easily distinguished from their surroundings, which are mostly volcanic in nature. Previous studies have demonstrated the potential of Landsat Thematic Mapper data to map compositional zoning within the Salar de Llullia-Ilaco (Chapman et al., 1989) and the Salar de Atacama (Houston, 2006). Bands 4, 5, and 7 (at 0.772–0.898, 1.547–1.749 and 2.064–2.345 μm respectively) were found to be efficient at capturing the majority of the mineralogical information and were used as color composites to map the different evaporate mineral zones within the salars. In this study, we make use of the equivalent bands on the Landsat 8 instrument by performing a 5, 6, 7 band color composite (Fig. A.2) (bands are at 0.851–0.879, 1.566–1.651, 2.107–2.294 μm respectively). Landsat 8 image LC82330762014345 covers the Salar de Atacama to the east as well as most of the Andean salars, including the four in our study. Core and marginal zones within the salars are easily distinguished on the RGB color composite, and mapped as different colors (Fig. A.2 a). Previous field investigations (e.g., Houston, 2006) and present investigations confirm that distinct mineral assemblages are observed within specific zones of an individual salar, with the exception of the red zones that correspond to wet soils. Distinct mineral assemblages are also observed between the various salars. Surrounding volcanic terrains appear in various tones of black, gray, green, and blue (Fig. A.2 a).

The lower elevation Salar de Atacama, located in the Andean pre-depression, is characterized by a unique, thick halite crust at its center (gray color on the Landsat 5, 6, 7 RGB, Fig. A.2 a), whereas various assemblages of sulfates or mixed sulfates and chlorides (white tones) and clays/carbonates (yellow tones) were found at its margin. Most of the Andean salars are mapped in tones of white, orange and red on this color composite, suggesting wet soils and a composition possibly closer to the margins of

the Salar de Atacama (Fig. A.2 a). Houston (2006), however, suggested that the lower albedo of the Salar de Atacama core (gray on Fig. A.2 a) could be a result of dust covering on the old halite crust, and that a halite crust that was frequently inundated and re-crystallized should have a higher albedo and appear in tones of white, like some of the salts at the margins.

Consequently, parameters were developed to highlight the possible differences between the Andean salars and the Salar de Atacama margins on the Landsat 8 data (Fig. A.2 c,d). Band ratios 4/7 and 5/7, which are adapted from previous Landsat sulfate parameters (Amos and Greenbaum 1987; Mougenot et al. 1990; Mougenot, 1993) show high values in the some of the Andean salars (Laco, Tuyajto, Aguas Calientes 3) and on the eastern margin of the Salar de Atacama and other salars (e.g., Quisquiro, Aguas Calientes 2) (Fig. A.2 c). The Salar de Quisquiro and Salar de Aguas Calientes 2 have low values in their central parts, that correlate with lower albedo material on the visible optical imagery. Based on previous work (Epema, 1986, 1990; Mougenot et al., 1990), band ratios 5/2 and 4/2 should also help track the effect of salt dilution on soils. These ratios have higher values in the Andean highlands, likely highlighting the difference in bedrock composition with the eastern Atacama basin, which is underlain by sediments (Fig. A.2 d).

A.4.2. Field observations

A variety of salt crusts have been observed and previously reported in the northern Chilean salars (e.g., Stoertz and Ericksen, 1974). Soils in the Atacama desert are either covered by salt rich fines or cemented by a hard saline crust. In the present study area, salt crusts were found to be generally thin (< 5 cm) with a sharp transition to underlying clay, silt or sand-rich alluvial deposits. The only exception lies within the Salar de Atacama, where the lower limit of the hard (halite) crust could not be observed, but is estimated to be at least a few meters deep (Stoertz and Ericksen, 1974).

Salt crusts were classified in the field into multiple types based on their morphology (Figs. A.3, A.4). The main categories include (1) thick, sharp, blocky, hard crust (red squares in Fig. A.3), (2) thick, smooth, hard crust (magenta square in Fig. A.3), (3) thin, dry and friable soft crust (dark blue squares in Fig. A.3), (4) smooth, moist soft crust (green squares in Fig. A.3). Other common terrain types include (5) muddy surfaces with polygonal cracks, sometimes covered with thin salt deposits accumulated in topographic lows (light blue squares in Fig. A.3), and (6) cm-scale rock pebbles forming a beach near the water (purple square in Fig. A.3). To the first order these morphologies correlate to mineralogy based on field spectra (cf. next section).

Type 1 is a hard saline crust, which was mostly observed in the field within the core section of the Salar de Atacama (Fig. A.4 a–d). This crust is massive, > 10's of centimeters to meters thick, and made of sharp, irregular blocks with clinkerlike texture, forming a rugged, hummocky surface (Fig. A.4 a, b). Stoertz and Ericksen (1974)

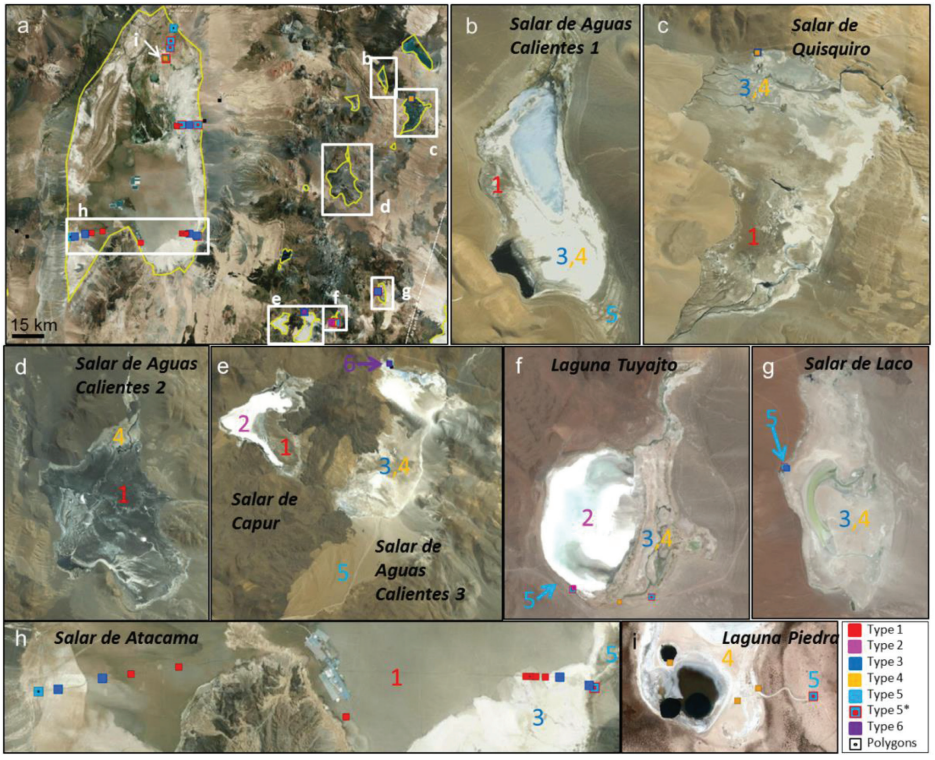

Figure A.3: Remote sensing views of the salars in the study areas and types of terrains. a) Classification of crust types at the location visited in the field. b-i) Close-up of various salars. The squares indicate the location visited on the field. Colored numbers indicate different crust types as inferred from field and remote sensing data (DigitalGlobe images).

noticed that this crust is usually associated with the zone of chlorides, in permanently (or nearly) dry areas. Type 1 crusts appear in dark tones on the aerial and spaceborne images as they are older and generally covered by a thin layer of dust or sand from the underlying sediments, which are trapped in pits (Fig. A.3 a, h). At the hand specimen scale, outcrops are characterized by colorless crystals, consistent with halite, sometimes covered or containing brown sediments. On the eastern part of the Salar de Atacama, this crust transitions to a Type 3 crust in an area where the crust appears less rugged, and is characterized by half a meter scale polygons with upturned edges and layering of the massive rock salt in the upper 5 cm (Fig. A.4 c, d). White, high purity rock salt can be seen in the central, flat part of the polygon, suggesting recent salt precipitation. Spaceborne images suggest Type 1 crust could also be present in the Salar de Aguas Calientes 1 and 2, Salar de Capur and in parts of the Salar de Quisquiro that were not accessible in the field but appear dark-toned on visible space imagery (Fig. A.3 a–e, h).

Type 2 is a thick but smooth, flat hard crust, and was observed in the core area of the Laguna Tuyajto (Fig. A.4 e, f). This type of crust was wet, suggesting that pure salt are nearly continuously renewed at the surface. This crust appears white on visible images (Fig. A.3 a, f). This crust is a few centimeters thick, and fractured by meter-scale polygons. Fractures between the polygons appear randomly oriented and infilled with salts. Based on spaceborne visible and Landsat imagery, this very white, wet crust could also be present in the inaccessible Salar de Capur (Fig. A.3 e).

Type 3 is a soft, dry friable crust, that was observed at the margins of the Salar de Atacama, Salar de Quisquiro, Salar de Laco and Salar de Aguas Calientes 3 (Figs. A.3, A.4 g–i). The surface in these areas appears undulated at a scale of about 20 cm and rigid. This crust is, however, easily crumbled with fingers into a loose dry powder. In contrast to Types 1 and 2, Type 3 crusts are not made up of nearly pure salt, but rather consist of the underlying sands or silts cemented together in the upper centimeter. Less saline, moist material is found at depths of 20–30 cm, suggesting that the surface is kept in a puffy condition by crystallization of salts in the capillary fringe of the water table (Stoertz and Ericksen, 1974). Previous authors (e.g., Goodall et al., 2000) have suggested that puffy and powdery textures (crust type 3) are consistent with salts formed by efflorescence; whereas crusts formed by precipitation more commonly show blocky or polygonal morphologies (crust type 1, 2), consistently with our observations. A former, 1 cm-thick carbonate-rich white crust was observed at 20 cm depth in the Salar de Laco, confirming the previous assumptions made on airborne images that this salar must have been occupied by a deeper lake in the past (Stoertz and Ericksen, 1974).

Type 4 is a smooth, moist crust and is observed in marginal zones, close to water ponds and lagoons, in the Salar de Atacama (near Laguna Cejar and Laguna Piedra), Laguna Tuyajto and the Salar de Quisquiro (Fig. A.4 j–l). These areas are characterized by a shallow fluctuating groundwater table that keeps the surface moist (Stoertz and

Ericksen, 1974). Type 4 crusts are extremely thin and show various color shades in the field (from white to dark gray) and on spaceborne images, suggesting variable saline contents or types, or suggesting the substrate is showing through (Figs. A.3, A.4 j–l). Gypsum-rich ramparts sometimes terminate this crust at the edge of the saline ponds.

Type 5 terrains consist of clastic sediments, ranging from clay, silt and fine sand (clay playa) to coarser sands and gravels (lake sediments) (Fig. A.4 m–o). Clay playas are often marked by mud-cracked polygons (10's of cm scale, smaller than the polygons seen in halite-rich terrains of crust type 1 and 2) and are observed in the marginal areas of the Salar de Atacama, salar de Laco and Laguna Tuyajto (Fig. A.3 a, f, g, h). Clay playa result from the infrequent flooding of marginal areas, creating extensive ephemeral lakes, that can dry up in a few days to weeks (Stoertz and Ericksen, 1974). Coarser clastic sediments are observed in the most distal part of Laguna Tuyajto and beneath the salt crust of most salars. Erosion of the surrounding high volcanoes during storms that trigger mud-flows is likely the source of these lake sediments. A thin, patchy, white saline material is sometimes accumulated in topographic lows suggesting temporary rises of the groundwater table in these marginal areas (Fig. A.4 o).

Type 6 terrain is made of cm-scale angular pebbles, and was observed next to the water pond in the Salar de Aguas Calientes 3. It is interpreted as a local, beach facies (Figs. A.3 e, A.4 p, q).

Our observations, derived from field observations at five salars and spaceborne imagery, are consistent with the many observations made by Stoertz and Ericksen (1974, their figure 11) based on aerial imagery and field observations at the Salar de Atacama. A few differences on the distribution of hard and soft crusts are observed and can be attributed to changes over time, given that at the time of their research there was no water body (and a hard crust) in the Laco and Tuyajto locations, but there was an ephemeral lake in the south-east part of the Salar de Atacama, that we did not observe (mapped as a clay playa, Fig. A.3 h).

A.4.3. VNIR spectroscopy

Over a hundred VNIR spectra were acquired in the field; a representative set is presented in Fig. A.5, along with a comparison to reference spectra from the USGS spectral library (Clark et al., 2007). Most of the samples show absorption features around 1.4 and 1.9 μm, and eventual overtones around 0.97 and 1.2 μm, that are attributed to adsorbed water and hydrated minerals in general (e.g., Hunt and Salisbury, 1970; Fig. A.5 b). The relative strength of these two absorptions, the symmetry of the bands and the positions of the absorptions centers vary with the mineral structure and composition. In some samples (e.g., sample J2L2R3, J9L2R1, Fig. A.5 b) the water saturation results in an additional features near 1.85 μm. Narrower absorptions in the 2.1–2.5 μm domain are used to distinguish among the different types of OH-bearing minerals.

Sulfates were identified thanks to a drop in reflectance at 2.4 μm caused by vibrations of the SO_4 group (e.g., Gendrin et al., 2005; Cloutis et al., 2006; Bishop et al., 2009).

Although a similar feature can also be attributed to chloride salts or chlorine oxyanion salts (e.g., Lynch et al., 2015), additional absorptions allow for the identification of specific sulfate minerals. Ca-sulfates such as gypsum ($CaSO_4$, $2H_2O$) show a diagnostic triplet at 1.45, 1.49, and 1.54, single bands near 1.75 and 1.94 μm, and a doublet at 2.22 and 2.27 μm (Bishop et al., 2014a; Fig. A.5 a). In bassanite ($CaSO_4$, $0.5H_2O$), these bands are shifted towards shorter wavelengths and occur as a triplet at 1.44, 1.47 and 1.54 μm, single bands at 1.78 and 1.93, and a doublet at 2.16 and 2.26 μm (Bishop et al., 2014a). Anhydrite ($CaSO_4$) often displays a band centered at 1.94 μm due to adsorbed water. Additional absorptions also differ in Na-sulfates depending on their hydration state and additional cations that might be present. Thenardite ($NaSO_4$) in the USGS library shows diagnostic absorptions at 1.42, 1.94 and 2.11 μm indicating it is partially hydrated, whereas mirabillite ($NaSO_4$, $10H_2O$) shows diagnostic absorptions at 1.46, 1.77, 1.96 and ~2.2 μm (Fig. A.5 e). Reference libraries are incomplete for mixed sulfates but bloedite (Na 2 Mg(SO_4) 2,$4H_2O$) is present in the USGS spectral library and shows absorptions at 1.47, 1.7 (broad), 1.96, 2.09, and 2.44 μm (Fig. A.5 b, Clark et al., 1990, 2007; Cloutis et al., 2006). Anhydrous chlorides and perchlorates (e.g., NaCl, $MgCl_2$, NaClO 4) show little to no features in the VNIR domain except for adsorbed water features (Drake, 1995; Bishop et al., 2014c; Fig. A.5 b, c). Na-, Ca-, Fe- and Mg- bearing chloride hydrates share some spectral absorptions with sulfates near 1.19, 1.45, 1.96 and 2.42 μm (Hanley et al., 2014, 2015; Bishop et al., 2014b).

Borates have also been previously reported in the Chilean salars. Na-borate spectra exhibit overtones/combinations of the B-O vibrations in the 1.55, 1.75, 2.15, and 2.25 μm regions (Cloutis et al., 2016). Ulexite (NaCaB 5 O 6 (OH) 6,$5H_2O$) and pinnoite (MgB_2O_4, $3H_2O$) spectra are characterized by a strong decrease in reflectance from 0.5 to 2.5 μm and absorption features at 1.43–1.46 (doublet), 1.96, 2.13–2.18 (doublet), 2.25 μm for ulexite, 1.44, 151–1.55 (doublet), 1.64, 1.98, 2.13–2.22 (doublet) for pinnoite (Crowley, 1990; Clark et al., 2007; Fig. A.5 d).

Carbonates and clays can be identified by their metal-OH absorptions in the 2.1–2.5 μm domain. Smectite clays are commonly characterized by water absorptions centered at shorter wavelengths than sulfates (1.40–1.41 and 1.90–1.92 μm). In contrast to the Al-phyllosilicates that have a diagnostic Al-OH absorption band at 2.19–2.21 μm, spectra of Fe- and Mg-rich phyllosilicates exhibit Fe-OH and Mg-OH bands at longer wavelengths (e.g. Bishop et al., 2008; Fig. A.5 e): 2.28–2.29 μm for nontronite, 2.30–2.31 μm for saponite, 2.31–2.33 μm for serpentines, and 2.33–2.37 μm for chlorites. Carbonates are more easily identified by absorptions near 3.4–3.5 and 3.9–4.0 μm, but can also be characterized by overtones near 2.30–2.33 and 2.50–2.53 μm (e.g., Gaffey, 1986; Ehlmann et al., 2008, 2009; Bishop et al., 2013; Fig. A.5 f).

All these minerals have been identified at diverse locations of the study areas. Broad absorptions at 1.43 and 1.93 μm are observed in the spectra of the rocks collected in the Salar de Atacama (J1L1R1) and Salar de Quisquiro hard crusts (J11L1R4) and on the thin white salt deposits sometimes covering clay playas (e.g., J9L2R1).

Those absorptions are characteristic of water, and given that all samples are morphologically consistent with halite, we interpreted those spectra as hydrated halite (Fig. A.5 b). A few samples collected east of the Salar de Atacama (J7L10, J7L14) have absorptions centered at 1.46, 1.78, 1.98 and 2.24 μm that are more consistent with $MgCl_2$ (Fig. A.5 c). Additional absorptions in many spectra are sometimes present near 2.2 μm and could be attributed to a Cl-O combination, an Al-OH combination or an Si-OH combination (Cloutis et al., 2006; Bishop et al., 2008). The location of the band center suggest the presence of clay impurities in many cases (2.21 μm absorption, J7L8, J2L2R4 on Fig. A.5 f). An additional band at 2.31 μm in sample J1L1R2 (Fig. A.5 f) is present and could be due to the presence of calcium carbonates or Fe/Mg-rich clays. Clays are detected in some of the clay-bearing playa thanks to their absorptions centered at 1.41, 1.91, 2.21 μm (J7L4, Fig. A.5 e), but most clay-bearing playas exhibit spectra with bands centered at longer wavelengths (e.g., bands at 1.42, 1.93 and 2.21 μm in J8L1, Fig. A.5 e), suggesting a mixture with additional material such as halite and sulfates. Gypsum is detected in the samples of all five salars in both dry and wet crusts (e.g., J5L1R4, J2L2R2, Fig. A.5 a), sometimes mixed with halite (e.g., J5L1R3, Fig. A.5 a). The resulting spectra exhibit flat-bottomed absorption features at 1.94–1.98 μm and a stronger 1.4 absorption feature relative to the 1.9 μm feature. Absorptions at respectively 1.44, 1.96, 2.12–2.18 μm and 1.44, 1.74, 1.94, 2.12–2.22 μm in some spectra of dry crust within the Salar de Atacama are best matched by the borates ulexite (J1L1R4, Fig. A.5 d) and pinnoite (J1L1R3, Fig. A.5 d).

Finally, a 0.68 μm absorption is present in the spectra of two samples (J2L2R2 and J9L2R3, Fig. A.5 a) that were taken in wet areas, near water ponds located respectively at laguna Tuyajto and laguna Cejar. The samples contain green microbial mats visible with the naked eye; chlorophyl in those mats could be responsible for this sharp feature in the visible part of the spectra.

A.4.4. Raman spectroscopy

Raman spectra are presented in Fig. A.6, along with a comparison to reference spectra from the American Mineralogist Crystal Structure Database available on RRUFF (Downs and Hall-Wallace, 2003). Since Raman spectra were acquired on raw rocks (unprepared samples), minerals were identified by their main peak, which is found around 970 cm^{-1} for borates, 990 for Na sulfates, 1008 for gypsum, 1015 for anhydrite, 1085 for calcite (Fig. A.6 b). Distinguishing between different minerals within the same group is, however, challenging due to the precision of the instrument. Carotenoids were also detected in several samples of wet crusts thanks to a set of 3 peaks located around 1005, 1150 and 1510 cm^{-1} (e.g., Hooijschuur et al., 2015; Verkaaik et al., 2015).

A.4.5. Quantitative analysis from XRD

XRD analyses provide quantitative insights into the mineral assemblages within the crystalline phase of the samples. A list of key sample compositions is given in Table A.2

. With the exception of margins/clay-playa rocks and samples taken at depth, all samples have a crystallinity index > 90%, indicating that they contain very little to no amorphous material. Gypsum and halite form the most abundant mineral phase for the majority of salar crusts, and are often coupled with calcium carbonates (calcite or aragonite). Additional carbonates such as natrite, natron and dolomite are detected in the samples of: the Salar de Aguas Calientes 3, Laguna de Cejar/ de la Piedra (Salar de Atacama), Laguna Chaxa (Salar de Atacama; Table A.1), respectively. Detrital material (anorthite or albite, quartz) are present in most samples, with increasing proportions at the salar margins or at depth. Additional minor mineral phases include a range of Ca and Na-sulfates such as bassanite (in the Salar de Atacama and Salar de Quisquiro), anhydrite (Salar de Atacama, Salar de Quisquiro, Salar de Aguas Calientes 3), alunite (lauguna Tuyajto), glauberite, hydroglauberite, bloedite, thenardite, mirabillite (Salar de Atacama), borates such as pinnoite, ulexite, nobleite (Salar de Atacama) and chlorides such as sylvite, hydrophilite (Salar de Atacama) (Table A.2, Fig. A.7).

A.5. Discussion

A.5.1. Correlation between field (VNIR) and lab (Raman, XRD) analyses

There is agreement with the mineralogy determined from Raman and VNIR analyses, with the exception of some carbonate-bearing samples that are difficult to characterize with VNIR compared to Raman analysis (e.g., sample J7L4; Table A.3, Fig. A.8). Raman data were a good indicator of the presence of anhydrous sulfates, such as anhydrite, which are difficult to identify solely by VNIR spectroscopy. Raman analyses were performed at a smaller scale (grain scale) than VNIR analyses, resulting in more heterogeneities in the analyses of a single sample. The measurements are, however, consistent with all of the minerals identified in the homogenized samples from the XRD analyses. Field observations were also a helpful complementary tool because some minerals such as halite displayed characteristic morphology that facilitate their identification.

For the Atacama salt crusts, VNIR and Raman spectroscopy were often redundant as most samples are well-crystallized. XRD analysis, however, provided significant additional information for these samples as 1) it allowed the detection of minerals that have featureless spectra in the VNIR domain such as halite, quartz, and anorthite, 2) it allowed the detection of all the most abundant mineral phases, 3) it allowed quantitative mineral abundance measurements. XRD analysis was also a powerful tool for distinguishing between different minerals within the same family (e.g., glauberite and hydroglauberite, thenardite and mirabillite). These minerals should have distinct VNIR properties, however, spectral libraries for sulfates are incomplete. Additionally, XRD analysis also distinguished between hydrated sulfates and hydrated Cl salts, which can have similar VNIR spectra, making detections sometimes problematic (e.g.,

Table A.2: Summary of XRD detections for all samples. For crystallinity values, the + , ++ and +++ symbols indicate the following ranges of values, respectively: > 40%, > 60%, > 80%. For mineral abundances, the -, + , ++ and +++ symbols indicate the following ranges of values, respectively: present but < 10%, > 10%, > 50%, > 80%. Gray lines indicate samples of lower crystallinity (< 80%). Sample names starting with A- indicate that the samples were also collected in sterile conditions for biology analyses (see Martini et al., 2016). Gyp = gypsum, Hal = halite, Cal = calcite, Ara = aragonite, Do = dolomite, Natri = natrite, natro = natron, An = anorthite, Alb = albite, Qz = quartz, Bass = bassanite, Anh = anhydrite, Gla = glauberite, Blo = blodite, The = thenardite, Mir = mirabilite, Pin = pinnoite, Ul = ulexite, Nob = Nobleite, Sylv = Sylvite, Hydg = hydroglauberite, Hydp = hydrophilite, Al = alunite, phyl = phyllosilicates.

Sample origin location	Crust type	Sample name	Cristallinity	Gyp	Hal	Cal	Ara	Do	Natri	Natro	An	Alb	Qz	Bass	Anh	Gla	Blo	The	Mir	Pin	Ul	Nob	Sylv	Hydg	Hydp	Al	Phyl
Salar de Aguas Calientes 3 - center	T6	A-J5L1R3Z1	+++	++	+	+									–												
Salar de Aguas Calientes 3 - center - 20 cm depth		A-J5L1R3Z2	+++	+++	–	–			–																		
Salar de Aguas Calientes 3 - margin	T3	A-J5L1R4Z1	+++	+	++						+																
Salar de Aguas Calientes 3 - margin - 20 cm depth		A-J5L1R4Z2	+++	+++	–	–																					
Laguna Tuyajto - center	T2	A-J2L2R3Z1	+++	+	+++																						
Laguna Tuyajto - center - 20 cm depth		A-J2L2R3Z2	++	++	+	+	–				+		–														
Laguna Tuyajto - margin	T5*	A-J2L2R4Z1	+++	–	+++	–					+																
Laguna Tuyajto - margin - 20 cm depth		A-J2L2R4Z2	+		–	–					+++		–														
Laguna Tuyajto - margin	T4	A-J2L2R2	++	++	++	+					+																
Laguna Tuyajto - margin	T5*	A-J2L2R1	++	++	++	–					–		–													–	
Salar de Laco - center	T3	A-J2L1R1Z1	++	++	+						+		–	–													
Salar de Laco - center - 20 cm depth		A-J2L1R1Z2	++	+++	–						+		–														
Salar de Laco - margin	T5*	A-J2L1R2Z1	++	+	+	+					+		–														
Salar de Laco - margin - 20 cm depth		A-J2L1R2Z2	+		–	+					++		+														
Salar de Laco - margin - 20 cm depth former crust		A-J2L1R2Z2crust	++	–		+	++					–	–														
Salar de Atacama - N margin	T5	J8L1	+		–							++	+														+
Salar de Atacama - Laguna de Cejar -center	T4	J9L1R1	+++	++	+	+										+											
Salar de Atacama - Laguna de Cejar -center	T4	J9L1R2	+++		+++																						
Salar de Atacama - Laguna de Cejar -center	T4	J9L1R3	+++	++	+	+							–			–											
Salar de Atacama - Laguna de Cejar/de la Piedra -margin	T5*	J9L1R4	++	–	+	+				–	+		–		–												
Salar de Atacama - Laguna de Cejar/de la Piedra -margin	T5*	J9L1R5	+++	+	++	–						–	–	+		–											
Salar de Atacama - Laguna de la Piedra -center - ponds	T4	J9L2R1	+++	+	+											++	–	–	–					–	–		
Salar de Atacama - Laguna de la Piedra -center	T4	J9L2R2	+++	+	+											++	–	–	–					–	–		

Table A.2: Continued from previous page.

Sample origin location	Crust type	Sample name	Cristallinity	Gyp	Hal	Cal	Ara	Do	Natri	Natro	An	Alb	Qz	Bass	Anh	Gla	Bio	The	Mir	Pin	Ul	Nob	Sylv	Hydg	Hydp	Al	Phyl
Salar de Atacama - Laguna de la Piedra -center	T4	J9L2R3	+++	+++	–																						
Salar de Atacama - Laguna Chaxa -center	T1	J1L1R1	+++	–	+++							–			–								–				
Salar de Atacama - Laguna Chaxa -center	T1*	J1L1R2	++		–		+++																				
Salar de Atacama - Laguna Chaxa -margin	T5*	J1L1R3	++		+							+	–								++		–				
Salar de Atacama - Laguna Chaxa -margin	T3	J1L1R4	++		+			–				+	–		–			+		+	+	–					
Salar de Atacama - Laguna Chaxa -margin	T5*	J1L1R5	++		+						+		+	–	–	+											
salar de Quisquiro - margin	T4	J11L1R1	++	+	++						–		–	+													
Salar de Quisquiro - margin	T4	J11L1R2	++	+	++						–		–	+													
Salar de Quisquiro - margin (water pond)	T4	J11L1R3	++	+	++						–		–	+													
Salar de Quisquiro - center	T3	J11L1R4	++		++						+		–		+												
Salar de Atacama - E margin	T5	J7L4	++		–	+	–					+	+														–
Salar de Atacama - E margin	T3	J7L5	+++		+++	–						–	–		–												
Salar de Atacama - E margin	T3	J7L6	+++		++							+	+		–												–
Salar de Atacama -center	T1	J7L7	+++		+++							–	–		–												
Salar de Atacama -center	T1	J7L8	+++		+++								–		–								–				
Salar de Atacama -center	T1	AJ7L9	+++		+++								–		–												
Salar de Atacama -center	T1	J7L10	+++		+++																						
Salar de Atacama -center	T1*	J7L11	+++		+++																						
Salar de Atacama -center	T1	J7L12	+++		+++																		–				
Salar de Atacama -W margin	T3	A-J7L14	+++		+++							–			–												
Salar de Atacama -W margin	T5*	A-J7L16Z1	++		–							+	+		++												
Salar de Atacama -W margin - 20 cm depth		A-J7L16Z2	++	+	+							+	+		–												

Table A.3: Comparison of VNIR, Raman and XRD data mineralogic interpretation for a subset of representative samples, shown in Fig. A.8 (Also see A.5.1). Gray lines indicate the set of samples which VNIR spectra are shown in Fig. A.5. For the Raman column: N = no peaks, C = carotenoids.

Sample ID	Context	VNIR dominant mineral	Raman dominant mineral	Most abundant mineral from XRD
J1L1R1	Salar de Atacama - core area	PHS	Anhydrite	Halite
J1L1R2	Salar de Atacama - core area, small concretions	Carbonate + PHS	Carbonate	Carbonate
J1L1R3	Salar de Atacama - margin, east of Laguna Chaxa	Pinnoite + PHS	N	Borate
J1L1R4	Salar de Atacama - margin, east of Laguna Chaxa	Ulexite + pinnoite	Na-sulfate	Na-sulfate
J1L1R5	Salar de Atacama - margin, east of Laguna Chaxa	PHS + clays	N Anorthite	
J2L1R1	Salar de Laco - core area	Gypsum	Gypsum	Gypsum
J2L1R2	Salar de Laco - margin area	Gypsum + PHS	Gypsum + C	Anorthite
J2L2R1	Laguna Tuyajto - far margin area	Gypsum	Gypsum	Gypsum
J2L2R2	Laguna Tuyajto - far margin area (wet)	Gypsum	Gypsum	Halite
J2L2R3	Laguna Tuyajto - core area	PHS	Gypsum + C	Halite
J2L2R4	Laguna Tuyajto - margin area	PHS + clays + sulfates	N	halite
J5L1R3	Salar de Aguas Calientes 3 - 'beach' area	Gypsum + PHS	Gypsum	Gypsum
J5L1R4	Salar de Aguas Calientes 3 - margin area	Gypsum	Gypsum	Halite
J7L4	Salar de Atacama - margin area	PHS + clays Carbonate	Albite + clays	
J7L5	Salar de Atacama - margin area	Clays + PHS	Anhydrite	Halite
J7L6	Salar de Atacama - core area	PHS + clays	Unindentified peak at 150	Halite
J7L7	Salar de Atacama - core area	PHS + clays + sulfates	N	Halite
J7L8	Salar de Atacama - core area	PHS + clays + sulfates	Anhydrite	Halite
J7L9	Salar de Atacama - core area	PHS + sulfates	N	Halite
J7L10	Salar de Atacama - core area	PHS (MgCl2?)	Anhydrite	Halite
J7L11	Salar de Atacama - core area	PHS + sulfates	Anhydrite	Halite
J7L12	Salar de Atacama - core area	PHS + clays	N	Halite
J7L14	Salar de Atacama - margin area	PHS (MgCl2?)	Anhydrite	Halite
J7L16	Salar de Atacama - margin area	Na-sulfate	N	Albite
J8L1	Salar de Atacama - margin area	PHS + clays + gypsum	150 peak	Albite + clays
J9L1R1	Laguna de Cejar - core area	PHS	Gypsum + Na-sulfate + C	Gypsum
J9L1R2	Laguna de Cejar - core area	PHS	Na-sulfate + C	Halite
J9L1R3	Laguna de Cejar - core area	Gypsum	Gypsum + Na-sulfate	Gypsum
J9L1R4	Laguna de Cejar - marginal area	Gypsum + clays	N	Halite
J9L1R5	Laguna de Cejar - marginal area	Gypsum + sulfates	Gypsum	Halite
J9L2R1	Laguna de la Piedra - core area, pool of white crystals	PHS	Na-sulfate	Halite
J9L2R2	Laguna de la Piedra - core area	Na-sulfate	Gypsum + C	Na-sulfate
J9L2R3	Laguna de la Piedra - core area, ramparts	Gypsum + PHS	Gypsum + C	Gypsum
J11L1R1	Salar de Quisquiro - margin area	PHS	Gypsum + C	Halite
J11L1R2	Salar de Quisquiro - margin area	Gypsum + PHS	Gypsum	Halite
J11L1R3	Salar de Quisquiro - margin area (wet)	Gypsum + PHS	Gypsum + C	Gypsum
J11L1R4	Salar de Quisquiro - core area	PHS	Anhydrite	Halite

J. Hanley et al., 2015; Lynch et al., 2015).

Laboratory XRD analysis also represents a powerful asset to estimate the benefits and limitations of VNIR spectroscopy; VNIR spectroscopy however represents an easy, rapid, passive and non destructive tool during field surveys. Remote sensing VNIR spectroscopy is also commonly used in planetary sciences to survey the composition of surfaces (e.g., the OMEGA (Observatoire pour la Mineralogie, l'Eau, les Glaces et l'Activité), CRISM (Compact Reconnaissance Imaging Spectrometer for Mars) and M3 (Moon Mineralogy Mapper) instruments, see Bibring et al., 2004; Murchie et al., 2007; Pieters et al., 2009) and VNIR spectrometers, such as MicrOmega, MA-MISS (Mars Multispectral Imager for Subsurface Studies), ISEM (Infrared Spectrometer for ExoMars), LIS (Lunar Infrared Spectrometer) and SuperCam, are being developed for the next generation Mars and Moon landers and rovers (Pilorget and Bibring, 2013; De Angelis et al., 2014; Korablev et al., 2015, 2016; Maurice et al., 2015).

Qualitative VNIR spectral interpretation allows identification of one or two minerals present in mineral mixtures/common rock samples, however, comparison with XRD analysis reveals that: 1) most samples are made of a much more complex mineral assemblage than inferred from VNIR data alone, and 2) the spectrally dominant mineral is not necessarily the most abundant. An example is given in Fig. A.8 and Table A.3 that presents the comparison between the results of the VNIR spectral analyses (spectrally dominant mineral, 8a) and the Raman (Fig. A.8 b) and XRD analyses (most abundant mineral, A.8 c). Sulfates generally dominate the VNIR spectra when present even though they are not necessarily the most abundant mineral: for instance in sample J2L1R2 (far margin of Salar de Laco) gypsum only represents ~10% of the crystalline phase but the VNIR signature is typical of this mineral (Table A.2). This is also true for samples J11L1R1 and J11L1R2 from the salar de Quisquiro margin, which are dominated by halite with 10–20% of both gypsum and bassanite but whose spectra are dominated by gypsum absorptions. However, the lower average reflectance values, the rounded shape of the absorptions and the relative strength of the 1.4 and 1.9 μm features allow us to deduce the presence of another hydrated material. In one sample of the Salar de Atacama (J1L1R4), borates appear spectrally dominant in the VNIR whereas Na-sulfates are slightly more abundant (about 40% thenardite against 23% pinnoite + ulexite), nevertheless this sample contains ~50% amorphous material that could also contribute to the spectral signature. In contrast anhydrous minerals such as feldspar, or anhydrous chlorides, such as halite, are more difficult to identify with VNIR or Raman spectroscopy that are more sensitive to minerals having H_2O, OH, CO_3, SO_4 or ClO_4 in their structure such as clays or sulfates. Although halite is more abundant in most samples from the Salar de Atacama (e.g., J11L1R2, J9L1R5, J7L4, J2L2R4, J2L2R2), the VNIR spectra are often dominated by clays and/or sulfates which are present as impurities or very minor phases. XRD analysis and Raman spectroscopy also detected carbonates in multiple samples (Salar de Laco J2L1R2, Laguna Tuyajto J2L2R2, Salar de Atacama J7L4, J9L1R1, J9L1R4) that were almost never detected in the

VNIR data in our study when mixed with sulfates. Spectra of anhydrous carbonates exhibit strong absorptions near 2.3, 2.5, 3.4 and 3.9 μm, but these features become weakened for hydrous carbonates (Bishop et al., 2013), and the IR domain was not fully covered in our study. One caveat of the XRD analysis we performed is the absence of information on amorphous phases, which are minor in the samples we collected but could contribute to spectral features in the VNIR. Additionally, the semi-quantitative XRD technique used in the present study is not adapted for the characterization of clay minerals, which have been identified from morphologic observations in the clay-playa and some of the salar margins. Clays have been detected in VNIR spectra, however, they appear often mixed with sulfates, which can mask their signature if less than 30% abundance (Stack and Milliken, 2011). Therefore, although VNIR spectroscopy represents a powerful tool to distinguish between different types of terrains, deriving detailed mineralogy for complex samples as in this study is difficult with only VNIR spectra as some minerals, especially sulfates, can dominate the spectra even if present at low abundances. A suite of instruments / analyses is required to fully characterize complex mineral assemblages, and used together, VNIR spectroscopy and XRD analyses provided a powerful tool to distinguish different types of well-crystallized salt crusts.

A.5.2. Correlation between spaceborne and ground data

Multiple zones are observed within the salars on the Landsat 8 RGB composite of three different bands (Fig. A.2 a). Each colored zone was visited in the field and outcrops were classified into multiple types based on their morphology (Section 3.2). There is a good agreement in general between the various zones as mapped from space and the field observations in terms of: 1) crust types, as assigned from morphological observations and 2) mineralogy, as determined from VNIR, Raman, and XRD analysis. To the first order, field observations in terms of morphologies correlate to mineralogy derived from VNIR and XRD analyses. The type 1 crust, as observed in the central part of the Salar de Atacama, is made of > 90% halite that may contain traces of detrital material (clays, feldspar, quartz) and dry sulfates (thenardite, anhydrite). Nearly pure halite is observed in wetter areas, which appear whiter on the Landsat RGB composite (Fig. A.2 a), and exhibit large scale polygons. The type 2 crust, as observed in the center part of Laguna Tuyajjto, is also a wet crust that exhibits polygons and is made of 80% halite and 20% gypsum (dark orange on Landsat RGB composite (Fig. A.2 a). Sulfates such as gypsum, glauberite, mirabillite are found in greater abundance in wetter areas where the Type 4 crust is observed, and correspond to brown to orange-toned terrains on Fig. A.2 a. Type 4 crusts appear to be formed in wetter areas and near water ponds at margins or around small-scale lagoons located within the Salar de Atacama (e.g;, Laguna de Cejar). Type 4 crusts display a highly variable mineralogy and variable color-tones at the meter scale, with ponds more enriched in halite or gypsum or Na-sulfates. Type 3 crusts are also characterized by multiple mineral assemblages, but

are often dominated by gypsum or anhydrite mixed with detrital material. There are found mostly in marginal and dry areas, where salts are formed by efflorescence (white to yellow tones on Landsat RGB, Fig. A.2 a). Type 3 and 4 crusts are more consistently found where the Landsat 8 sulfate parameter (Fig. A.2 c) has higher values. Type 5 terrains (clay playas) are mapped as gray tones on the Landsat RGB composite (Fig. A.2 a) and correspond to dry, marginal areas where the higher proportions of amorphous and clay material are detected.

Combining field and laboratory observations, however, reveal some observational bias: sulfate crusts were generally found to be thin (< 5 cm) with a sharp transition to the underlying clay, silt, or sand-rich alluvial deposits that cannot be observed from space. Therefore, even though clays and carbonates are almost always observed at shallow depths below salt crusts in the central part of the salars, and are morphologically identified in marginal areas under a thin salt efflorescence (< 1 mm), they are very difficult to detect without digging. Drilling also allowed the identification of a former, 1 cm-thick calcite-rich crust that was observed at 20 cm depth in the Salar de Laco, confirming the hypothesis derived from airborne images that this salar must have been occupied by a more alkaline lake in the past. The only exception to thin crusts lies within the Salar de Atacama where the lower limit of the hard (halite) crust was not observed, but is estimated to be at least a few meters deep. Therefore, although multispectral imagery such as Landsat represents a powerful tool to map large-scale mineralogy variations in desert areas, it presents limitations regarding the vertical extent of salt crusts that can be thin and provides little information on the nature of the underlying material in regions with no active erosion or continuous precipitation, such as playa lakes.

A.5.3. Mineralogy of Chilean salars

Mineralogic zonation (large scale horizontal heterogeneities) was observed within most salars from both spaceborne and field analyses. Whereas the central part of the salars is occupied by highly crystalline salt crusts, made of halite and/or gypsum, margins are characterized by a higher concentration of detrital material, carbonates and clays. Halite and gypsum are detected at most margins where they form efflorescent salts deposited in the capillary fringe. Combining geochemical and flow modelling, previous hydrology studies in the Salar de Atacama have shown that meteoric water infiltrated from elevated areas in the Andes is transported to the Atacama basin where it drains laterally from east to west (Risacher et al., 2003; Vasquez et al., 2013). Where groundwater reaches the surface, discharged aquifers form lagoons or playa. Evaporation can only occur where water is available and is, therefore, concentrated around the margins of the salar (Houston, 2006). As clays, carbonates, sulfates, and chlorides precipitate, the remaining brines become more saline with minor discharges occurring by evaporation. Mineral precipitation is responsible for a strong reduction in permeability in the salt flat nucleus associated with halite and calcite formation and

could explain the unique preservation of the thick halite crust (Vasquez et al., 2013).

Additionally, distinct mineral assemblages have been identified within the various salars. Possible causes of these differences include: (1) the presence of water, near or, at the surface, (2) the nature of the bedrock, (3) the composition of the feeding brines, (4) the dimension of the basin/salar, and (5) the temperature and evaporation rate. The environmental parameters (temperature, evaporation rate) do not differ much for the investigated salars. Temperature and evaporation are slightly higher in the Salar de Atacama compared to the Andean salars which are exposed to similar conditions (Table A.1). Whereas the Andean salars are emplaced on volcanic bedrock, the Salar de Atacama, a much larger salt flat, is emplaced on sedimentary bedrock. A previous survey by Risacher et al. (2003) showed that bedrock composition can partially explain the nature of the various brines involved in salt flat formation. Brines in the Atacama were found to be either sulfate-rich or calcium-rich, near-neutral or slightly acidic brines. Alkaline brines are almost completely lacking from the area due to the presence of gypsum-rich desert dust and the oxidation of native sulfur, whose dissolution results in brine acidification. Theoretically, SO_4-rich inflow waters and their derived SO_4-rich brines should be found in the intravolcanic basins of the Andes because of the nature of the bedrock and ubiquity of native sulfur. Previous workers (e.g., Risacher et al., 2003) have shown, however, that some of the Andean salars (e.g., Salar de Quisquiro) belong to the Ca-rich brines group, or mixed brines group (e.g., Salar de Aguas Calientes 3), which may indicate the presence of older sedimentary formations at depth. Ca-rich brines generally prevail in sedimentary basins of lower elevation, where Ca-rich minerals are abundant, although it appears that the Salar de Atacama, which should belong to this category, is fed by two different sources of Ca (to the west) and SO_4 (to the east) and is, therefore, classified as formed from mixed brines (Risacher et al., 2003). Water undergoing evaporative concentration should precipitate a sequence of minerals in order of increasing solubility, starting with calcite and Mg- carbonates and silicates (Hardie and Eugster, 1970) followed by gypsum. Gypsum induces a new divide of the neutral path producing either Ca-rich/SO_4-poor or SO_4-rich/Ca-poor waters, according to the Ca/SO_4 ratio at the beginning of gypsum saturation (Risacher et al., 2003). A few cases of extreme acidification, leading to acid-sulfate brines, due to hydrothermal processes and enriched sulfur contents have been reported in Chile (Salars de Gorbea and Ignorado) and Australia (e.g., McArthur et al., 1991; Long et al., 1992; Risacher et al., 2002) and might be relevant to Mars (cf. next section), but these are not observed in the salars of our study area. In their final stage, SO_4-rich brines should precipitate a mixture of Na/Ca-sulfates and halite whereas Ca-rich brines are more likely to precipitate chlorides (Hardie and Eugster, 1970; Risacher et al., 2003).

A thick, ancient halite crust was only observed in the field in the Salar de Atacama and the presence of a possibly active halite crust was inferred from spaceborne imagery in the Salar de Quisquiro, Salar de Aguas Calientes 1 and 2 and Salar de Capur,

which are all derived from Ca-rich brines. No halite thick crust was observed in the salars derived from SO_4-rich brines, although halite is present as a mixed component in the rock samples. The presence of a halite-dominated crust could be related to the nature of the brines, although as halite is rapidly dissolved and most brines are unsaturated, its formation and preservation might also depend on evaporation rates and permeability. The unique setting of the Salar de Atacama downslope from the Andean salars and its higher aridity could also explain the thickness of its halite crust that could have precipitated and accumulated from the chloride salts previously dissolved in the Andean salars. Alternatively the larger size of the salar (correlated with a higher basin size, Table A.1) could also somehow account for this unique, thick halite crust.

Whereas gypsum has been detected in all salars, a greater mineral diversity, including Na-rich sulfates and borates, was found at Laguna Tuyajto and Laguna Chaxa/ Laguna de Cejar/ Laguna de la Piedra, which all appear to be derived from SO_4-rich brines. A greater diversity is also observed in wetter areas that are often colonized by life forms including sulfur-reducing bacteria (e.g., Stivaletta et al., 2012). Therefore, the nature of the brine and soil wetness, among other factors, ultimately influenced the final mineral assemblage as observed in the salt flats.

A.5.4. Relevance to Mars

A variety of hydrated minerals have been detected on Mars, including clays, carbonates, sulfates, and Cl salts (e.g., Poulet et al., 2005; Bibring et al., 2006; Osterloo et al., 2008, 2010; Murchie et al.,2009; Ehlmann et al., 2011; Carter et al., 2010, 2013). Whereas clays are commonly detected in the ancient, Noachian (> 3.7 Gy) highlands, the distribution of chloride, sulfate, and carbonate-bearing materials on Mars is not as pervasive (e.g., Bibring et al., 2006; Carter et al., 2013). Mg, Fe and Ca-rich carbonates have been detected at a few locations of the surface in association with exhumed, Noachian crustal, altered rocks (Ehlmann et al., 2008; Michalski et al., 2010; Bultel et al., 2015; Wray et al., 2016), but not in lake or playa contexts. Proposed chloride-bearing materials are identified based on their spectral distinctiveness in the TIR images and association with light-toned, indurated, fractured material often found in topographic lows (Osterloo et al., 2008, 2010; Glotch et al., 2010; Fig. A.9 c,d), and draped on both Noachian and Hesperian (3.7–3.0 Gy) units. Based on their context and the existence of fractures and polygonal textures, proposed chloride-bearing materials have been inferred to originate from both ponding of surface runoff, and groundwater upwellings, followed by evaporation (Osterloo et al., 2010). Mg, Fe and sometimes Ca-sulfates are commonly detected in association with kilometer-thick Hesperian layered deposits (e.g., Gendrin et al., 2005; Flahaut et al., 2010, 2014, 2015) and polar dunes (Langevin et al., 2005; Masséet al., 2010), although more localized detections were also reported (e.g., Wray et al., 2011; Loizeau et al., 2015; Fig. A.9 b). Although their origin is debated, the morphology and mineralogy of some sulfate salts (e.g., sulfate-rich depostis in Meridiani Planum), and their distribution in regions where

groundwater upwellings are predicted, is consistent with an evaporitic origin (e.g., Ardvison et al., 2005; Andrews-Hanna et al., 2007; Osterloo et al., 2010; Davila et al., 2011; J. Flahaut et al., 2015). The observation of karstic features such as dolines, ridges and pans in the etched terrains of Meridiani Planum region supports the groundwater hypothesis and points to the existence of martian sulfate-rich salars locally (Baioni et al., 2013; J. Flahaut et al., 2015; Fig. A.9 a). Both sulfates and high levels of Cl (which could be attributed to chlorides) were detected in situ by the Opportunity Rover in the hematite plains of Meridiani Planum, which lies directly above the etched terrains unit (Ardvison et al., 2006; Squyres et al., 2006).

Therefore, some of the processes involved in the formation of the Chilean salars are likely to be active or have been active on Mars. This study also employed similar spectroscopic wavelength ranges and resolutions to those used by orbiting instruments to examine Martian mineralogy. From our observations we can infer that horizontal and vertical zonation is expected in the martian salars and could be observed, providing that we have enough spatial resolution. Landsat imagery (~30 m/pixel) has a similar ground pixel size as the MRO/CRISM instrument (~20 m/pixel) which should be able to capture horizontal features. Landsat spectral resolution is far less, but sufficient to distinguish between various salt crusts providing promising results for multispectral cameras such as PanCam on the ExoMars rover (Griffiths et al., 2006). The high resolution of VNIR Instruments such as Micromega and ISEM (Pilorget and Bibring, 2013; Korablev et al., 2015, 2016) should distinguish between various types of salts and salt crusts on Mars, but could meet the same difficulties we evidenced with the ASDinc Fieldspec measurements in the case of mixtures. XRD analyses have been performed on the Curiosity Rover in an attempt to quantify mineralogic assemblages, with two major caveats: (1) the rover can only perform disoriented preparations which are not well-suited for clay identification, (2) the rover analyzed samples containing up to 50% amorphous materials (Morris et al;, 2015) that could not be characterized by XRD techniques (but could potentially be identified by VNIR techniques). Martian VNIR data sets also have a higher degree of noise that our Atacama spectra because of the contribution of atmospheric CO 2, aerosols and dust.

A climate-change related lacustrine to playa transition over time has also been suggested for Mars and is well documented at the Salar de Laco, where evidence for a former alkaline lake is found in the field (sampled calcite crust at a 20 cm depth) and also in spaceborne images (presence of paleoshores). The composition of martian bedrock is likely to be more basaltic than the andesitic Andean highlands, resulting in more Fe/Mg-rich brines and minerals, but similar complex evaporitic sequences and mineral assemblages are expected, with possible variations from one site to another. A major issue is whether these assemblages can be determined from VNIR surface spectroscopy solely given that in the presence of hydrated sulfates, a wide range of minerals can be masked (e.g., clays, carbonates, felsic and mafic minerals). In addition, given that carbonates are the first to precipitate from an evaporitic sequence,

they are likely to concentrate at the margins and bottom of the salars and be subject to burial. As shown here and in recent studies (e.g., Hanley, 2015; Lynch, 2015), it might be complicated to distinguish some hydrated chloride salts and hydrated chlorine oxyanion salts from sulfate salts, making martian sulfate detections potentially debatable. For instance, Na-rich sulfates and chlorides are expected to precipitate alongside with Mg-rich sulfates from $MgSO_4$-rich brines on Mars, but they have yet to be detected in the km-thick interior layered deposits of Valles Marineris or the etched terrains deposits of Meridiani Planum. However a recent study from Wang et al. (2016) interprets the presence of monohydrated Mg-sulfates at the bottom of the layered deposits as indicative of the presence of associated chlorides and Na-rich sulfates that would help overcome the metastability of starkeyite (polyhydrated Mg-sulfates); starkeyite being only detected at higher elevations (e.g., Fueten et al., 2014; Noel et al., 2015). Determining the exact mineral assemblages on Mars is key to characterizing past Martian surface chemistry, which should benefit in the coming decades by the development of spectral libraries (that are still incomplete for sulfates and chlorides) and the study of the spectral properties of lab mixtures and analog rock samples.

In addition, combining VNIR spectroscopic data with other datasets can aid with inferring the context and sometimes the mineralogy if certain characteristic patterns are present. For instance, El-Maarry et al. (2015) noticed that desiccation fractures are especially present in clay and chloride-rich deposits formed from evaporation. We concur with this from our field observations and further noticed that larger scale polygons are present in chloride deposits compared to clay deposits. The texture of the crust as observed in the Atacama salars was also found to be related to its dominant mineralogy and formation mechanism (efflorescence versus precipitation). Finally, in the Atacama salar there is a strong relationship between the dominant mineralogy and the albedo (higher for sulfate-rich area, and lower for clay-rich playas) of the deposits as seen from space, with the exception of unfrequently flooded, dust-covered crusts being darkened.

Understanding the formation of martian salts is also key to providing insight into the planet's habitability. Evidence for biomaterials is present in the VNIR data (e.g., chlorophyll absorption at 0.68 μm at Laguna Tuyajto J2L2R2 and Laguna de la Piedra J9L2R3), Raman data (carotenoid peaks in Laguna Tuyajto sample J2L2R3 and Salar de Quisquiro J11L1R1) and XRD data (presence of pigments in several samples, including Laguna Tuyajto J2L2R3 and Laguna de la Piedra J9L2R2) described above. A complementary survey carried out by Monaghan et al. (2016) aims to determine the type of organisms that thrive in the Atacama extreme environments and study their dependence on the mineralogy among other factors. Although perchlorates were not directly detected in our samples, they have been reported at other locations of the Atacama desert and on Mars (e.g., Catling et al., 2010) and could play a role in the development of life and biosignature preservation.

A.6. Conclusions

We performed a coordinated remote sensing and field survey of the Chilean Atacama salars, which were studied with various techniques (VNIR reflectance and Raman spectroscopy, morphologic analyses, XRD analysis). Remote sensing and field observations, as well as observations made with various techniques led to consistent results. Although VNIR analyses proved to be an efficient first-order, quick and non-destructive tool for mineralogic investigation, XRD analyses in the lab provided more complete information on assemblages, especially those that are spectrally dominated by sulfate signatures, which can mask the presence of other minerals (clays, chlorides, carbonates, feldspar).

Landsat multispectral imagery was used to map mineral zones that are easily identified in the absence of vegetation, and because most units are homogenous on large-scales. Both orbital and field data show that the formation mechanism of the salar through groundwater evaporation at topographic breaks in lowlands result in horizontal (margin vs. center) and vertical (salt crust at the surface) zonation. Clays, carbonates and detritic material are found at the margins of the salars and at depth, whereas salt-rich crust (halite and/or Ca-sulfates) form at their centers. A variability of Na-rich sulfates and borates are also present near wet areas. The nature of the salt crusts varies between the different salars and appear to be a function of the local bedrock but also brine chemistry and wetness. Similar processes are expected on Mars, where salars have been previously reported, although more acidic/ Mg-rich brines are expected and should result in slightly different mineral assemblages.

Acknowledgments

The authors are grateful to all of those who made this project and the field excursion possible, especially our local guide Mathilde Monseu, our astrobiologist partners Pascale Ehrenfreund, Euan Monaghan and Simone Martini at Leiden University, Andreas Kaufer at ESO and Bernard Foing at ESA, who provided us with logistical support. Our team was hosted by the wonderful APEX staffat the Sequitor base camp near San Pedro de Atacama; to Felipe, Carlos, Karl, Paulina, Francisco, Thomas, Luis, Pablo and others: many thanks for your warm welcome, your support and making this visit so unforgettable! We will see you again in the Atacama! The field VNIR spectra were collected with an ASDinc FieldSpec 4 that was generously loaned to N.J Potts through the 2015 Goetz Instrument Support Program. We are particularly grateful to Tom Ulrich at ASDinc for his support regarding our research project. The authors are also thankful to all the data instrument teams: Landsat, ASTER (The ASTER GDEM is a product of METI and NASA), DigitalGlobe, CTX and the Earth Explorer and USGS L8SR web services. The Context Camera (CTX) images are generously made available by the team on the Planetary Data System (PDS) archive and were processed using the e-mars web application (emars.univ-lyon1.fr). The author would like to thank the e-mars team including C. Quantin and L. Lozach for their help. The authors would also like to thank Ruben Vera and the XRD facility at the Centre de Diffractométrie Henri Longchambon of the University Lyon 1 (France) for their valuable advice and support during and after the XRD analyses. Raman analyses were performed at the Raman laboratory of the Vrije University Amsterdam with the help of Freek Ariese and Roel van Elsas for sample preparation. The campaign was funded by a Netherlands Organisation for Scientific Research (N.W.O.) VENI Innovational Research grant attributed to J. Flahaut. Additional support to J. Bishop from the NASA Astrobiology Institute is appreciated. Finally the authors would like to thank the editor and two anonymous reviewers for their valuable comments that helped improve the manuscript. Sample material and spectral

data can be made available on a simple request to the first author, pending availability.

References

- Amos, B.J., Greenbaum, D., 1987. Alteration detection using TM imagery: the effects of supergene weathering in an arid climate. ERIM, 21th International Symposium on Remote Sensing of Environment. Oct. 26-30, Ann Arbor, Michigan, USA, 795

- Andrews-Hanna, J.C., Phillips, R.J., Zuber, M.T., 2007. Meridiani planum and the global hydrology of mars. Nature 446 (7132), 163–166

- Arvidson, R.E., et al., 2005. Spectral reflectance and morphologic correlations in eastern terra Meridiani, mars. Science 307 (5715), 1591–1594

- Arvidson, R.E., et al., 2006. Nature and origin of the hematite-bearing plains of terra meridiani based on analyses of orbital and mars exploration rover data sets. J. Geophys. Res. 111, E12S08. http://dx.doi.org/10.1029/2006JE002728

- Armijo, R., Lacassin, R., Coudurier-Curveur, A., Carrizo, D., 2015. Coupled tectonic evolution of andean orogeny and global climate. Earth-Sci. Rev. 143, 1–35

- Baioni, D., Sgavetti, M., 2013. Karst terrains as possible lithologic and stratigraphic markers in northern sinus Meridiani, mars. Planet. Space Sci 75, 173–181 http://dx.doi.org/10.1016/j.pss.2012.08.011

- Bao, H., Jenkins, K.A., Khachaturyan, M., Díaz, G.C., 2004. Different sulfate sources and their postdepositional migration in atacama soils. Earth Planet. Sci. Lett. 224 (3), 577–587

- Berger, I.A., Cooke, R.U., 1998. The origin and distribution of salts on alluvial fans in the atacama Desert, northern chile. Earth Surface Process. Landforms 22 (6), 581–600

- Bibring, J.-P. et al., 2004. OMEGA: observatoire pour la minéralogie, l'eau, les glaces et l'activité, ESA-SP, p. 1240

- Bibring, J.-P., et al., 2006. Global mineralogical aqueous mars history derived from OMEGA/Mars express data. Science 312, 400–404 http://dx.doi.org/10.1126/ science.1122659

- Bishop, J.L., Lane, M.D., Dyar, M.D., Brown, A.J., 2008. Reflectance and emission spectroscopy of four groups of phyllosilicates: smectites, kaolinite–serpentines, chlorites, and micas. Clay Miner 43, 35–54 http://dx.doi.org/10.1180/claymin.2008.043.1.03

- Bishop, J.L., et al., 2009. Mineralogy of juventae Chasma: sulfates in the light-toned mounds, mafics in the sand, and opal in the plains. J. Geophys. Res. 114 E00D09. http://dx.doi.org/10.1029/2009JE003352

- Bishop, J.L., Perry, K.A., Darby Dyar, M., Bristow, T.F., Blake, D.F., Brown, A.J., Peel, S.E., 2013. Coordinated spectral and XRD analyses of magnesite-nontronite-forsterite mixtures and implications for

carbonates on mars. J. Geophys. Res. 118 (4), 635–650

– Bishop, J.L., Lane, M.D., Dyar, M.D., King, S.J., Brown, A.J., Swayze, G., 2014a. Spectral properties of Ca-sulfates: gypsum, bassanite and anhydrite. Am. Mineralogist 99, 2105–2115

– Bishop, J.L., Quinn, R.C., Dyar, M.D.,2014b. Spectral and thermal properties of perchlorate salts and implications for mars. Am. Mineralogist 99, 1580–1592

– Bishop, J.L., Ward, M.K., Roush, T.L., Davila, A., Brown, A.J., McKay, C.P., Quinn, R., Pollard, W., 2014c. Spectral properties of Na, Ca-, Mg-and Fe-chlorides and analyses of hydrohalite-bearing samples from axel heiberg island. Lunar and Planetary Science Conference, Vol. 45

– Bultel, B., Quantin-Naraf, C., Andréani, M., Clénet, H., Lozac'h, L., 2015. Deep alteration between hellas and isidis basins. Icarus 260, 141–160. doi: 10.1016/j.icarus. 2015.06.037

– Caracas, R., Bobocioiu, E.,2011. The WURM project—a freely available web-based repository of computed physical data for minerals. Am. Mineralogist 96 (2-3), 437–443

– Carr, M.H., Head III, J.W., 2010. Geologic history of mars. Earth Planet. Sci. Lett 294 (3–4), 185–203 http://dx.doi.org/10.1016/j.epsl.2009.06.042

– Carter, J., Poulet, F., Bibring, J.-P., Murchie, S.,2010. Detection of hydrated silicates in crustal outcrops in the northern plains of mars. Science 328 (5986), 1682–1686 http://dx.doi.org/10.1126/science.1189013

– Carter, J., Poulet, F., Bibring, J.-P., Mangold, N., Murchie, S.,2013. Hydrous minerals on mars as seen by the CRISM and OMEGA imaging spectrometers: updated global view. J. Geophys. Res. Planets 118, 831–858 http://dx.doi.org/10.1029/2012JE004145

– Catling, D.C., Claire, M.W., Zahnle, K.J., Quinn, R.C., Clark, B.C., Hecht, M.H., Kounaves, S., 2010. Atmospheric origins of perchlorate on mars and in the atacama. J. Geophys. Res. 115 (E1)

– Chapman, J.E., Rothery, D.A., Francis, P.W., Pontual, A., 1989. Remote sensing of evaporite mineral zonation in salt flats (salars). Remote Sens (Basel) 10 (1), 245–255

– Clark, R.N., et al., 1990. High resolution reflectance spectroscopy of minerals. J. Geophys. Res. 95 (B8), 12653–12680

– Clark, R.N., et al.,2007. USGS digital spectral library splib06a. U.S. Geological Survey, Digital Data Series 231

– Cloutis, E.A., et al., 2006. Detection and discrimination of sulfate minerals using reflectance spectroscopy. Icarus 184, 121–157

– Cloutis, E., Berg, B., Mann, P., Applin, D., 2016. Reflectance spectroscopy of low atomic weight and Na-rich minerals: borates, hydroxides, nitrates, nitrites, and peroxides. Icarus 264, 20–36

– Crowley, J.K., 1990. A spectral reflectance study (0.4-2.5 μm) of selected playa evaporite mineral deposits and related geochemical processes. In: 10th Annual International Geoscience and Remote Sensing Symposium-IGARSS'90, Vol. 2, p. 965

– Davila, A., et al., 2011. A large sedimentary basin in the terra sirenum region of the southern highlands of mars. Icarus 212 (2), 579–589. doi: 10.1016/j.icarus.2010. 12.023

– De Angelis, S., De Sanctis, M.C., Ammannito, E., Di Iorio, T., Carli, C., Frigeri, A., Capria, M.T., Federico, C., Boccaccini, A., Capaccioni, F., Giardino, M., 2014. VNIR spectroscopy of mars analogues with the exomars-mamiss instrument. MSAIS 26, 121

– Dingman, R., 1962. Tertiary salt domes near san pedro de atacama. Chile. US Gcol. Sun., Praf. Pap, (4S), pp.92–94

– Dingman, R.J., 1967. Geology and ground-water resources of the northern part of the salar de atacama, Antofagasta Province, Chile (No. 1219). US Govt. Print. Off. Drake, N.A., 1995. Reflectance spectra of evaporite minerals (400-2500 nm): applications for remote sensing. Int. J. Remote Sensing 16 (14), 2555–2571

– Downs, R.T., Hall-Wallace, M., 2003. The american mineralogist crystal structure database. Am. Mineralogist 88, 247–250

– Ehlmann, B.L., et al., 2008. Orbital identification of carbonate-bearing rocks on mars. Science 322, 1828–1832. doi: 10.1126/science.1164759

– Ehlmann, B.L., et al., 2009. Identification of hydrated silicate minerals on mars using MROCRISM: geologic context near nili fossae and implications for aqueous alteration. J. Geophys. Res 114 E00D08. http://dx.doi.org/10.1029/2009JE003339

– Ehlmann, B.L., et al., 2011. Subsurface water and clay mineral formation during the early history of mars. Nature 479, 53–60 http://dx.doi.org/10.1038/nature10582..

– El-Maarry, M.R., Watters, W.A., Yoldi, Z., Pommerol, A., Fischer, D., Eggenberger, U., Thomas, N., 2015. Field investigation of dried lakes in western united states as an analogue to desiccation fractures on mars. J. Geophys. Res. 120 (12), 2241–2257

– Epema, G.F., 1986. Processing thematic mapper data for mapping in tunisia. ITC J. 1, 30–34

– Epema, G.F., 1990. Effect of moisture content on spectral reflectance in a playa area in southem tunisia. In: Proceedings of the International Symposium on Remote Sensing Water Ressources. IAH, august 20-24. Enschede, The Netherlands, pp. 301–308

– Ericksen, G.E., 1981. Geology and the origin of the chilean nitrate deposits, geol. Soc. Amer. Spec. Paper 1188 (1981), 37

– Ericksen, G.E., 1983. The chilean nitrate Deposits: the origin of the chilean nitrate deposits, which contain a unique group of saline minerals, has provoked lively discussion for more than 100 years. Am. Sci. 71 (4), 366–374

– Fassett, C.I., Head, J.W., 2008. Valley network-fed, open-basin lakes on Mars: distribution and implications for noachian surface and subsurface hydrology. Icarus 198 (1), 37–56

– Flahaut, J., Quantin, C., Allemand, P., Thomas, P., Le Deit, L., 2010. Identification, distribution and possible origins of sulfates in capri chasma (Mars), inferred from CRISM data. J. Geophys. Res. 115, E11007. doi: 10.1029/20 09JE0 03566

– Flahaut, J., Massé, M., Le Deit, L., Thollot, P., Bibring, J.P., Poulet, F., Quantin, C., Mangold, N., Michalski, J., Bishop, J.L., 2014. Sulfate-rich deposits on Mars: a review of their occurences and geochemical implications. LPI Contributions 1791, 1196

– Flahaut, J., Carter, J., Poulet, F., Bibring, J.-P., van Westrenen, W., Davies, G.R., Murchie, S.L., 2015. Embedded clays and sulfates in meridiani Planum, mars. Icarus 248, 269–288. doi: 10.1016/j.icarus.2014.10.046

– Fueten, F., Flahaut, J., Stesky, R., Hauber, E., Rossi, A.P., 2014. Stratigraphy and mineralogy of candor Mensa, west candor Chasma, Mars: insights into the geologic history of valles marineris. J. Geophys. Res. 119, 1–24

– Irons, J.R., J.L. Dwyer, J.A. Barsi, 2012. The next landsat satellite: the landsat data continuity mission remote sensing of environment, 122, pp. 11–21

– Gaffey, S.J., 1986. Spectral reflectance of carbonate minerals in the visible and near infrared (O. 35-2.55 microns); calcite, aragonite, and dolomite. Am. Mineralogist 71 (1-2), 151–162

– Gendrin, A., et al., 2005. Sulfates in martian layered terrains: the OMEGA/Mars express view. Science 307, 1587–1591

– Glotch, T.D., Bandfield, J.L., Tornabene, L.L., Jensen, H.B., Seelos, F.P.,2010. Distribution and formation of chlorides and phyllosilicates in terra Sirenum, mars. Geophys. Res. Lett. 37 (16)

– Goodall, T.M., North, C.P., Glennie, K.W., 2000. Surface and subsurface sedimentary structures produced by salt crusts. Sedimentology 47 (1), 99–118

– Grazulis, S., et al., 2009. Crystallography open Database–an open-access collection of crystal structures. J. Appl. Crystallograph. 42 (4), 726–729

– Griffiths, A.D., Coates, A.J., Jaumann, R., Michaelis, H., Paar, G., Barnes, D., Josset, J.L., 2006. Context for the ESA exomars rover: the panoramic camera (PanCam) instrument. Int. J. Astrobiol. 5 (03), 269–275

– Hanley, J., Dalton, J.B., Chevrier, V.F., Jamieson, C.S., Barrows, R.S., 2014. Reflectance spectra of hydrated chlorine salts: the effect of temperature with implications for europa. J. Geophys. Res. 119 (11), 2370–2377

– Hanley, J., Chevrier, V.F., Barrows, R.S., Swaffer, C., Altheide, T.S., 2015. Near-and mid-infrared reflectance spectra of hydrated oxychlorine salts with implications for mars. J. Geophys. Res. 120 (8), 1415–1426

– Hooijschuur, J.H., Verkaaik, M.F.C., Davies, G.R., Ariese, F., 2015. Will raman meet bacteria on Mars? An overview of the optimal raman spectroscopic techniques for carotenoid biomarkers detection on mineral backgrounds. Neth. J. Geosci doi: 10.1017/njg.2015.3

– Hardie, L.A., Eugster, H.P., 1970. In: The Evolution of Closed-Basin Brines, 3. Mineralogical Society of America Special Publication, pp. 273–290

– Houston, J., Hartley, A.J., 2003. The central andean west-slope rainshadow and its potential contribution to the origin of hyper-aridity in the atacama desert. Int. J. Climatol. 23 (12), 1453–1464

– Houston, J., 2006. Evaporation in the atacama Desert: an empirical study of spatio-temporal variations and their causes. J. Hydrol. 330 (3), 402–412

– Hunt, G.R., Salisbury, J.W., 1970. Visible and near infrared spectra of minerals and rocks. Mod. Geol. 1, 283–300

– Hynek, B.M., Beach, M., Hoke, M.R., 2010. Updated global map of martian valley networks and implications for climate and hydrologic processes. J. Geophys. Res. 115 (E9)

– Kabekkodu, S.N., Faber, J., Fawcett, T., 2002. New powder diffraction file (PDF-4) in relational database format: advantages and data-mining capabilities. Acta Crystallograph. Section B 58 (3), 333–337
Korablev, O., et al., 2015. Development of a mast or robotic arm-mounted infrared AOTF spectrometer for surface moon and mars probes. In: Proceedings of SPIE, Vol. 9608, pp. 960801–960807

– Korablev, O., et al., 2016. Infrared spectrometer for exomars (ISEM), a mast mounted instrument for the rover. Under reviews at. Astrobiology

– Langevin, Y., Poulet, F., Bibring, J.P., Gondet, B.,2005. Sulfates in the north polar region of mars detected by OMEGA/Mars express. Science 307 (5715), 1584–1586

– Loizeau, D., Mangold, N., Poulet, F., Bibring, J.P., Bishop, J.L., Michalski, J., Quantin, C., 2015. History of the clay-rich unit at mawrth Vallis, Mars: high-resolution mapping of a candidate landing site. J. Geophys. Res. 120 (11), 1820–1846

– Long, D.T., Fegan, N.E., McKee, J.D., Lyons, W.B., Hines, M.E., Macumber, P.G., 1992. Formation of alunite, jarosite and hydrous iron oxides in a hypersaline system: lake Tyrrell, Victoria, australia. Chem. Geol. 96 (1), 183–202

– Lynch, K.L., Horgan, B.H., Munakata-Marr, J., Hanley, J., Schneider, R.J., Rey, K.A., Spear, J.R., Jackson, W.A., Ritter, S.M., 2015. Near-infrared spectroscopy of lacustrine sediments in the great salt lake Desert: an analog study for martian paleolake basins. J. Geophys. Res. 120 (3), 599–623

– Martini, S., Monaghan, E.P., Flahaut, J., Martinot, M., Aerts, J.W., Myrgorodska, I., Meinert, C., Meierhenrich, U.J., Ehrenfreund, P., 2016. Biomolecule preservation in mars soil analogues. Biomarkers and Molecular Isotopes: International Workshop of Organic Geochemistry. Osaka, Japan July 4-5

– Massé, M., Bourgeois, O., Le Mouélic, S., Verpoorter, C., Le Deit, L., Bibring, J.P., 2010. Martian polar and circum-polar sulfate-bearing deposits: sublimation tills derived from the north polar cap. Icarus 209 (2), 434–451

– Maurice, S., Wiens, R.C., Le Mouélic, S., Anderson, R., Beyssac, O., Bonal, L., Clegg, S., DeFlores, L., Dromart, G., Fischer, W., Forni, O., 2015. The supercam instrument for the Mars2020 rover. In: European Planetary Science Congress 2015, Vol. 10, p. 185. Abstract #EPSC2015-185

– McArthur, J.M., Turner, J.V., Lyons, W.B., Osborn, A.O., Thirlwall, M.F.,1991. Hydrochemistry on the yilgarn block, western Australia: ferrolysis and mineralisation in acidic brines. Geochim. Cosmochim. Acta 55 (5), 1273–1288

– McKay, C.P., Friedmann, E.I., Gómez-Silva, B., Cáceres-Villanueva, L., Andersen, D.T., Landheim, R., 2003. Temperature and moisture conditions for life in the extreme arid region of the atacama Desert: four years of observations including the el niño of 1997-1998. Astrobiology 3 (2), 393–406

– Michalski, G., Böhlke, J.K., Thiemens, M.,2004. Long term atmospheric deposition as the source of nitrate and other salts in the atacama Desert, Chile: new evidence from mass-independent oxygen isotopic compositions. Geochim. Cosmochim. Acta 68 (20), 4023–4038

– Michalski, J.R., Niles, P.B., 2010. Deep crustal carbonate rocks exposed by meteor impact on Mars, nat. Geosci 3, 751–755. doi: 10.1038/ngeo971

– Monaghan et al., Amino acids and signs of life in atacama desert soils, in prep. 2016. Morris, R.V., et al., 2015. Transmission X-ray diffraction (XRD) patterns relevant to the MSL chemin amorphous component: sulfates and silicates. Lunar Planet. Sci. XLII Abstract #2434

– Mougenot, B., Zante, P., Montoroi, J.P., 1990. Détection e t évolution saisonnière des sols salés et acidifiés du domaine jluvio-marin de basse casamance au sénégal par imagerie satellitaire. Télédétection et sécheresse. Paris, Aupelf-Uref, John Libbey Eurotext 173–179

– Mougenot, B., 1993. Effets des sels sur la réflectance et télédétection des sols salés. Cahiers ORSTOM, Serie Pedologie 28, 45–54. Murchie, S., et al., 2007. Compact reconnaissance imaging spectrometer for Mars (CRISM) on Mars reconnaissance orbiter (MRO). J. Geophys. Res 112 (E5), E05S03 `http://dx.doi.org/10.1029/2006JE002682..`

– Murchie, S.L., et al., 2009. A synthesis of martian aqueous mineralogy after 1 Mars year of observations from the Mars reconnaissance orbiter. J. Geophys. Res. 114, E00D06 `http://dx.doi.org/10.1029/2009JE003342..`

– Navarro-González, R., Rainey, F.A., Molina, P., Bagaley, D.R., Hollen, B.J., de la Rosa, J., Small, A.M., Quinn, R.C., Grunthaner, F.J., Cáceres, L., Gomez-Silva, B., 2003. Mars-like soils in the Atacama Desert, Chile, and the dry limit of microbial life. Science 302 (5647), 1018–1021

– Noel, A., Bishop, J.L., Al-Samir, M., Gross, C., Flahaut, J., McGuire, P.C., Weitz, C.M., Seelos, F., Murchie, S., 2015. Mineralogy, morphology and stratigraphy of the light-toned interior layered deposits at juventae chasma. Icarus 251, 315–331

– Osterloo, M.M., et al., 2008. Chloride-bearing materials in the southern highlands of mars. Science 319 (5870), 1651–1654

– Osterloo, M.M., Anderson, F.S., Hamilton, V.E., Hynek, B.M., 2010. Geologic context of proposed chloride-bearing materials on Mars. J. Geophys. Res. 115 (E10)

– Piatek, J.L., Hardgrove, C., Moersch, J.E., Drake, D.M., Wyatt, M.B., Rampey, M., Carlisle, O., Warren-Rhodes, K., Dohm, J.M., Hock, A.N., Cabrol, N.A., 2007. Surface and subsurface composition of the life in the Atacama field sites from rover data and orbital image analysis. J. Geophys. Res.: Biogeosciences 112 (G4)

– Pieters, C.M., Boardman, J., Buratti, B., Chatterjee, A., Clark, R., Glavich, T., Green, R., Head, J., Isaacson, P., Malaret, E., McCord, T., 2009. The Moon mineralogy mapper (M3) on Chandrayaan-1. Curr. Sci 96 (4), 500–505

– Pilorget, C., Bibring, J.P., 2013. NIR reflectance hyperspectral microscopy for planetary science: application to the micromega instrument. Planet. Space Sci. 76, 42–52

– Poulet, F., et al., 2005. Phyllosilicates on Mars and implications for early martian climate. Nature 438, 623–627 http://dx.doi.org/10.1038/nature04274..

– Rech, J.A., Quade, J., Hart, W.S., 2003. Isotopic evidence for the source of ca and s in soil gypsum, anhydrite and calcite in the Atacama desert, Chile. Geochim. Cosmochim. Acta 67 (4), 575–586

– Risacher, F., Alonso, H., Salazar, C., 2002. Hydrochemistry of two adjacent acid saline lakes in the andes of northern chile. Chem. Geol. 187 (1–2) 39–35

– Risacher, F., Alonso, H., Salazar, C., 2003. The origin of brines and salts in Chilean salars: a hydrochemical review. Earth-Sci. Rev. 63 (3), 249–293

– Squyres, S.W., et al., 2006. Two years at meridiani Planum: results from the opportunity rover. Science 313, 1403–1407 http://dx.doi.org/10.1126/science.1130890.

– Stack, K.M., Milliken, R.E., 2011. Reflectance spectroscopy of clay–sulfate mixtures: implications for quantifying hydrated minerals and determining depositional environments on Mars. Lunar Planet. Sci. XLII Abstract #2024

– Stivaletta N., Barbieri R, Billi D., 2012. Microbial colonization of the salt deposits in the driest place of the Atacama desert (Chile), orig life evol biosph. 2012 Jun; 42 (2-3): 187–200. doi: 10.1007/s11084-012-9289-y

– Stoertz, G.E., & Ericksen, G.E., 1974. Geology of salars in northern Chile (No. 811). USGPO

– Sutter, B., Dalton, J.B., Ewing, S.A., Amundson, R., McKay, C.P., 2007. Terrestrial analogs for interpretation of infrared spectra from the martian surface and sub-surface: Sulfate, nitrate, carbonate, and phyllosilicate-bearing Atacama desert soils. J. Geophys. Res.: Biogeosciences 112 (G4). USGS, 2015. Provisional landsat 8 surface reflectance product guide. http://landsat.usgs.gov/documents/provisional_l8sr_product_guide.pdf

– Vasquez, C., Ortiz, C., Suárez, F., Muñoz, J.F., 2013. Modeling flow and reactive transport to explain mineral zoning in the atacama salt flat aquifer, Chile. J. Hydrol. 490, 114–125

– Verkaaik, M.F.C., Hooijschuur, J.H., Davies, G.R., Ariese, F., 2015. Raman spectroscopic techniques for planetary exploration: detecting microorganisms through minerals. Astrobiology 15, 697–707

– Wang, A., Jolliff, B.L., Liu, Y., Connor, K., 2016. Setting constraints on the nature and origin of the two major hydrous sulfates on Mars: monohydrated and polyhydrated sulfates. J. Geophys. Res. Planets 121, 678–694. doi: 10.1002/ 2015JE004889

– Wettergreen, D., Bapna, D., Maimone, M., Thomas, G., 1999. Developing nomad for robotic exploration of the Atacama desert. Robot. Autonom. Syst. 26 (2), 127–148

– Wray, J.J., Milliken, R.E., Dundas, C.M., Swayze, G.A., Andrews-Hanna, J.C., Baldridge, A.M., Chojnacki, M., Bishop, J.L., Ehlmann, B.L., Murchie, S.L., Clark, R.N., 2011. Columbus crater and other possible groundwater-fed paleo-lakes of Terra Sirenum, Mars. J. Geophys. Res. 116 (E1)

– Wray, J.J., Murchie, S.L., Bishop, J.L., Ehlmann, B.L., Milliken, R.E., Wilhelm, M.B., Seelos, K.D., Chojnacki, M., 2016. Orbital evidence for more widespread carbonate-bearing rocks on Mars. J. Geophys. Res. Planets 121, 652–677. doi: 10.1002/ 2015JE004972

– Wynne, J.J., Titus, T.N., Diaz, G.C., 2008. On developing thermal cave detection techniques for Earth, the Moon and Mars. Earth Planet. Sci. Lett. 272 (1), 240–250.

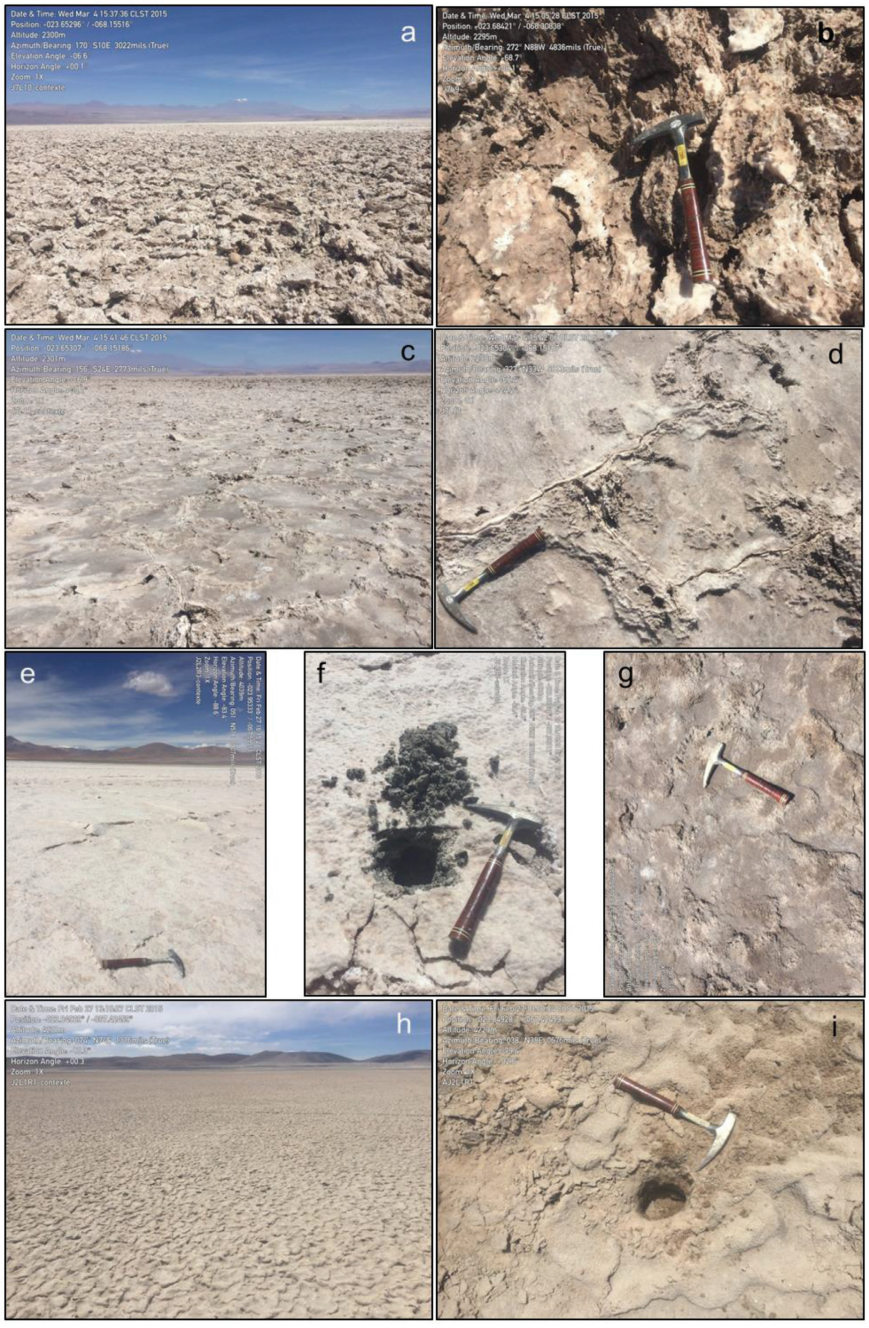

Figure A.4: Field impressions and crust types. a to f: hard crust, type 1 (a to d = Salar de Atacama, a = J7L10, b = J7L9 with c and d being a wetter, transition zone (J7L11)) and type 2 (e,f = Laguna Tuyajto (J2L2R3)). g to i: soft, dry crust (type 3), g = Salar de Quisquiro (J11L1R4), h, i = Salar de Laco (J2L1R1). j,k,l: type 4 soft, moist crust (j = Laguna de Cejar (J9L1), k = Laguna Tuyajto (J2L2R2), l = Salar de Quisquiro (J11L1R3)). m, n, o: type 5 clay playa m, n = northern Salar de Atacama (J8L1), o = Laguna Tuyajto (J2L2R4) .p, q: type 6 beach pebbles at Salar de Aguas Calientes 3 (J5L1R3).

Figure A.4: Continued

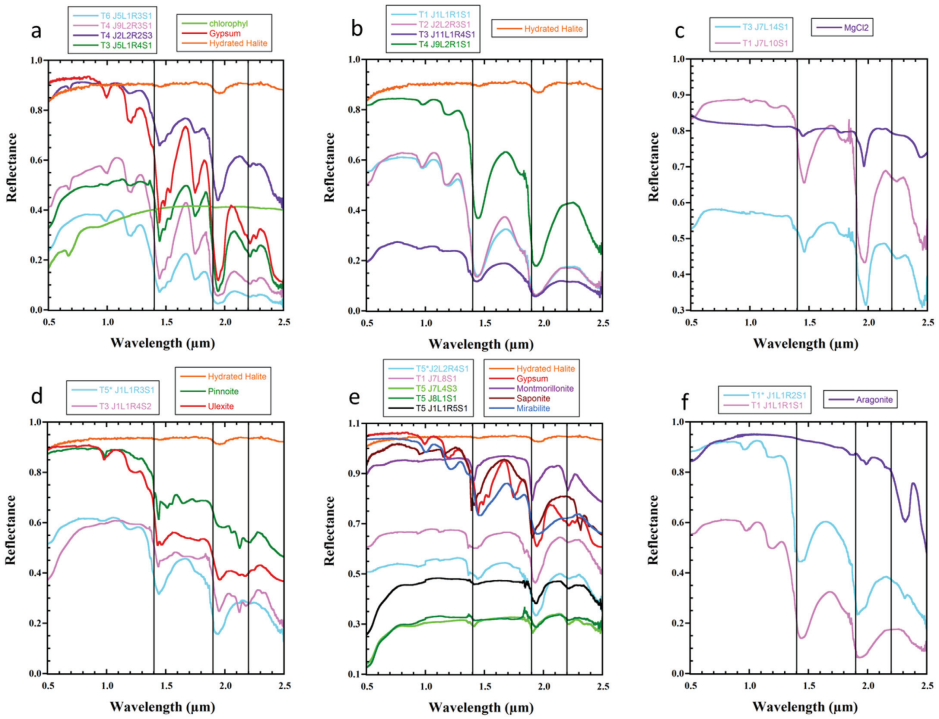

Figure A.5: VNIR reflectance spectra of selected field samples are compared with reference library spectra (Source: USGS spectral library, unless specify otherwise). a) Gypsum- bearing spectra from the Salar de Aguas Calientes 3 (J5L1R3, J5L1R4), laguna Tuyajto (J2L2R2) and laguna de la Piedra (J9L2R3). The rounded 1.9 μm band in samples J5L1R3 and J9L2R3 is best matched by a mixture of gypsum and another hydrated material such as the hydrated halite presented in b. b) Featureless, water-bearing spectra of samples from the Salar de Atacama (J1L1R1), Salar de Quisquiro (J11L1R4), Laguna Tuyajto (J2L2R3), laguna de la Piedra (J9L2R1) are all consistent with hydrated material, which is identified by morphologic observations as (hydrated) halite. c) Shifted water absorptions in some samples from the Salar de Atacama (J7L10, J7L14) and a kink at 2.24 μm are more consistent with $MgCl_2$ (reference spectra from Bishop et al., 2014c). d) In the central part of the Salar de Atacama, and in the marginal area of laguna Chaxa, mixtures of pinnoite and ulexite (J1L1R4) and halite and pinnoite (J1L1R3) can be inferred from VNIR spectra. e) Absorptions in the spectra collected at laguna Tuyajto (J2L2R4) and various locations of the Salar de Atacama (J7L4, J7L8, J8L1, J1L1R5) are consistent with mixed halite and Al-rich clays such as montmorillonite (e.g., J7L4). The width of the 1.4 μm absorption feature suggest the additional presence of Ca or Na-sulfates such as gypsum or mirabilite in samples J7L8 and J2L2R4. f) Absorptions in spectrum J1L1R2 are consistent with a mixture of hydrated halite (such as in J1L1R1) and carbonates such as aragonite (reference spectra from Bishop et al., 2013).

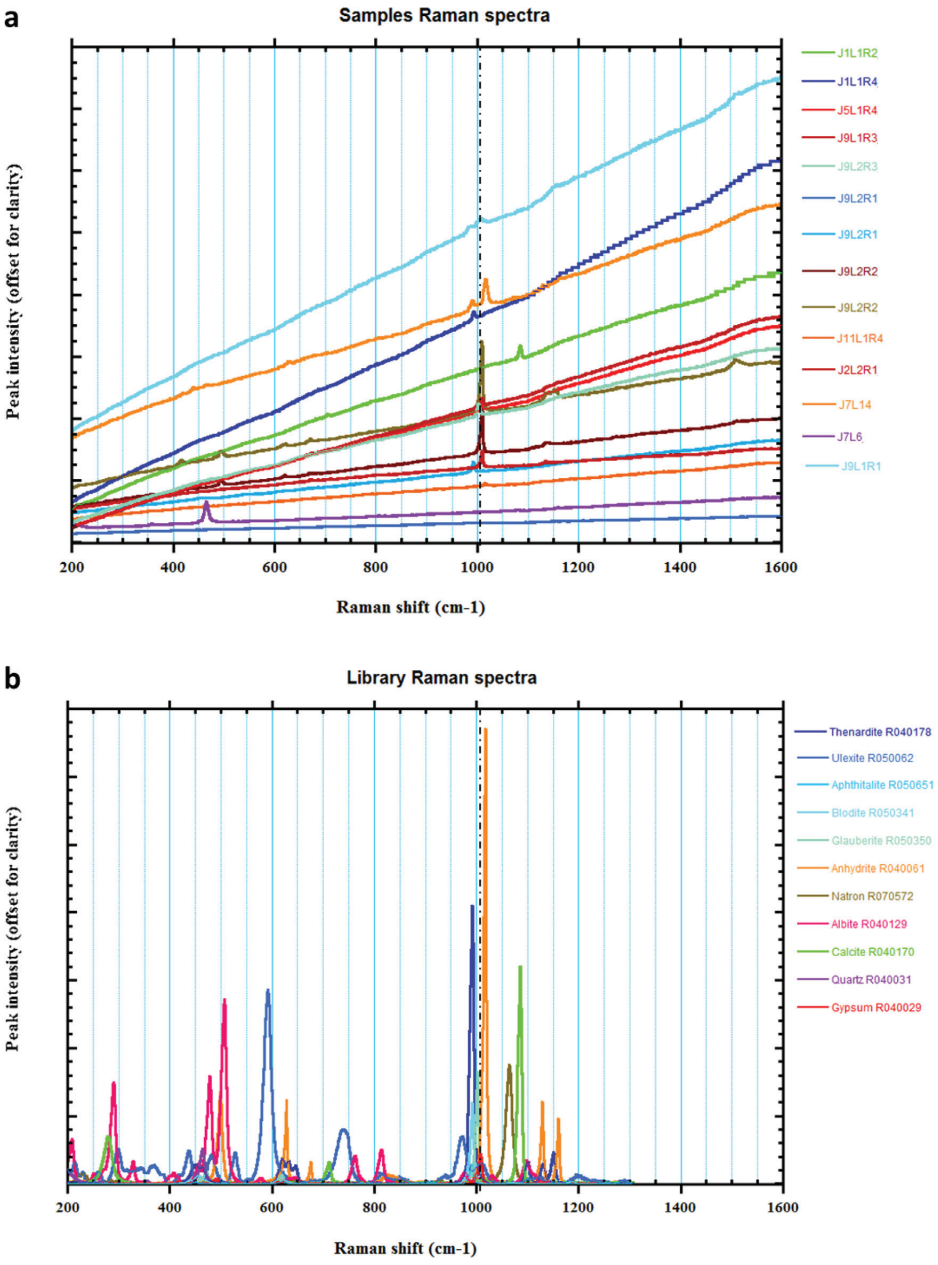

Figure A.6: a) Raman spectra of a subset of samples that showed interesting peaks. b) Reference library spectra of the minerals commonly identified in the samples are given for comparison. The black dashed line indicate the location of the main gypsum peak at 1007, which is detected in most samples.

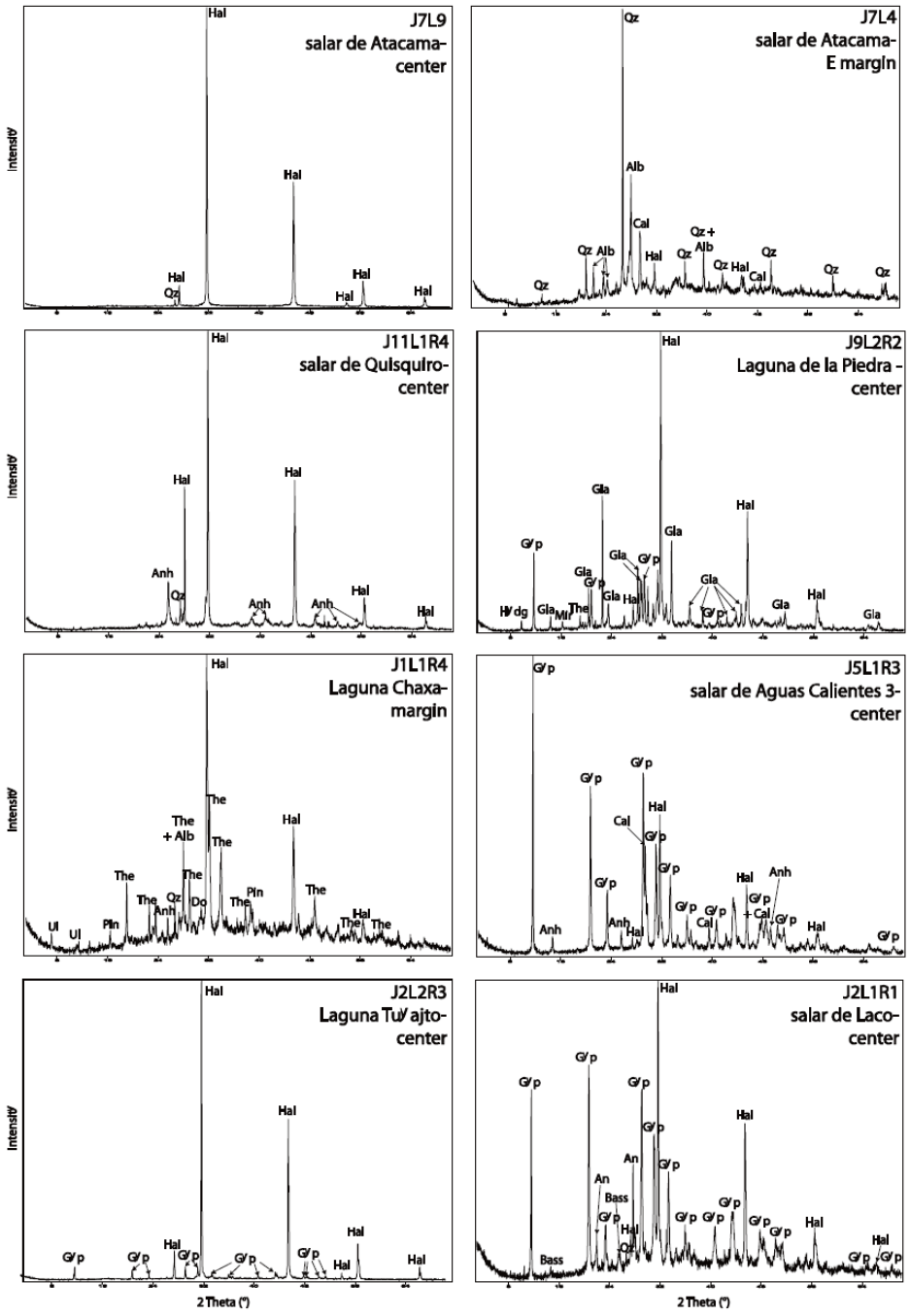

Figure A.7: XRD patterns of a set of representative samples. The strongest peaks are identified for each sample. Hal = halite, Gyp = gypsum, Qz = quartz, Anh = anhydrite, The = thenardite, Ul = ulexite, Pin = pinnoite, Do = dolomite, Alb = albite, Cal = calcite, Hydg = hydroglauberite, Gla = glauberite, Mir = mirabilite, An = anorthite, Bass = bassanite.

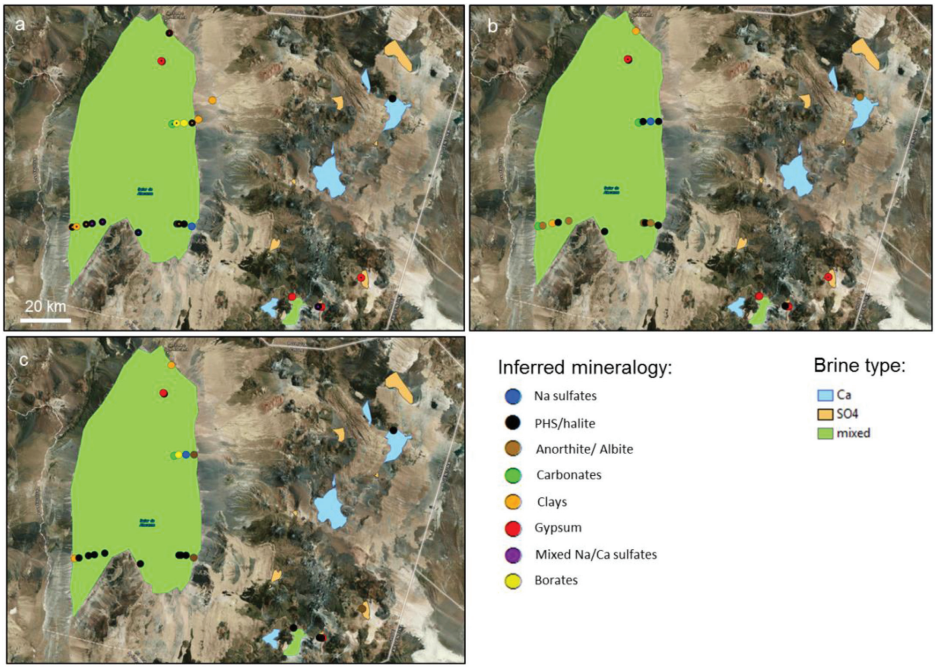

Figure A.8: Comparison of the mineralogy ("dominant" mineral phase in each sample) inferred from various instrument data (also see Table A.3). a) Spectrally dominant mineral as interpreted from the VNIR spectra, b) Spectrally dominant mineral as interpreted from Raman spectra (superimposed black points indicate the presence of carotenoids), c) Dominant mineral (= most abundant in this case) as interpreted from XRD patterns. Outlines of the salars are colored according to the type of brines they originate from (blue = Ca-rich, red = SO_4-rich, magenta = mixed brines (from Risacher et al., 2003). There is a general agreement between the various instrument data, although some minerals can be masked or dominate the VNIR spectra when mixed with other material (see Section A.5.1).

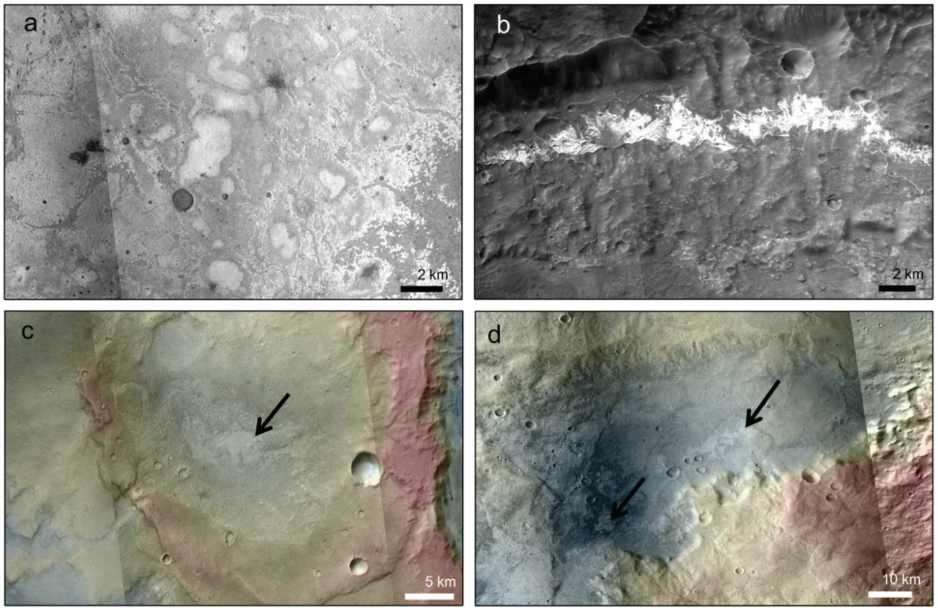

Figure A.9: Example of salt-rich deposits on Mars (Context Camera images at 6 m/pixel, Mars Reconnaissance Orbiter mission). a) Sulfate-rich salt pans and karstic features in the Meridiani Planum region of Mars (modified after J. Flahaut et al., 2015), b) Sulfate-rich deposits of groundwater origin deposited on a bench in the Columbus crater wall (modified after Wray et al., 2011), c) Proposed chloride-bearing deposits from Osterloo et al. (2010), located in a topographic low south of the Meridiani Planum area (Colorized MOLA elevation is projected in transparency over CTX imagery, elevations range from -1800 m (blue) to -1000 m (red)). Proposed chloride-bearing deposits from Osterloo et al. (2010), located in the Terra Sirenum region of Mars (Colorized MOLA elevation is projected in transparency over CTX imagery, elevations range from 2100 m (blue) to 3200 m (red)).